Beiträge zur Geologie der Schweiz, Geotechnische Serie
Materiaux pour la Géologie de la Suisse, Série Géotechnique

No. 93, 2000

Zirconolite: Experiments on the Stability in Hydrothermal Fluids

Jan Christian Malmström

Herausgegeben von der Schweizerischen Geotechnischen Kommission
Publié par la Commission Géotechnique Suisse

ISBN 3-907997-26-3
ISSN 0582-1630

BEITRÄGE ZUR GEOLOGIE DER SCHWEIZ
GEOTECHNISCHE SERIE
herausgegeben von der
Schweizerischen Geotechnischen Kommission
(Organ der Schweizerischen Akademie der Naturwissenschaften)

Lieferung
93

MATERIAUX POUR LA GEOLOGIE DE LA SUISSE
SERIE GEOTECHNIQUE
publiés par la
Commission Géotechnique Suisse
(Organe de l'Académie Suisse des Sciences Naturelles)

Zirconolite: Experiments on the Stability in Hydrothermal Fluids

Jan Christian Malmström

2000

Vertrieb durch die Schweizerische Geotechnische Kommission, ETH-Zentrum, 8092 Zürich
Publiziert mit Unterstützung der Schweizerischen Akademie der Naturwissenschaften

Dissertationsschrift, Diss ETH Nr. 13717
Eidgenössische Technische Hochschule Zürich, 2000
Referent: Prof. Dr. V. Trommsdorff
Korreferenten: Dr. E. Reusser, Prof. Dr. R. Gieré, Dr. G.R. Lumpkin

Dissertation ermöglicht mit finanzieller Unterstützung durch ETH-Fonds Nr. 31706.

Der Druck dieser Arbeit wurde teilweise durch den Werenfels-Fonds der Freiwilligen Akademischen Gesellschaft Basel sowie durch das Institut für Mineralogie und Petrographie der ETH Zürich finanziert.

Redaktion und Satz: Schweizerische Geotechnische Kommission
Lithographie und Druck: Fotorotar AG, 8132 Egg/ZH
Gedruckt auf chlorfrei gebleichtem Papier

ISBN 3-907997-26-3; ISSN 0582-1630

VORWORT DER SCHWEIZERISCHEN GEOTECHNISCHEN KOMMISSION

Die sichere oder risikoarme Endlagerung von mittel- und hochradioaktiven Abfällen stellt weltweit eines der grössten Umweltprobleme unserer modernen Gesellschaft dar und hat in jüngster Zeit zunehmend zu massiven Diskussionen und Protesten in der breiten Öffentlichkeit geführt. Insbesondere die ausgeprägte Langlebigkeit einiger Abfallprodukte stellt sehr hohe Anforderungen sowohl an den geologischen Untergrund wie auch an die Bauweise und die Abdichtung eines möglichen Endlagers.

Die vorliegende Arbeit von Herrn Jan Malmström befasst sich mit der Korrosionsbeständigkeit des Minerals Zirkonolit, einer Hauptkomponente von Synroc (synthetisches Gestein zur Verfestigung und Endlagerung von flüssigen, radioaktiven Abfallstoffen), bei erhöhten Druck- und Temperaturbedingungen in verschiedenen Flüssigkeiten. Sie beruht im Wesentlichen auf einer an der ETH Zürich ausgeführten Dissertation und stellt eine wertvolle Ergänzung zu früheren materialtechnologischen und mineralogischen Publikationen in der Reihe der «Beiträge zur Geologie der Schweiz, Geotechnische Serie» dar.

Zirkonolit kann sowohl Aktiniden als auch einige Spaltprodukte derselben im Kristallgitter einbauen und spielt somit eine wichtige Rolle in Synroc. Als Träger von radioaktiven Abfällen sollte Zirkonolit stark korrosionsbeständig sein.

Ziel der vorliegenden Arbeit ist es, anhand von zahlreichen hydrothermalen Experimenten die Stabilität von Zirkonolit in verschiedenen fluiden Lösungen über einen weiten Temperatur- und Druckbereich aufzuzeigen, wie er in einem Endlager durch Wärmeproduktion beim radioaktiven Zerfall einerseits und durch die Gebirgsüberlast andererseits zu erwarten ist. In sauren Flüssigkeiten konnte dabei bis 500 °C lediglich eine schwache Korrosion von Zirkonolit, und bei höheren Temperaturen eine etwas ausgeprägtere Alteration zu Rutil und Anatas festgestellt werden. In basischen Lösungen hat sich dagegen gezeigt, dass Zirkonolit in Abhängigkeit von Druck und Themperatur zusehends instabil wird und zu Perowskit, Calzirtit sowie bei höherem Druck auch Baddeleyit zerfällt. Die dabei freigesetzten radioaktiven Abfallstoffe werden jedoch sofort wieder in diese sekundären Produktphasen, insbesondere Perowskit, eingebaut und können somit nicht aus dem System entweichen. Dieses Resultat ist besonders wichtig hinsichtlich einer langfristigen Prognose für die Sicherheit eines Endlagers.

Da in einem Endlager dennoch immer das Risiko eines direkten Kontaktes zwischen radioaktiven Abfallstoffen und dem Grundwasser besteht, ist ein zusätzlicher Schutz durch äussere Barrieren stets notwendig. Diese sollten eindringendes Wasser zu einem hohen pH-Wert puffern können, um die Bildung von Perowskit als sekundärer Abfallbinder beim Zerfall von Zirkonolit zu begünstigen. Zu diesem Zweck eignen sich Zement und Bentonit als technische Barrieren am besten.

Die Schweizerische Geotechnische Kommission dankt dem Autor für die Möglichkeit, diese wertvolle, zukunftsorientierte Arbeit in ihre Schriftenreihe aufzunehmen, sowie für die gute Zusammenarbeit und die sorgfältige Durchsicht des Manuskriptes bei der Drucklegung.

Im weiteren sei dem Werenfels-Fonds der Freiwilligen Akademischen Gesellschaft Basel und dem Institut für Mineralogie und Petrographie für deren finanzielle Unterstützung beim Druck der vorliegenden Arbeit gedankt.

Für den Inhalt von Text, Tabellen und Figuren ist der Autor allein verantwortlich.

Zürich, im Dezember 2000

Der Präsident der Schweizerischen Geotechnischen Kommission

V. Dietrich

ACKNOWLEDGEMENTS

The time I worked on my PhD at the Mineralogical Institute of the ETH Zürich was an interesting experience for me. The thesis arose under the supervision of Prof. Dr. V. Trommsdorff and Prof. Dr. R. Gieré, and was additionally accompanied by Dr. E. Reusser and Dr. G. Lumpkin. Thank you Reto for starting the whole project and to all others for their support. Most work was carried out at the Mineralogical Institute of the ETH Zürich. In the meanwhile, I got the chance for three trips to Sydney to spend some time at the Materials Division of ANSTO, where I learned to fabricate ceramic samples and to work on the transmission electron microscope. In addition I got the chance to see Australia not only as a tourist!

The experimental work was only possible because of the support of Sven Girsperger, who was very helpful during the whole thesis. He always provided very useful comments. Also a big thank you to Detlef Günther for providing me high-precision data from the (LA-)ICP-MS. In addition a big hug to the whole SEM-Team at Basel (Marcel, Däni and Prof. Guggenheim) for the excellent ESEM support. Thanks also to the workshop (Bruno Zürcher and Urs Graber) for providing the technical support.

A big thank you to all my collegues at ETH, also for the «social» support, namely Ralf Kägi, Andi Meier, Andi Stucki, André Puschnig, Othmar Münthener, Anne-Chantal Risold, Caterina Talerico, Trudi Semeniuk, Marcel Pfiffner, Roger Rütti, and my «poor» office collegue Felix Mattenberger. Also a big thanks to my mates down under: Kath Smith, Lou Vance, Kay Hart, Tim Nicholls, Michael Colella, Darren Attard, Bruce Begg, Gordon Thorogood, Christopher Barbe, Gilles Leturcq, Kim Finnie (thanks for the IR-work) and all others.

A big kiss to all my family and my girlfriend Silvia for their support and patience.

This study was made possible by the financial support of the ETH grant Nr. 31706. In addition, many thanks to the Swiss Geotechnical Commission (especially Rainer Kündig and Marcel Pfiffner) for facilitating and printing this publication as well as to the Werenfels-Fonds and the Institute for Mineralogy and Petrography for their financial support which made this publication possible.

TABLE OF CONTENTS

LISTS OF TABLES AND FIGURES

List of tables

List of figures

ABSTRACT

Zirconolite, ideally $CaZrTi_2O_7$, is a major constituent of Synroc nuclear waste forms. Synroc is a synthetic rock, designed to solidify and dispose liquid, radioactive high-level waste (HLW), where zirconolite acts as a principal host phase for actinides and certain fission products (e.g., rare earth elements). As a host for HLW at the disposal site, it has to be highly corrosion resistant. A high resistance against corrosion is reported from the natural occurrence of zirconolite and from experiments in deionized water at temperatures up to 150 °C. In this thesis, the stability of zirconolite at higher temperatures, at elevated pressure, and in various fluids has been investigated. Hydrothermal experiments were carried out over a temperature range from 150 up to 700 °C, at pressures of 50 and 200 MPa. Beside deionized water, diluted NaOH, HCl, H_3PO_4, SiO_2, and CO_2 fluids were used to study the corrosion behavior of zirconolite. As starting material single-phase, polycrystalline zirconolite-2M, doped with REEs, Hf and U as actinide analogues and/or neutron absorbers was used. Experiments were performed in a closed system in externally heated pressure vessels. Fluid run products and solid reaction products were analyzed by various analytical techniques, including ESEM, SEM, TEM, EPMA, XRD, RAMAN-spectroscopy, IR-spectroscopy, and ICP-MS.

In general, the results indicate that zirconolite is not corroded at the resolution of ESEM at temperatures below 250 °C, but they reveal various degrees of alteration at higher temperatures. In acidic environments (HCl, H_3PO_4), corrosion is weak up to 500 °C, but more pronounced above that temperature, and various TiO_2 phases, including rutile and anatase, are observed as alteration products (possibly quench phases). In a basic environment (NaOH), on the other hand, zirconolite shows increasing corrosion up to 500 °C. At this temperature and at 50 MPa, zirconolite breaks down to the solid product phases perovskite ($CaTiO_3$), calzirtite ($Ca_2Zr_5Ti_2O_{16}$), and hydrated Al in the fluid. At a higher pressure (200 MPa), the solid breakdown products are perovskite and baddeleyite (ZrO_2).

Further investigations focused on the relationship between primary zirconolite and the secondary product phases. For the experiments in acidic fluids, no chemical or structural details could be obtained due to the limited size and number of product phases. They could be phases formed during temperature quench of the experiments. Different though for the product phases after experiments in NaOH, where line scans by AEM revealed a sharp chemical boundary between perovskite and zirconolite. They also indicated that more weight units of REE are incorporated into the secondary perovskite than were present in primary zirconolite. This may be seen as an increasing incorporation during fractionation of all released REE into perovskite. The high-resolution TEM analysis from a grain boundary revealed epitaxial growth of perovskite on zirconolite.

Our data provide information on the time-dependent fractionation of the waste elements and neutron absorbers released from zirconolite, between the fluid and the different product phases. Those elements were determined in much higher concentrations in acidic fluids (HCl) than in basic fluids (NaOH). In the latter case, they are preferentially incorporated into the product phases perovskite and calzirtite. Most of the large cations (e.g., trivalent REEs) fractionate, controlled by their ionic size, on the large Ca site in perovskite.

The presence of Na or possibly other alkalis in the fluid are very important for the mobilization of the HFSE.

All data indicate that the corrosion and formation of product phases is strongly dependent on the ionic strength, the composition of the fluid, time, temperature, and pressure. Although our results obtained by electron microscopy document zirconolite breakdown in strong NaOH at temperatures above 500 °C, they provide clear evidence for retention of most of the actinide analogues and neutron absorbers by the breakdown phases. These phases thus may act as secondary waste form. These data are essential for the assessment of the long-term behavior of zirconolite-based nuclear waste forms in final repositories.

Even though zirconolite never acts as single waste form and always is surrounded by additional outer barriers (technical and geological), a certain risk for contact with the fluid in the repository exists. Therefore, the closely related environment of the wasteform itself should buffer the incoming fluid towards a Na-rich fluid with a high pH to force the system to form perovskite, if a certain temperature (~500 °C) is reached. This may be achieved by the technical barriers bentonite and concrete and by a geologic environment like clays or salts.

ZUSAMMENFASSUNG

Zirkonolit, stöchiometrisch geschrieben als $CaZrTi_2O_7$, ist eine Hauptkomponente von Synroc. Dieses synthetische Gestein wurde zur Verfestigung und späteren Endlagerung von flüssigen, radioaktiven Abfallstoffen (hochaktiv) entwickelt. Zirkonolit spielt darin eine wichtige Rolle als Hauptphase für den Einbau von Aktiniden sowie einiger Spaltprodukte (z.B. seltene Erden) im Kristallgitter. Als Träger von hochaktiven Abfällen sollte Zirkonolit stark korrosionsbeständig sein. Diese Eigenschaft wird durch sein natürliches Vorkommen und Experimente in deionisiertem Wasser bei Temperaturen bis 150 °C prognostiziert. Während dieser Arbeit soll nun die Beständigkeit von Zirkonolit bei höheren Temperaturen, erhöhtem Druck und in verschiedenen Flüssigkeiten untersucht werden. Dazu wurden hydrothermale Experimente über einen Temperaturbereich von 150 bis 700 °C bei einem Druck von 50 und 200 MPa ausgeführt. Neben deionisiertem Wasser wurden auch verdünnte Lösungen mit HCl, NaOH, H_3PO_4, SiO_2 und CO_2 verwendet. Als Ausgangsmaterial dienten einphasige, polykristalline Zirkonolite (2M), welche mit seltenen Erden, Hafnium sowie Uran versetzt wurden. Diese Elemente dienten als Analogmaterialien für Aktinide sowie als Neutronenabsorber. Die Experimente wurden in aussenbeheizten Druckgefässen, also in einem geschlossenen System ausgeführt. Sowohl feste als auch flüssige Produkte der Experimente wurden durch verschiedene analytische Methoden untersucht (Umwelt Raster Elektronenmikroskop (UREM), Raster Elektronenmikroskop (REM), Transmissions Elektronenmikroskop (TEM), Mikrosonde (EPMA), XRD, RAMAN-Spektroskopie, IR-Spektroskopie sowie ICP-MS).

Ganz allgemein gesehen zeigen die Resultate, dass bei Temperaturen unter 250 °C mit dem UREM auf der Oberfläche von Zirkonolit keine Korrosion erkannt wird. Bei höheren Temperaturen wurden dann verschiedene Stufen von Umwandlungen festgestellt. In sauren Flüssigkeiten (HCl, H_3PO_4) wurde bis 500 °C nur eine schwache Korrosion festgestellt. Bei höheren Temperaturen ist diese dann ausgeprägter, und verschiedene TiO_2 Phasen (Rutil und Anatas) treten als Alterationsprodukte auf (möglicherweise als Ausfällung während der Abkühlungsphase). Andererseits zeigt Zirkonolit in basischen Flüssigkeiten (NaOH) stetig zunehmende Alterationsspuren. Bei einem Druck von 50 MPa wird Zirkonolit oberhalb von 500 °C instabil und durch die Produktphasen Perowskit ($CaTiO_3$) und Calzirtit ($Ca_2Zr_5Ti_2O_{16}$) ersetzt. Bei einem höheren Druck von 200 MPa kann dann Baddeleyit (ZrO_2) neben Perowskit als Produkt festgestellt werden.

Weitere Untersuchungen waren auf die Beziehung zwischen dem Ausgangsmaterial und den sekundären Produktphasen ausgelegt. Für die Experimente in saurer Lösung konnten keine chemischen oder strukturellen Details bestimmt werden, was auf die begrenzte Grösse und Anzahl der sekundären Produktphasen zurückzuführen ist. Diese könnten aber wegen ihres oberflächlichen Auftretens auch während dem Temperaturabfall als Ausfällung entstanden sein. Demgegenüber stehen die Resultate der Experimente in basischen Lösungen. Mit AEM konnte eine scharfe chemische Grenze zwischen Zirkonolit und Perowskit festgestellt werden. Diese zeigten auch, dass mehr seltene Erden (in Gewichts-Einheiten) in sekundärem Perowskit als im Ausgangsmaterial vorhanden sind. Dies wiederum kann als eine Anreicherung während der Fraktionierung aller frei gewordenen seltenen Erden betrachtet werden. Mit dem TEM gemachte hochauflösende Strukturanalysen zeigen ein epitaxiales Wachsen von Perowskit auf Zirkonolit.

Unsere Daten geben auch Anhaltspunkte für die zeitabhängige Fraktionierung der von Zirkonolit stammenden Elemente zwischen den verschiedenen Produktphasen und dem Fluid. Die Konzentrationen dieser Elemente in sauren Lösungen sind bedeutend höher als in basischen. Im zweiten Fall wurden diese vorzugsweise in Perowskit und Calzirtit eingebaut. Aufgrund ihrer Ionengrösse wurden die meisten dieser Ionen auf den grossen Ca-Gitterplatz im Perowskit eingebaut.

Die Anwesenheit von Na oder allenfalls anderer Alkalielemente hat einen grossen Einfluss auf die Mobilisierung der HFSE.

Die Daten zeigen, dass die Korrosion von Zirkonolit sowie die Bildung von Produktphasen stark von der Ionenstärke und Zusammensetzung des Fluids sowie von der Zeit, der Temperatur und dem Druck abhängig ist. Obwohl unsere Daten die Instabilität von Zirkonolit in NaOH-reichen Lösungen bei Temperaturen oberhalb 500 °C zeigen, können auch klare Evidenzen für das Festhalten der Abfall simulierenden Elemente und Neutronenabsorber durch die

Produktphasen gegeben werden. Dabei übernehmen diese die Aufgabe eines sekundären Abfallrezipienten. Diese Daten sind wichtig für die Erstellung langfristiger Prognosen von auf Zirkonolit basierenden Abfallrezipienten in einem Endlager.

Obwohl Zirkonolit nie als einphasiger Abfallrezipient dienen wird und immer zusätzlicher Schutz durch äussere Barrieren (technisch und geologisch) notwendig ist, besteht immer ein Risiko zum direkten Kontakt mit dem Bodenwasser im Endlager. Deshalb sollte die benachbarte Umgebung des Abfalles das eindringende Wasser zu einem hohen pH und Na Gehalt puffern. Dadurch kann das System zur Bildung des sekundären Abfallrezipienten Perowskit gezwungen werden, falls die notwendige Temperatur erreicht wird (~500 °C). Dies wird am besten durch die technischen Barrieren Bentonit (Na reich) und Zement (hoher pH) und durch eine geeignete geologische Umgebung wie Tone oder Salze erreicht.

ABBREVIATIONS AND SYMBOLS USED

°C	Degree Celsius
Å	Angström
AC	Alternating Current
ACT	Actinides
AEM	Analytical Electron Microscopy Analysis
EDX	Energy Dispersive X-ray Spectroscopy
EELS	Electron Energy Loss Spectroscopy
EPMA	Electron Probe Microanalysis
ESEM	Environmental Scanning Electron Microscope
fO_2	Oxygen Fugacity
g	Gram
GPIB	General Purpose Interface Bus
h	Hour
HFSE	High Field Strength Elements
HLW	High Level Waste
HREE	Heavy Rare Earth Elements
ICP-MS	Inductively Coupled Plasma Mass Spectroscopy
ILW	Intermediate Level Waste
km	Kilometer
LLW	Low Level Waste
LREE	Light Rare Earth Elements
m	Meter
M	Molal
min	Minute
mm	Millimeter
MOX	Mixed Oxides
MPa	Mega Pascal
MW	Megawatt
nm	Nanometer
P	Pressure
PID	Proportional Integral Differential Controller
REE	Rare Earth Elements
rpm	Rotations per Minute
s	Second
SA/V	Solid Surface Area per Fluid Volume Ratio
SEM	Scanning Electron Microscope
SNF	Spent Nuclear Fuel
T	Temperature
t	Tons
TEM	Transmission Electron Microscope
µm	Micrometer

1 INTRODUCTION

1.1 General Introduction

The aim of this Ph.D. project is to investigate the stability of zirconolite in various hydrothermal fluids at elevated pressures and temperatures. Natural zirconolite is reported to be a host phase for various rare earth elements and actinides (e.g., U). Its occurrence in nature reveals a high corrosion resistance to natural ground and surface waters, even though it is often metamict due to the radioactive decay of the incorporated elements. Therefore zirconolite is used as a major constituent of the Synroc nuclear waste form, where it is a principal host phase for actinides and certain fission products. Synroc is designed for the disposal of high level nuclear waste (HLW).

Prior leaching experiments with Synroc in deionized water up to 150 °C revealed a high durability of zirconolite compared to the other phases present in Synroc. Following these results, the experiments during this thesis were designed to investigate zirconolite leaching up to higher temperatures and pressures and in an extended variety of fluid compositions. Single phase zirconolite was used as starting material to gather information on the behavior of the isolated zirconolite phase.

The work was mainly performed at the Institute of Mineralogy and Petrography of the Swiss Federal Institute of Technology in Zürich, where all experiments were carried out. Intervening working periods were carried out at the Materials Division of ANSTO in Sydney. In their laboratories, the starting material was synthesized and at a later stage of the project the solid product phases were analyzed by TEM. All investigations by ESEM were performed at the SEM Laboratory at University of Basel.

1.2 Nuclear Fuel Cycle

1.2.1 Introduction

During this thesis, detailed investigations of the behavior of zirconolite under specific conditions (fixed P, T, fluid) are made. However, those are only a small but important part of the the current major problems of safe radioactive waste disposal. This chapter gives some important background for a better understanding of the entire nuclear fuel cycle.

Since nuclear energy is part of our daily life (434 power plants produce 17% of the worldwide used electricity in 1998, NUCLEAR EUROPE WORLDSCAN, 1999), human beings have to deal with the resulting waste and its disposal. As a first necessary production step, several chemical processes generate nuclear fuel from mined uranium ore. This ore contains at least 0.1 wt% total uranium and has to be enriched up to 100% UO_2 with at least 3.2% $^{235}U/^{238}U$ needed for the chain reaction in thermal reactor types. During the burn down of the nuclear fuel, 1 kg uranium decomposes and forms 35 g fission products and 10 g transuranic elements (e.g., ^{85}Kr, ^{90}Sr, ^{137}Cs, ^{239}Pu). Most of the starting material (97%) may be reused after reprocessing as plutonium containing nuclear fuel (U-oxide + Pu-oxide => MOX-fuel) for fast reactor types (see figure 1.2.1). This process is also used for the production of plutonium needed for nuclear weapons.

Radioactive waste is defined as «material that contains or is contaminated with radionuclides at concentrations or activities greater than clearance levels established by the regulatory body and for which no use is foreseen» (IAEA, 1993). High level radioactive waste consists of spent nuclear fuel (SNF) from nuclear power reactors, liquid waste from reprocessing of spent nuclear fuel (high level waste: HLW) and waste generated by nuclear weapon manufacturing and dismantling during the next years. Today, two different ways of disposal are followed internationally. The first one is the direct disposal of spent nuclear fuel (SNF) after an adequate storing time (mainly USA). Other countries (Great Britain, France, Japan, and Switzerland) still follow the idea of reprocessing spent nuclear fuel by dissolving the fuel rods and regaining plutonium and uranium by chemical processes. The resulting highly radioactive liquid wastes (HLW) have to be solidified by vitrification or inclusion into ceramics to produce an appropriate waste form, which then can be disposed. Reprocessing reduces the waste volume but adds an additional dangerous process step and creates more mobile liquid materials.

All these processes also produce a certain amount of radioactive intermediate level (ILW) and low level waste (LLW). Such LLW is also produced by different applications in medicine, science and during processing of consumer goods and food. New projects plan a monitored safe disposal giving the possibility to recycle any waste after new technical developments in the future. Waste classifica-

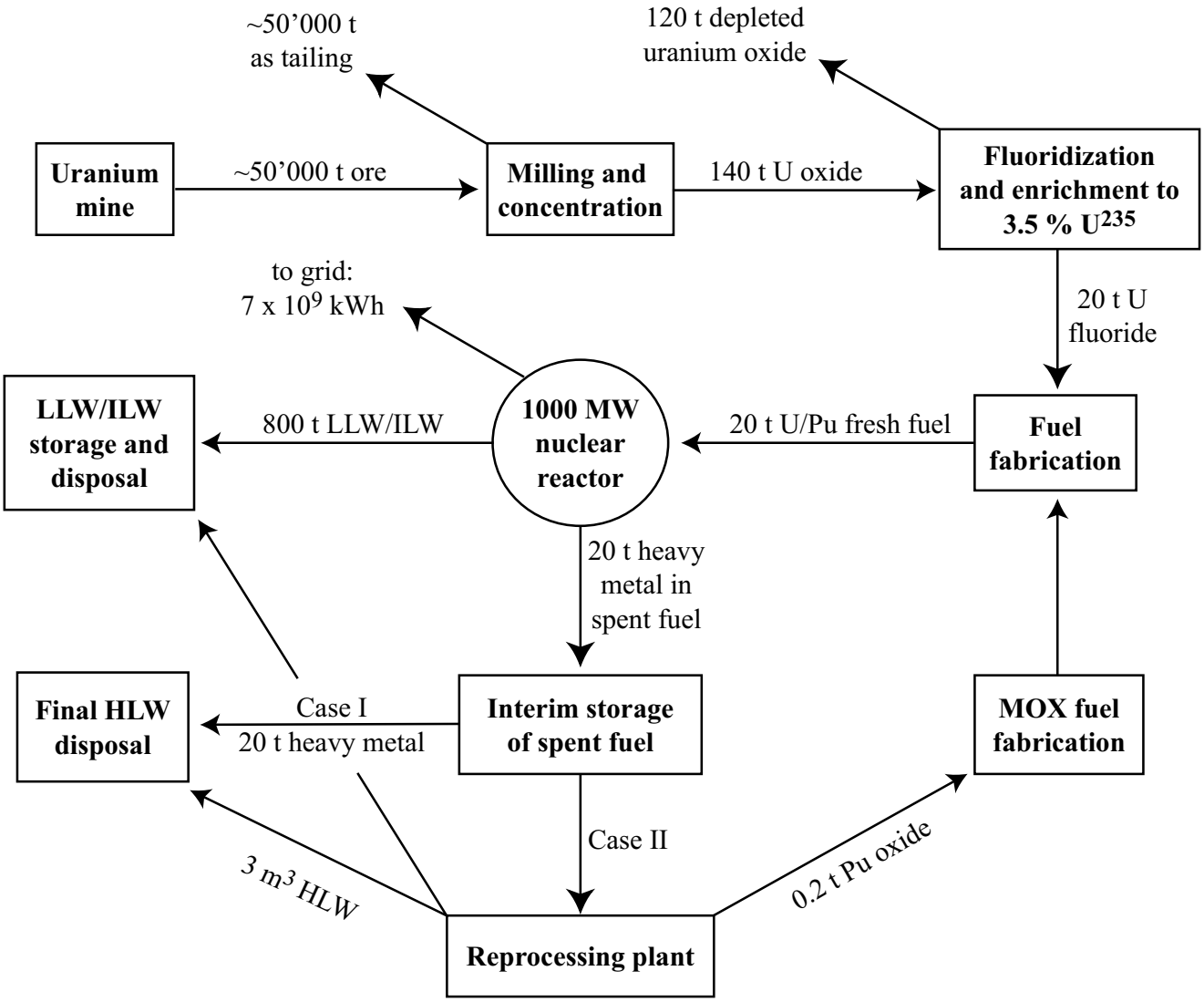

Figure 1.2.1: *The nuclear fuel cycle. Approximate yearly flows of material for the operation of a 1000 MW nuclear reactor (fast reactor type). Case I: once-through cycle. Case II: closed fuel cycle. (Source IAEA, 1994).*

tions are slightly different in France, UK, USA, Japan and Italy and are described in detailed reports by the International Atomic Energy Agency (IAEA, 1995).

Safe disposal of radioactive waste is required because ionizing radiation can cause various health effects. These may be classified as either non-stochastic or stochastic. The non-stochastic effects have an increasing damage with increasing exposure to large amounts of radiation, which results in skin reddening and cell destruction. Stochastic effects are based on long-term exposure to low levels of radiation resulting in cancer and mutations. Furthermore, a distinction has to be made between somatic and genetic effects, that is to say large amounts of radiation are very dangerous for single individuals whereas long-term radiation will result in genetic changes. Supplementary risk for the biosphere is generated by plutonium as an extremely toxic element (Bair & Thompson, 1974).

1.2.2 Radioactive Waste Disposal

A safe final disposal of SNF and HLW has the aim to minimize, if not entirely preclude any migration of radionuclides into the biosphere over a long period of time (e.g., half-life time ^{139}Pu is 24'110 years). To ensure that only minimum quantities of radioactive material reach the biosphere and finally human beings, several barriers between waste and biosphere are designed. Each barrier has a specific role in preventing nuclide migration and is optimized for its own and as a multi-barrier system (figure 1.2.2):

1) The first and most important barrier is the waste form itself (several different glass and/or ceramic compositions with incorporated waste). Many considerations are made on its suitability, which will be discussed separately later.
2) As an intermediate boundary layer, different technical barriers are used to avoid any waste loss from the waste

form itself into the geosphere. These technical barriers, containing the spent nuclear fuel or solidified waste, are durable containers composed of Cu, Ti, Ni, Al or stainless steel. These containers are then thought to be embedded in an overpack (usually concrete). Between the overpacked containers and the host rock, a buffer material will be placed. It is designed to minimize the access of water and to protect the containers from chemical and physical damage. This material is called backfill and consists mostly of compacted clay (e.g., bentonite). The remaining volume of the disposal vault will be sealed up (backfilled) with the same, fluid impermeable material. Upon contact with pore-water, those clay layers will produce basic conditions (pH 8–11; MURINEN & LEHIKOINEN, 1998).

3) As the final and ultimate barrier, optimal tectonic and geochemical conditions in a stable geologic formation are required for a possible disposal site. Present international efforts focus on Precambrian shield areas with low tectonic and volcanic activities, surrounding host-rock with a very low fluid permeability (possibly granite, basalt, salt, tuff, or clay), and zones with a low fracture abundance.

Each of these barriers must act independently but they also have to complement each other to generate the best possible solution for radioactive waste disposal.

The concept for a final disposal site has to fulfill many conditions. Governments propose different environmental radiation protection standards for the safety of mankind. The first essential scientific question is: What are the changes in physical properties (e.g., volume changes, fracture toughness and hardness), chemical properties (e.g., presence or absence of fluids, and leach rate), and stored energy as a function of radiation dose, temperature and time? The second question should be: How can the changes in physical and chemical properties to relevant radiation doses be simulated in accelerated experiments (for a waste form age of 10'000 – 1'000'000 years)? These issues are discussed and summarized in detail by EWING et al. (1995).

For all described barriers, laboratory data are needed to predict the behavior under various conditions and especially in contact with radioactive material. For validation of laboratory data (often incompatible with nature) additional tests are carried out in natural systems (e.g., Nagra Felslabor, Mont Terry) and are carefully compared to geological observations. Most present schemes go 300–1000 m below the surface and involve temperatures up to 300 °C and water pressures up to 10 MPa. Additional studies are made under conditions simulating deep boreholes (up to 6000 m) resulting in even higher temperatures and pressures. These conditions range from the lowest grades of diagenesis to the upper limit of the zeolite facies of regional metamorphism. This is a regime where mineral water reactions proceed slowly and metastable equilibrium abounds. However, dehydration processes are very important and generate aqueous fluids at these conditions.

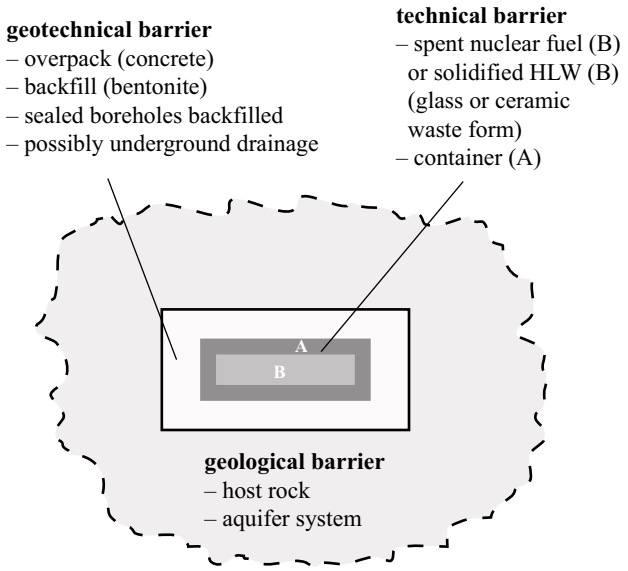

Figure 1.2.2: *Sketch of the different barriers (geological, geotechnical and technical) required for safe radioactive waste disposal.*

Long-term predictions (up to 10^6 years) are difficult to assess only from experiments in laboratories. Therefore final tests are carried out in possible waste disposal sites in different countries (e.g., Yucca Mountain, Nevada, USA and Forsmark, Sweden). Until now, no final disposal site for HLW is sealed and thereby surrendered back to nature.

1.2.3 High Level Waste (HLW)

HLW is generated as liquid waste from reprocessing of SNF and the production and dismantling of nuclear weapons (defense waste) and has to be solidified prior to its disposal. The earliest history of the development of these radioactive waste forms is described by LUTZE (1988). The first major efforts in the 1950s focused on the incorporation of radioactive waste into glasses of different compositions. First choice was a nepheline syenite glass from Chalk River in Canada with a processing temperature for waste incorporation of 1350 °C. Major programs during the 1960s in the USA, Canada, France, Germany, Italy, UK, Japan and in the former Soviet Union tried to develop glass compositions with a lower melting point. Lower temperatures decrease the loss of radionuclides by volatilization and form more durable glasses for waste incorporation without phase separation. Lead is incorporated to absorb nuclear radiation due to its high density and the large cross section for neutron absorption. Borosilicate glass is now the choice for most nations. Industrial processing is in progress since 1978 in Europe and since 1996 in the USA.

Since 1978 new ceramic waste forms were also under development, resulting from natural analogue studies (durable minerals incorporate radioactive elements). The best known of these is Synroc (SYNthetic ROCk), a titanate ceramic waste form initially developed by the Australian

Professor A.E. Ringwood based on an idea from Penn State University (USA). Other ceramic alternatives to the mostly used borosilicate glass are still under investigation in various laboratories all over the world (e.g. Sandia, USA; ANSTO, Australia; CEA, France). They include zirconium-titanates, phosphates and tailored ceramics as single and multi phase ceramics (e.g., rutile, monazite, apatite), cementitious waste forms, glass ceramics, polyphase ceramics with high metal contents as well as mixed glass-crystalline slags. HLW is present differently in each waste form.

The detailed characteristics of the different waste forms are described by Ewing et al. (1995) and Lutze & Ewing (1988). They are important for understanding the damage resulting from radiation. The predominant radiation effects in HLW waste forms are heating, radiolysis and radiation damage. Heating is mainly due to the β-decay of fission products (e.g., ^{90}Sr, ^{137}Cs) during the first period of waste storage. Radiolysis means that the ionizing radiation can decompose the surrounding water to a more oxidizing reactant. Radiation damage is caused by α- and β-decay (details see chapter 1.2.4).

The waste loading ultimately determines the radiation dose and the thermal history (energy from any type of radiation absorbed in a solid increases the temperature). Polyphase waste forms show partitioning of radionuclides, actinides and fission products into different phases. This may result in selective amorphization and isotropic or anisotropic expansion during amorphization and may lead to microfractures and disaggregation of the waste form. The final damage is a function of accumulated damage microstructures and for crystalline waste forms the kinetics of annealing.

1.2.4 Synroc

General

As a ceramic waste form, Synroc is designed for the disposal of HLW which has to be solidified for long-term storage in the repository. It creates an independent immobilization barrier (increased degree of security) in the event of unexpected failure of the geological barrier or the technical barriers. The idea of using ceramics was initially developed with the aim to provide a waste form with much greater resistance to leaching by groundwater than borosilicate glass (Ringwood, 1978; Ringwood et al., 1979). The constituent minerals, or close structural analogues, having survived in a wide range of geochemical environments for periods of 20 – 4'500 Myr whilst immobilising the same elements present in nuclear wastes lead to the basis of this concept (Ringwood et al., 1979). Synroc is the only ceramic waste form other than glass that was developed and studied to a degree that the processing technology could be evaluated or demonstrated with actual waste.

Composition

Synroc is a polyphase assemblage principally consisting of the four titanate phases zirconolite ($CaZrTi_2O_7$), perovskite ($CaTiO_3$), hollandite ($BaAl_2Ti_6O_{16}$) and titanium oxides (TiO_2). These phases together have the capacity to incorporate nearly all elements found in HLW into their crystal structure as solid solution (table 1.2.1). Partitioning of the waste elements between the different phases is due to the different crystal structures of the phases (Blackford et al., 1992; Lumpkin et al., 1995b; Smith et al., 1993; Vance, 1994).

Out of the starting materials, several distinct formulations were developed for different waste compositions. Synroc A and B were designed to increase the physical quality and chemical equilibrium as a ceramic material. Formulation C is designed for commercial waste (Purex type) and D for waste of the US Army (Savannah River). Synroc E is based on the same phases as Synroc C, but with different proportions, with the goal of incorporating microphases of Synroc C into surrounding TiO_2 as highly corrosion resistant microenvironments. Synroc F is designed for the confinement of non recycled spent fuel as direct disposal (table 1.2.2). Due to the preferential incorporation of specific waste elements into the different phases of the waste form,

Table 1.2.1: *Host phases for principal high-level waste elements in Synroc (Ringwood et al., 1988; Ringwood et al., 1979). Actinide elements and rare earth elements preferentially enter zirconolite when this phase is present. However, they can also be accommodated by perovskite.*

Mineral	*Formula*	*Elements incorporated*
Hollandite	$BaAl_2Ti_6O_{16}$	Cs^+, Rb^+, K^+, (Na^+), Ba^{2+}, Mo^{4+}, Ru^{4+}, Rh^{3+}, Fe^{3+}, Cr^{3+}, Ni^{2+}, Fe^{2+}
Zirconolite	$CaZrTi_2O_7$	U^{4+}, Pu^{4+}, Np^{4+}, Zr^{4+}, Am^{3+}, Y^{3+}, Gd^{3+}, La^{3+}, Na^+
Perovskite	$CaTiO_3$	Sr^{2+}, (U^{4+}), (Y^{3+}), (Gd^{3+}), (La^{3+})
metallic phases		Tc, Ru, Rh, Pd, Cd, Fe, Ni, Mo, Ti

Table 1.2.2: *Different Synroc formulations and their mineralogical composition in percent of the total volume.*

Name and formulation	*Vol%*
Synroc A: initial formulation, 10 vol% waste load	
Hollandite ($BaAl_2Ti_6O_{16}$)	29 %
Zirconolite ($CaZrTi_2O_7$)	26 %
Perovskite ($CaTiO_3$)	6 %
Ba-Feldspar ($BaAl_2Si_2O_8$, celsian)	13 %
Kalsilit ($KAlSiO_4$)	15 %
Leucite ($KAlSi_2O_6$)	11 %
Synroc B: no waste added	
Hollandite ($BaAl_2Ti_6O_{16}$)	40 – 35 %
Zirconolite ($CaZrTi_2O_7$)	35 – 31 %
Perovskite ($CaTiO_3$)	25 – 22 %
Rutile (TiO_2)	0 – 7 %
Synroc C: formulation B with 10–20 vol% waste load	
Hollandite ($BaAl_2Ti_6O_{16}$)	40 – 35 %
Zirconolite ($CaZrTi_2O_7$)	30 %
Perovskite ($CaTiO_3$)	20 – 15 %
Rutile (TiO_2)	15 %
Hibonite ($Ca(Al,Ti)_{18}O_{19}$), Magnetoplumbite ($Pb(Fe,Mn)_{18}O_{19}$)	< 5 %
Alloy	< 5 %
Synroc D: specific for US waste containing Fe, Na	
Zirconolite ($CaZrTi_2O_7$)	16 – 19 %
Perovskite ($CaTiO_3$)	11 – 15 %
Nepheline ($NaAlSiO_4$)	18 %
Spinel ($FeAl_2O_4$, Fe_2TiO_4)	55 – 48 %
Synroc E: designed for micro encapsulation in TiO_2	
Hollandite ($BaAl_2Ti_6O_{16}$)	2 – 5 %
Zirconolite ($CaZrTi_2O_7$)	4 – 7 %
Perovskite ($CaTiO_3$)	4 – 7 %
Rutile (TiO_2)	80 – 81 %
Synroc F: direct waste loading up to 50 %	
Hollandite ($BaAl_2Ti_6O_{16}$)	5 %
Rutile (TiO_2)	10 %
Pyrochlore ($[Ca,U]Ti_2O_7$)	} 85 %
Perovskite ($[Ca,U]TiO_3$)	
Uraninite ($[Ca,U]_xTiO_2$)	

these various formulations are necessary to achieve a high degree of chemical equilibration and homogeneity amongst the various chemical components of the entire waste form.

Several different techniques were used to produce Synroc. In the early stages, the traditional «oxide-route» (mechanical milling of ingredients and hot pressing for densification) was used to prepare the precursor material. This procedure yielded only unsatisfactory material, due to incomplete homogenization. Other techniques such as the «Sandia» method (reactive precursor with high specific surface area as powder or slurry), the «hydroxide-route» (hydrolyzed homogeneous mixture of alkoxides developed at ANSTO in 1985), crystallization from a melt (Vance et al., 1996) and the application of sol-gel chemistry processing (Sizgek et al., 1998; Sizgek et al., 1994) yielded much better qualities. Upgrading of laboratory scale batches (0.1–1 kg) to large production batches resulted in lower final densities, which might lead to higher leach rates for some materials.

In the 1990s, alternative Synroc formulations have been developed (Jostsons et al., 1995; Vance et al., 1992) primarily for actinide-rich wastes and weapons Pu.

Radiation effects

Radioactivity is a process where an atomic nucleus decays spontaneously and thereby emits α-, β-, or γ-radiation. Radiation interacting with matter then induces changes to the material; these are called radiation effects. Most promi-

nent effects are heating, radiolysis and ionic displacements. The β-decay of fission products adds a significant amount of heat to the repository in addition to the natural heat flow and therefore has an effect on the mineral stability and the fluid migration processes in the vicinity of the waste form. It may also affect the stability of the canisters containing the waste form. The surrounding water may be radiolytically decomposed by ionizing radiation, which turns water into a more oxidizing solution, thereby changing the solubility of the waste form itself.

Radiation damage induced by α- and β-decay are the most dangerous radiation effects for a crystalline waste form due to the possible amorphization of the crystal structure. Three processes cause this damage: (1) inelastic collisions between nuclear particles and host matrix atoms; (2) ionization; and (3) transmutation. Most important is the α-decay resulting in inelastic collisions causing structure displacements. When the α-particle is ejected from the parent atom, the resulting product nucleus is significantly recoiled (α-recoil track). Whereas the α-particle loses most of its energy by ionization, the recoil atom loses its energy mainly by displacement, leading to physical and chemical changes in the waste form (figure 1.2.3). The final result is the metamictization of the primary crystalline phases.

This metamictization, primarily a result of α-decay of actinides (e.g., ^{235}U) because β-decay does not lead to amorphization by itself, is accompanied by an increasing volume of the unit cells, which can lead to microfractures. Therefore many research projects were planned to understand this problem by analyzing synthetic samples with various neutron irradiation techniques and by analyzing natural samples which contain α-decay damage comparable to that which will be experienced by Synroc. All experimentally induced radiation dose rates are much higher (factor of 10^4–10^5) than the ones active wasteforms will

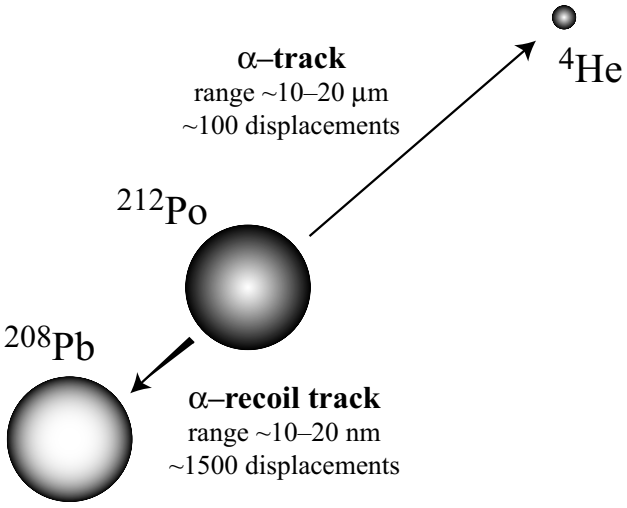

Figure 1.2.3: *Schematic demonstration of the α-decay (e.g., ^{212}PO) revealing the ejection of the small α-particle (^4He) and the recoil of the much larger product nucleus (e.g., ^{208}Pb) leading to the α-recoil track.*

encounter. In addition, all phases of the irradiated samples experience the same fast-neutron flux, even hollandite, which is normally less affected because it does not contain actinides as α-emitting radionuclides in the proposed waste form. On the other hand natural samples are exposed to lower dose rates (factor of 10^2–10^3) than those encountered by active waste. But this factor is smaller than the one from laboratory irradiated tests hence radiation doses from natural analogues are closer to those from active waste. Therefore natural samples are more relevant for the prediction of radiation damage effects (Ringwood et al., 1988). A detailed overview is given by Ewing et al. (1995), who also discusses the impact of radiation on glass waste forms. Additionally, individual phases of Synroc were doped with actinides to test their individual behavior during α-decay. Specific results have been described by various authors (Ewing et al., 1982; Ewing & Headley, 1983; Lumpkin et al., 1986; Pudovkina et al., 1974; Sinclair & Ringwood, 1981; Weber et al., 1985). These single phases were also studied in nature. Investigations on old metamict zirconolites (completely amorphous due to radiation damage) revealed exact zirconolite stoichiometry without elemental zoning (Lumpkin et al., 1986). No specific material loss by leaching was observed and therefore a very resistant behavior of zirconolite in natural ground waters may be proposed (Gieré et al., 1994; Gieré et al., 1998; Hart et al., 1996; Lumpkin et al., 1994a).

Leaching behavior

For each waste form it is very important to determine the chemical durability. Therefore different leach tests were carried out and compared to hydrothermally altered minerals. Experiments under static conditions in deionized water at 90 °C by Ringwood & Kelly (1986) showed that the initial leaching of Synroc is highly incongruent with respect to the different elements, time, temperature, and phase. The overall leach rate decreased by a factor of 1000 after 80–90 days (Ringwood et al., 1988; Solomah & Zumwalt, 1982; figure 1.2.4). For most elements, leach rates decreased rapidly for the first ten days and then reached a plateau value. For some other elements (e.g., Cs, Sr) the leach rate decreased over a period of up to 100–300 days (Levins et al., 1986; Lumpkin et al., 1991; Oversby & Ringwood, 1982; Reeve et al., 1982; Smith et al., 1996; Smith et al., 1997a; Smith et al., 1992; Smith et al., 1997b). Ringwood et al. (1981) explained the initial high leach rates due to incomplete equilibrium during hot pressing which caused small proportions of some elements to be located at grain boundaries or other metastable phases, or a higher porosity present at the surface received during preparation. Various reports and authors showed different leach rates for different precursor materials and fabrication mechanisms (Oversby & Vance, 1995). The temperature dependence of the leach rate of Synroc is discussed by Reeve et al. (1981) and Solomah (1983) and increases over the temperature range of 45–300 °C by a factor of 25 (figure 1.2.5). Increasing the waste loading in Synroc (with the desirable effect of lowering the hot-pressing temperature for full

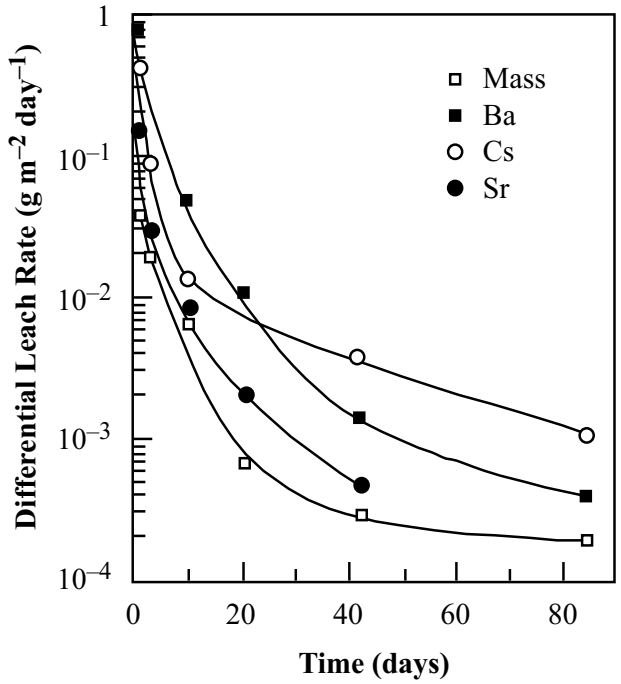

Figure 1.2.4: *Leach rate from Synroc-C (10 wt% simulated HLW) under static conditions in deionized water at 90 °C (data from* Ringwood & Kelly, *1986).*

densification) has no serious effect on the chemical durability before metamictization (Oversby & Ringwood, 1982; Reeve et al., 1983). Various effects on the chemical durability are induced by different impurities. Even low additions of silica (0.2 wt% SiO_2) had a significant deleterious effect on the leach rate of the more leachable elements (doubled for Cs; Levins et al., 1985). But other elements like Na as impurities showed beneficial effects and are easily incorporated into perovskite (Kesson & Ringwood, 1981). Na is mostly not present but may be added to intermediate level wastes as a production contaminant from reprocessing. Other impurities mostly have no effects (Myhra et al., 1987). Because Belgium is considering the disposal of their HLW packages in a Boom clay layer as surrounding host rock, leaching experiments in Boom clay media were carried out. The effect of its interaction with Synroc was mainly to increase the solubility of Ti, Zr and the REEs in solution (Hart et al., 1995; Van Iseghem et al., 1996).

From studies of weathered or hydrothermally altered minerals and from other laboratory-based studies it is known that the different phases in Synroc exhibit distinct leaching behavior under identical experimental conditions. These studies revealed that perovskite is less durable than hollandite and especially zirconolite. They also indicate that under certain circumstances perovskite breaks down to anatase and brookite and a protective TiO_2-enriched rim is developed (Myhra et al., 1987; Nesbitt et al., 1981; Ringwood et al., 1988; Ringwood et al., 1981). These results were confirmed by leaching experiments producing secondary phases (TiO_2 polymorphs and monazite) on specific phases (mainly perovskite) of the Synroc surface (Lumpkin et al., 1995a). These secondary phases acting as a more resistant shield may in part explain the decrease in leach rate over time observed for Synroc.

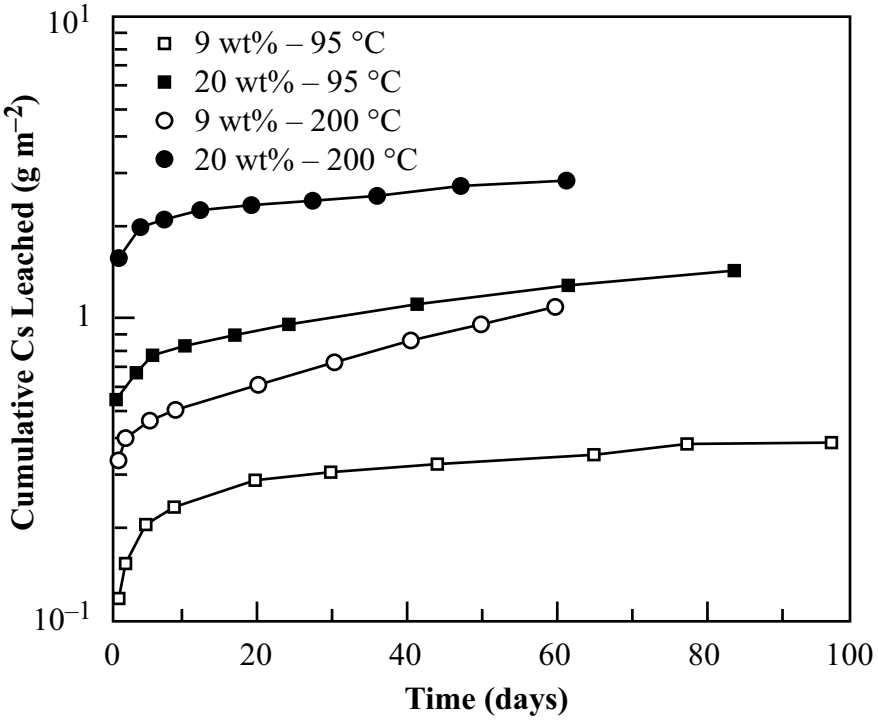

Figure 1.2.5: *Effect of increasing temperature and simulated HLW loading on the Cs release from Synroc-C (data from* Oversby & Ringwood, *1982).*

However, to describe the leaching behavior for Synroc in natural systems with active waste, two competing processes have to be considered. (1) Leaching decreases with time, but (2) it increases with higher temperature. Due to the radioactive decay in the repository, the temperature increases rapidly but cools down slowly at the disposal site with time (RYBACH, 1975) resulting in higher leach rates as shown in figure 1.2.5. This assumption is shown as a sketch in figure 1.2.6.

Comparison with glass

At the present time, the waste form of choice for most countries is still borosilicate glass. This choice is mainly based on:

1) The ease of glass fabrication due to the easy mixing with the liquid waste supported by the low melting point and the consistent glass composition for different waste compositions.
2) This technology is well demonstrated and used for actual waste.
3) The assumption that glass more easily accommodates the large variation of HLW composition (up to 30 components) because its structure is aperiodic and that the HLW elements are evenly distributed throughout the solid.
4) Glass has cheaper production costs than ceramics.

But more detailed analyses point to the outstanding characteristic of Synroc and its much higher resistance to leaching by groundwater than glass at ambient temperatures and in particular at elevated temperatures due to:

1) A lower solubility of the titanium- and zirconium-oxide dominated ceramic matrix relative to the sodium borosilicate matrix. The solubility of TiO_2 is much lower than that of SiO_2 under hydrothermal conditions (table 1.2.3). Leaching experiments revealed a better resistance by three orders of magnitude (NESBITT et al., 1981; REEVE et al., 1987; figure 1.2.7).
2) Experiments by LEVINS & SMART (1984) exhibited a much lower leaching dependence of Synroc to pH compared to glass (figure 1.2.8).
3) In ceramics the radionuclides occupy specific atomic positions in the periodic structure of the crystalline phases and they partition unequally between different phases. In contrary, in glass forms the radionuclides are distributed homogeneously throughout the solid.
4) Synroc accommodates the same amount of HLW in only 60% of the volume required by glass waste forms (GIERÉ, 1999).
5) Natural analogues of individual ceramic phases allow investigations on the long-term radiation damage features and leaching behavior on a geologic time scale in natural environments (GIERÉ et al., 1994; GIERÉ et al., 1998; HART et al., 1996; LUMPKIN et al., 1986; LUMPKIN et al., 1994a).

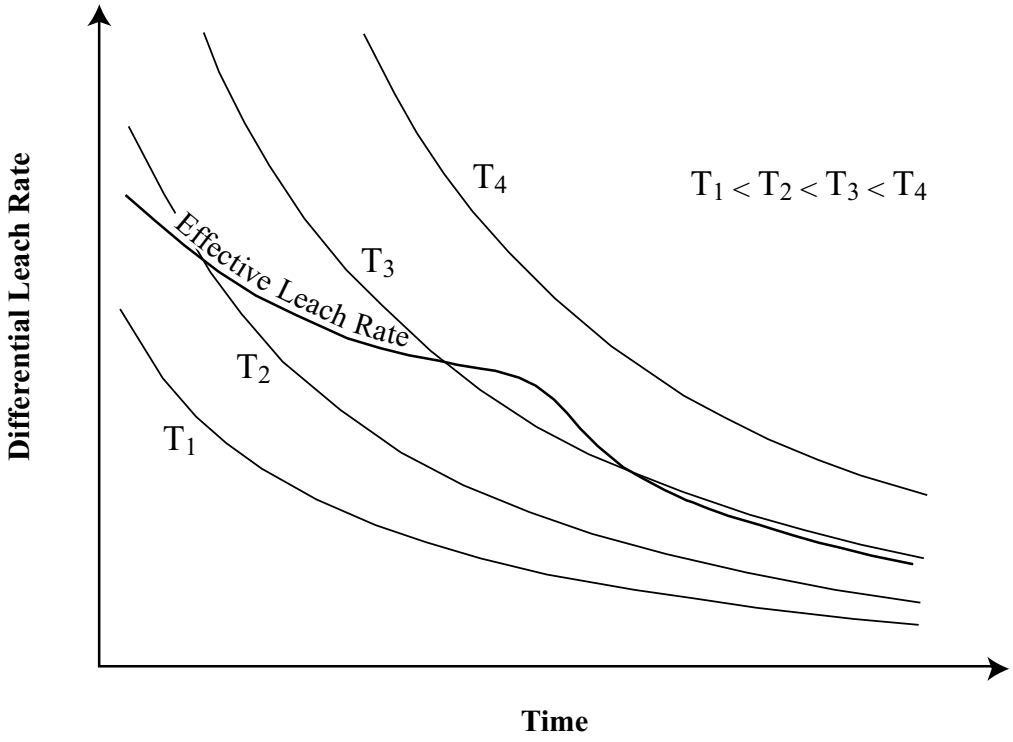

Figure 1.2.6: *Sketch of the effective leach rate as a combination of the increasing leaching rate from heating due to the radioactive decay and the decreasing leach rate with time. Most heat generation decreases after several hundred years after ^{90}Sr and ^{137}Cs have decayed, resulting in a decreasing effective leach rate.*

Table 1.2.3: *Mass and elemental leach rates [g m^{-2} d^{-1}] of Synroc and borosilicate glass in deionized water at 90 °C after 28 days (Ringwood et al., 1988).*

	Synroc C, batch 325, 10 wt% HLW simulate	*Waste glass, PNL 76-78, 33 wt% waste simulate*
Mass	0.005	0.42
Al	< 0.01	not available
Ba	0.036	not available
Ca	0.0065	0.068
Cs	0.033	1.03
Mo	0.12	1.40
Na	< 0.2	1.32
Sr	0.010	0.075
Ti/Si [a)]	< 0.00005	0.73
Zr/B [a)]	< 0.0006	1.12

a) Synroc data are for Ti and Zr as its principal components, glass data for Si and B as principal components.

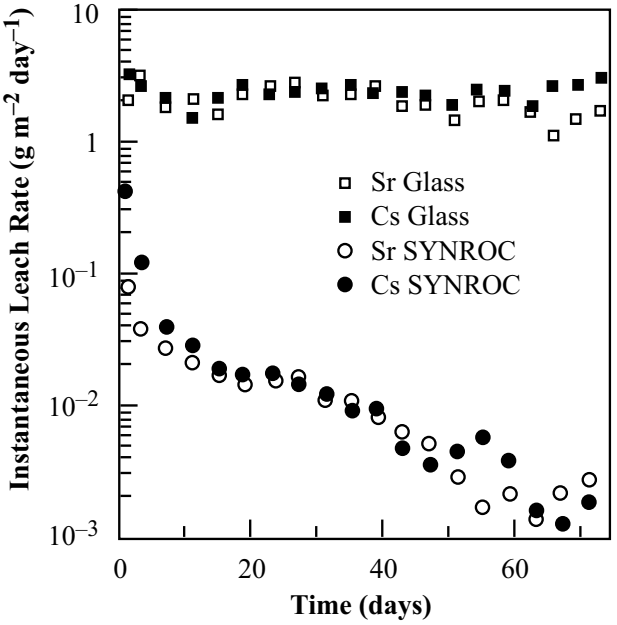

Figure 1.2.7: *Leach results for Cs and Sr from Synroc-C (10 wt% simulated HLW) and waste glass (PNL 76-68) at 100 °C in deionized water. The leachant was replaced daily (data from Reeve et al., 1982).*

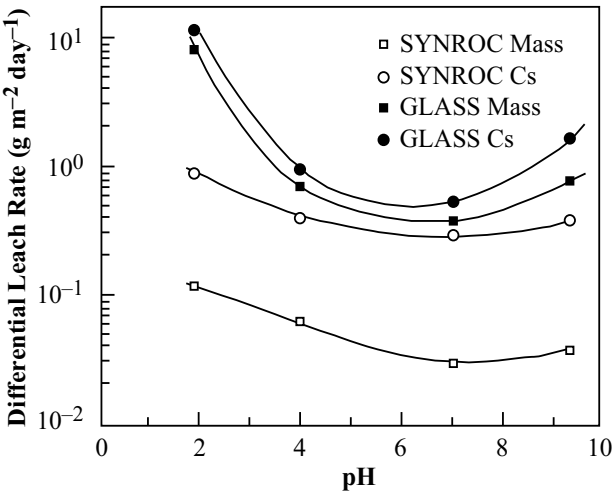

Figure 1.2.8: *Comparison of the effect of pH on the leach rates of Synroc-C (10 wt% simulated HLW) and waste glass (PNL 76-78) at 90 °C (data from Levins & Smart, 1984).*

6) Devitrification of glass and the crystallization of phases including spinel (Hrma & Casler, 1999) are predicted for a high level waste glass at elevated temperatures (Orlhac et al., 1999). This process is very undesirable and could lead to fractures and an unbalanced elemental fractionation.

Ceramic waste forms in general have not been developed and tested to the same degree as glass with the exception of Synroc (operative demonstration plant at ANSTO). Therefore the basis for the comparison of second generation ceramics with glass mostly relies on tests performed with surrogate elements (see Hart et al., 1998, for an exception). Despite this shortcoming, the radiation effects on ceramic waste forms are very well analyzed.

1.2.5 Other Ceramic Waste Forms

Several polyphase ceramics have been prepared on the laboratory scale as second generation high level nuclear waste matrices, but all are somewhat related to Synroc. They all are based on silicate, titanate, phosphate, aluminate, titanosilicate and alumosilicate phases. Reviews of these alternatives have been given by Clarke (1983), Fielding & White (1987) and Lutze (1988).

Glass ceramics have been developed in Germany and Canada (Hayward, 1988). The latter consist of discrete crystals of sphene (titanite), within a matrix of aluminosilicate glass.

As a first major application of pure ceramics, the US Department of Energy decided to use a pyrochlore-rich titanate ceramic for the immobilization of the excess weapons plutonium (Jostsons et al., 2000; Jostsons et al., 1995). The schedule for this immobilization program is bound to the START-II agreements between Russia and USA.

2 SOLID PHASES

2.1 Introduction

The following part provides some important information on the solid phases used for, and obtained as product phases during the experiments. For understanding all processes taking place during hydrothermal experiments, the crystal chemical data of the involved phases are very important.

2.2 Zirconolite

2.2.1 Introduction

Zirconolite is a relatively rare accessory mineral with the ideal formula of $CaZrTi_2O_7$. Until today only 52 terrestrial and 7 lunar sites as well as 1 meteorite are reported as localities where zirconolite occurs (Williams & Gieré, 1996; Gieré et al., 1998). Because zirconolite is easily overlooked by light-microscopy studies (similar to ilmenite or rutile), it may actually occur at many more sites. Interestingly these few occurrences are reported from a wide range of rock types. Zirconolites from different geological environments show a large compositional variation and often a significant deviation from the theoretical composition. The two following samples are simplified data from Williams & Gieré (1996, zirconolite C47 and M50):

$$(Ca_{0.452}REE_{0.538}Th_{0.006}U_{0.007})(Zr_{0.997}Hf_{0.011})(Ti_{1.225}Si_{0.022}Mn_{0.037}Fe_{0.423}Nb_{0.291})O_7$$

$$(Ca_{0.698}REE_{0.041}Th_{0.134}U_{0.227})(Zr_{0.940}Hf_{0.013})(Ti_{1.506}Mg_{0.228}Fe_{0.130}Al_{0.048}Nb_{0.056})O_7.$$

Gieré et al. (1998) proposed a series of substitutions and best suited end-members to describe the natural chemical variation.

This knowledge is important for designing zirconolite-based wasteforms. Zirconolite is also an ideal natural analogue for its behavior in such wasteforms, because of the significant incorporation of rare earth elements, actinides and other elements in nature. The variability of substituted cations, host rocks, ages and climates of weathering are ideal for studying the relations between radiation damage and geochemical alteration (Hart et al., 1996; Lumpkin et al., 1994a; Lumpkin et al., 1998; Lumpkin et al., 1994b; Lumpkin et al., 1997).

2.2.2 Crystal structure

Three different crystal structures of the composition $CaZrTi_2O_7$ exist with monoclinic, orthorhombic and trigonal symmetries named polymignite, zirkelite and zirconolite (Rossell, 1980). They are all polytypes (White et al., 1984) or polytypoids (Bayliss et al., 1989). Table 2.2.1 shows the most recent nomenclature approved by the International Mineralogical Association (IMA) under Bayliss et al. (1989).

For the experiments carried out during this thesis, zirconolite-2M was used exclusively and therefore only this polytype is described. The monoclinic structure is close to the one of fluorite and pyrochlore; it can be described as an anion deficient superstructure derived from the fluorite-type structure (c is parallel to (111) of the fluorite subcell). The lattice of the monoclinic supercell is C-centered and has eight times the volume of the distorted fluorite subcell. The unit cell has a size of 12.611 (a) x 7.311 (b) x 11.444 (c) Å, a beta angle of 100.52°, and belongs to the space group C 2/c (Gatehouse et al., 1981; White, 1984). Zirconolite has five different cation sites, these being one Ca site (8-coordinated), one Zr site (7-coordinated) and three Ti sites (two [I, III] 6-coordinated, one [II] 5-coordinated). The Ti–O octahedra are arranged in two-dimensional layers in contrast to the three dimensional network in cubic pyrochlore. Therefore the structure can be described as a layered structure parallel to (001) with layers of Ti polyhedra alternating with layers containing Ca and Zr. The Ti layer is built as a layer of 6-membered rings of TiO_6 polyhedra (M6 site) that are connected by the corners. Each ring surrounds a statistically occupied 5-coordinated Ti site (M5 site). Alternating chains of CaO_8 cubes (M8 site) and ZrO_7 polyhedra (M7 site) form the Ca- and Zr-rich layers between the Ti layers (see figure 2.2.1). The polyhedral volumes of the five different cation sites vary by a factor of four from M5 to M8 (table 2.5.1). These are the reasons for the large variety of possible elemental substitutions.

Natural zirconolite forms typically prismatic crystals elongated along c (Anthony & John, 1997) and polysynthetic twinning has been observed along the (111) plane (Vlasov, 1966).

2.2.3 Crystal chemistry

Stoichiometrically ideal zirconolite contains 16.5 wt% CaO, 36.5 wt% ZrO_2, and 47.2 wt% TiO_2. These major element contents may range in natural samples from 2.63 to

Table 2.2.1: *IMA-approved nomenclature of the $CaZrTi_2O_7$ polytypoids and their structure after* Bayliss *et al. (1989).*

Polytypoid	*Structure*
zirconolite	undetermined polytypoid, may be metamict
zirconolite-2M	monoclinic, two-layered, aristotype [1]
zirconolite-3T	trigonal, three-layered
zirconolite-3O	orthorhombic, three-layered
zirconolite-4M [2]	monoclinic, four-layered, supercell of zirconolite-2M
zirconolite-6T [2]	trigonal, six-layered, supercell of zirconolite-3T
zirkelite	cubic, $(Ti,Ca,Zr)O_{2-x}$
polymignite	identical to metamict zirconolite

[1] White et al. (1984)
[2] Smith & Lumpkin (1993)

16.5 wt% CaO, from 24.3 to 45.4 wt% ZrO_2, and from 13.6 to 45.9 wt% TiO_2 (table 2.2.2; Gieré et al., 1998). A compilation of chemical analyses from natural zirconolite showing the extensive range of the accommodated elements and the degree of substitutions has recently been published by Williams & Gieré (1996). Thirty or more chemical elements may be present at more than 0.1 wt%. The necessary substitutions or exchange vectors for the complex zirconolite system comprises simple single-site substitutions as well as more complex coupled substitu-

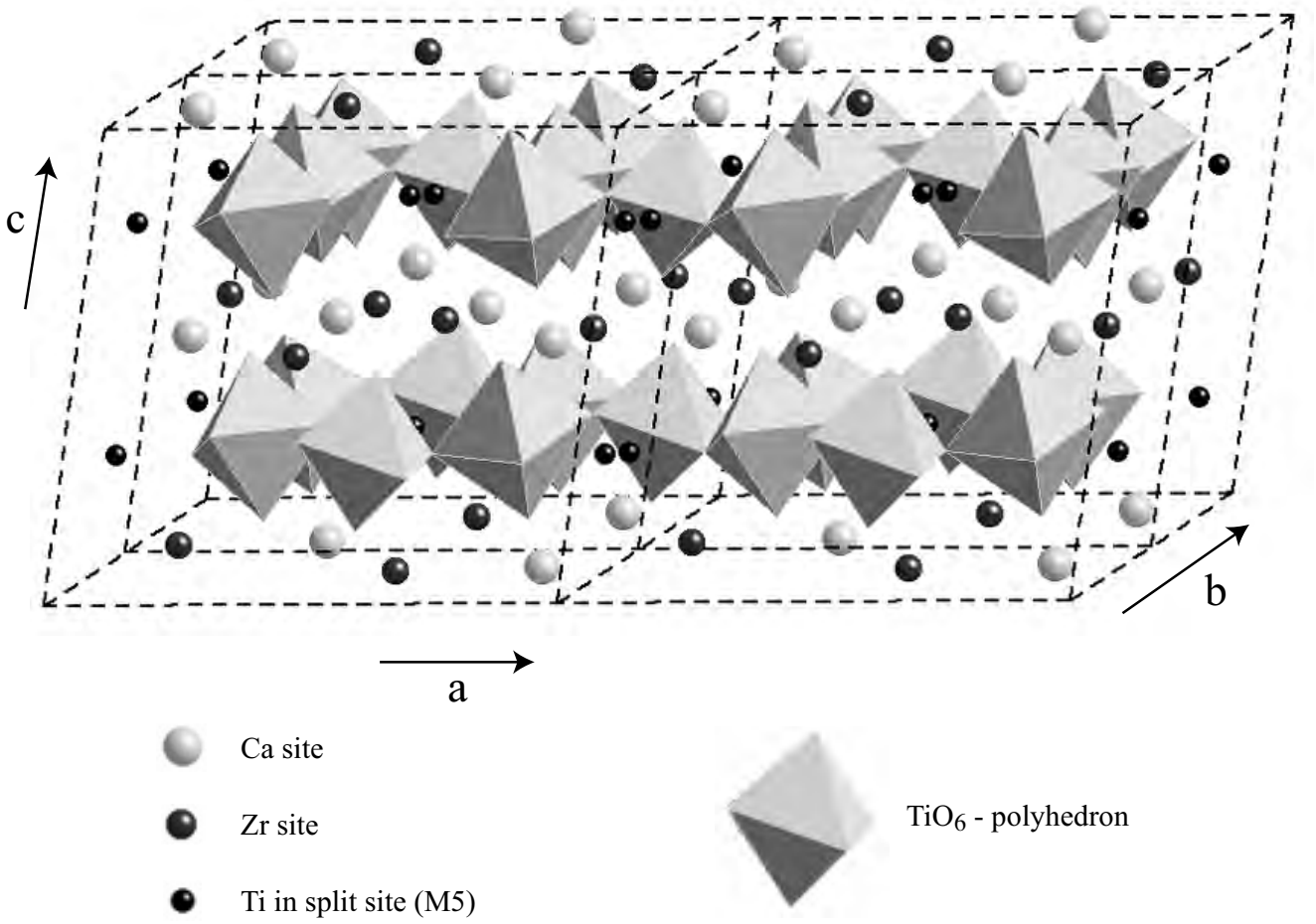

Figure 2.2.1: *Crystal structure of zirconolite-2M showing the two-dimensional layers of TiO_6 polyhedra respectively, Ca and Zr site layers (by Crystal Maker 4.0 using data from* Gatehouse *et al., 1981).*

Table 2.2.2: *Extent of site substitutions in natural and synthetic zirconolite.*

Site		*Element*	*Max/Min % in site*	*Reference, locality and host rock*
M8	natural	Ca	min. 21.2	[1)] Apollo 15, lunar basalt L11
	natural	∑ (REE)	max. 78.8	[1)] Apollo 15, lunar basalt L11
	natural	∑ (U + Th)	max. 40.4	[1)] Adamello, Italy, metasomatic
M7	natural	Zr	min. 97.6	[1)] Apollo 15, lunar basalt L9
	natural	Hf	max. 2.4	[1)] Apollo 15, lunar basalt L9
	synthetic	Hf	max. 97.0	Swenson et al. (1996)
	synthetic	REE (e.g. Nd, Ce)	max. 50	Vance et al. (1994)
	synthetic	ACT (e.g. U, Pu)	max. 50	Vance et al. (1995)
M5/6	natural	Ti	min. 34.8	[1)] Kaiserstuhl, Germany, carbonatite C71
	natural	∑ (Nb + Ta)	max. 41.2	[1)] Kovdor, Russia, carbonatite C15
	natural	Fe	max. 30.5	[1)] Apollo 14, lunar lithic fragment L7
	natural	Mg	max. 14.8	[1)] Tchivira Mt., Angola, nepheline syenite NS14
	natural	Al	max. 11.3	[1)] Tchivira Mt., Angola, nepheline syenite NS14
	natural	Mg	max. 14.8	[1)] Tchivira Mt., Angola, nepheline syenite NS14
	natural	Al	max. 11.3	[1)] Tchivira Mt., Angola, nepheline syenite NS14

[1)] Data from refer to table 3 in Williams & Gieré (1996).

tions on one site or two different sites and were discussed by Gieré et al. (1998).

2.2.4 Petrography

Several authors described the occurrence of zirconolite as accessory mineral in a wide range of different host rocks including kimberlite, metamorphic ultrabasic rocks, dendritic anorthosite, gabbro pegmatite, syenite, nepheline syenite, carbonatite, metasomatic and metamorphic rocks. The most commonly observed minerals in contact with zirconolite are apatite, baddeleyite, calcite, calzirtite, dolomite, geikielite, ilmenite, perovskite, phlogopite, pyrochlore and spinel. The existence of zirconolite is dependent on the availability of Zr, Ti and REE as well as on the SiO_2 content of the melt, fluid or rock during formation. More detailed petrographic information is given by Bellatreccia et al. (1999), Bulakh & Nesterov (1996), Bulakh et al. (1999), Gieré (1986), Gieré (1990), Gieré (1996), Gieré & Williams (1992), Gieré et al. (1998), Williams (1996), Williams & Gieré (1988) and Williams & Gieré (1996).

2.3 Perovskite

2.3.1 Introduction

Perovskite belongs to the large group of mixed oxides of the type $A^{2+}B^{4+}O_3$. Compounds of the perovskite structure are of great scientific and economic importance. Geophysically and mineralogically it is of tremendous significance because $MgSiO_3$-perovskite is the most abundant mineral in the mantle. Synthetic perovskite as ceramics exhibiting a wide range of electrical and optical properties from insulators to semiconductors and superconductors to nonlinear optical properties (e.g., $KNbO_3$). The following explanations are all specific to the end member $CaTiO_3$, which also has given its name to the whole family of perovskites. It was first described by Gustav Rose (1839) and named after the vice president of Russia, Earl Lew Aleksejewitsch from Perowski.

2.3.2 Crystal structure

Natural perovskite is orthorhombic (pseudocubic, space group Pnma) with cell parameters a = 5.37 Å, b = 5.44 Å, and c = 7.62 Å (Hu et al., 1992). Other investigators described different space groups like Pcmn (Kay & Bailey, 1957) or Pbnm (most material scientists). The transformation of cubic to orthorhombic is mainly a consequence of small displacements of Ca and O atoms from cubic positions; b is doubled and a and c are no longer equivalent. The Ca site is ideally 12-coordinated; due to rotations (Koopmans et al., 1983) and significantly larger distances between four of all oxygens and the cation (0.32 nm instead of the 0.25 nm mean distance, Fielding & White, 1987) the coordination number often reduces to eight. The Ti site is 6-coordinated (see figure 2.3.1). Cubic mirror planes are not present in orthorhombic perovskite and therefore, obvious twin planes are the two nonequivalent systems {112} and {110}. Several different lattice planes have almost identical d-values because of the relationship

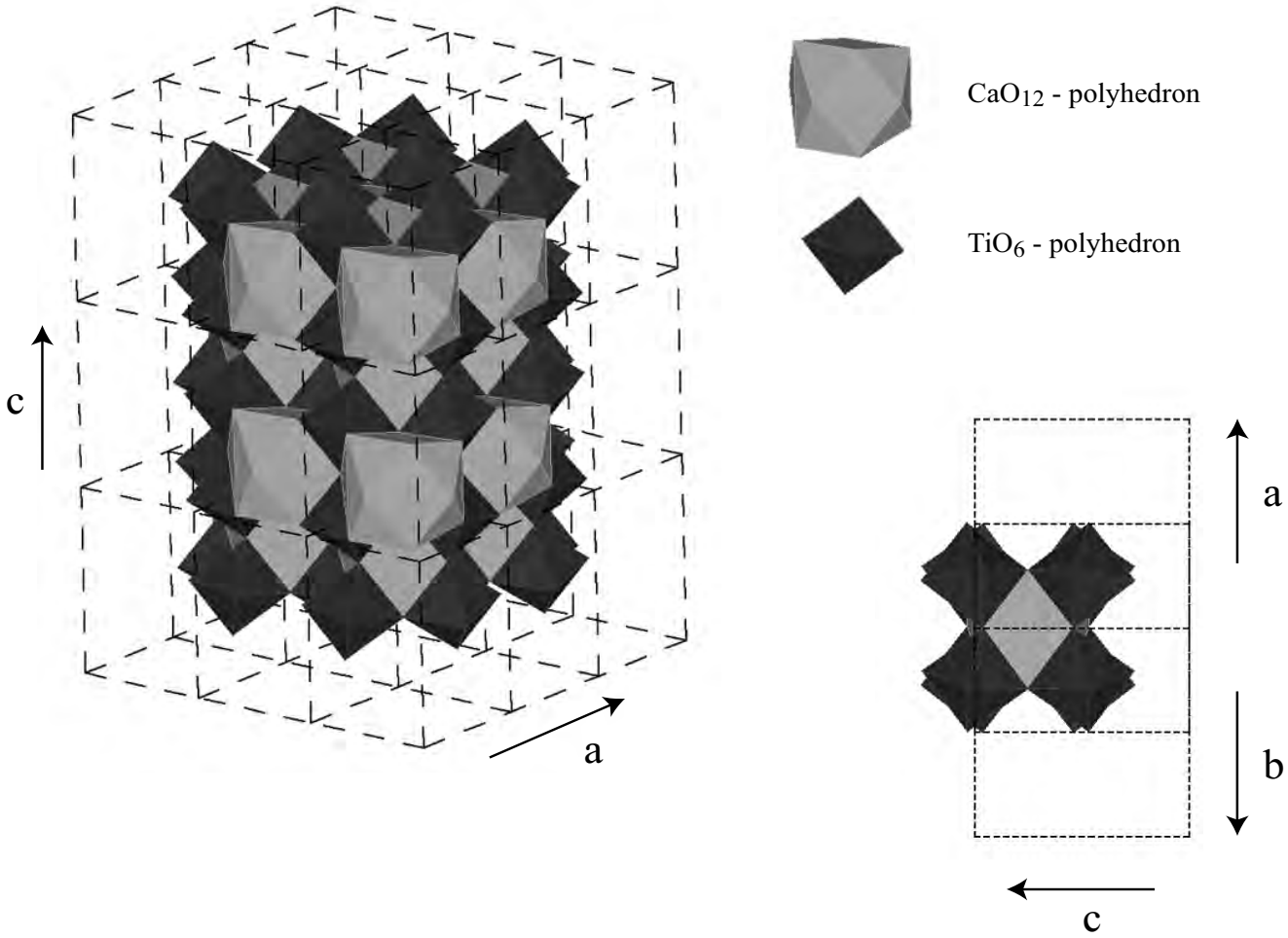

Figure 2.3.1: *The pseudo-cubic crystal structure of perovskite with alternating Ca and Ti sites (by Crystal Maker 4.0 using data from* Koopmans *et al., 1983).*

$$a \approx b \approx \sqrt{2}/c\,,$$

which makes indexing of selected area diffraction patterns often difficult. The most reliably indexed lattice planes are those with systematic absences of either h, k or l.

The natural crystals commonly form distorted cubes, rarely also cuboctahedral or octahedral morphologies. Twinning mostly occurs 90° and 180° about [110] or rarely 180° about [112]. Twins often form complex penetration features, but lamellar or sector twins also occur.

2.3.3 Crystal chemistry

Stoichiometrically ideal perovskite contains 41.25 wt% CaO and 58.75 wt% TiO_2. The mineral group is defined by the two parameters

$$x_{Ca} = \frac{Ca}{Ca + Na + REE + K + ...} \geq 0.5 \quad \text{and}$$

$$x_{Ti} = \frac{Ti}{Ti + Nb + Al + Si + ...} \geq 0.5\,.$$

This shows that up to 50 wt% other elements may be incorporated, following mostly single site substitutions, on the Ca and the Ti site. These elements are mostly alkalis or REEs on the Ca site and often Nb or Ta on the Ti site. Several specific varieties are described by Deer et al. (1966), Mitchell (1996), or Nickel & McAdam (1963). However, many of the given names are obsolete (not IMA approved) and the possible names are discussed in chapter 5.2.3.

2.3.4 Petrography

Perovskite has been found all over the world at many localities as an accessory mineral in basic and alkaline type igneous rocks. There it is commonly found as an alteration product often in association with nepheline, leucite and melilite. It was also observed in kimberlites, carbonatites, and in calcareous skarns where it is stable relative to rutile and calcite at low X_{CO_2}. In some carbonaceous chondrites it is a common accessory phase occurring in Ca- and Al-

rich inclusions. In general it is frequently associated with åkermanite-gehlenite, ilmenite, magnetite, nepheline and titanite (ANTHONY & JOHN, 1997). Additionally it is reported as a breakdown product of titanian clinohumite in the Malenco serpentinite (TROMMSDORFF & EVANS, 1980).

2.4 Calzirtite

2.4.1 Introduction

Calzirtite is an even rarer mineral than zirconolite with a chemical composition (Ca–Zr–Ti-oxide) closely related to the chemical composition of zirconolite and zirkelite. But it shows much less compositional variability and therefore a lower potential for elemental substitution than zirconolite as observed in the few presently known localities.

2.4.2 Crystal structure

This Ca–Zr–Ti-oxide mineral has two different crystal structures. Mostly it occurs as tetragonal mineral (space group $I4_1/acd$, ROSSELL, 1982; SINCLAIR et al., 1986) but was also found to be orthorhombic (space group Pbca, CALLEGARI et al., 1997). After heating, the orthorhombic variety spontaneously recrystallizes in the tetragonal crystal system. The detailed structure is described as an anion-deficient distorted fluorite-related superstructure. The fluorite subcell is tripled along the a- and b-axes and doubled along the c-axis. This results in a tetragonal unit cell with the lattice parameter 15.2203 (a) x 10.1224 (c) Å and a volume that is eight times larger than that of fluorite. The Ca site (M3) is 8-coordinated, the Ti site (M2) is 6-coordinated, and four of the five Zr sites (M4) are 7-coordinated; the remaining fifth of the Zr cations (M1) randomly occupy one of two sites in

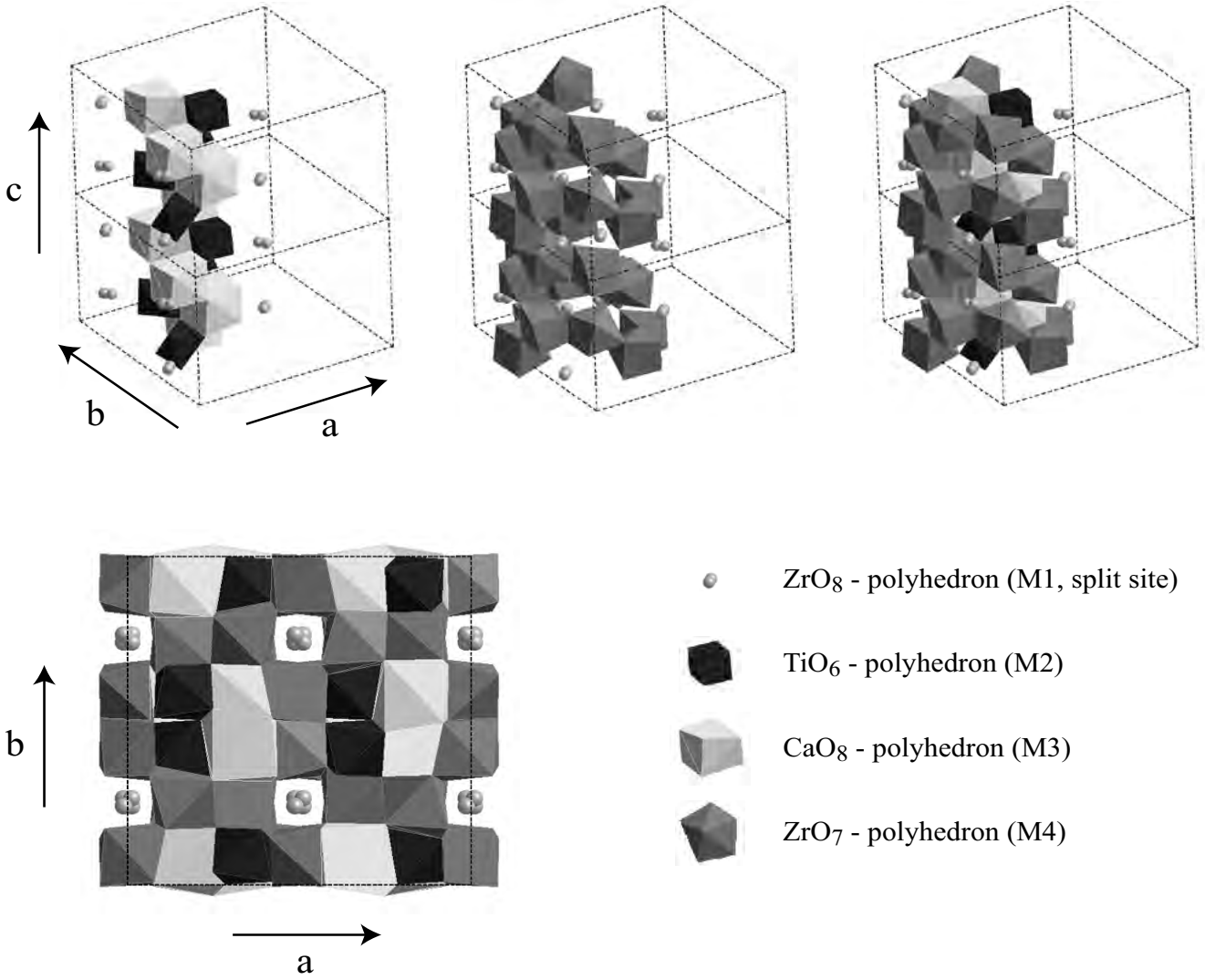

Figure 2.4.1: *The crystal structure of calzirtite revealing two, in direction of c, clockwise upwards turning strings. These consist of edge sharing CaO_8- respectively corner sharing TiO_6-polyhedra (A). They are surrounded by edge sharing ZrO_7-polyhedra (B) forming columns (C). Each of these is surrounded by four M1 site ZrO_8 polyhedra strings parallel to c (by Crystal Maker 4.0 using data from ROSSELL, 1982).*

a distorted cube with oxygen at each corner (split site). Parallel to (010), the cations are ordered into planes forming alternating layers of M2, M3 and M4 between layers of M1 and M4. As a result of the distribution of interstices, vacant and alternating positions (details see SINCLAIR et al., 1986), the structure of calzirtite displays alternating clockwise upwards turning helices of M2 and M3 strings surrounded by a M4 double helix (see figure 2.4.1).

Natural calzirtite often forms twinned crystals (BULAKH & NESTEROV, 1996) or even pseudotrapezohedral multiple twins (trillings) and exhibits, as single crystal, a prismatic dipyramidal habit (ANTHONY & JOHN, 1997). Frequent intergrowths with zirkelite and zirconolite have been observed by BULAKH et al. (1999).

2.4.3 *Crystal chemistry*

The ideal composition mostly is given as $Ca_2Zr_5Ti_2O_{16}$ (PYATENKO, 1971) but sometimes also as $CaZr_3TiO_9$ (ZDORIK et al., 1961; ZHABIN et al., 1962). This difference in the chemical composition results from the many unknowns of this mineral due to the few natural samples found. Stoichiometrically ideal calzirtite ($Ca_2Zr_5Ti_2O_{16}$) contains 12.6 wt% CaO, 69.4 wt% ZrO_2, and 18.0 wt% TiO_2, or 11.99 wt% CaO, 72.41 wt% ZrO_2, and 15.60 wt% TiO_2 ($CaZr_3TiO_9$). Generally the chemical variation in all analyzed natural samples shows a much lower variability than zirconolite (BELLATRECCIA et al., 1999). The only exceptions are niobium and tantalum, which may occupy up to 30% of the Ti site (Kaiserstuhl, Germany; SINCLAIR et al., 1986).

2.4.4 *Petrography*

The described localities for this accessory mineral are metasomatic rocks from Siberia and Japan, Italy, several carbonatite rocks from Russia, Germany, Brazil, Ceylon and Canada as well as alluvial deposits (mostly disaggregated carbonatite). It is primarily associated with apatite, baddeleyite, calcite, forsterite, magnetite, perovskite, phlogopite, pyroxene and zirconolite (ANTHONY & JOHN, 1997).

Table 2.5.1: *This table shows for the phases zirconolite, perovskite, calzirtite and baddeleyite the cation acceptor sites and their size.*

Mineral	*Coord. number*	*Polyhedron*	*Metal-oxygen bond lengths (Å)*	*Polyhedral volume (Å ^{3}) [1)]*	*Ref.*
Zirconolite:					[2)]
Ca site	VIII	cube	2.38 – 2.42	21.3	
Zr site	VII	monocapped octahedron	1.90 – 2.39	15.0	
Ti site (I)	VI	octahedron	1.91 – 2.10	10.2	
Ti site (II)	V	trigonal bipyramid	1.76 – 2.29	5.7	
Ti site (III)	VI	octahedron	1.86 – 2.01	9.2	
Perovskite:					[3)]
Ca site	XII	cuboctahedron	2.50 – 3.20	56.2	
Ca site	VIII	cube	2.50 – 2.68	30.4	
Ti site	VI	octahedron	1.92 – 1.93	9.5	
Calzirtite:					[4)]
Ca site (M3)	VIII	cube	2.35 – 2.54	~ 21	
Zr site (M1)	VIII	cube	2.04 – 2.67	~ 20	
Zr site (M4)	VII	monocapped octahedron	2.06 – 2.22	~ 15	
Ti site (M2)	VI	octahedron	1.90 – 2.02	~ 10	
Baddeleyite					[5)]
Zr site	VII	monocapped octahedron	2.05 – 2.28	~ 15	

[1)] Polyhedral volume data for zirconolite and perovskite after FIELDING & WHITE (1987), and thereafter estimated for calzirtite;
[2)] after GATEHOUSE et al. (1981);
[3)] after KOOPMANS et al. (1983);
[4)] after ROSSELL (1982); SINCLAIR et al. (1986);
[5)] after SMITH & NEWKIRK (1965)

2.5 Baddeleyite

2.5.1 *Introduction*

Baddeleyite is a rare zirconium oxide found as accessory mineral in a variety of environments. It is named after Joseph Baddeley, who found the original specimens in Sri Lanka in 1890.

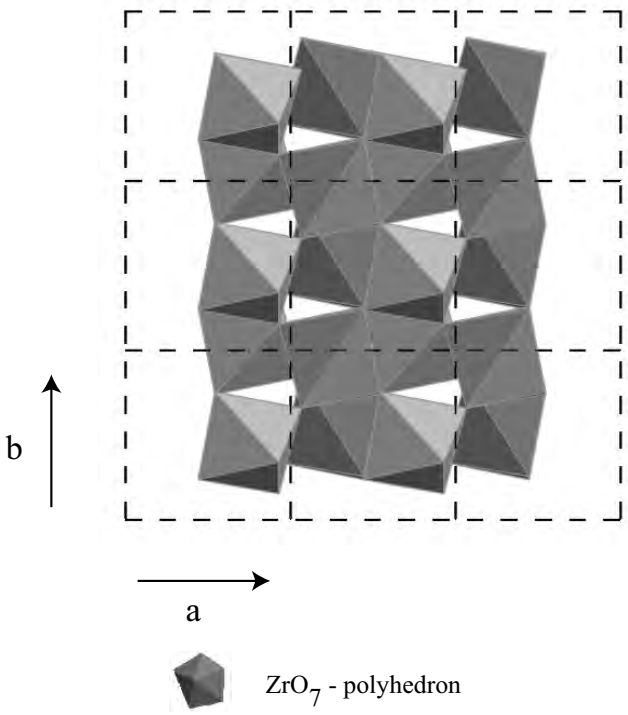

Figure 2.5.1: *The monoclinic crystal structure of baddeleyite revealing planes parallel to (100) (by Crystal Maker 4.0 using data from Smith & Newkirk, 1965).*

2.5.2 *Crystal structure*

This Zr-oxide mineral belongs to the monoclinic prismatic crystal system with the space group $P2_1/c$. One unit cell contains 4 ZrO_2 units (Roberts et al., 1990). It is a simple oxide where Zr is sevenfold coordinated with a cation charge of 4+. The structure can be described as a distortion of the cubic fluorite structure. The detailed structure analyses (Smith & Newkirk, 1965) reveal that all three axis are closely related with axial ratios of a:b:c = 0.9893:1:1.0216 (unit cell with the lattice parameter 5.1477 (a) x 5.203 (b) x 5.3156 (c) Å) and the β-angle is 99.38°. The O atoms have two different positions, both arranged as planes parallel to (100) (figure 2.5.1). Along these plains occur also the common polysynthetic twins.

2.5.3 *Crystal chemistry*

Stoichiometrically ideal baddeleyite (ZrO_2) contains 74.03 wt% Zr and 25.97 wt% O. Generally the chemical variation in all analyzed natural samples shows a low variability containing mostly around 95 wt% ZrO_2 (Hiemstra, 1955). This is mainly due to only one cation site which is limited in size and therefore only a few elements are possible to substitute (table 2.5.1). But it is often known to incorporate significant amounts of U and therefore is used for the determination of U–Pb ages together with zircon.

2.5.4 *Petrography*

Baddeleyite is found in a variety of environments including kimberlite, syenite and gabbro (Ferry, 1996; Hiemstra, 1955; Roberts et al., 1990; Smith & Newkirk, 1965). It often survives weathering as detrital mineral. It is reported to occur as coating on zircon at several localities, including kimberlites and a lamprophyre diatreme.

3 EXPERIMENTAL PART

3.1 Introduction

The aim of this study is to investigate the stability and corrosion behavior of zirconolite in hydrothermal fluids under conditions simulating those expected in a possible repository or at even higher p and T. Most present schemes for radioactive waste disposal go 300–1000 m below surface, whereas other projects discuss the disposal in deep boreholes, which are 4000–6000 m deep. However, this results in high temperatures (up to 700 °C) and pressures (up to 200 MPa) in the disposal caverns. These temperatures are estimated by using a geothermal gradients of 30–40 °C/km plus an additional factor of self heat (several hundred degrees) due to the decay of fission products (EWING et al., 1995; RYBACH, 1975). The pressure is calculated using a lithostatic fluid pressure gradient of 33 MPa/km depth. Down to a certain depth (several hundred meters) the fluid system could still be under the influence of hydrostatic fluid pressure (one third of the lithostatic pressure), but the high permeability of a hydrostatic system (open pores) would be very undesirable for a repository. Chemical reactions (and their equilibria) are only predictable for slowly migrating systems (reaching saturation). This is easier to achieve under the fluid water table than above, where gaseous phases have to be considered as well. Below approximately 4–5 km depth, the fluid system is controlled by grain boundary fluids and ductile processes. Even though most international waste programs do not plan to dispose under such high pressure conditions expected for deep boreholes, it is always important to understand the stability of a waste form under P–T-conditions higher than expected, especially, because the long-term predictions of the stability of a waste form are highly extrapolated from experimental data.

However, most experiments were conducted at 50 MPa, which corresponds to 1500 m depth over a temperature range of 150 up to 700 °C. These physical conditions are much higher than most present schemes expect, but may be caused by the above explained geological and radiogenic processes. In addition, experiments under high P and/or T allow an estimation or determination of the upper boundary of the stability field of a crystal phase. Such experiments are also essential in evaluating multi barrier scenarios, where each barrier is designed to provide independent immobilization capacity in the event of failure of one or several barriers.

Zirconolite is a principal host for actinides and certain fission products. Therefore, the starting material was doped with different REEs, Hf and U as actinide analogue and/or neutron absorbers. This is essential for the understanding of the behavior of diverse elements. For safety reasons during the experiments only depleted (natural) uranium is used and plutonium is not used at all. As a substitute for plutonium, cerium is used because they both have similar ionic sizes at the same valence and therefore should reside on the same sites in the host lattice (BEGG & VANCE, 1997; BEGG et al., 1998). Because of two possible valences (3+ and 4+), the behavior of cerium is more difficult to understand but still very important due to its affinity to plutonium.

The elemental fluid compositions used for the experiments were chosen according to natural ground waters. The corresponding elemental concentrations were chosen to be similar to or higher than those found in natural ground waters (see chapter 3.3). All experiments were always conducted with only one specific element in the fluid besides hydrogen and oxygen.

3.2 Designing the Solid Starting Material

3.2.1 Introduction

All the design of the starting material was carried out in the laboratories of the Materials Division at ANSTO. To fulfil the aim of the experiments which is to investigate the stability of zirconolite it was very important to obtain a 100% single-phase starting material. Reaching this goal turned out to be more difficult than expected.

3.2.2 Sintering of Zirconolite

A whole series of chemically different samples was synthesized following the fabrication process baseline: Sintering by the alkoxide/nitrate liquid route (RINGWOOD et al., 1988) using wet milling (VANCE et al., 1997). This method comprises the following steps:

Primarily a precise calculation of the masses of the ingredients has to be made (precursor materials, table 3.2.1). Then the first process is to weigh the alkoxides (elements Al, Ti, and Zr) and dilute them in ethanol by a ratio 1:1, followed by weighing the nitrates (REEs) and diluting them

in a different container with deionized water. The Ca carbonate powder is weighed and put in a third container together with the approximately similar amount of deionized water and then dissolved with nitric acid to form a clear solution. While using a shear mixer (2000 rpm) the water-based solutions are added to the alkoxide solution. The whole mixture is then stirred until a smooth jelly-like liquid is formed. Then, the thickening material is transferred to an oven set at 110 °C to dry overnight (Ebbinghaus, 1998).

After reducing the dried clumps to a coarse powder with a scoop, the sample material is transferred into a calcining container (Al-oxide crucible). Static bed calcination is performed at 750 °C for a hold time of 1 hour under air. Heating and cooling rates were chosen at 5 °C/min. After calcining, all material is weighed to check the completion of calcination and that no material was lost during the process (calculated final weight should be reached at this stage; Woolfrey et al., 1988).

The sample is then wet milled (together with deionized water) in a Teflon container with zirconium balls as grinding agent for 16 hours. The feed slurry is then dried in an oven at 110 °C. The formed dried clumps have to be size reduced by an agate mortar and pestle and then pushed through a nylon sieve to obtain particles smaller than 1 mm. The powder is then pressed by a hydraulic powder press to small pellets (9–50 mm in diameter) using oleic acid as die lubricant on the die set. The pressure is kept constant at 80 MPa for 30 seconds.

The pellets are sintered on platinum foil for 60–100 hours at 1400 °C under air. This temperature seems to be most suitable for forming a single phase zirconolite-2M, close to its melting temperature at 1470 °C (Vance et al., 1990). Heating rate is set at 5 °C/min, cooling rate at 10 °C/min. Due to the volume decrease during cooling, some samples cracked and therefore have to be reground and resintered for 20 hours to obtain dense pellets (figure 3.2.1).

Table 3.2.1: *Precursor materials.*

Oxide	*Precursor water soluble*	*Precursor ethanol soluble*	*Common name*
Al_2O_3		$Al(OC_4H_9)_3$	ASB
CaO	$CaCO_3$ and HNO_3		
CeO_2	$Ce(NO_3)_3 \cdot 6H_2O$		
Gd_2O_3	$Gd(NO_3)_3 \cdot 6H_2O$		
HfO_2		$Hf(OC_4H_9)_4$	
Nd_2O_3	$Nd(NO_3)_3 \cdot 6H_2O$		
TiO_2		$Ti(OC_3H_7)_4$	TPT
UO_2	$UO_2\ (NO_3)_2 \cdot 6H_2O$		
ZrO_2		$Zr(OC_4H_9)_4$	TBZ

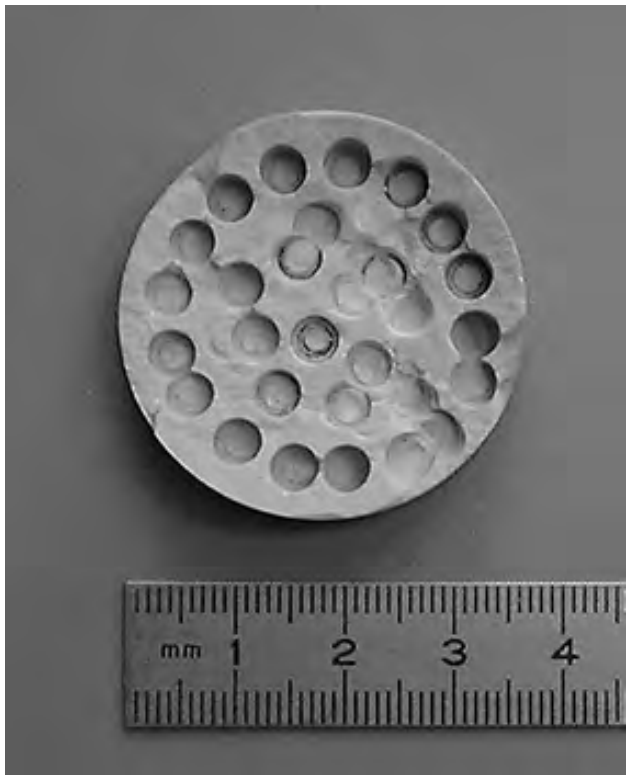

Figure 3.2.1: *Photograph of a sintered zirconolite batch showing the drill holes for core sampling. The cylindrical cores are further used in the experiments as polycrystalline zirconolite samples.*

3.2.3 Other Fabrication Techniques Used

Sol-gel and spray-drying:

Another attempt to produce single phase zirconolite was made by using an additional fabrication technique in collaboration with E. Sizgek at ANSTO. A sol-gel and spray-drying process replaces the process of mixing and calcining the chemical ingredients to the sinterable powder (Sizgek et al., 1998; Sizgek et al., 1994). This process is designed for large-scale quantities (> 50 kg), and is much less time consuming, but the results obtained are not as good as by alkoxide mixing. Only about 80–90% of the obtained powder was zirconolite beside other phases (e.g. perovskite). This unsatisfactory result may be due to the starting chemicals, which were probably not as pure, or to a particle fractionation effect during spray drying.

Hot uniaxial pressing:

Hot uniaxial pressing is a process, which replaces cold pressing and sintering and was developed at ANSTO (Levins et al., 1986; Ringwood et al., 1983). The mixed and calcined powder is filled into a steel bellow, closed by a steel lid. This bellow is then placed into a graphite die and

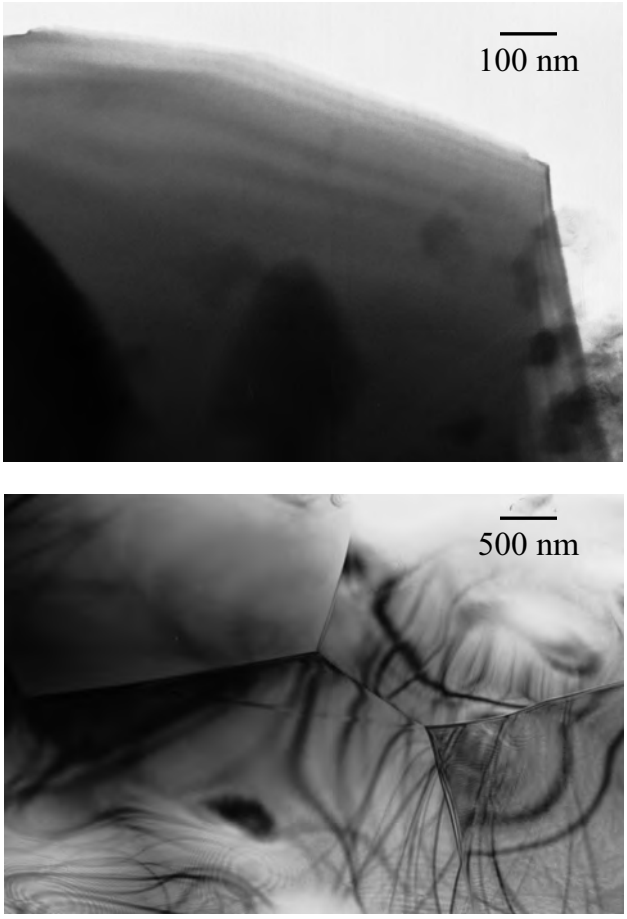

Figure 3.2.2: *TEM bright field image of sintered (top) and HIPed (bottom) zirconolite-2M revealing the strain fringes in zirconolite crystals obtained from HIP processing.*

hot-pressed for 2 hours at 1250 °C, using an applied uniaxial pressure of 23 MPa. This method is supposed to form a much denser material than sintering. The fO_2 is buffered internal by the graphite dies. The resulting fO_2-buffer (CCO: carbon-carbon-monoxide) is very close to the iron-wuestite buffer reaction representing reducing conditions (Huebner, 1971). Due to these reducing conditions about 20 vol% of perovskite are formed instead of zirconolite. Therefore this method can not be used to form single-phase zirconolite even though it increases the density of multi-phase Synroc samples (Oversby & Vance, 1995).

Hot isostatic pressing:

Hot isostatic pressing (HIP) is a process to reduce the pore volume of a presintered ceramic (Harker & Flintoff, 1984). The sintered pellets are placed into a pressure chamber (Ar gas as pressure medium) at 200 MPa for 2 hours at a temperature of 1350 °C. In the literature the density after the process is above 99% of the theoretical possible value. Our sample showed a very high density (at least 99%), but minor amounts of perovskite were formed as main reason not to use HIP to form single phase zirconolite. In addition, TEM bright field images of the zirconolite crystals showed heavy strain fringes revealing grain deformation (figure 3.2.2). Such weakened crystal structures of high energy react more easily than unstrained crystals. Such a weakening is undesirable for a product that is supposed to be very corrosion resistant.

Summary:

The three additional fabrication techniques discussed above were not suitable to our purpose of forming a single-phase zirconolite. But they are applicable to the fabrication of Synroc, which is simpler to fabricate because of its multi-phase composition.

3.2.4 Characterization of Starting Material

From all starting materials polished samples were made and analyzed in back-scattered electron imaging mode on the SEM to detect any additional phase beside zirconolite. The same polished cross sections were afterwards analyzed by the EPMA to determine the precise chemical composition of the zirconolite. Moreover, these values were used to determine the experimental k-factors for use in the analytical TEM. Table 3.2.2 (and appendix C6) shows the exact composition of the starting materials used in the experiments. Powdered starting material was analyzed by XRD to determine the zirconolite polytypoid. This was then again used to define the electron diffraction pattern, which had to be subtracted from the measured patterns of corroded sample surfaces after the experiment. The starting material was also analyzed as a crushed grain sample by electron diffraction on the TEM. The obtained diffraction patterns revealed a perfect zirconolite-2M (figure 3.2.3). The bright field images showed no internal strain (in contrast to the zirconolites obtained by HIPing). The ESEM was used to characterize the broken or polished surface of all samples before each experiment. This technique has the advantage of no need for any type of coating and therefore, the sample was not contaminated by the coating material before the experiment. The broken surface has smooth clear faces with sharp edges, whereas the polished surface showed the mechanically added scratches (figure 3.2.4).

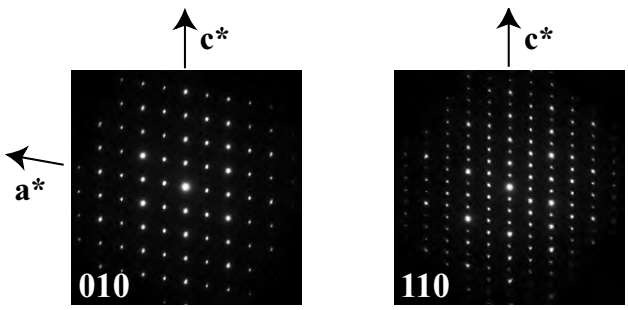

Figure 3.2.3: *Selected area diffraction patterns showing perfect zirconolite-2M. Visible is the fluorite subcell with $[111]_f$ parallel to c^*_z. The volume of the zirconolite supercell is 8-times the volume of the subcell.*

3.2.5 *«Quality» of the Products*

Table 3.2.3 gives a summary of all zirconolite samples synthesized. This list shows also that only a few samples fulfill the aim of forming a 100 % single-phase zirconolite. A tendency for the formation of perovskite at the expense of zirconolite was also reported in the literature (VANCE et al., 1994; WHITE, 1984). Some observations have been made during these syntheses resulting in a list of difficulties preventing the formation of single-phase zirconolite:

1) The single-phase field of zirconolite in the system CaO–TiO_2–ZrO_2 is very limited (figure 3.2.5, COUGHANOUR et al., 1955) and therefore not easy to achieve.
2) Impurities added during the processing (e.g., silica from mortar and pestle) lead to the formation of additional phases.
3) The composition of the alkoxides changes with time due to evaporation out of the unsealed containers and therefore, the ingredients are not always what they are supposed to be.
4) During all processes, some minor amounts of the bulk material get lost during changing of the containers. If this happens prior to a homogenous distribution of the ingredients, the proportions between the chemicals are changed and therefore, the single-phase field could be reached accidentally.

Most of these problems are very difficult to avoid in routine sample production.

The majority of the experiments were finally carried out with single phase Nd-doped zirconolite. At a second stage experiments were carried out with a single phase zir-

Table 3.2.2: *Analytical electron microscopy (AEM) analysis of untreated zirconolite analyzed before the experiment from the two different starting materials (standard deviation (s.).*

wt%	**zirconolite-(Nd) (n = 15)**				**zirconolite-(Gd) after (n = 5)**			
	mean	*s.*	*min*	*max*	*mean*	*s.*	*min*	*max*
Na_2O	0.02	0.07	0.00	0.28	0.00	0.00	0.00	0.00
Al_2O_3	2.73	0.21	2.46	3.19	1.50	0.21	1.16	1.68
CaO	12.14	0.41	11.31	13.06	12.74	0.11	12.65	12.93
TiO_2	40.14	0.97	38.26	41.88	41.82	1.26	40.80	44.00
FeO	0.11	0.04	0.02	0.17	0.12	0.03	0.09	0.15
ZrO_2	33.90	0.94	32.63	35.84	28.75	0.89	27.21	29.45
Ce_2O_3					4.17	0.15	4.02	4.35
Nd_2O_3	10.36	0.54	9.37	11.59				
Gd_2O_3					5.32	0.14	5.10	5.46
HfO_2	0.60	0.13	0.37	0.84	5.58	0.08	5.45	5.65
sum	100.00				100.01			
Formula based on 7 oxygens								
Na	0.00	0.01	0.00	0.03	0.00	0.00	0.00	0.00
Al	0.19	0.01	0.17	0.22	0.11	0.02	0.08	0.12
Ca	0.78	0.03	0.72	0.84	0.83	0.01	0.81	0.84
Ti	1.80	0.03	1.73	1.86	1.91	0.05	1.87	1.98
Fe	0.01	0.00	0.00	0.01	0.01	0.00	0.00	0.01
Zr	0.99	0.03	0.94	1.05	0.85	0.03	0.80	0.87
Ce					0.09	0.00	0.09	0.10
Nd	0.22	0.01	0.20	0.25				
Gd					0.11	0.00	0.10	0.11
Hf	0.01	0.00	0.01	0.01	0.10	0.00	0.09	0.10
sum	4.00				3.99			
∑ REE [1)]	0.22	0.01	0.20	0.25	0.20	0.01	0.19	0.20
∑ Zr, Hf [1)]	1.00	0.03	0.95	1.06	0.95	0.03	0.89	0.97

[1)] This sum is relative to one measurement and not the sum of the min/max of different measurements.

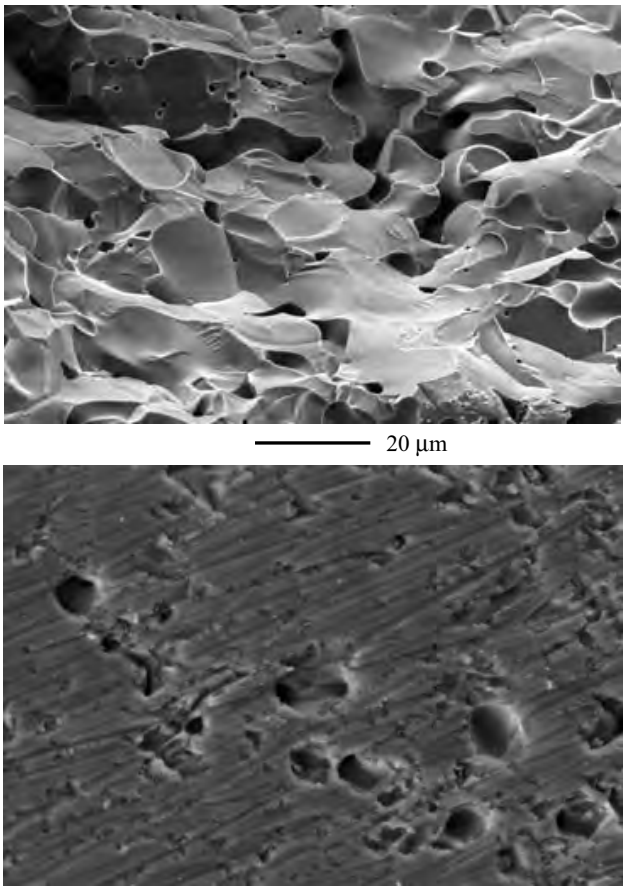

Figure 3.2.4: *Secondary electron images by ESEM show a broken surface (top) with smooth clear faces and sharp edges. The polished surfaces (bottom) reveal the mechanically added scratches. Both show the closed porosity. During the first series of experiments broken surfaces were used to characterize the corrosion after the experiments, for the later (more detailed) experiments, polished surfaces were used.*

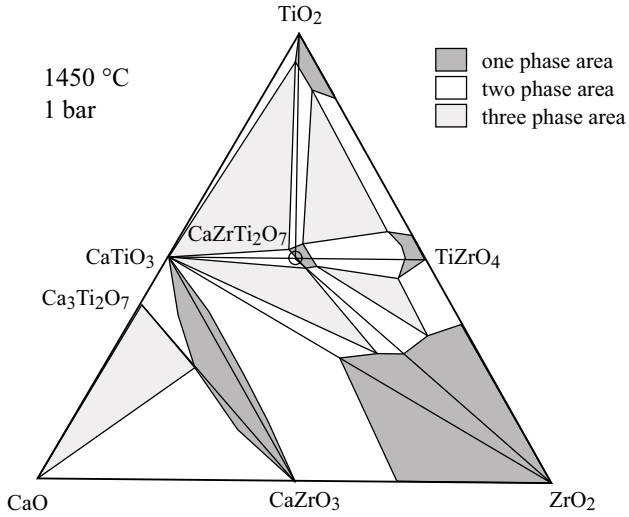

Figure 3.2.5: *Phase diagram after* Coughanour *et al. (1955) of the ternary system CaO–TiO2–ZrO2 revealing the limited single-phase field of zirconolite at 1450 °C.*

conolite doped with Ce, Gd and Hf. Additional experiments finally were carried out with U- and Gd–Hf–U-doped zirconolite. These were all produced by sintering but were not completely single phase.

3.3 Fluid Composition

Most standard leach tests for the determination of the corrosion resistance of glass, Synroc, or single crystalline phases are generally carried out in deionized water at 90 or 150 °C. Natural ground waters have different compositions (Bird & Fyfe, 1982; Bruno et al., 1997; Deutsch et al., 1982; Fritz & Lodemann, 1990; Fritz & Frape, 1982; Nagra, 1990) and may reach extreme salinity. In this study, we have taken a simplified but systematic approach towards these complex fluid compositions.

All experiments were carried out with only one element beside hydrogen and oxygen added to the deionized water. The added element was chosen according to the composition of natural groundwater in granitic rocks from the Swiss Alps (Nagra, 1990), Sweden (Bruno et al., 1997) and Yucca Mountain (US DOE, 1994). The main ions of these waters are Ca^{2+}, Na^{+} and Cl^{-} (figure 3.3.1). However, no experiments were carried out with Ca-containing waters, because zirconolite already contains up to 13 wt% Ca. Most experiments were carried out in NaOH or HCl enriched fluids with ionic concentrations similar or higher than those found in natural waters. Some additional experiments were carried out with some minor ions present in natural ground waters, namely Si^{4+}, PO_4^{3-} and CO_2. These experiments were carried out in much higher concentrations than expected in nature. Table 3.3.1 lists all experimentally used fluids with their molal concentration and pH at ambient conditions (25 °C and 0.1 MPa). The pH during the actual experiment differs considerably under elevated pressure and temperature. Higher temperatures result in lower pH. Some calculations for the actual pH during the experiment were made, but above 400 °C and 50 MPa, the aqueous species equations are beyond the range of applicability. At 400 °C and 50 MPa the neutral pH is 5.678. Figure 3.3.1 shows the composition and concentration of natural ground waters compared to the experimentally used fluids.

As the geotechnical barrier in a possible repository, bentonite is used as backfill (buffer). Bentonite mainly consists of Na-rich montmorillonite. Additionally the waste form is placed into cement. A fluid flowing through these two materials will achieve a high Na concentration from the bentonite and a high pH from the cement. Therefore basic

Table 3.2.3: *Summary of all zirconolite samples synthesized.*

Name	*Intended composition*	*Determined composition* [1)]	*Procedure*	*Other phases*
Z1	$CaZrTi_2O_7$		sintered	1% perovskite
Z2	$CaZrTi_2O_7$		sintered and HIPed	3% perovskite
Z3	$Ca_{0.95}Zr_{1.05}Ti_{1.9}Al_{0.1}O_7$			perovskite, TiO_2, $ZrTiO_4$
Z4	$Ca_{0.99}Zr_{1.07}Ti_{1.94}O_7$			1–2% $ZrTiO_4$
Z5	$CaZrTi_2O_7$		sol-gel and hot pressed	15% perovskite 5% baddeleyite
Z6	$CaZrTi_2O_7$		sol-gel and sintered	5% perovskite
Nd-Z1	$Ca_{0.8}Nd_{0.2}ZrTi_{1.8}Al_{0.2}O_7$	$Ca_{0.78}Nd_{0.22}Zr_{0.99}Ti_{1.80}Al_{0.19}O_7$	sintered	no other phases!
Nd-Z2	$Ca_{0.8}Nd_{0.2}ZrTi_{1.8}Al_{0.2}O_7$		sintered and HIPed	1% perovskite
Y-Z	$Ca_{0.8}Y_{0.2}ZrTi_{1.8}Al_{0.2}O_7$		sintered	2% perovskite
La-Z	$Ca_{0.8}La_{0.2}ZrTi_{1.8}Al_{0.2}O_7$		sintered	2% perovskite
Gd-Z	$Ca_{0.85}Ce_{0.1}Gd_{0.1}Zr_{0.85}Hf_{0.1}Ti_{1.9}Al_{0.1}O_7$	$Ca_{0.83}Ce_{0.09}Gd_{0.11}Zr_{0.85}Hf_{0.10}Ti_{1.91}Al_{0.11}O_7$	sintered	no other phases!
U-Z 1	$Ca_{0.8}U_{0.2}ZrTi_{1.6}Al_{0.4}O_7$		sintered	3% $ZrTiO_4$
U-Z 2	$Ca_{0.85}U_{0.1}Gd_{0.1}Zr_{0.85}Hf_{0.1}Ti_{1.8}Al_{0.2}O_7$	$Ca_{0.85}U_{0.11}Gd_{0.11}Zr_{0.84}Hf_{0.1}Ti_{1.86}Al_{0.11}O_7$	sintered	no other phases!

[1)] The composition was only determined if the BSE images on the SEM showed sufficiently good results (no secondary phases).

fluids (high pH) with a high Na content are expected in a possible repository. These circumstances show the importance of experiments to be carried out in Na-rich fluids.

Table 3.3.1: *All experimentally used fluids, their composition and pH at ambient conditions.*

Fluid	*concentration*	*pH at 25 °C and 0.1 MPa*	*preparation of chemicals*
deionized H_2O		7	doubly deionized water
HCl	0.1 M 0.01 M 0.001 M	1 2 3	diluted from HCl suprapur 65%
NaOH	0.1 M 0.01 M 0.001 M	13 12 11	diluted titration solution 1 M NaOH
H_3PO_4	0.1 M	1.02	diluted from H_3PO_4 suprapur 30%
SiO_2	0.1 M	7	pure synthetic quartz powder
CO_2	0.1 M	4.5	diluted oxalic acid

3.4 Experimental Techniques

3.4.1 Introduction

In this part the hydrothermal apparatus, some other experimental equipment and specific procedures used for the experiments during this work is described.

3.4.2 Hydrothermal Apparatus

S. Girsperger designed the hydrothermal apparatus used at the experimental petrology laboratories at ETH Zürich (figure 3.4.1). All experiments were performed in externally heated pressure vessels. This laboratory has been described by various authors (Gunter et al., 1983; Mok, 1993; Philipp, 1988; Raz, 1983; Vavrecka-Sidler, 1998).

The cold seal pressure vessels used are made out of nickel alloy (Nimonic 105 and René 41). They are 485 mm long, have an outer diameter of 50 mm and a 455 mm deep 6.45 mm bore. The closure cap is a screwed on male cone, which holds the filler rod inside the bore of the autoclave and, on the outside, the thermocouple, the capillary pressure tubing and the pressure transducer. The filler rod (stainless steel tube) firstly holds the sample in a 3–6 cm long slot at the internal end together with the thermocouple at the hot spot of the furnace, and secondly reduces the dead volume of the apparatus and reduces thermal convection in the bomb. The temperature gradient at the hot spot was determined for each furnace experimentally at ambient pressure (no influence of pressure on the thermal gradient according to Raz,

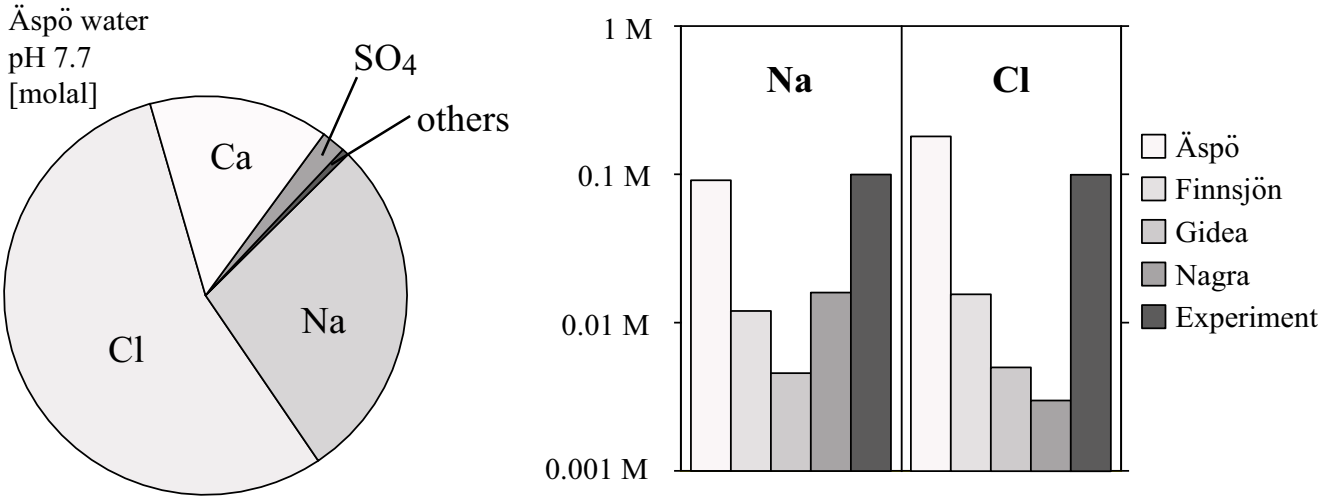

Figure 3.3.1: *Elemental composition of natural ground water from Äspö (left) and variation of the Na and Cl concentration in natural ground waters compared to the experimentally used concentrations (data from* Bruno *et al., 1997;* Nagra, *1990).*

1983). Figure 3.4.2 shows this setup and the thermal gradients at the desired furnace temperature in the pressure vessels measured by a thin thermocouple embedded in corundum beads (to reduce convection). After reaching equilibrium the thermocouple was moved through the whole length of the bore in steps of 1 cm out of the vessel. The position of the slot in the filler rod at the hot spot was chosen to keep the temperature gradient over the whole sample below 1 °C. The hot junction of the thermocouple was adapted about 1 mm into the slot.

The used furnaces are designed to keep the temperature fluctuations over the period of an experiment below 1 °C. This was reached by a manually set PID-controller (proportional-integral-differential), which continuously controlled the AC heating current by means of two thyristors. This PID-controller is connected to a chromel-alumel thermocouple at the hot spot of the furnace. The density distribution of the heating wires (Kantal) is apportioned to achieve isothermal conditions around the hot spot (thermal gradient below 1 °C for at least several centimeters). The furnaces are packed with compressed ceramic fibers for insulation into cubic Eternit™ casks. The maximum heating rate with this type of furnace is ~10 °C/min.

Temperature was measured by commercial inconel sheathed nicrosil-nisil (NiCrSi–NiSi type N) thermocouples. They had an overall length of 600 mm and a diameter of 1.0 mm and a specially condensed MgO insulation to prevent a collapse of the hot junction under pressure. They were fitted tightly into the filler rods and brazed into a steel pressure fitting. The position of the fitting is chosen so, that the thermocouple tip is in contact or as close as possible to the sample. As zero-point reference a conventional ice bath was used. To avoid thermal stratification in the ice bath, a large ice block was mechanically kept below the surface in the water.

An air driven membrane pump generated the pressure (up to 300 MPa). Argon 5.0 (> 99.999%) was used as pressure medium and was fed into the autoclave over pressure capillaries with an inner diameter of 0.1 mm. Each pressure vessel can be disconnected from the pressure line by manually operated high-pressure valves.

As a new part of the hydrothermal apparatus, pressure transmitters (WIKA) measured pressure during the experiments. Pressure can be determined up to 400 MPa with a precision of 0.01 MPa. Before each experiment, externally calibrated Heise gauges were used for pressure calibration.

3.4.3 Data Acquisition

A Pentium 330 MHz Dell Optiplex PC controlled the experiments. Highly accurate measurements were possible using a PCI-GPIB interface card (NI-488.2M) and a 6 $^{1}/_{2}$ digit multimeter (Keithley model 2001) with a 10 channels 2-pole scanner card (Keithley model 2000-SCAN). This setup allowed measuring temperature and pressure of the four furnaces used at the same time. The basic hardware functions are supported by software routines, which can be called by conventional software languages or by Lab View™. The latter one has the big advantage of saving programming time when changing experimental setups. The data acquisition and control program developed for the experiments is shown in appendix B. This program controls and monitors online the process-variables, graphs, numerical and boolean indicators and controls like an instrument panel. It shows for individually determined time steps the temperature and pressure variations during the experiment (most due to room temperature changes) for all four vessels. It also generates a text-file with time-stamped pressures and temperatures during the whole experiment on the hard-disc.

3.4.4 Capsule Loading

The solid starting materials were small cylinders, drilled out of the sintered zirconolite batch with a diameter of 2.3 mm and a height of 1.0 mm resulting in an average weight of 0.02 g (min. 0.016 g, max. 0.024 g, depending on the exact height of the cylinder, figure 3.2.1). For the first series of experiments those cylinders had a broken surface, whereas for the more detailed experiments one side was polished (figure 3.2.4). Before the experiments all cylinders were ultrasonically cleaned in deionized water to remove small grains and dust.

Electrolytically pure gold was chosen as capsule material because it is inert against the used corroding fluids. 500 mm long gold tubes with an outer diameter of 5.0 mm and a wall thickness of 0.3 mm were cut into 25 mm long pieces and welded on one side. Then the zirconolite cylinder together with the 25 µl of fluid (added with a piston-stroke pipette) is filled into the capsule. Its upper half is immediately pressed together and marked by dies with the experiment number. Then they are placed into a liquid nitrogen container (–196 °C) to avoid fluid loss during welding by a plasma-arc welder. Each capsule was heated up to 140 °C in the oven at atmospheric pressure before the experiment. Thereby tight capsules showed no mass loss. The sequences of the capsule preparation are documented in figure 3.4.3. The closed capsules then represent a closed system.

Figure 3.4.1: *Laboratory at ETH where all experiments are carried out. The photo (top) shows the furnaces containing the pressure vessels. In front of the vessels are the pressure transducers and the connecting wires to the voltmeter. Temperature and pressure are continuously computer controlled. Detailed photos (bottom left) of the pressure vessel (length 485 mm) and the filler rod containing thermocouple and pressure supplies. The gold capsule (bottom right) is placed in the slit at the end of the filler rod at the low temperature gradient position.*

The calculated ratio of the zirconolite surface area to fluid volume was 4–6 cm^{-1} at loading conditions.

3.4.5 Heating and Cooling

To start the experiment, the capsule was placed into the slot of the filler rod and placed at the hot spot of the vessel. After closing the vessel, pressure was added to the sample to avoid bursting of the capsule during heating due to the expansion of the fluid phase. Preferably more than 21.8 MPa are needed to avoid the liquid/gaseous phase transformation (critical point of water: 218 bar / 647.30 K). Then the furnaces were heated up to the desired temperature (reached after one hour), and the pressure was now adjusted to the exact pressure wanted.

For cooling at the end of the experiments the pressure vessels were taken out of the furnaces and cooled in a tube with compressed shop air. The cooling rate was about 110 °C/min. After releasing the pressure, the collapsed capsules are removed from the vessel and weighed to test for possible material loss during the experiment.

3.4.6 Runs

Because no data on the solubility of zirconolite at higher temperatures were available at the beginning of this project, a first series of leaching experiments was made over a broad range of temperature, time, and fluid compositions. The lowest temperature was chosen to begin at the highest temperature (150 °C) used in experiments conducted at the

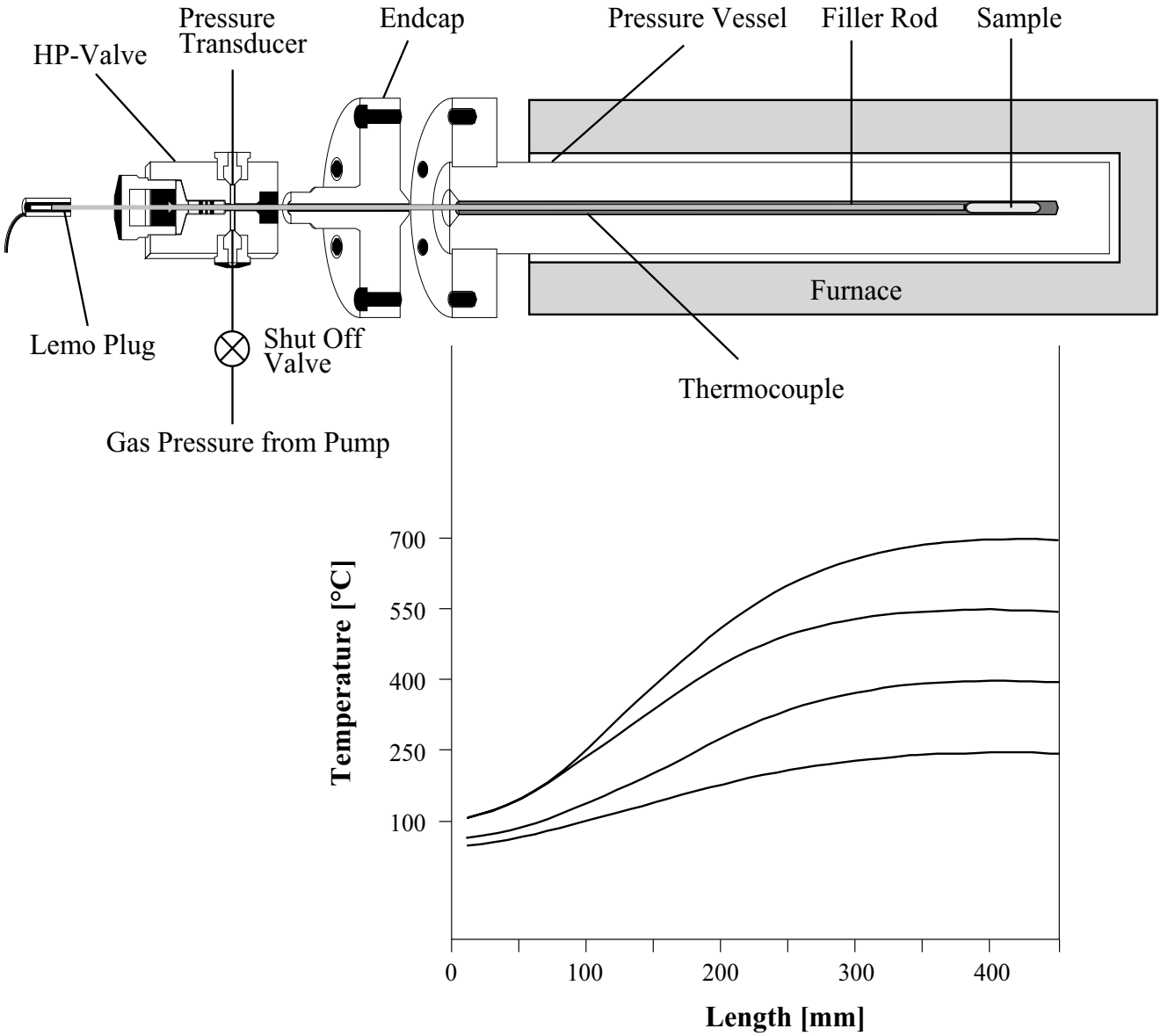

Figure 3.4.2: *Nimonic 105 pressure vessel and the standard setup for temperature-pressure analysis (top). The lower part shows the determined thermal gradients of the four furnaces used at a desired temperature (250, 400, 550 and 700 °C). These thermal gradients are below 1 °C at the best position for the samples.*

laboratories of ANSTO (LUMPKIN et al., 1995; MCGLINN et al., 1995; SMITH et al., 1997) and from there stepwise up to 700 °C at a pressure of 50 MPa, representing 1500 m depth. These experiments were conducted over 21, 63 and 189 days for various fluid compositions (NaOH, HCl, deionized water) and molalities (0.1–0.001).

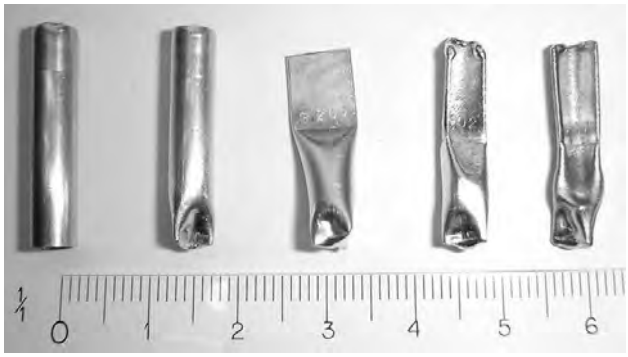

Figure 3.4.3: *Picture at the top shows the steps described in the text of the capsule preparation from a cut gold tube (left) to the capsule after the experiment (right). The lower picture shows the plasma-arc welding with the sample in liquid nitrogen (–196 °C).*

At a second stage, some additional experiments were carried out in H_3PO_4-,CO_2- and SiO_2-rich fluids. At the temperature of 550 °C two experiments were made at 100 MPa (3000 m depth) and 200 MPa (6000 m depth).

More experiments were carried out in 0.1 M NaOH at the specific conditions of 550 °C and 50 MPa. These experiments were performed over several different run times (one hour to 21 days) to determine the kinetics of the corrosion process.

A detailed list of all experiments can be seen in the appendix A. All experiments were performed in duplicate at the same time to test reproducibility and to avoid data loss if one capsule broke during the experiment.

3.4.7 Extraction of Solid and Fluid after the Experiment from the Capsule

After removing the collapsed capsules from the vessel, they were reheated with a hot air gun for some seconds to inflate the collapsed capsule, a necessary step to recover fluid and sample. Then the capsule was opened in a small container filled with 3 ml of 5% HNO_3 to stabilize the solution. Thereby the leachate was washed out of the capsule and diluted. This process had to be done extremely carefully in order to avoid any contamination. During this process the speciation of the diluted elements changes, because the pH of the fluid shifts from basic (experiments with NaOH) to acidic. But this does not affect the analysis by ICP-MS afterwards, because the elements are measured independent of their speciation. No elements are expected to precipitate because the solubility in 5% HNO_3 is comparable to that during the experiment and due to a strong dilution (> 100) the tendency towards solubility is even higher (D. GÜNTHER, personal communication).

The mass loss on the solid sample could not be determined by weighing because the small zirconolite cylinder usually broke into pieces during the experiment and/or opening of the capsule, and some bits were not recoverable.

4 ANALYSIS AND RESULTS OF THE EXPERIMENTS

4.1 Introduction

4.1.1 General

All through this thesis, corrosion of zirconolite during hydrothermal experiments (for details see chapter 3.4) has been investigated using a wide range of analytical techniques for solid and liquid run products to obtain qualitative and quantitative results. Experiments were carried out over a wide range of temperatures (150–700 °C) at a pressure of 50 MPa in various hydrous fluids (mainly NaOH and HCl). The results described in this chapter are mainly based on experiments carried out with two synthetic single-phase zirconolite-2M as starting material with the composition:

$$(Ca_{0.8}Nd_{0.2})Zr(Ti_{1.8}Al_{0.2})O_7$$

and zirconolite-2M with the composition:

$$(Ca_{0.85}Gd_{0.1}Ce_{0.05})(Zr_{0.85}Hf_{0.1}Ce_{0.05})(Ti_{1.9}Al_{0.1})O_7$$

(chapter 3.2). The dopant Hf plays the role of a neutron absorber, Gd as a neutron absorber and actinide analogue, and Nd and Ce as actinide analogues.

Additional experiments were carried out at 200 MPa and fluids containing H_3PO_4, CO_2 and SiO_2, respectively. In chapter 4.9 some results from experiments carried out with U-doped zirconolites are summarized. The first of these radioactive samples was doped only with U^{4+} (Al as charge balancing element), whereas the second sample is doped with U^{4+}, Gd and Hf (charge balanced by Al). Unfortunately these starting materials were not absolutely single phase.

4.1.2 Alteration

Mineral alteration in general is caused by fluid – mineral interactions. In a closed system, dissolution/precipitation is the main alteration process. Models for dissolution processes were established (e.g., MOUNTAIN & WILLIAMS-JONES, 1994) but may only be used with caution. External variables (e.g., pressure, temperature, fluid composition) play an important role as will be shown later in this chapter. In addition, the fluid evolution over time is not only dependent on the rock composition but also on the changing physical properties of the rock during alteration (e.g., surface).

4.2 Qualitative Surface Characterizations

After the experiments, the qualitative characterization of the corroded zirconolite surface and secondary run products was made by ESEM (appendix C.2). These observations permitted to estimate qualitatively the degree of corrosion during the experiment. Three different stages of corrosion can be discerned:

1) In the first stage, no surface reactions are observed at ESEM resolution (µm) and the run products exhibit the same features as the unreacted starting material (figure 4.2.1).
2) The second stage shows partly corroded crystal surfaces and edges. Moreover, some product phases (e.g., quench phases) are observed on the surface (figure 4.2.2).
3) In the third stage the entire zirconolite surface is covered by product phases or does not exhibit pristine surface features anymore (figure 4.2.3).

A complete table of all experiments carried out is given in appendix A. This table summarizes the qualitative corrosion stage (1 to 3) reached. If only a few features are visible on the surface, the rating was chosen to be 1–2.

Corrosion of the zirconolite surface as seen at ESEM resolution starts at crystal edges and grain boundaries and progressively embraces the entire surface. This is also confirmed by polished cross sections analyzed by EPMA which reveal that corrosion stage two takes place only at the outermost 2 µm of the individual crystal surfaces, but follows the grain boundaries into the polycrystalline bulk of the cylindrical sample (figure 4.2.4). For corrosion stage three, where the entire zirconolite surface is corroded, cross sections reveal transformations several tens of µm deep into the cylinders from the surface (figure 4.2.5). Over all stages of corrosion, the fluid migrates along the grain boundaries into the connected pore space and starts corrosion from there (MALMSTRÖM et al., 1999). All experiments carried out in NaOH and HCl showed a direct relationship between the extent of corrosion and temperature, molality of the fluid, and time, as schematically shown in figure 4.2.6.

Starting from the observation, that some individual grain surfaces are corroded more easily than others it is assumed

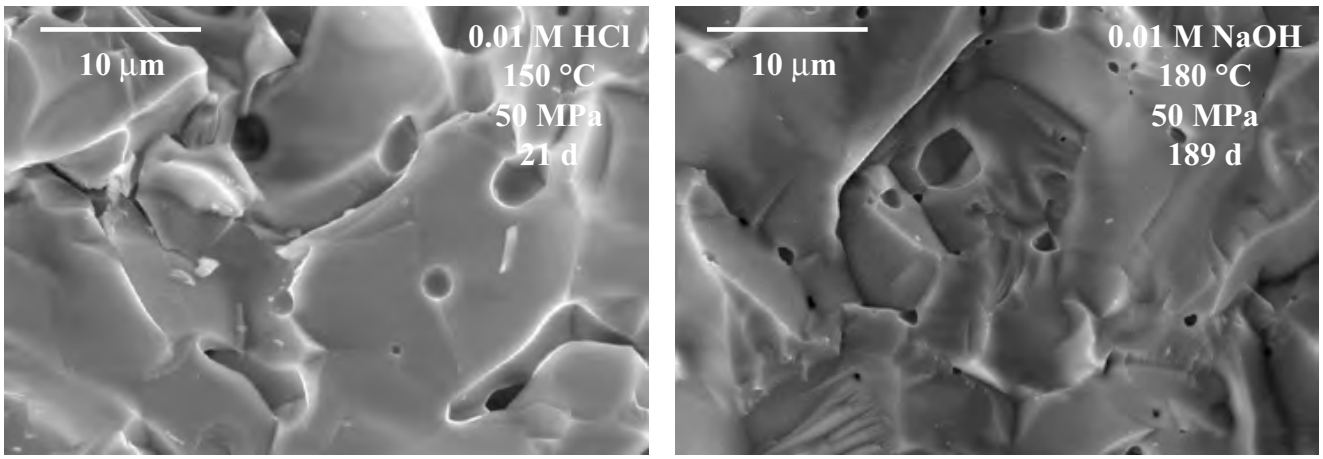

Figure 4.2.1: *Secondary electron images (by ESEM in low vacuum and wet mode) of zirconolite surface after experiments revealing first stage of corrosion.*

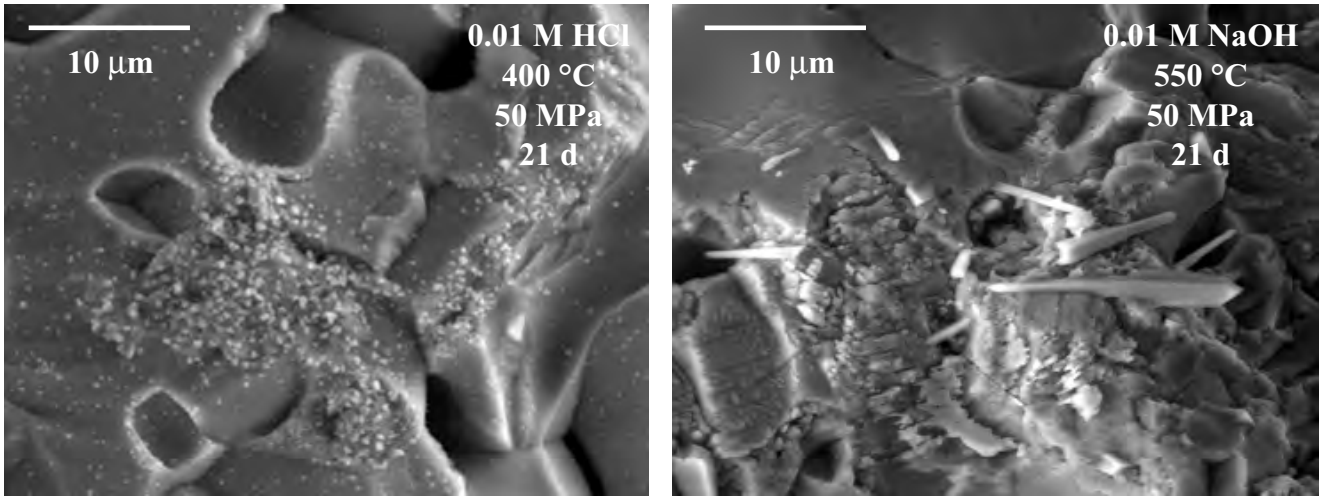

Figure 4.2.2: *Secondary electron images (by ESEM in low vacuum and wet mode) of zirconolite surface after experiments revealing second stage of corrosion.*

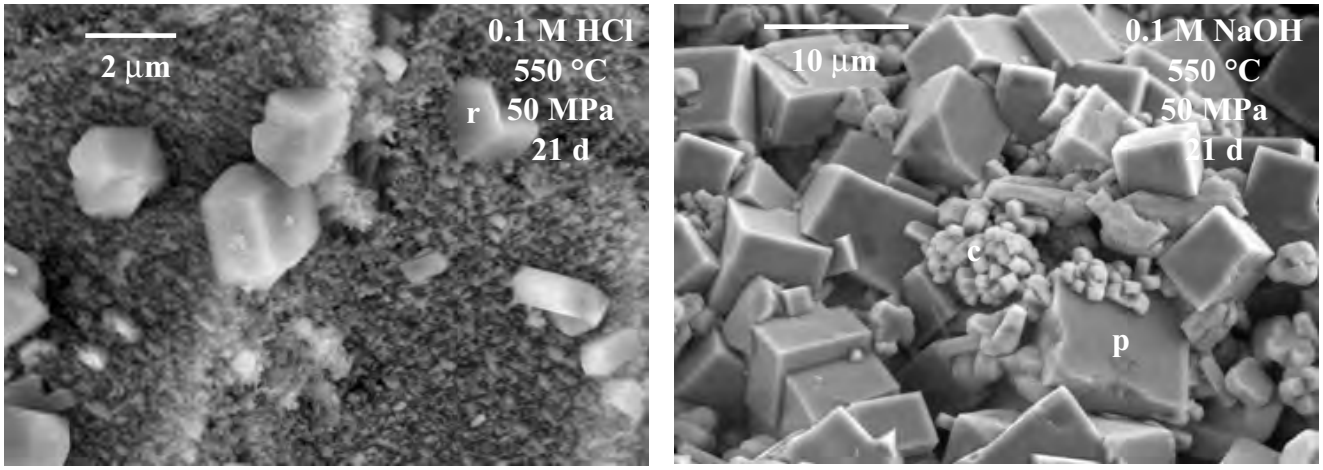

Figure 4.2.3: *Secondary electron images (by ESEM in low vacuum and wet mode) of zirconolite surface after experiments revealing third stage of corrosion and the product phases rutile (r), perovskite (p), and calzirtite (c).*

that the corrosion of zirconolite crystals depends on its crystallographic orientation (figure 4.2.7). This is not surprising for a monoclinic crystal with layer structure (see chapter 2.2).

The large range of different fluid compositions used during the experiments permits a qualitative comparison of the corrosion capability of a particular fluid on zirconolite. Experiments conducted with deionized water did not provide any evidence for corrosion up to 400 °C and, only some very weak corrosion indicators (e.g., quench products) were observed at higher temperatures. The experiments with a CO_2- and SiO_2-rich fluid both revealed next to no corrosion, as with deionized water (figure 4.2.8). They all barely reached corrosion stage two. The experiment in a H_3PO_4-rich fluid showed significantly higher corrosion than those in deionized water, CO_2- or SiO_2-rich fluids and reached stage two of corrosion after 21 days (figure 4.2.9). The third stage of corrosion (entire zirconolite surface corroded) was only observed in HCl- and NaOH-rich fluids above 500 °C. At these temperatures, NaOH is probably even more corrosive than HCl whereas at lower temperatures (< 500 °C) the opposite effect was observed. No unique pH dependence of the corrosion has been observed. Experiments at 90 °C showed also just a weak pH-dependence with slightly higher corrosion at a low pH (McGlinn et al., 1995).

4.3 Product Phases

4.3.1 Introduction and Characterization

Beside the observed surface corrosion, secondary product phases (e.g., quench crystals) were noticed on the surface and in the closed pores of the starting zirconolite after the experiment. With increasing temperature and time, first, they were observed as isolated crystals, then as clusters and finally they covered the entire surface. These three different ways of accumulation of product phases are comparable to the earlier (chapter 4.2) described corrosion stages (isolated crystals => stage 1–2; clusters => stage 2; fully covering surface => stage 3). The size of the secondary phases is mostly below 2 µm. Only the experiments in higher concentration of NaOH at temperatures above 500 °C formed larger phases with a length exceeding 10 µm. Many of these secondary phases are quench products, but

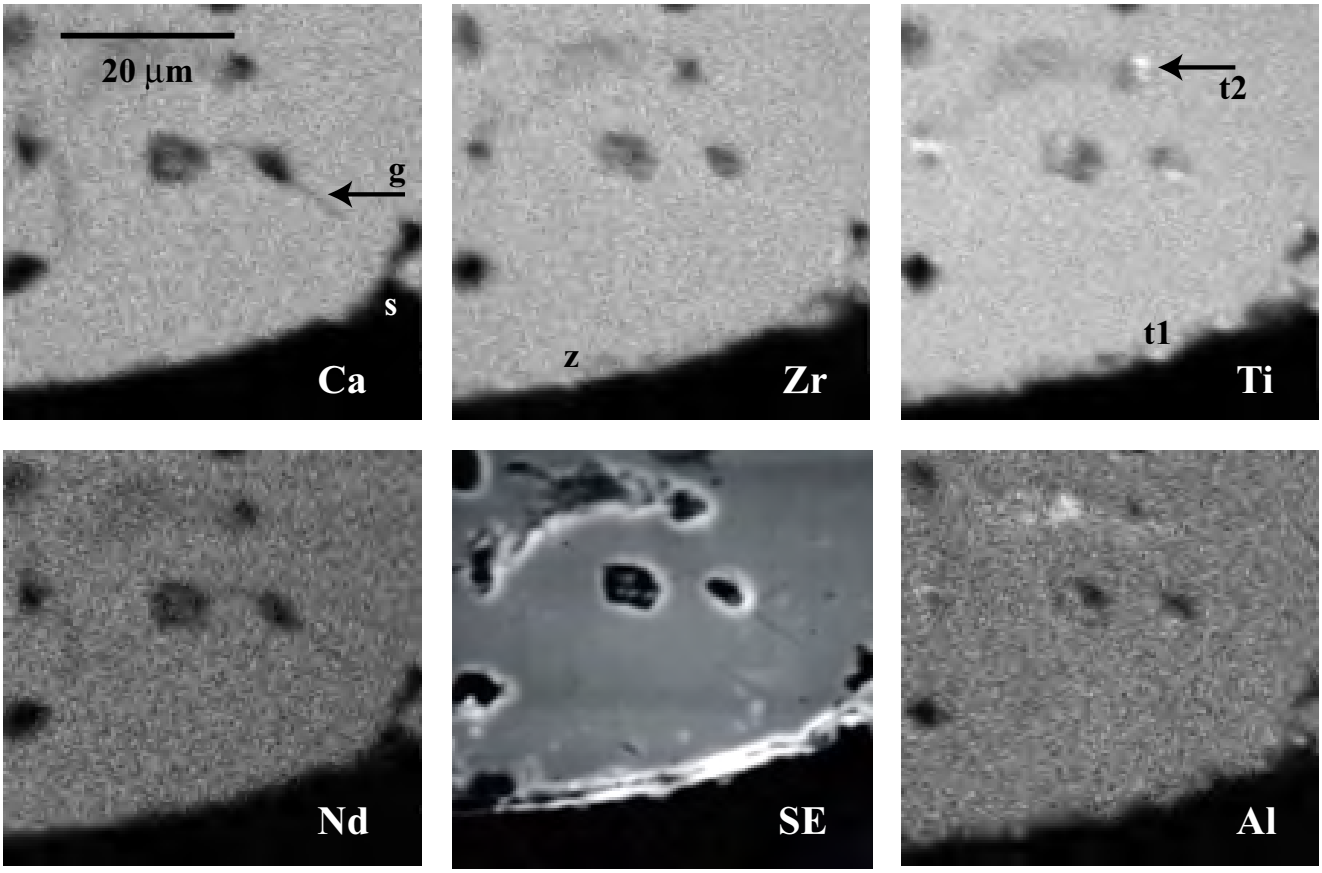

Figure 4.2.4: *EPMA X-ray elemental distribution maps and secondary electron image (SE) from a cross section through zirconolite (figure 4.2.2 left) treated with 0.01 M HCl for 21 days at 400 °C and 50 MPa reaching the second stage of corrosion. On the surface (s) and along grain boundaries (g) Ca is depleted. On the surface (t1) and in the pores (t2), Ti is enriched. Some parts on the surface are enriched in Zr (z). The crystals are corroded only on the outermost 2 mm, but the fluid migrates along the grain boundaries several tens of mm into the pores (black areas).*

the detailed and individual crystallization process of these secondary phases will be discussed later.

Because many of these product phases occurred at a small size and low abundance, it was impossible to identify all of them. For the characterization of these newly grown phases a large variety of analytical methods was used (appendix C) each having its specific advantages and disadvantages. By ESEM only qualitative phase descriptions (specific phase morphology) were made. The attached EDX was used to obtain qualitative information on the chemistry. Experience gained during this study showed that for XRD phase detection, most of the remaining zirconolite surface needed to be covered by secondary phases (> 50%) for its phase detection, which only rarely was achieved. Another problem appeared for the TEM sample preparation (crushed grain and ion beamed thin section), which required a minimum of secondary phases beside the remaining zirconolite to be statistically detected by the TEM. For analyzing samples by EPMA, a properly polished surface is needed. During polishing, the thin layer of secondary phases on the surface mostly was ripped away. Additionally the analytical volume of the probe (1–3 µm in diameter) was too big to measure the small particles. Raman-spectroscopy finally had the big advantage of no special sample preparation, but the secondary phases had to be visible (> 2–5 µm) by an optical microscope to determine them. Therefore not all secondary phases are unequivocally specified in the following descriptions.

4.3.2 Experiments with HCl

No corrosion was observed on the zirconolite surface after the experiments in HCl below 250 °C. In contrast, those conducted in more concentrated HCl (0.1 M) and above 250 °C revealed quench phases with various morphologies showing a bimodal size distribution. Some are extremely small (< 0.5 µm) whereas others are found to occur in the range of 1–3 µm (figure 4.2.3 left). No clues could be made for the smaller ones.

For the larger phases, a generally high Ti content was determined by ESEM/EDX as well as by X-ray maps on the EPMA (figure 4.2.4). By TEM, only one crystal was found and determined as TiO_2, but because of its small size and orientation, the structure could not be analyzed. By Raman-spectroscopy, the two TiO_2 polymorphs rutile and anatase were qualitatively determined (appendix C.5). In addition, rutile could be confirmed by XRD on the same sample. All surface quench products showed different morphologies as distinctive features by ESEM. Rutile revealed its typical morphology with knee twins (figure 4.2.9) and parallel

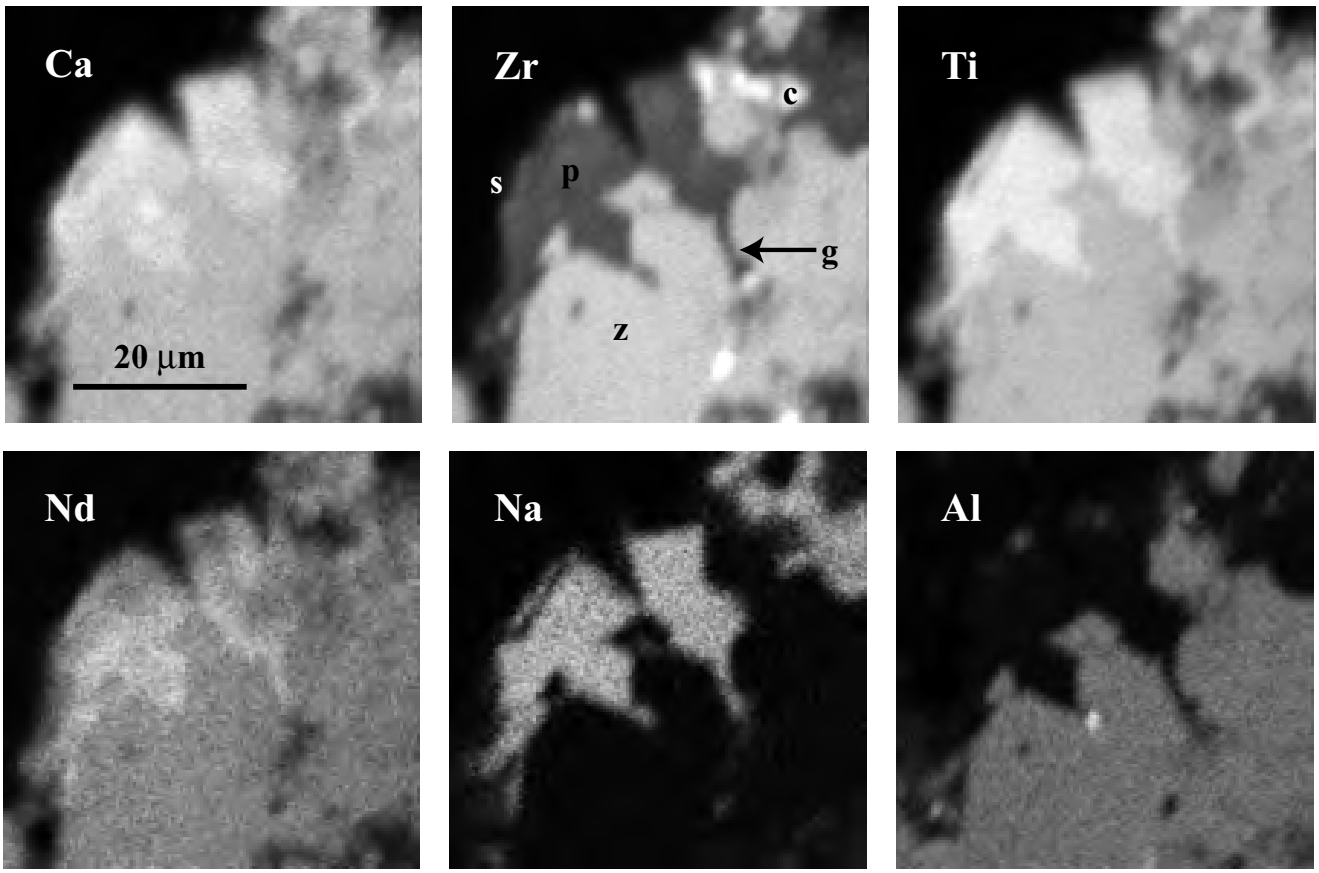

Figure 4.2.5: *EPMA X-ray elemental distribution maps from a cross section through zirconolite (figure 4.2.3 right) treated with 0.1 M NaOH for 21 days at 550 °C and 50 MPa reaching the third stage of corrosion. The zirconolite matrix (z) is replaced by two different phases perovskite (p) and calzirtite (c). Replacement starts from the surface (s) and the grain boundaries (g).*

intergrowth (figure 4.3.1) whereas the other TiO_2 polymorph anatase showed its typical tetragonal bipyramidal morphology (figure 4.3.1). The presence of the third natural TiO_2 polymorph, brookite, is not assumed due to its instability in fluids at a low pH (Vogler-Pazeller, 1990). Because of the small size and number of all phases, however, their exact composition and structure is undetermined and the fate of Nd, originally present in zirconolite, is unknown at the present time (Malmström et al., 1999). The incorporation into TiO_2 is very unlikely, but Cl^- complexing with REEs is expected (for further discussion see chapter 5).

4.3.3 Experiments with NaOH

Experiments in strong basic environments (0.1 M NaOH) at 400 °C and below revealed only a very weak corrosion of zirconolite starting material. No quench products could be determined and/or characterized. At 500 °C and higher, the corrosion strongly increases and two different product phases were observed to replace zirconolite. These two phases are easily discernible by size and shape (figure 4.2.3 right).

By ESEM, the larger secondary product phase (10 µm edge length) was morphologically recognized by crystallized cubes frequently showing twin features (figure 4.3.2 left). Sometimes these crystals also exhibited octahedral morphology. After short term experiments, a rough surface indicated incomplete crystallization. The EDX attached to the ESEM revealed a high Ti and Na content for this phase compared to zirconolite. Due to this morphology and chemistry, pseudocubic perovskite is presumed. A polished cross-section, analyzed by EPMA (figure 4.2.7), showed a composition, which is consistent with but not very common for perovskite. Analysis by XRD then clearly revealed

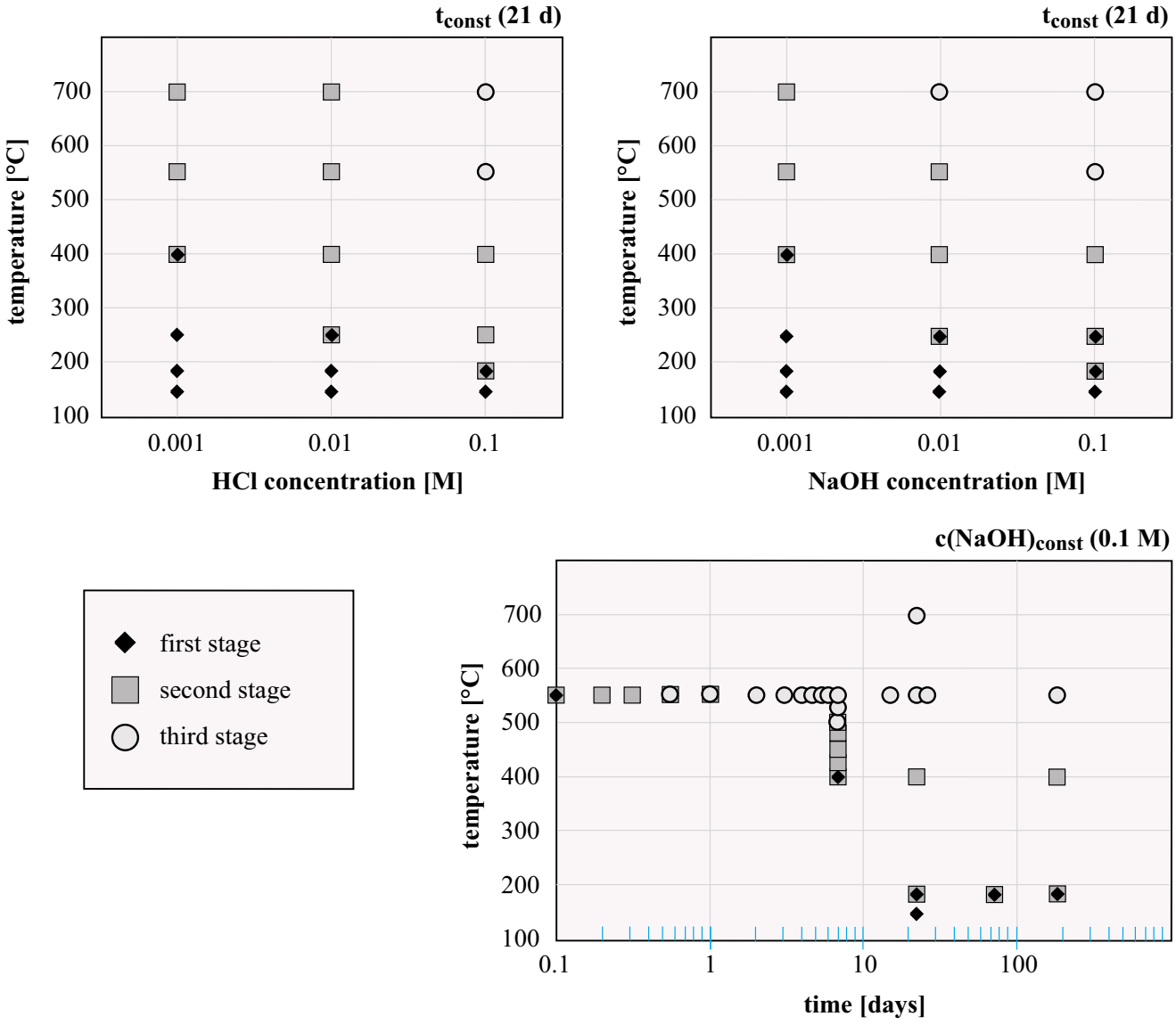

Figure 4.2.6: *Qualitative surface characterization of zirconolite in HCl (left) and NaOH (right) revealing a strong dependence on elemental concentration of the fluid, temperature and running time of the experiment.*

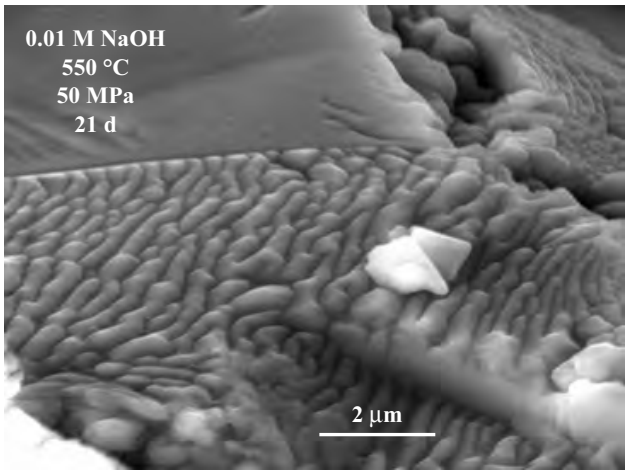

Figure 4.2.7: *Secondary electron images (by ESEM in low vacuum and wet mode) of zirconolite surface after an experiment revealing different surface corrosion of two grains due to different crystallographic orientation.*

perovskite. By TEM, this phase was subsequently analyzed in detail and identified as an orthorhombic perovskite. The very unusual crystal chemistry of this perovskite and other details are discussed in chapter 4.6.

The smaller secondary product phase analyzed by ESEM also displays cubic morphology, but with a much shorter edge (1–2 µm) often forming twins or even trillings, revealing the shape of a three dimensional cross (figure 4.3.2 right). ESEM/EDX analyses and X-ray maps from the EPMA showed a high Zr content compared to perovskite and zirconolite. Detailed analysis by TEM allowed the identification of this phase as tetragonal calzirtite (see chapter 4.7).

An experiment at the same temperature (550 °C) but with lower NaOH concentration (0.01 M) showed less corrosion features than those with higher concentration. While perovskite was observed as secondary phase, analysis by ESEM showed no calzirtite but another yet unidentified Zr rich

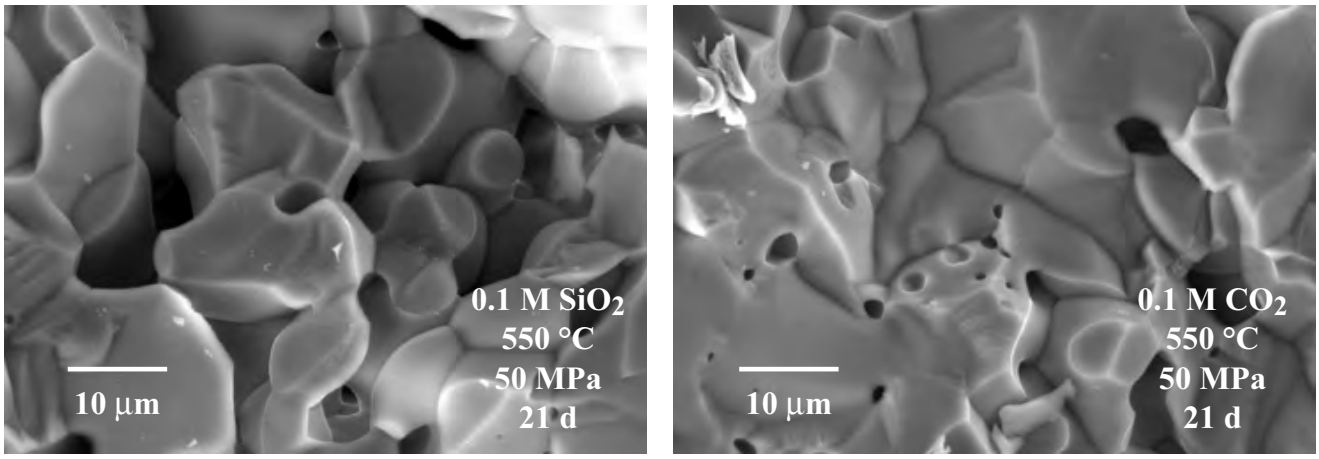

Figure 4.2.8: *Secondary electron images (by ESEM in low vacuum and wet mode) of zirconolite surface after experiments with SiO_2 and CO_2 revealing no surface corrosion at the resolution of ESEM.*

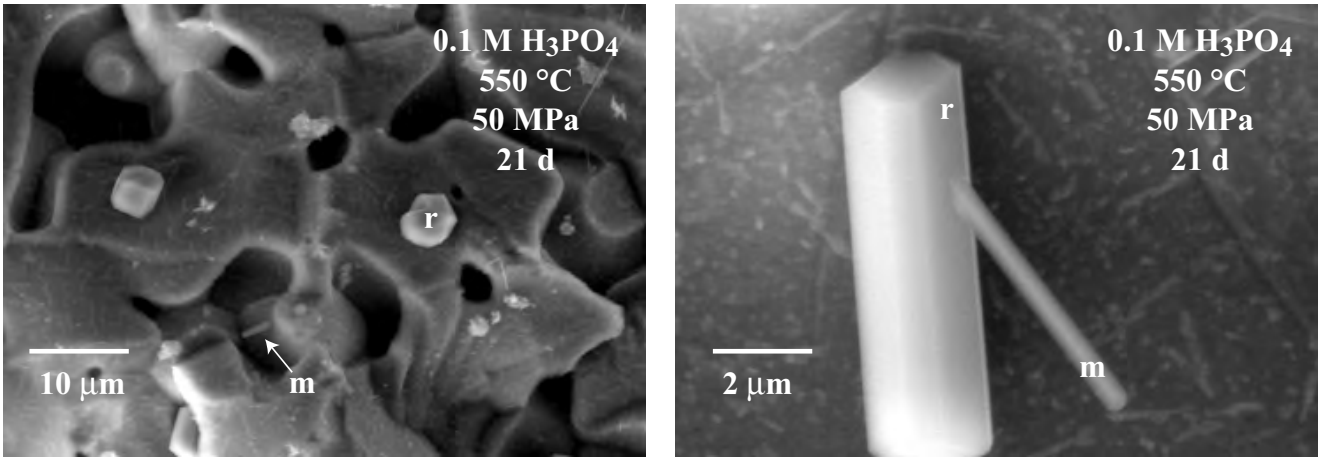

Figure 4.2.9: *Secondary electron images (by ESEM in low vacuum and wet mode) of zirconolite surface after experiments in H_3PO_4 showing rutile (larger secondary phases, r) and possibly monazite (smaller secondary phases, m).*

phase (ESEM/EDX) forming prismatic long columns with a square cross section (figure 4.3.3 left). XRD or Raman-spectroscopy did not provide further clues. The qualitative determination of this phase requires further experiments in order to obtain more material for TEM analysis. This experiment, however, revealed a strong dependence on the NaOH content in the fluid for the formation of secondary phases during hydrothermal zirconolite alteration.

Additional experiments at 550 °C in 0.1 M NaOH but at the higher pressure of 200 MPa were performed. They resulted in the formation of secondary perovskite, but calzirtite did not crystallize as an alteration product. As a second new phase, large (up to 50 µm) prismatic blades were observed by ESEM (figure 4.3.3 right). They all had a very high Zr content determined by ESEM/EDX. This morphology, their regular intergrowth, and the distinct idiomorphism are consistent with the ZrO_2 phase baddeleyite (Vlasov, 1966, see also chapter 4.5). Raman-spectroscopy subsequently confirmed these blades to be baddeleyite.

Generally, investigations by TEM on the structure and chemistry of zirconolite after the experiments showed no significant difference from the starting material. This indicates that selective leaching of Ca or other elements does not extend to any great depth into the zirconolite. If present, these effects must be localized near surface (see chapter 4.8). Any changes in structure and chemistry would reveal

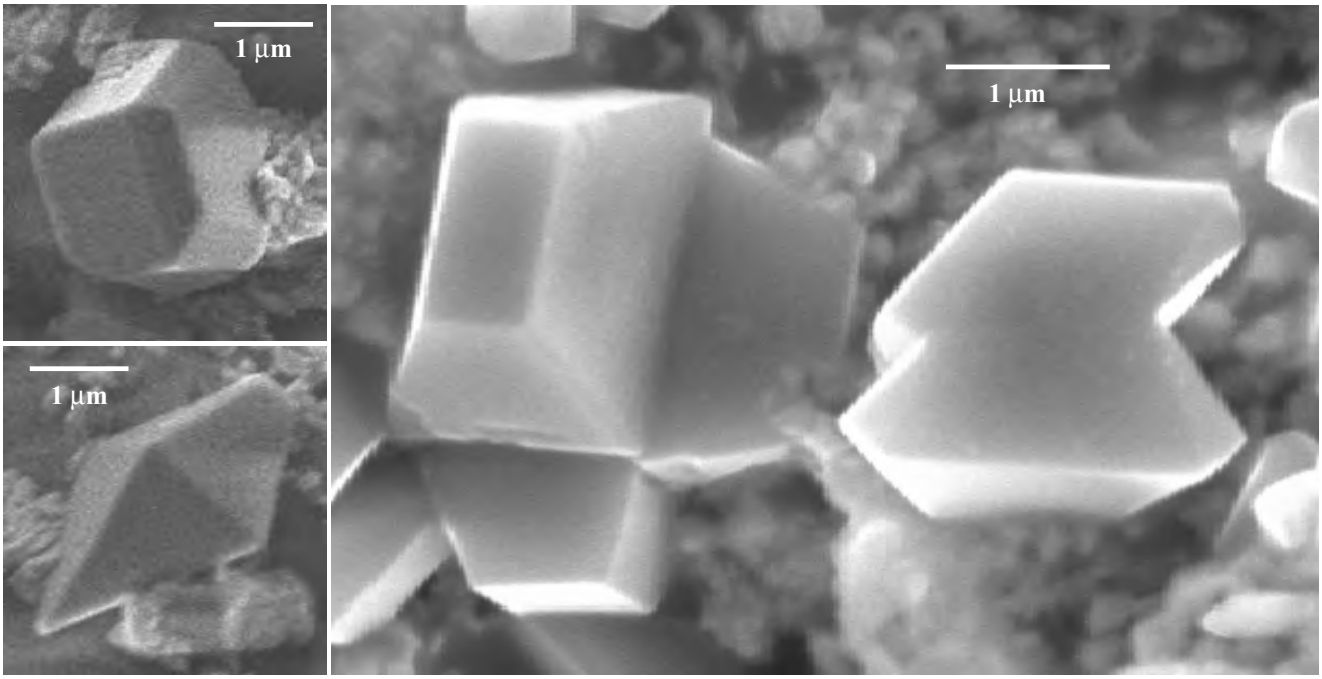

Figure 4.3.1: *Morphologic observations showing the typical features of the two TiO_2 polymorphs anatase and rutile. Anatase is typical tetragonal bipyramidal (upper left, lower left, center) and rutile shows the typical parallel intergrowth (right).*

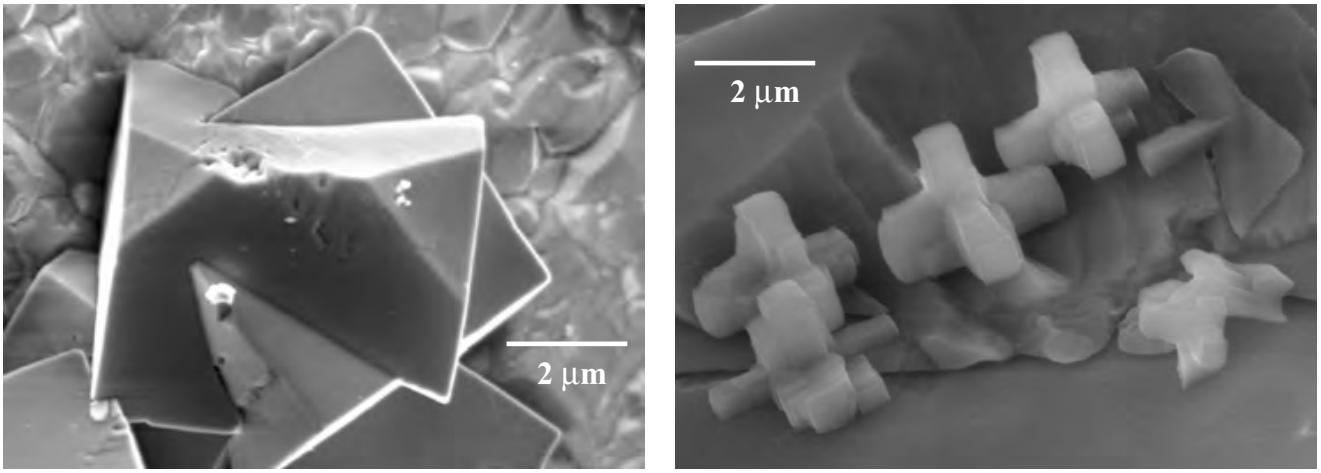

Figure 4.3.2: *Morphologic observations by ESEM showed twinning of perovskite (left) and mutually perpendicularly oriented trillings of calzirtite (right). Such trillings have been ovserved in nature by Zdorik et al. (1961).*

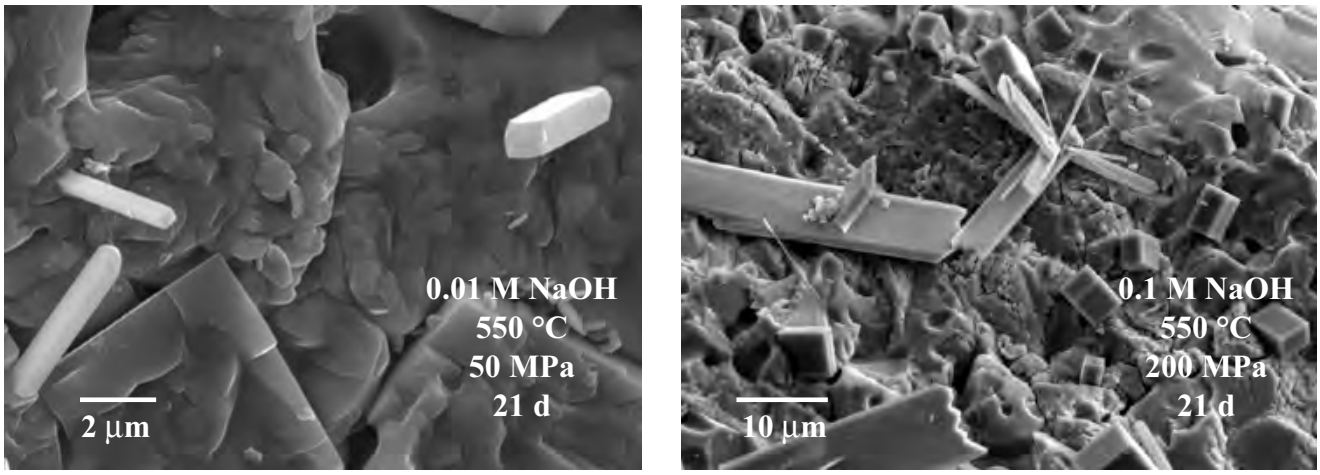

Figure 4.3.3: *Secondary electron images (by ESEM in low vacuum and wet mode) of zirconolite surface after experiments in 0.01 M NaOH revealing perovskite (larger squares) and an unidentified phase (smaller bars; picture left) and after an experiment in 0.1 M NaOH at a higher pressure (200 MPa) revealing the secondary phases perovskite (cubes) and baddeleyite (blades; picture right).*

crystallization of secondary zirconolite under hydrothermal conditions. All product phases are listed according to the experimental conditions in table 4.3.1.

4.3.4 Experiments with other Fluids

Introduction

To get more information on the behavior of zirconolite as a function of fluid composition, additional experiments were carried out with different fluid composition.

Deionized water

Previous studies have shown that zirconolite is highly resistant to leaching in deionized water at temperatures between 60 and 150 °C (Harker, 1988; Ringwood et al., 1988; Vance et al., 1996a; Vance et al., 1996b). After treatment at 150 °C, rutile and anatase have been described in previous studies as alteration product phases (Lumpkin et al., 1995; McGlinn et al., 1995; Smith et al., 1997).

At these low temperatures but at higher pressures (50 MPa), experiments conducted during this Ph.D. study confirm the high corrosion resistance of zirconolite in deionized water at ESEM resolution (µm). Only experiments above 400 °C in deionized water revealed corrosion features and some tiny quench phases appeared on the zirconolite surface. These had the shape of very fine needles (figure 4.3.4) and seemed to be Ti-rich phases as suggested by ESEM/EDX spectra, but they could not be identified because of their small number and size.

CO_2 and SiO_2

Experiments with CO_2 and SiO_2, respectively, in the fluid were carried out because most natural fluid systems include some CO_2 and/or SiO_2. During the examination by ESEM of the product of these experiments at 550 °C and 50 MPa, no alteration on the surface was observed (figure 4.2.8). This observation was very surprising, especially because zirconolite only crystallizes in SiO_2 poor systems (chapter 2.2). But because no other elements were present in the fluid necessary for the mobilization of elements during the experiment (further discussion chapter 5.4), and the pH decreased only slightly for CO_2 or stayed neutral for SiO_2, the fluid did not affect the stability of zirconolite.

H_3PO_4

Corrosion experiments in diluted phosphoric acid (0.1 M) resulted in the formation of two different quench products. One species crystallized as large (5–10 µm) tetragonal

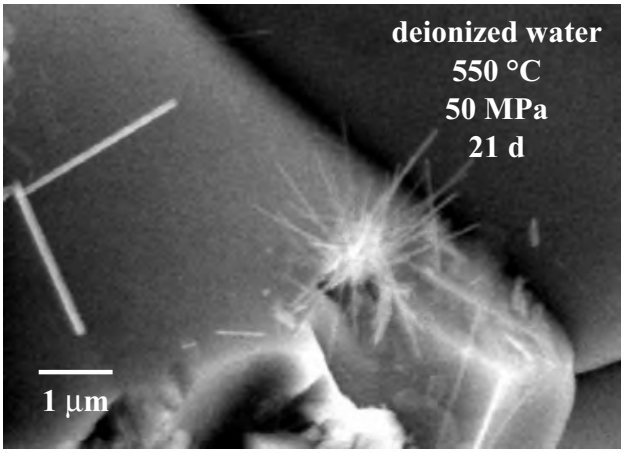

Figure 4.3.4: *Secondary electron images (by ESEM in low vacuum and wet mode) of zirconolite surface after experiments in deionized water revealing needles of undetermined composition.*

Table 4.3.1: *Product phases on zirconolite surface determined after experiments.*

Temperature (°C)	*Pressure (MPa)*	*Fluid*	*Concentration (M)*	*Product phases*
550	50	HCl	0.1	rutile & anatase
> 500	50	NaOH	0.1	perovskite & calzirtite
> 500	50	NaOH	0.01	perovskite & unknown (Zr-rich)
> 500	200	NaOH	0.1	perovskite & baddeleyite
550	50	H_2O		Ti-rich needles
550	50	CO_2	0.1	no
550	50	SiO_2	0.1	no
550	50	H_3PO_4	0.1	rutile & possibly monazite

columns, revealing a high Ti content by ESEM/EDX. Its morphology is typical for the TiO_2 phase rutile, which was also confirmed by Raman-spectroscopy.

The others were long, narrow blades forming clusters with a high phosphorus content (ESEM/EDX). Their chemical composition and characteristic morphology referred to Nd-monazite (figure 4.2.9). Other authors determined monazite after Synroc leaching experiments at 150 °C (Lumpkin et al., 1995; Lumpkin et al., 1991). Monazite is a highly durable phase, which is able to immobilize not only REEs but also trivalent and tetravalent actinides (Wood & Williams-Jones, 1994). Monazite is actually desirable as a secondary phase replacing zirconolite during the experiment (not as a quench phase) because of its durability and radiation resistance. Therefore, this result would support the development of monazite-based waste forms (Boatner & Sales, 1988).

4.3.5 Comment

As already described, many of the product phases present after the conducted hydrothermal experiments (table 4.3.1) could be determined by various analytical methods (appendix C). Some others would require newly designed experiments to obtain more and/or larger material for an unequivocal determination. Especially for XRD and TEM analysis a certain amount of material is required. Analysis by a Gandolfi camera would determine single crystals, but requires a certain size (> 50 µm). The problem of TEM cross-sections is that they are only successful for abundant secondary phases or thick alteration layers. The probability of getting a result is very poor when the abundance of secondary phases is low. Also, the surface is easily disturbed or damaged during the cutting/milling steps.

4.4 Fluid Data

4.4.1 Introduction

Mineral alteration is a process based on the interaction between solid mineral phase and fluid phase. The changes of the mineral phases were previously described. To understand the whole process of dissolution/precipitation it is important to obtain some information on the compositional changes in the fluid during the experiment. Unfortunately this goal was not easy to achieve. One major experimental problem was to extract the very small fluid volume (0.025 ml) from the capsule after the experiment (see chapter 3.4.7). Other analytical problems were the high dissolution factor resulting from the fluid extraction procedure. Finally, problems and non-availability of the ICP-MS laboratory made several series of fluids unusable. This is because the fluid was only usable immediately after terminating the experiment due to very fast complexing (and at a later stage precipitation) of several elements (e.g., Zr).

A combination of solid phase composition and fluid data is necessary to monitor the total mass balance during the experiments. Unfortunately not all elements in the fluid could be measured. Generally, the fluid mass balance could be calculated by the total charge balance, which is supposed to stay constant during the experiment in a closed system. But, due to hydrogen diffusion even through welded gold capsules (Girsperger, personal communication) at temperatures above 200 °C this calculation is not possible (disturbed mass balance due to diffusive loss of H_2).

4.4.2 Elemental Fluid Data

First, the elemental concentration in the capsule after the experiment was calculated from the measured elemental composition in the diluted leachate (by ICP-MS; appendix C.7). Then all obtained data were converted to mMol. Unfortunately the detection limit for Ca was too high for the concentration of interest.

Fluid determinations were carried out after experiments at 550 °C and 50 MPa after 7 days for the two fluids 0.1 M HCl and 0.1 M NaOH and both starting materials (Nd- and Gd-Ce–Hf-doped zirconolite). Unfortunately no data for the Gd–Ce–Hf-system were obtained at this temperature in NaOH (fluid got lost during capsule opening), therefore comparable data from 525 °C were used. In general, the results show a different behavior (solubility) of the involved elements in acidic and basic environment (figure

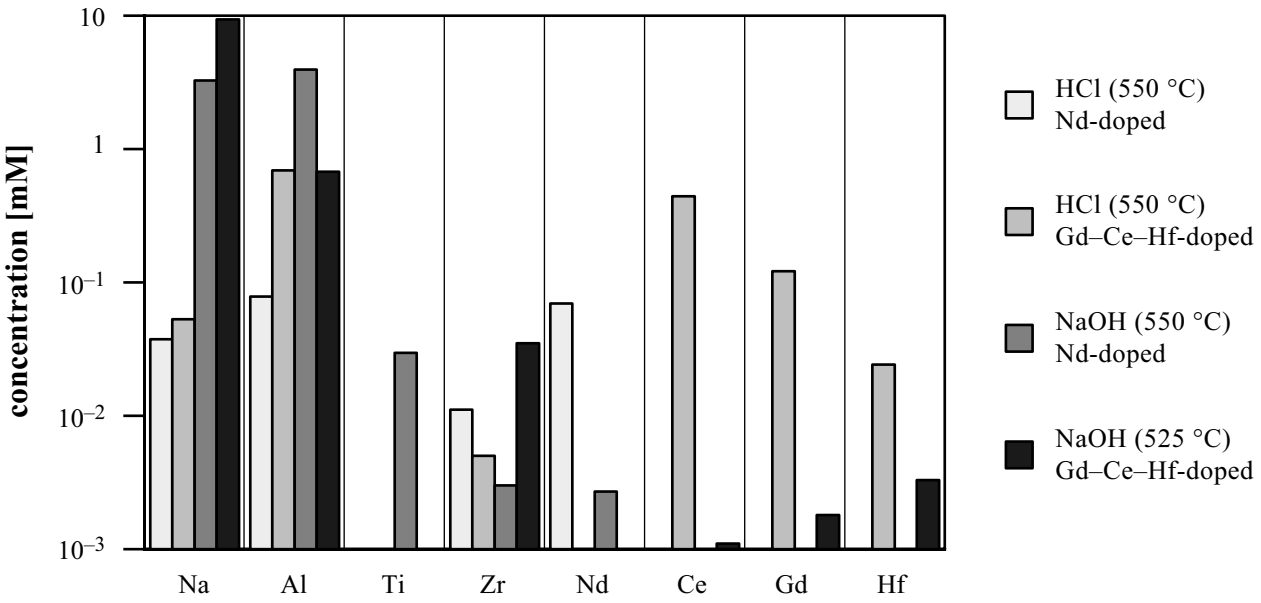

Figure 4.4.1: *Plot of elemental concentration in the leachate determined by ICP-MS after experiments in 0.1 M HCl respectively 0.1 M NaOH at 550 °C (or 525 °C, see text) and 50 MPa for 7 days with Nd-doped and Gd–Ce–Hf-doped zirconolite.*

4.4.1). For experiments conducted in NaOH, the higher Na concentration in the Gd–Ce–Hf-system after the experiment might be due to the fewer perovskite crystals formed (incorporating Na from the primary fluid) according to the lower experimental temperature (only 525 °C). This is supported by the higher Al concentration in the Nd system, which is released from zirconolite, but not incorporated into perovskite and calzirtite (for details see chapters 4.6 and 4.7) formed during these experiments. Therefore the total Al concentration after the NaOH experiments allows estimating the total zirconolite dissolution. No Na should be present after experiments with HCl (only contamination from processing). The Al concentrations after the experiments in HCl are inconclusive. This shows either that zirconolite is selectively dissolved or that Al is incorporated into an undetermined secondary phase.

The concentration of Ti in HCl is below the detection limit. This implied that all released Ti is incorporated into the described secondary TiO_2 polymorphs (chapter 4.3.2), whereas in NaOH some Ti remains in solution. The concentration of Zr stays relatively constant during all analyzed experiments. The concentrations of Ce, Nd, Gd and Hf (used as actinide analogues and/or neutron absorbers) are much higher in HCl than in NaOH. This implies that the secondary phases crystallizing during experiments in NaOH show a much higher ability to incorporate these elements into their crystal structure than those crystallizing in HCl. This is a very important observation, which implies that zirconolite-based waste forms should preferably be disposed in a basic, Na-rich environment (below a certain temperature).

Additional detailed fluid data will be discussed in relation to changing temperature and time in chapters 4.5.1 and 4.5.3.

4.4.3 Diamond Trapping

One series of experiments was made by a new experimental technique, designed to determine element partition coefficients using diamond aggregate extraction traps (Stalder et al., 1997). To each capsule, containing fluid and solid, a small gold container filled with diamond crystals (grain size 50 µm) was added before the experiment. As described in detail by Stalder et al. (1997), the pore space between the diamond grains traps the fluid during the experiment and preserves the elemental partitioning after quenching. The fluid compositions may easily be measured then by laser ablation ICP-MS from the polished cross sections of the diamond traps.

Unfortunately different results were observed during experiments containing diamond traps compared to the standard experiments. This was mainly indicated by different corrosion features and different secondary phases on the zirconolite surface (compare figure 4.4.2). These observations indicate that under the used experimental conditions additional processes occur and therefore no further experiments were made using diamond traps. Possible reasons could be that diamond is not completely inert at the experimental conditions and is therefore actively involved in the corrosion processes. C could change fluid by forming complexes as CO, CO_2, or CH_4. Another reason could be the variation of physical conditions (e.g., volume change) in the capsule by adding an internal capsule. Additionally, the total surface area of all materials in the closed system is much larger with diamond powder than without, leading to a massive reduction of the solid surface area to fluid volume ratio (SA/V) of zirconolite, which is an essential parameter to characterize leaching experiments. Its presence also could change the active fluid volume by trapping dissolved species.

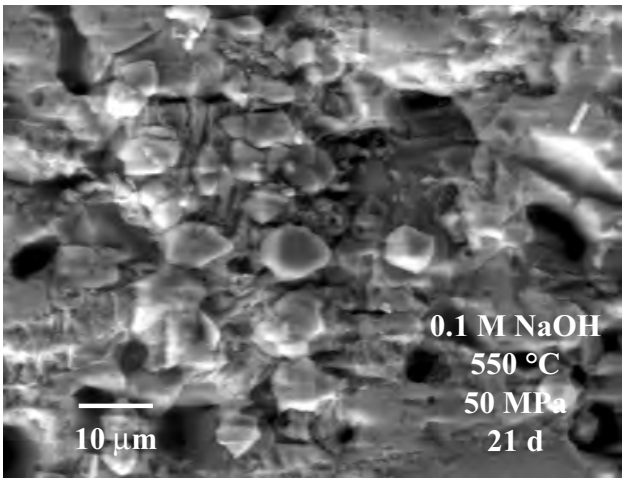

Figure 4.4.2: *Secondary electron images (by ESEM in low vacuum and wet mode) of zirconolite surface after experiments with diamond traps in the capsule. The corrosion features and secondary phases are completely different with respect to the same experiments without diamond traps (compare figure 4.2.3).*

4.5 Temperature, Pressure and Time Dependence of Experiments

4.5.1 Temperature

Experiments in HCl and NaOH were conducted from 150 °C to 700 °C. This range in temperature was chosen following experiments conducted earlier at ANSTO from 70 °C to 150 °C in various fluids (Lumpkin et al., 1995; McGlinn et al., 1995; Smith et al., 1997). Their results revealed that zirconolite is highly resistant to leaching, which is confirmed by our experiments, as no corrosion was observed at these low temperatures at ESEM resolution. Incremental temperature steps were first set to 150° over the whole range. They were then scaled down to 12° in the region of interest (400–550 °C) according to the obtained results (major changes observed). A strong dependence of the zirconolite corrosion rate on temperature in combination with fluids was already observed during the first series of experiments carried out over the whole temperature range (figure 4.2.6). Our data revealed that temperature is a limiting factor for the stability of zirconolite.

The results thus obtained reflect that the progressive alteration of zirconolite is not linear with increasing temperature. Short term experiments (7 days) with constant pressure (50 MPa) and fluid composition (0.1 M NaOH) between 450 and 550 °C revealed that zirconolite is barely affected up to 488 °C. Increasing the temperature to 500 °C strongly affected the surface and, at 512 °C, no pristine zirconolite surface may be observed anymore. Further increasing of the temperature up to 700 °C did not result in major changes. The stability of the observed secondary phases showed inverse temperature dependence. Whereas perovskite and calzirtite crystals are barely present at 488 °C, they are regularly present at 500 °C and cover the entire surface at 512 °C (figure 4.5.1). Interestingly, the two phases perovskite and calzirtite start crystallizing at the same temperature and are both still present at 700 °C.

Elemental fluid data from experiments over the temperature range of 475 to 525/550 °C in NaOH did not reveal fully consistent results for the Nd and Gd–Ce–Hf-doped system. In the Nd system, the elemental concentration of Nd and Zr in the fluid decreases parallel to the crystalliza-

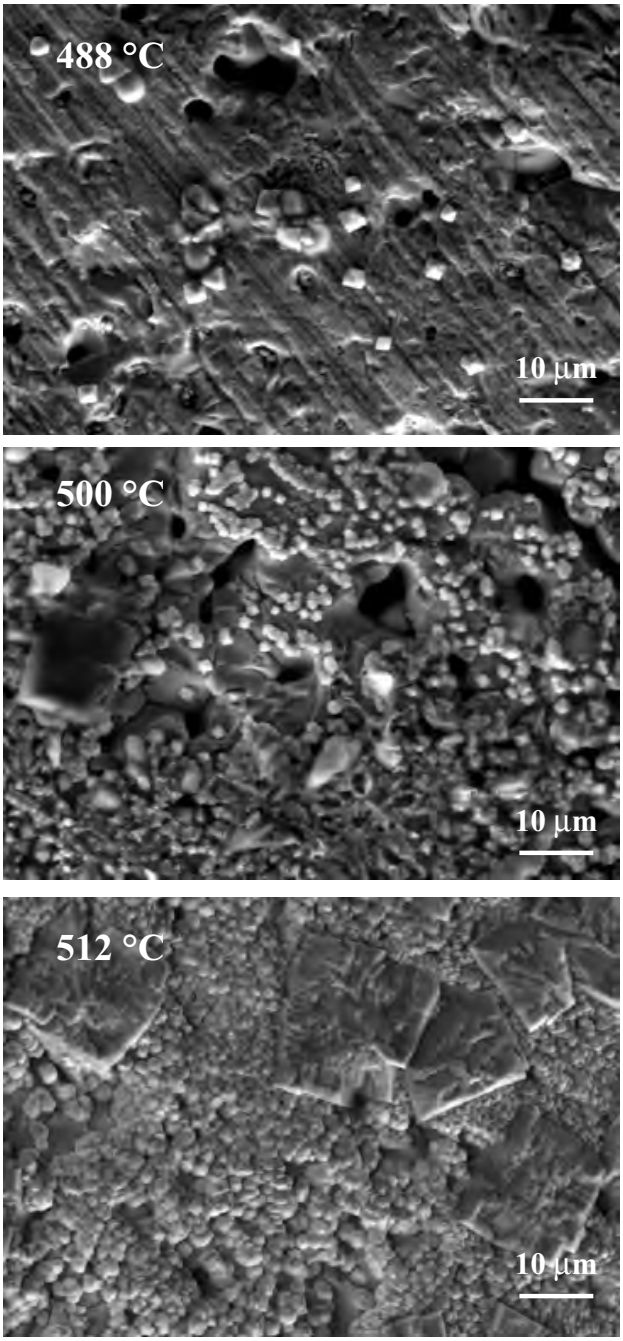

Figure 4.5.1: *Series of secondary electron images (by ESEM in low vacuum and wet mode) of Nd-doped zirconolite surface after experiments in 0.1 M NaOH at 50 MPa showing the temperature dependent breakdown of zirconolite to perovskite and calzirtite.*

tion of perovskite and calzirtite. Simultaneously the elemental concentration of Ti decreases slowly and, together with the elemental concentration of Na, decreases distinctively only at higher temperature, probably due to an increasing crystallization rate of the product phases. This is combined with the increasing elemental concentration of Al. In the Gd–Ce–Hf-system, only the elemental concentration of Gd and Hf decreases above 500 °C, whereas the other elemental concentrations level off over the analyzed temperature range or even increase (Zr). Unfortunately no data for 550 °C could be obtained that possibly would have shown an elemental concentration decrease similar to the Nd system (figure 4.5.2). But all fluid data reveal a general decrease of the waste simulating elements Nd, Gd and Hf except Ce, parallel to the crystallization of the product phases perovskite and calzirtite.

These results do not only document zirconolite corrosion, but also demonstrate the stability limits of the involved phases, which will be discussed in detail in chapter 5.3.

4.5.2 Pressure

Most experiments were conducted at the pressure of 50 MPa. To investigate the influence of increasing pressure on the stability of zirconolite, experiments were made at 100 and 200 MPa. The obtained results indicated only a weak, if any, relationship between corrosion and pressure, but a major influence of pressure on the crystallization of the product phases. The experiments at 550 °C in 0.1 M NaOH at 50, 100 and 200 MPa always resulted in the formation of perovskite, but calzirtite was only observed at 50 and 100 MPa (figure 4.2.3 right), whereas at 200 MPa baddeleyite was present (figure 4.3.3 right). Even though pressure has no significant influence on the corrosion of zirconolite, it determines together with temperature and fluid composition which product phases are formed. Calzirtite and baddeleyite, both revealing similar crystal structures (Zdorik et al., 1961), indicate crystallization in two different stability fields. Therefore, according to their chemical composition, a pressure dependent mass balance from calzirtite to baddeleyite and perovskite may be proposed:

calzirtite <=> 2 perovskite + 5 baddeleyite

Further discussions on the stability field of zirconolite and the secondary phases will be made in chapter 5.3.

4.5.3 Time

In general, long-term (up to 10^6 years) safety predictions for radioactive waste disposal are very difficult to make. The main problem is the high uncertainty in highly extrapolated data from experiments over various time steps. Such data are mostly generated using arbitrary curve fitting and do not follow physical or chemical laws, which would lead to more accurate and meaningful extrapolation results.

Increasing the experimental run time from 21 to 63 and 189 days at 200, 400 and 550 °C resulted in unique zirconolite alteration and gave no evidence for any dependence of zirconolite corrosion on time (figure 4.2.9). Therefore the experimental run time was decreased from 21 days to 14, 7, 6, 5, 4, 3, 2 and 1 day, and in a second series from 24 hours

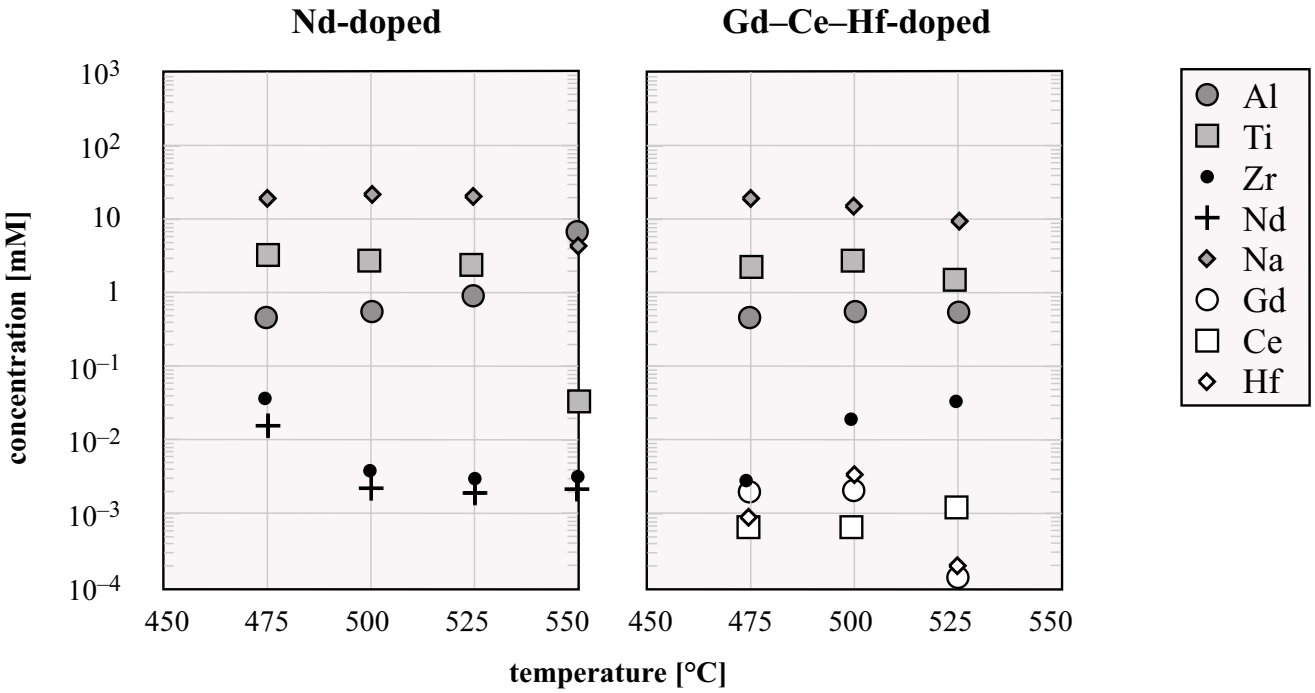

Figure 4.5.2: *Plot of elemental concentration in the leachate determined by ICP-MS versus temperature after experiments in 0.1 M NaOH at 50 MPa for 7 days with Nd-doped (left) respectively Gd–Ce–Hf-doped zirconolite (right).*

to 12, 6, 4, 3, 2, and 1 hour. Those experiments were conducted in 0.1 M NaOH at 550 °C and 50 MPa revealing strong alteration after 21 days.

The results thus obtained and analyzed by ESEM showed that the reaction at these conditions started after one hour with the corrosion of the zirconolite surface and with the formation of the product phase perovskite. The presence of calzirtite as the second product phase is observed several hours later. After 2 to 4 days, the zirconolite surface is completely covered by perovskite and calzirtite. After the initial period of perovskite growth, its grain size was observed to increase with increasing time (figure 4.5.3). This growth process dependent on time indicated that perovskite is a secondary phase growing during the experiment and is not a quench phase. Similar observations were made with the Gd–Ce–Hf-doped zirconolite.

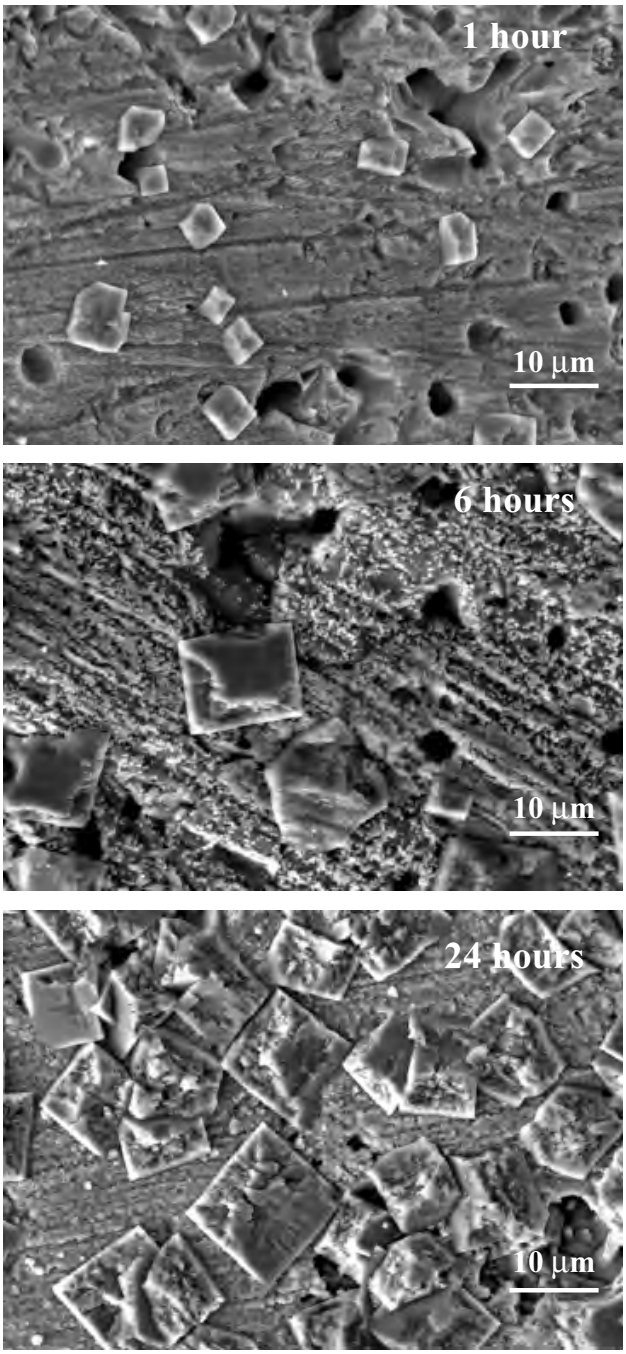

Figure 4.5.3: *Series of secondary electron images (by ESEM in low vacuum and wet mode) of Nd-doped zirconolite surface after experiments in 0.1 M NaOH at 550 °C and 50 MPa indicating time dependent reaction progress. They clearly show that perovskite (cubes) crystallizes earlier than calzirtite (grains on substrate).*

These details, together with the analyzed leachate data (figure 4.5.4) revealed that the corrosion process begins with dissolution of zirconolite indicated by a concomitant general concentration increase of the elements Zr, Ti, REE, Al in the fluid phase. Perovskite incorporates Na but no Al. The fast formation of perovskite between 6 and 24 hours is simultaneously reflected by the decrease of Na and the increase of Al in the fluid. The slightly later crystallization of calzirtite is reflected by the decreasing Zr concentration in the fluid after 12 hours and up to 3 days. The Al concentration increases to a high level in the fluid because it is not incorporated by the secondary phases. After this period, elemental release rates appear to decrease with time.

4.5.4 Conclusions

No results obtained so far show a linear or exponential progression. Rather, alteration of zirconolite was observed to advance in steps, which are related to the presence of secondary phases. One major step is very obvious for instance by the experiment at 512 °C after 12 hours showing a fully corroded surface, compared to the experiment at 500 °C after 7 days revealing only weak corrosion. This indicates that at a certain temperature not only dissolution, but also mineral reactions take place.

4.6 Secondary Perovskite

4.6.1 Introduction

After hydrothermal experiments above 500 °C in a NaOH rich environment, the main alteration product observed on zirconolite was perovskite. It covered up to 70% of the former zirconolite surface. Perovskite is, like zirconolite, a major constituent in Synroc nuclear waste forms. EPMA X-ray maps (figure 4.2.5) revealed that this secondary perovskite incorporates significant amounts of the REEs used as actinide analogue and/or neutron absorbers. Therefore detailed investigations were made on the crystal chemistry of perovskite (possibly acting as secondary waste form after the replacement of zirconolite).

4.6.2 Crystal Structure and Composition

As already described, the 5–20 µm large perovskite crystals show frequently twinned, octahedral to cubic morphologies (chapter 2.3). After investigations by TEM of crushed grain samples, selected area diffraction patterns (SAD)

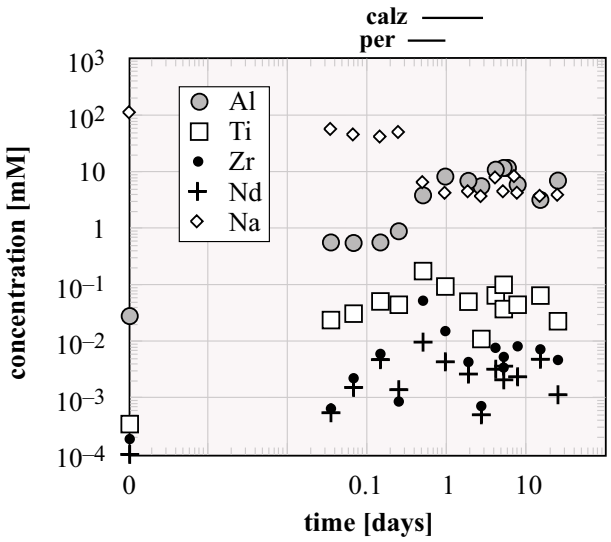

Figure 4.5.4: *Plot of elemental concentration in the leachate determined by ICP-MS versus experimental run time after experiments in 0.1 M NaOH at 550 °C and 50 MPa. The bars at the top indicate the main growth time of perovskite and calzirtite as reflected in the fluid.*

demonstrated a simple orthorhombic perovskite with no general high-order superstructure (figure 4.6.1). Only one of all analyzed perovskites showed some stacking faults, or an undefined superstructure, in one direction (figure 4.6.1, SAD [101], only visible on negative). These weak spots need to be studied in further detail.

The observed perovskite has an unusual chemical composition with an exceptionally high Zr content as determined by thin-film AEM analyses (table 4.6.1, for individual analyses see appendix C.6):

$Ca_{0.40}Na_{0.33}Nd_{0.13}Zr_{0.15}Ti_{0.96}O_3$
(Nd-system)

$Ca_{0.31}Na_{0.43}Gd_{0.04}Ce_{0.05}Zr_{0.16}Hf_{0.01}Ti_{0.98}O_3$
(Gd–Ce–Hf-system).

4.6.3 Discussion

Crystal chemistry

Three different working hypotheses were considered to explain the crystal chemistry of these unusual perovskites. In the first approach, all Zr was allocated to the Ti site which results in a large number of Ca-site vacancies (~30%) and oxygen vacancies. The crystal structure of perovskite may have large Ca-site or up to 15% O-site vacancies, but needs a full Ti-site occupation to avoid collapse of the structure (detailed description in Wyss, 1995). No general high-order superstructures, which are expected for many Ca-site vacancies, are observed by TEM (figure 4.6.1). In addition, Mitchell & Chakhmouradian (1998a) showed that such high-order superstructures in $Na_{1/2+x}La_{1/2-3x}Th_{2x}TiO_3$ perovskite only revealed ordering at the A-site with $x > 0.083$, accompanied by the change of structure from orthorhombic to tetragonal, which was not observed after our experi-

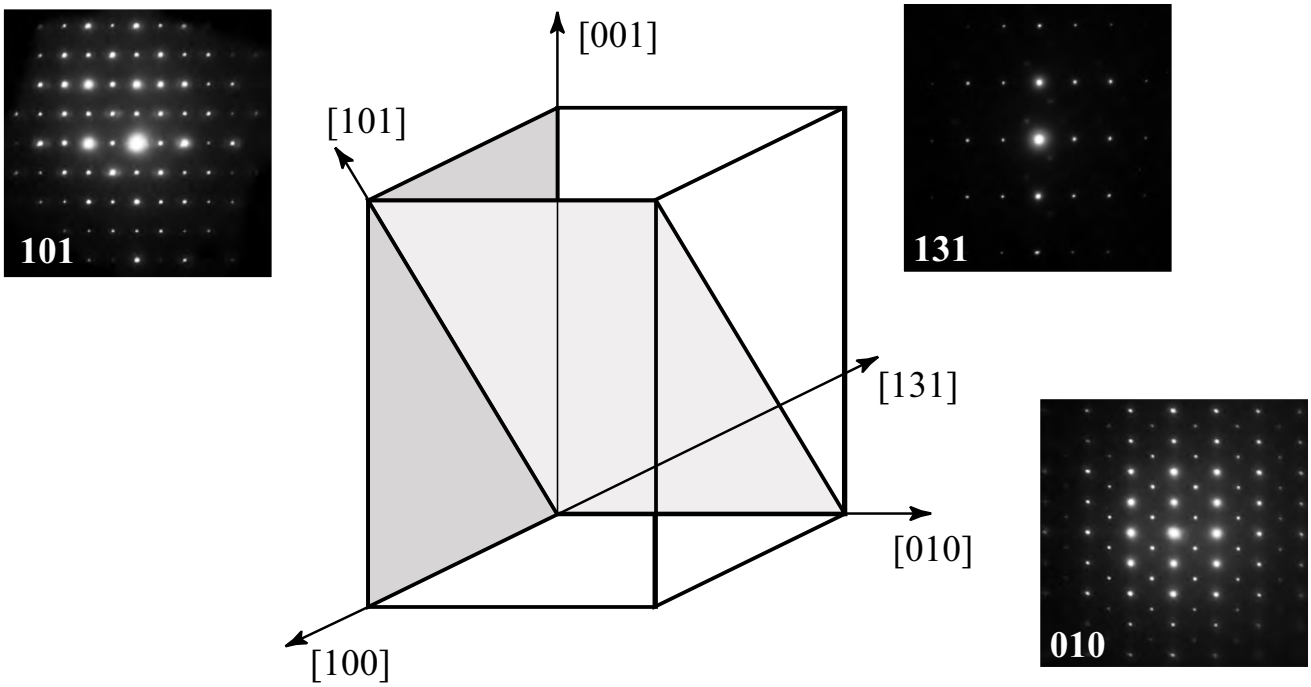

Figure 4.6.1: *Selected area diffraction patterns (SADs) and a sketch of the crystallographic unit cell of perovskite. The SADs show a simple orthorhombic perovskite with no strong high-order superstructure, which would indicate a cation-vacancy ordering.*

ments. In a hydrothermal system, perovskite could be hydrated and thereby charge balanced by OH^- on the oxygen site, a possibility that had to be investigated. Therefore, an attempt was made to collect IR-spectra of the secondary perovskite. But, because perovskite could not be fully separated from zirconolite, small zirconolite particles with a fully alterated surface were used (20–40 µm deep). Calculations based on cross-sections gave approximately 10 vol% perovskite. However, IR-spectroscopy analysis on these samples showed no OH^- (appendix C.8). In the second approach, all Zr was assigned to the Ca site, and as third hypothesis, Zr was distributed between both sites. Elemental site occupancies in minerals may be determined by axial electron-channeling analysis (Lumpkin, 1992; Rossouw et al., 1988a; Rossouw et al., 1988b; Rossouw et al., 1989). A [110] zone axis electron-channeling analysis was performed in order to test these hypotheses. Because this experiment was not made with a cold-stage and the studied crystal is a twin (discussed later in this section), the obtained data are only qualitative. However, the results (appendix D) indicate that Na, REEs, and most of the Zr occupy the 8-fold coordinated Ca site. Based on these results the following single-site substitutions were proposed:

$$REE^{3+} + Na^{+} <=> 2\,Ca^{2+} \quad (1)$$
$$Zr^{4+} + 2\,Na^{+} <=> 3\,Ca^{2+} \quad (2).$$

Unfortunately the calculated elemental correlations of all analyzed perovskite crystals are irregular and not fully conclusive (figure 4.6.2-a). For example, no strong correlations exist between REEs and Na or between Zr and Na (R^2 for Nd and Gd–Ce-doped samples below 0.24). Additionally no correlations exist between Ca and Zr or Zr and

Table 4.6.1: *Analytical electron microscopy (AEM) analysis of secondary perovskite resulting from the two different starting materials (standard deviation (s.)).*

wt%	**perovskite-(Nd) (n=14)**				**perovskite-(Ce) (n=19)**			
	mean	*s.*	*min*	*max*	*mean*	*s.*	*min*	*max*
Na_2O	6.75	1.00	4.71	8.81	8.99	1.52	6.49	11.46
Al_2O_3	0.01	0.05	0.00	0.19	0.02	0.10	0.00	0.42
CaO	15.08	1.38	13.49	18.25	11.70	2.18	8.37	14.32
TiO_2	51.44	2.15	46.51	54.34	52.67	1.60	49.37	56.97
FeO	0.52	0.23	0.13	1.04	0.23	0.18	0.00	0.61
ZrO_2	12.04	2.42	8.25	16.67	13.63	2.52	8.93	17.78
Ce_2O_3					5.79	1.67	3.22	9.28
Nd_2O_3	13.91	3.65	5.84	20.81				
Gd_2O_3					5.13	1.18	3.58	7.11
HfO_2	0.26	0.18	0.01	0.59	1.88	0.52	1.07	2.95
sum	100.02				100.04			
Formula based on 3 oxygens								
Na	0.33	0.05	0.23	0.43	0.43	0.07	0.31	0.56
Al	0.00	0.00	0.00	0.01	0.00	0.00	0.00	0.01
Ca	0.40	0.04	0.36	0.48	0.31	0.06	0.22	0.38
Ti	0.97	0.03	0.90	1.02	0.98	0.02	0.93	1.04
Fe	0.01	0.00	0.00	0.02	0.00	0.00	0.00	0.01
Zr	0.15	0.03	0.10	0.20	0.16	0.03	0.11	0.21
Ce					0.05	0.02	0.03	0.09
Nd	0.12	0.03	0.05	0.19				
Gd					0.04	0.01	0.03	0.06
Hf	0.00	0.00	0.00	0.00	0.01	0.00	0.01	0.02
sum	1.98				2.01			
∑ REE [1)]	0.12	0.03	0.05	0.19	0.10	0.02	0.06	0.13
∑ Zr, Hf [1)]	0.15	0.03	0.10	0.20	0.17	0.03	0.12	0.23

[1)] This sum is relative to one measurement and not the sum of the min/max of different measurements.

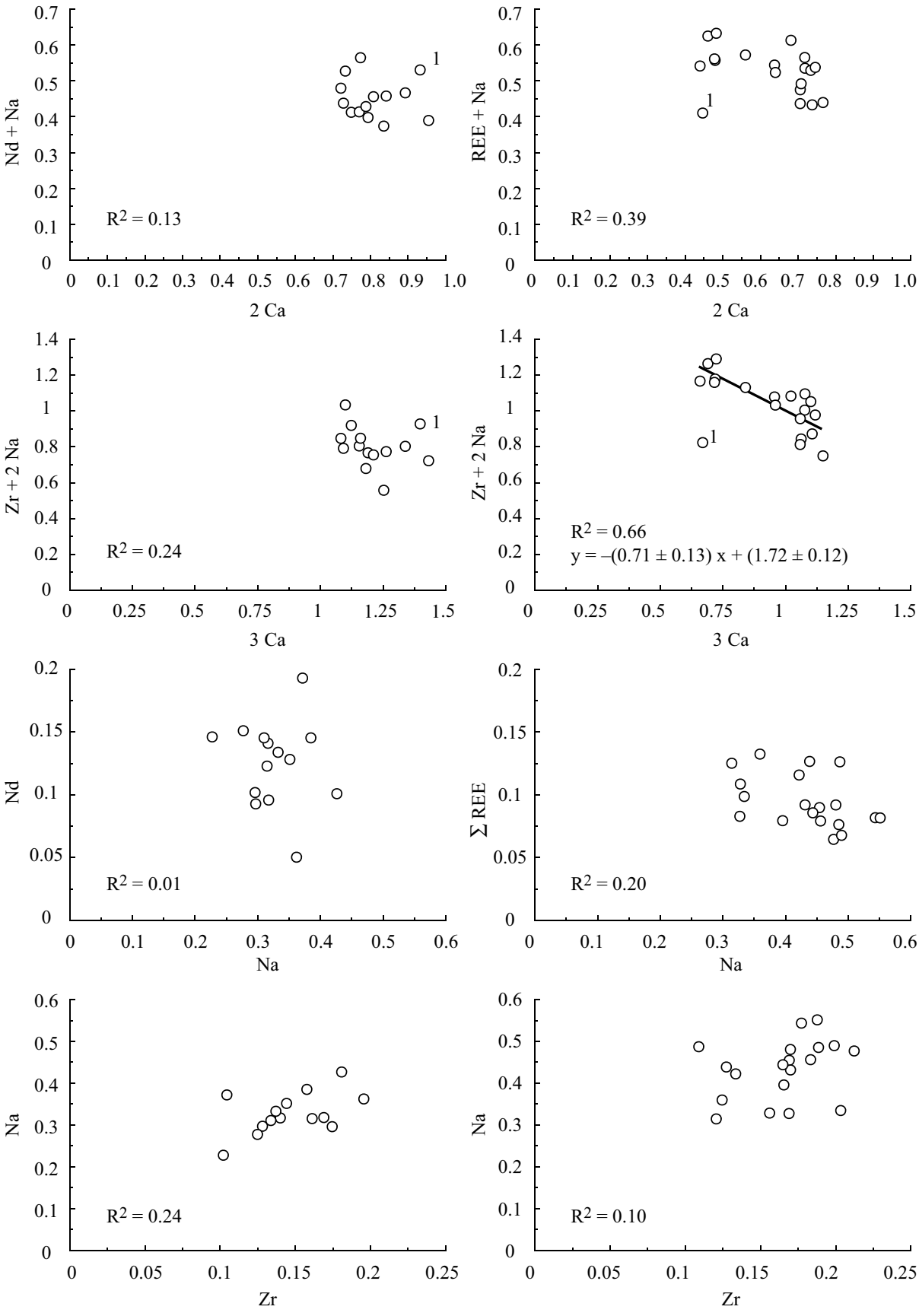

Figure 4.6.2-a: *Elemental correlation in secondary perovskite crystals of the Nd-doped system (left) and the Gd–Ce–Hf-doped system (right). Data measured by AEM (appendix C6). Data point Nr.1 is an outlier (> 4 s) and not taken for linear regression calculation. All plotted data have count statistics with 2s < 0.5% revealing that the size of the individual data points are larger than the error bars would be.*

Ti ($R^2 < 0.35$; figure 4.6.2-b), which would support the result from the zone axis electron-channeling experiment.

But a good negative correlation exists between REE and Zr ($R^2 = 0.62$ (Nd doped) and $R^2 = 0.80$ (Gd–Ce-doped)) indicating that these elements occupy the same lattice site (Ca site). Therefore a combination of the substitutions (1) and (2) resulting in substitution (3) shows much better elemental correlation ($R^2 > 0.5$; figure 4.6.2-c) and best explains the overall variability on the Ca site, with all excess Zr on the Ti site:

$$Ca^{2+} + REE^{3+} <=> Zr^{4+} + Na^{+} \qquad (3).$$

In the Nd doped system, the slope of the regression Nd versus Zr is close to minus one, and in the Gd–Ce-doped system, the slope is close to minus two thirds, revealing that 2 REE ions are substituted by 3 Zr ions (figure 4.6.2-c). These two different gradients reveal on one side a total compatibility between Nd and Zr, and on the other side a decreased compatibility between REE (Gd and Ce) and Zr which may be due to the possible tetravalent oxidation state of Ce (discussed later in this section). Only these elements reveal good elemental correlations compared to all other analyzed elements and therefore probably are not included into any other substitution. But Na incorporation for perovskites with higher Zr or REE content is necessary for charge compensation (substitution (1) and (2)) and is indicated in figure 4.6.2-a. Interestingly, multi-site substitutions (involving two or more lattice sites in a crystal structure) were not observed, even though they are important in natural perovskites.

The compositional variation of perovskite was observed to be quite large (e.g., the Na and Zr contents varied by a factor of two; table 4.6.1). This variation was observed to be constant over all experiments, which means that each experiment formed grains of different composition, but comparable perovskites were formed during different experiments. This variability may be due to an inhomogeneous fluid distribution in the cell, to a change of the fluid composition with time, to boundary layer effects or simply that no equilibrium was obtained. This is supported from the observation that the perovskite has a different appearance (shape) after different experimental run times. Possibly also quench phases of various composition are present after the experiment beside the hydrothermal secondary perovskite.

Even though EDX line scans by TEM revealed high internal homogeneity in the individual perovskite crystals (figure 4.6.3), the total Na concentration decreases from one side to the other (perovskite2) from 8 to 5 oxide wt% parallel to a slightly increasing Ca concentration from 14 to 15 wt%. A second observation is that deviations in the total Ti content are inversely correlated to the Zr content. This could be due to the earlier described excess Zr on the Ti site. A third observation is that Zr and Ce exhibit a weak negative correlation. This is illustrated on TEM Zr and Ce X-ray maps from the same crystal (figure 4.6.4). They reveal that this idiomorphic perovskite exhibits sector zoning indicated by the negative correlation of Ce and Zr (figure 4.6.5). The compositions of all analyzed perovskite crystals reveal a general good correlation of Ce and Zr ($R^2 = 0.68$).

As described above, the sum of Gd and Ce behaves different from Nd. Interestingly no correlation exists between the REE Gd and Ce ($R^2 = 0.12$, figure 4.6.5). If both were present as trivalent cations, they would show a positive correlation due to similar properties of trivalent REE. The observed variation of Ce, which is more similar to Zr than to Gd leads to the hypothesis that part or all of the Ce is tetravalent. This assumption is supported by the fact, that Ca is well correlated with Gd ($R^2 = 0.83$) but not with Ce ($R^2 = 0.11$, figure 4.6.5). Ca and trivalent REE should be positively correlated according to substitution (3), which is demonstrated for Ca and Gd. Another disparity is the overall variability of Ce in perovskite, which is much higher than the overall variability of Gd (0.03–0.09 versus 0.03–0.06). This is consistent with two different processes, one is described by substitution (3) and the second is revealed by sector zoning and the negative correlation of Ce and Zr.

For charge balancing, monovalent Na on the bivalent Ca site controls the total possible accommodation of tri- and tetravalent REE and tetravalent Zr on the Ca site. Table 4.6.1 shows that there is enough Na for charge balance and only minor amounts of excess Zr would be present on the tetravalent Ti site. The Na content in the perovskite of the Gd–Ce-doped system is always higher than in the Nd system. This even supports the presence of tetravalent Ce in perovskite.

Crystal growth

The crystallographic orientation of the idiomorphic perovskite revealing sector zoning was determined by electron diffraction analysis ([–110]; figure 4.6.6). This idiomorphic grain analyzed and oriented by TEM was used as a basis for indexing the crystal faces of other analyzed orthorhombic perovskites by ESEM. Similar pseudo-cubic grains with truncated corners were frequently observed by ESEM after many experiments (figure 4.6.7 A–D).

In general, the anisotropic, orthorhombic perovskite crystals nucleate from a combination of pseudo-cubic faces and pseudo-octahedral faces. Growth in a hydrothermal environment provides ideal conditions for supplying the nucleus with the desired elements from the fluid. The growth velocity is larger for octahedral than for cubic faces (Strobel, 1971). Therefore the octahedral sides grow further than the cubic sides leading to smaller octahedral surface-areas and larger cubic surface-areas (sketch in figure 4.6.7). During the experiments similar features were observed. Figure 4.6.7 pictures A to D show several sequences of the crystallization process with increasing time, forming pseudo-cubic crystal morphologies from initially octahedral crys-

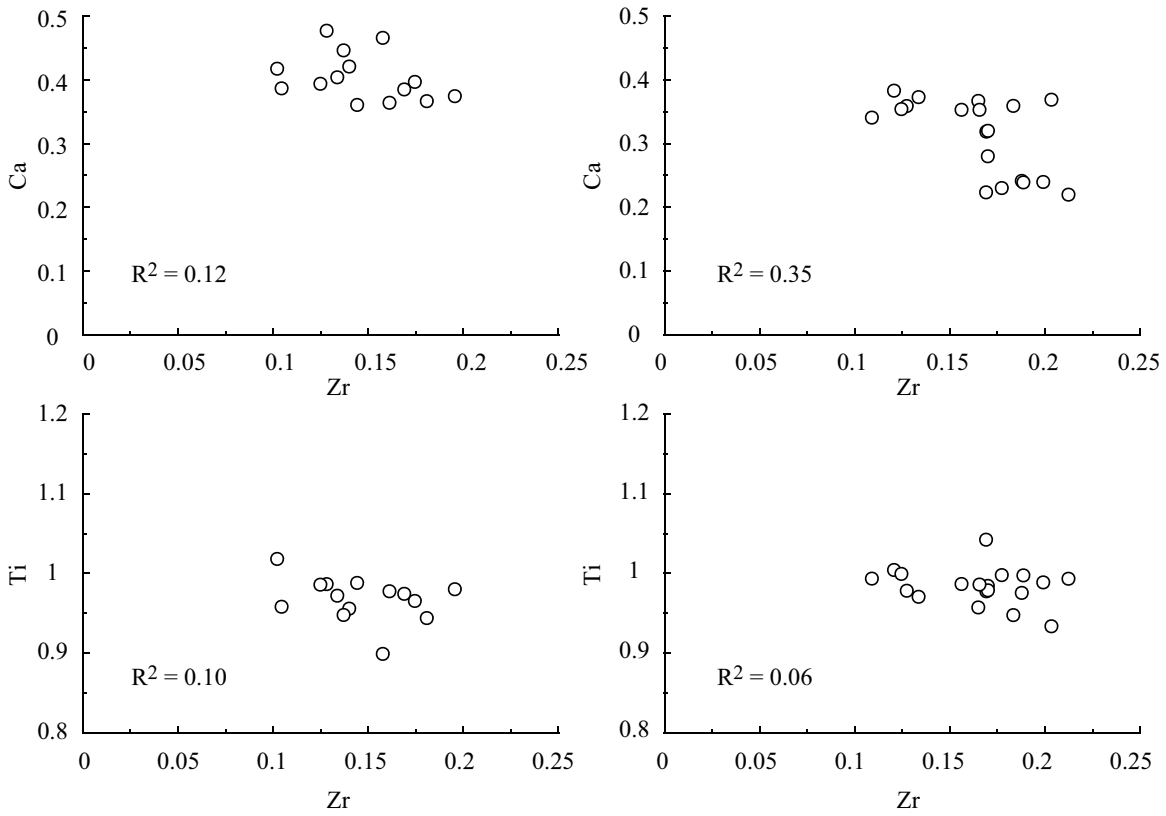

Figure 4.6.2-b: *Elemental correlation in secondary perovskite crystals of the Nd-doped system (left) and the Gd–Ce–Hf-doped system (right). Data measured by AEM (appendix C6). Error: 2s < 0.5%.*

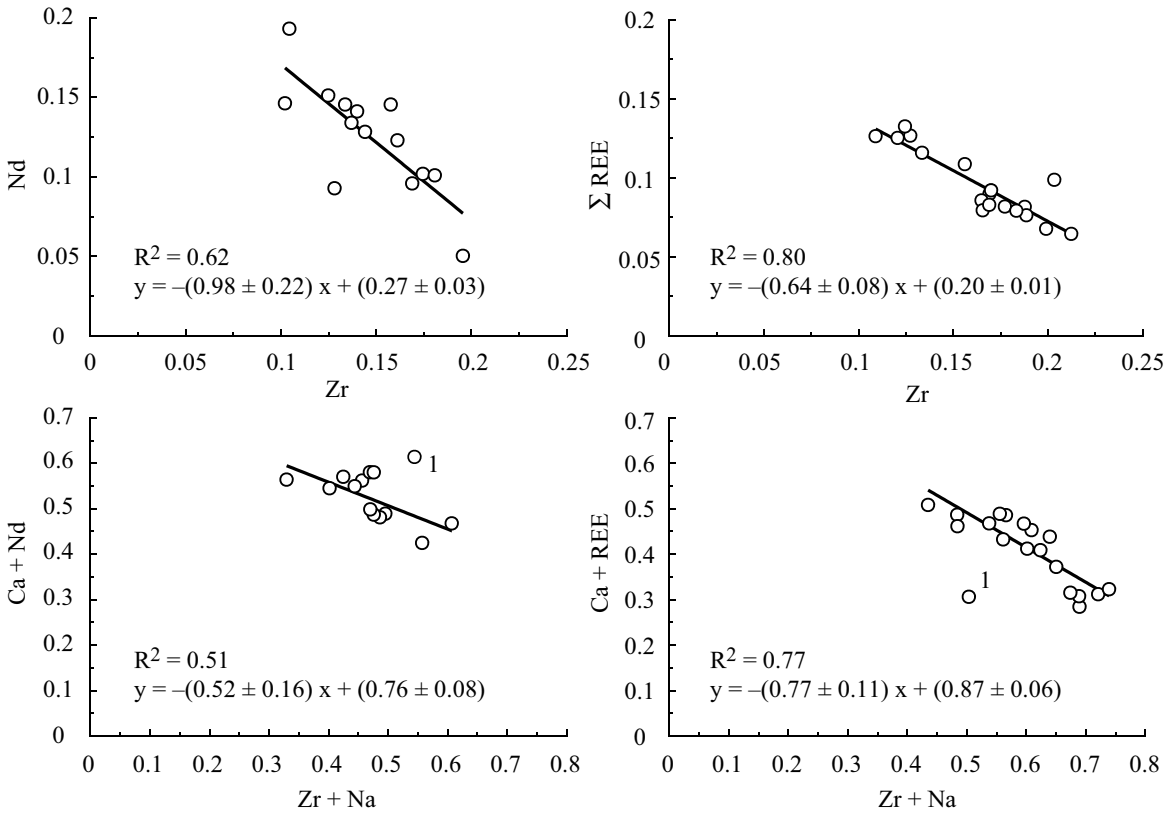

Figure 4.6.2-c: *Elemental correlation in secondary perovskite crystals of the Nd-doped system (left) and the Gd–Ce–Hf-doped system (right). Data measured by AEM (appendix C6). Data point Nr.1 is an outlier (> 4 s) and not taken for linear regression calculation. Error: 2s < 0.5%.*

tals (only visible as one triangular surface). Whereas sketch A in figure 4.6.8 shows all orientations of the octahedral and cubic faces of perovskite, sketch B provides a possible orientation for the octahedral and cubic faces of the just described crystal. For the crystallization of secondary perovskite, elements released from zirconolite in combination with Na from the fluid are used. Therefore, simultaneous to the decreasing Na level in the fluid, the crystallization of perovskite levels off or stops (chapter 4.5.3). Figure 4.6.7 pictures E and F show the incomplete crystallization of perovskite probably caused by the low Na concentration in the fluid.

Sector zoning: This interesting feature has been described in the literature from experimental hydrothermal synthesis of clinopyroxene (KOUCHI et al., 1983), but also occurs naturally in various minerals from magmatic rocks (titanite, Ca-augite, zircon), from sedimentary rocks (calcite) and metamorphic rocks (staurolite, monazite). A detailed overview is given by KRZEMNICKI (1996). Sector zoning is

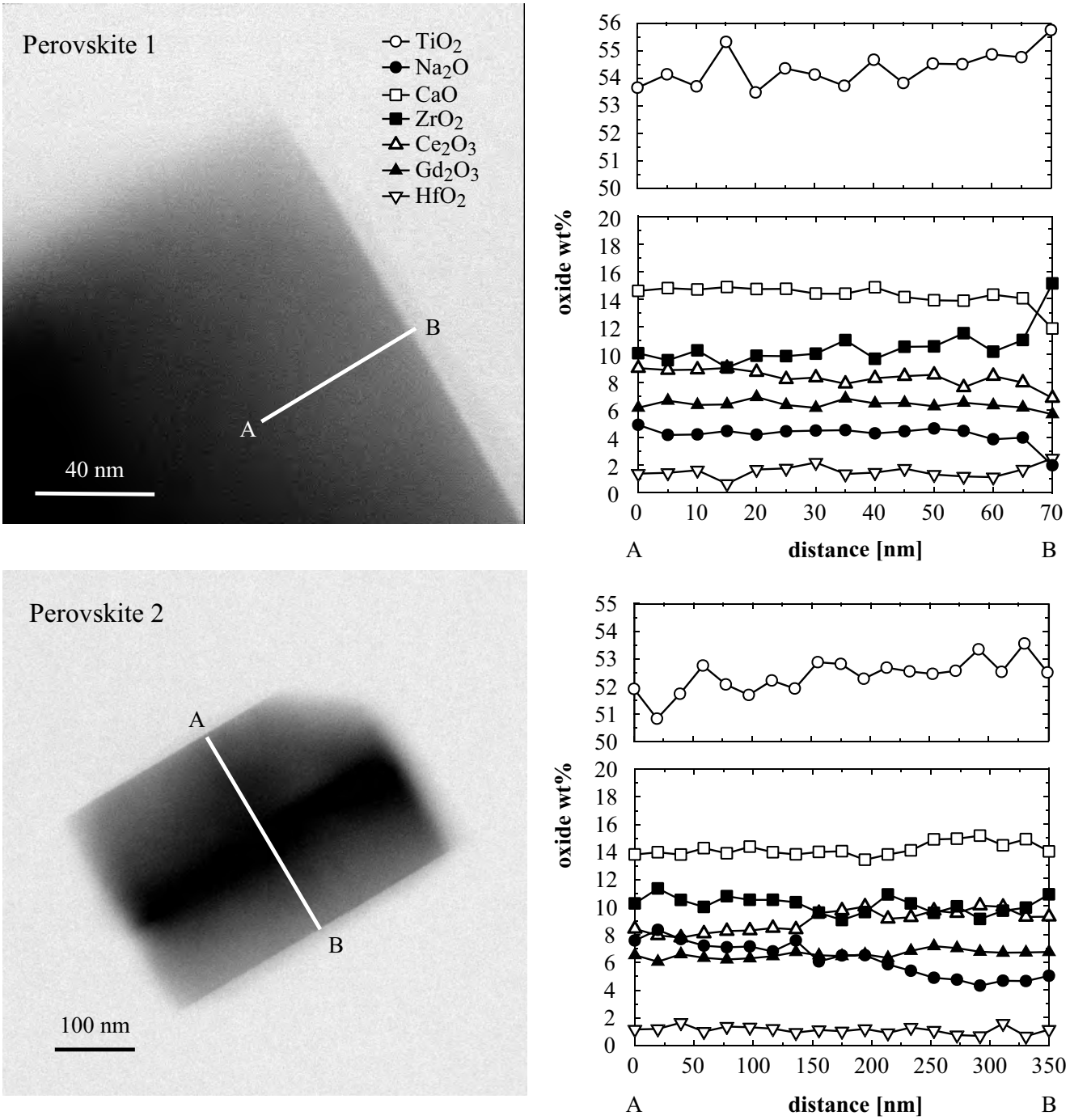

Figure 4.6.3: *TEM bright field images of perovskite showing the position of the EDX line scans with two different step sizes (5 nm respectively 20 nm). Corresponding the obtained elemental composition quantified in oxide wt%.*

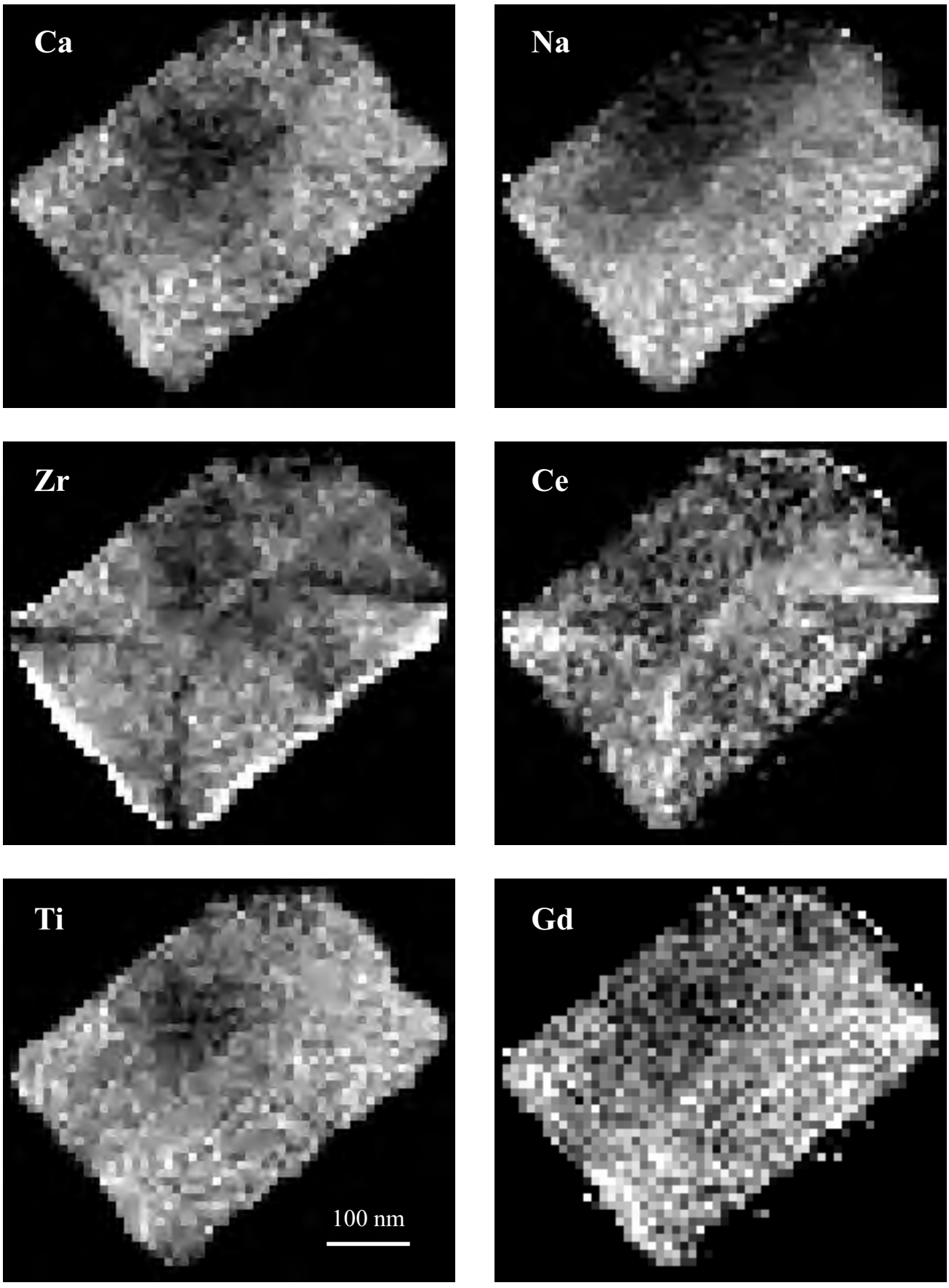

Figure 4.6.4: *TEM X-ray maps from an idiomorphic perovskite showing sector zoning visible by the negative correlation of Ce and Zr. Data are corrected for specimen thickness but not for absorption of X-rays due to carbon contamination (visible as spot in the upper center of the grain).*

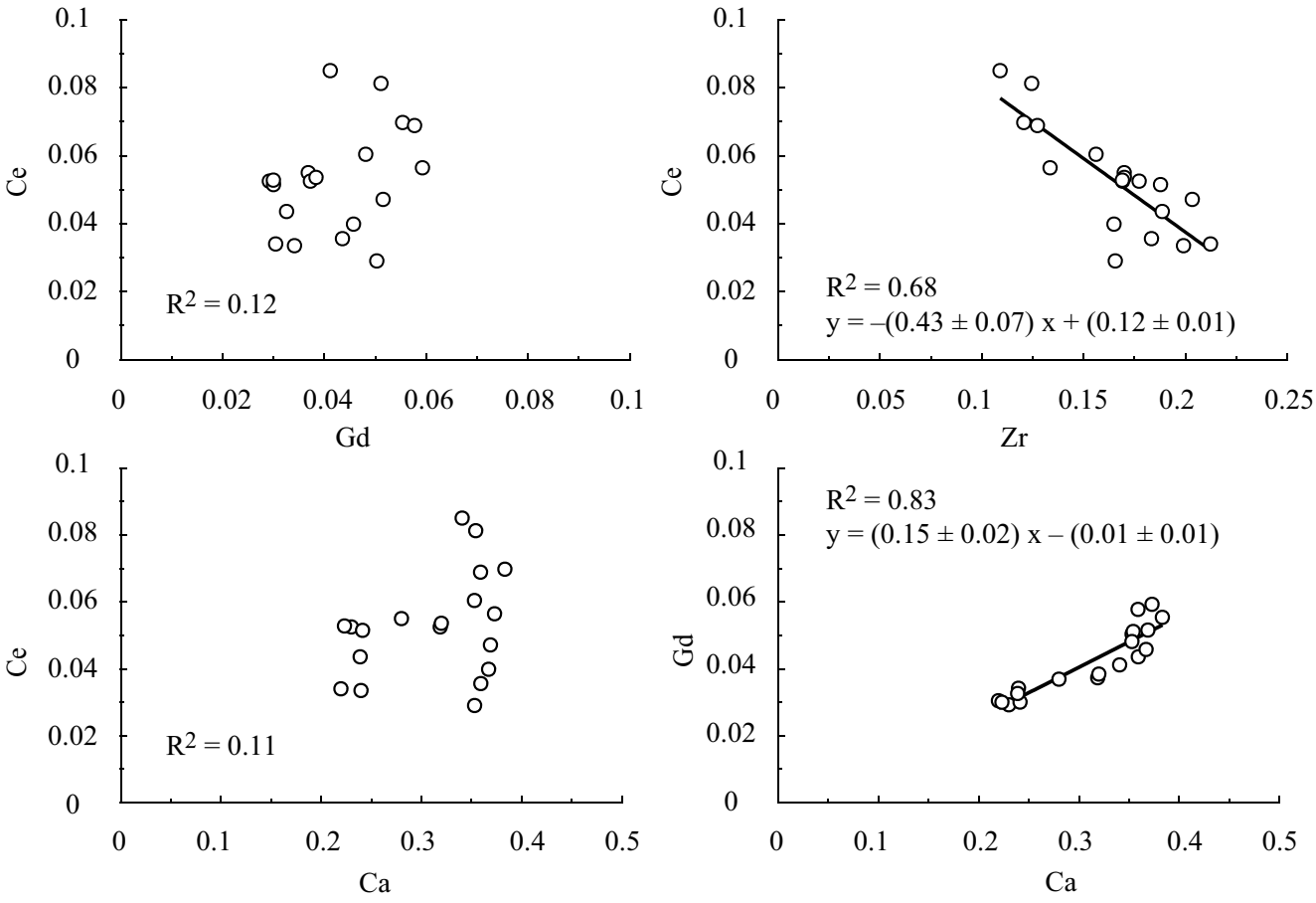

Figure 4.6.5: *Elemental correlation in secondary perovskite crystals of the Gd–Ce–Hf-doped system, specifically focusing on the behavior of Ce and Gd. Data obtained by TEM-EDX (appendix C6). Error: 2s < 0.5%.*

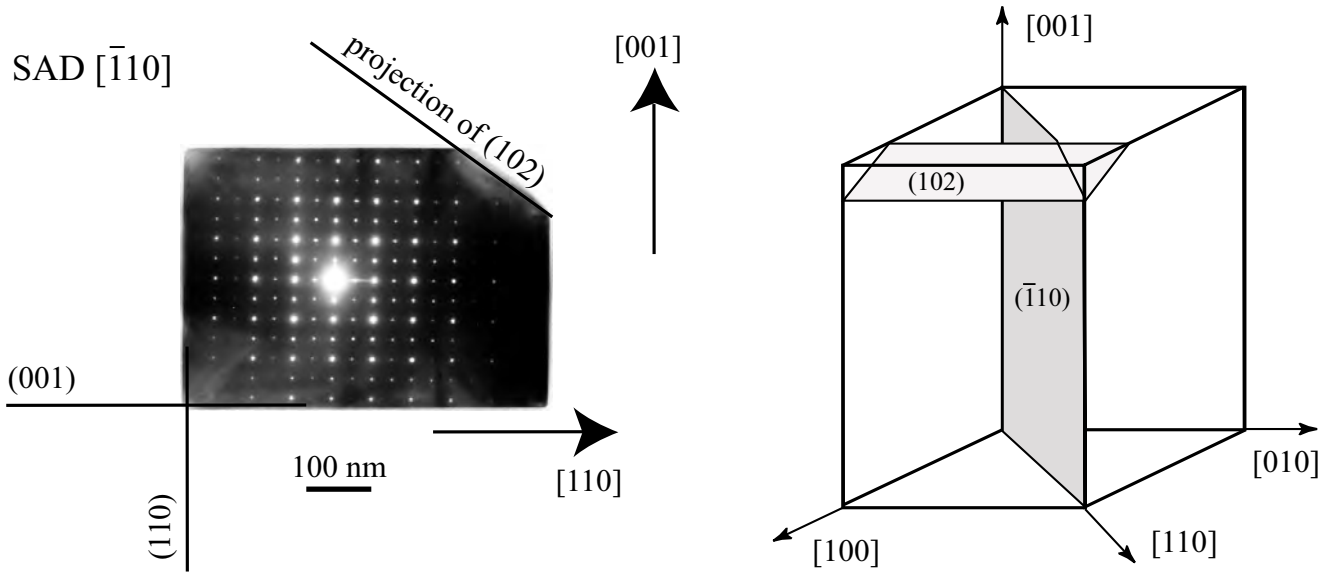

Figure 4.6.6: *Selected area diffraction pattern (SAD) and TEM bright field image showing the orientation of a pseudo-cubic idiomorphic perovskite crystal [–110] already shown in figure 4.6.4. This crystal is limited by the pseudo-cubic faces (110) and (001), which are both TiO_6-polyhedral lattice planes and the truncated edge is the projection of the fast growing pseudo-octahedral face (102) (see also figure 4.6.8). The SAD reveals twinning with {110} and {001} as twin planes.*

caused, at least partially by selective element adsorption on different growth surfaces with different growth rates of anisotropic minerals (DOWTY, 1976). This is based on the concept that each sector has a specific capacity for elemental adsorption on the crystal-fluid interface. Further discussions by PATERSON & STEPHENS (1992) and WATSON & LIANG (1995) introduce several factors such as normal and lateral growth velocities of crystal/fluid interfaces and specific diffusion of incorporating elements in the fluid as well as in the lattice plains.

From the data in figure 4.6.4 it is clear that the difference in probability of Zr and Ce uptake is controlled by the different crystal structure and crystal chemical properties of the surfaces of the growing crystal. Whereas the probability of the uptake of all other elements is essentially constant, it appears to be a relationship between the size of the ions and the probability of uptake via the different growth surfaces of the crystal. The ionic size for 8-fold coordination (after SHANNON, 1976) of Zr^{4+} (0.84 nm) is closer to the size of Ce^{4+} (0.97 nm) than that of Ce^{3+} (1.14 nm), which implies to conclude that a simple substitution of Zr^{4+} by Ce^{4+} and vice versa takes place. For a coupled substitution, any other element in perovskite should be observed to show a related variation in concentration. However, the general negative correlation between Zr and Ce measured through all perovskites (figure 4.6.5) reveals that other perovskite crystals than this show sector zoning as well. Therefore we conclude that most Ce is present at a tetravalent oxidation state.

Figure 4.6.9 shows schematically the boundaries between the sectors in the discussed sector zoned perovskite grain. The crystallographic orientations (Miller indices) of the individual sectors were calculated according to sketch C in figure 4.6.8, which in turn is based on the SAD shown in figure 4.6.6. The growth directions of the four visible sectors representing the pseudo-octahedral faces are all parallel to (010) whereas those representing the pseudo-cubic crystal faces are parallel to (110).

Figure 4.6.10 shows the crystal chemical composition of the cubic and octahedral faces indicated by CrystalMaker 4.0™. TiO_6-polyhedral lattice planes limit all six cubic faces. The four octahedral faces parallel to the [001] axis are limited by TiO_6-polyhedral lattice planes whereas those four parallel to the [010] axis are limited by alternating Ti-Ca lattice planes. The latter are those depleted in Zr and enriched in Ce and belong to the faster growing octahedral system (see figure 4.6.4). This indicates that during fast growth the larger Ce^{4+} is preferentially accommodated by the large Ca site in perovskite than the smaller Zr^{4+}, thus resulting in sector zoning. This result is supported by data from CRESSEY et al. (1999) on monazite which revealed that this process is governed by the size of the REE ion and by the variations in orientation and geometry of the acceptor sites on each growth surface.

Twinning

The TEM SAD pattern obtained from the perovskite (figure 4.6.6) reveals twinning with {110} and {001} as twin planes. This specific twin feature was described by WHITE et al. (1984) as a remarkable display of even three recognizable composition planes. Their study revealed {110}, {001} and {112} as twin boundary planes. Perovskite domains related by this twin law are identified by a diffraction pattern yielding a pseudospacing of 7.6 Å, which was also observed in our study. Further detailed investigations by WHITE et al. (1984) showed that these twin interfaces do not result in a displacement of the Ti atoms from their special positions. The Ti array will suffer only minimal distortion and should be perfectly coherent across the interface. The author could not show any change in the twin behavior of perovskite due to the incorporation of trivalent REEs and tetravalent actinide elements. These elements also failed to reveal any presence of cation ordering leading to superstructures. Therefore our high chemical variability on the A-site does not affect the possibility for the formation of twins.

HU et al. (1992) report that the twin system {112} is caused by the doubling of the c-axis, e.g., as a result of the transformation of cubic to tetragonal perovskite. They also showed that twinning along {110} is due to the transformation of tetragonal to orthorhombic symmetry. Already HOLMQUIST (1897) noted that all defects (e.g., twinning) are generally more common in nonstoichiometric perovskites. He also observed that twinning was more prominent in Ce-rich varieties. These observations are confirmed by our experiments.

4.7 Secondary Calzirtite

4.7.1 Introduction

The hydrothermal experiments carried out in 0.1 M NaOH above 500 °C at 50 MPa formed always perovskite and calzirtite as secondary phases. Calzirtite is not a constituent of the Synroc nuclear waste form, but is often associated with zirconolite in nature. They both have similarities in their chemical composition (mainly Ca, Zr and Ti) and structure (distorted fluorite subcell) and show the ability to incorporate a large variety of other elements. Therefore the occurrence of calzirtite calls for further investigations. Details on calzirtite were discussed in chapter 2.4.

4.7.2 Crystal Structure and Composition

After the experiments, calzirtite is aggregated between the larger perovskite crystals and morphologically forms short prismatic, sometimes almost cubic crystals (1–3 µm in size, figure 4.2.3). They are frequently found as T-shaped trillings or twins of prismatic individuals, which are oriented

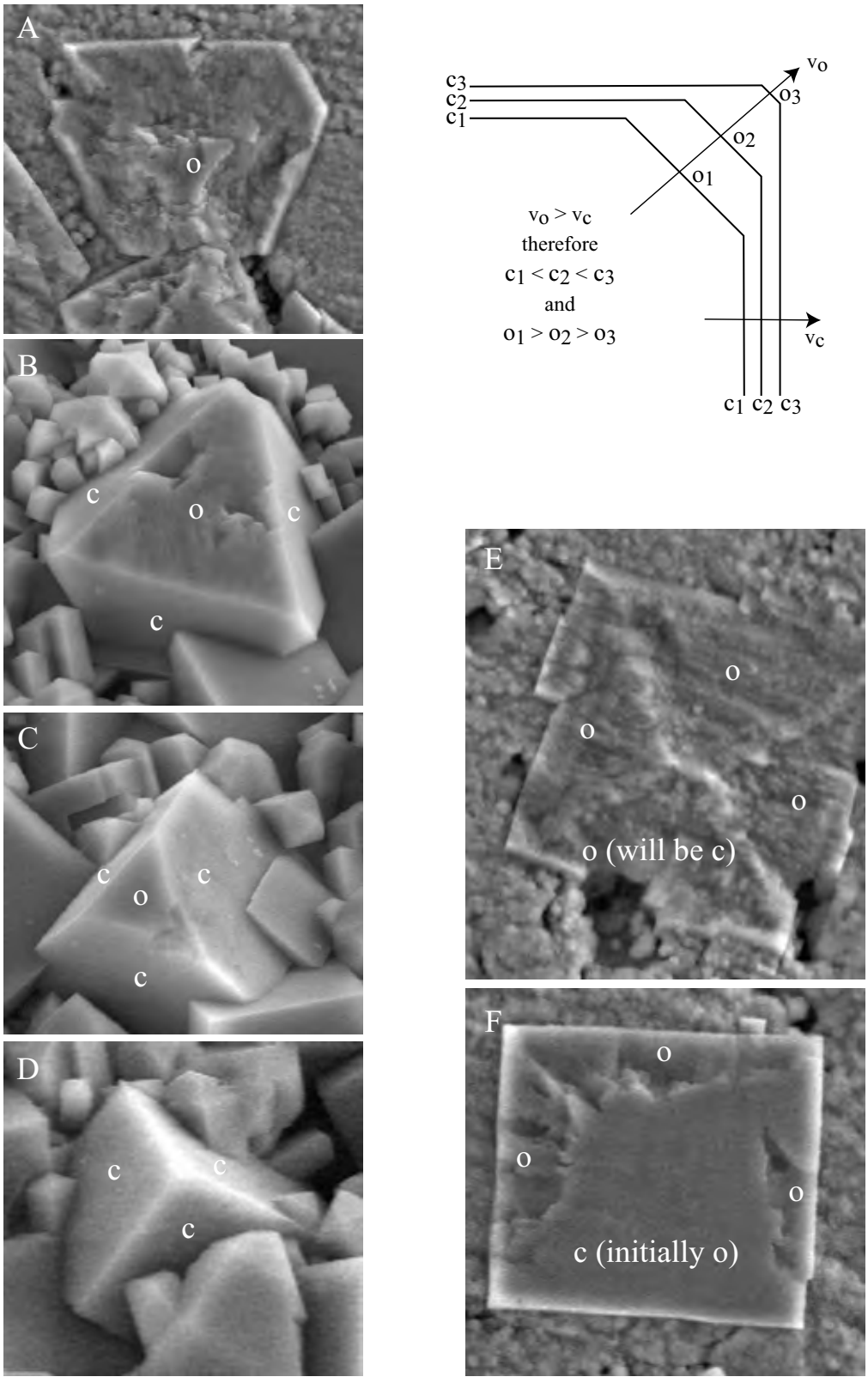

Figure 4.6.7: *Pictures A to D show a time series of the crystallization process of pseudo-cubic perovskite transformation from octahedral to cubic morphology (compare figure 4.6.8). This process is due to different growth velocities (v) of orthorhombic (o) and cubic (c) crystal faces. A higher growth velocity results in a smaller crystal face with time as explained in the sketch. Pictures E and F show possibly the same process, but from a different direction. The face c is parallel to the initial o-face (compare sketch D in figure 4.6.8). No actual growth rate may be given, because different stages were found after the same experiment revealing different starting times or growth rates for different crystals.*

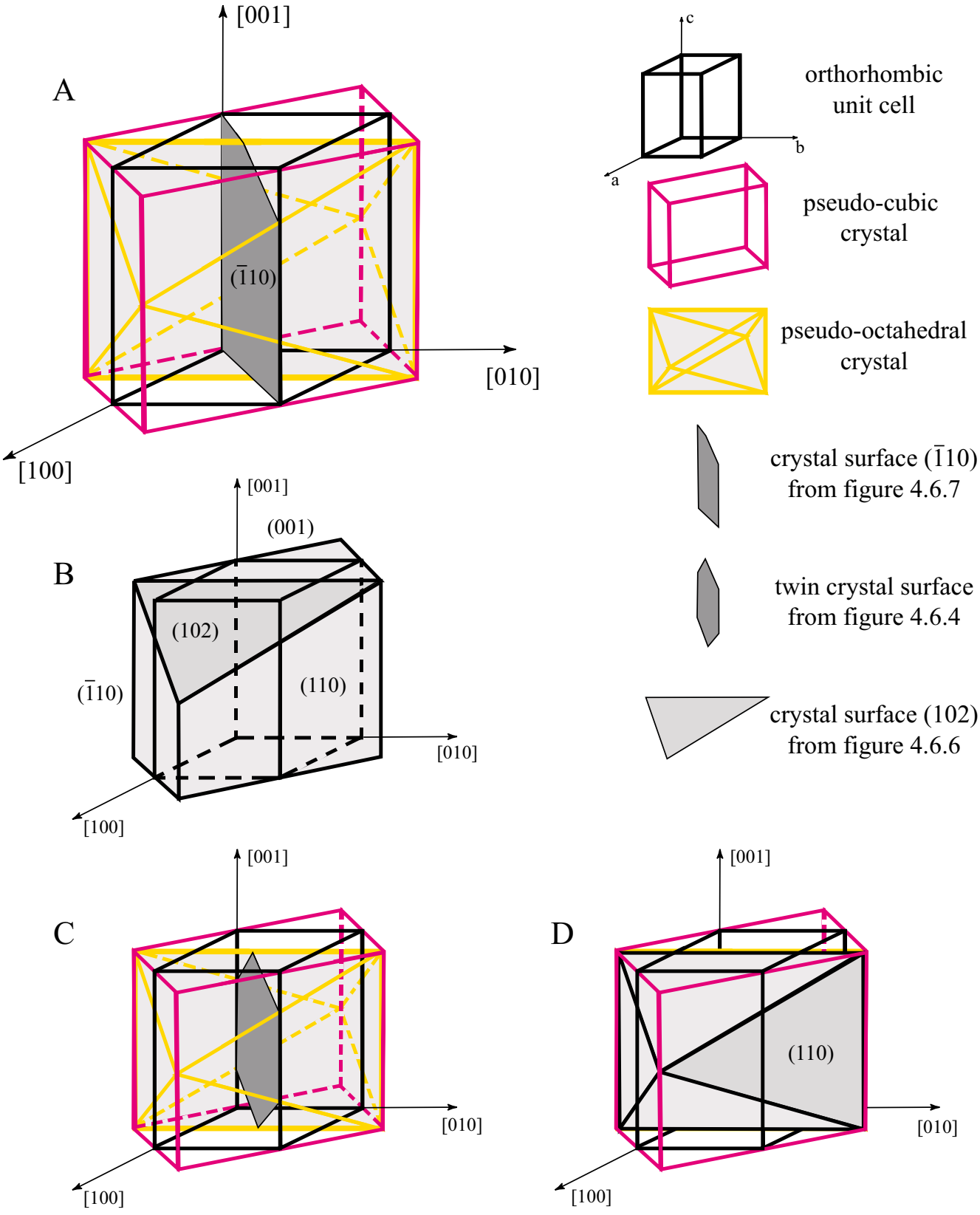

Figure 4.6.8: *Sketches of the crystallographic orientation of pseudo-cubic perovskite. A shows the orientation of the pseudo-cubic and pseudo-octahedral system in the orthorhombic unit cell with the orientation of the earlier described two dimensional crystal surface (figure 4.6.3 – 4.6.6). B shows the same crystal in three dimensions revealing the assignment of the visible faces to the cubic (light) and octahedral (dark) system. C shows the orientation of the sectional plane between cube and octahedra. D reveals one face belonging to both crystal orientations, which does not change during morphology transformation.*

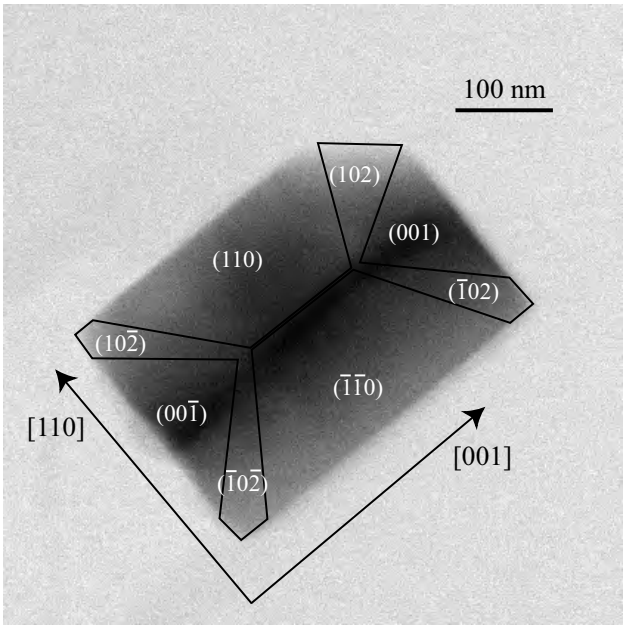

Figure 4.6.9: *TEM bright field image of the perovskite (figure 4.6.4) showing sector zoning. The sectors and their growth directions are oriented according to figure 4.6.8 (sketch C) showing the cubic and octahedral system, respectively.*

mutually perpendicular to one another (figure 4.3.2). Interestingly, the same features are described from natural calzirtites where XRD analysis allowed to consider that they are cubic (Zhabin et al., 1962) and from calzirtites from eastern Siberia where frequently trillings were found (Zdorik et al., 1961).

The TEM diffraction patterns of this experimentally produced secondary phase revealed a tetragonal calzirtite. The calzirtite structure is formed due to a tripling of the a- and b-axes, and a doubling of the c-axis of the fluorite subcell which is visible in the diffraction patterns [110], [010] and [023] of figure 4.7.1.

Two tilting experiments by TEM were performed starting with a crystal at the position [010] to obtain detailed analyses of the structure. The grain was tilted around the a-axis respectively c-axis for 45°, and all encountered zone axes were recorded. All diffraction patterns and their corresponding tilting angles were then compared to those calculated by Desktop Microscopist™. This comparison confirmed that all zone axes up to order three were observed. The difference between measured and calculated angles was less than 1%.

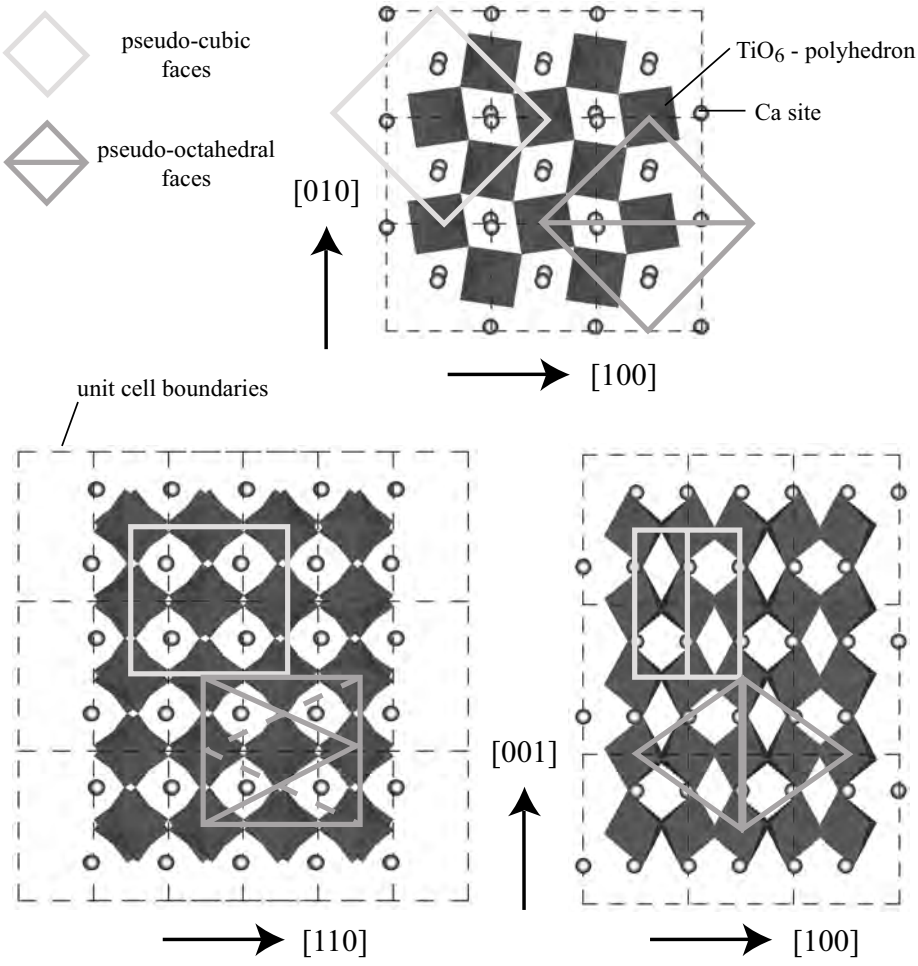

Figure 4.6.10: *Crystal structure and orientation of the pseudo-cubic and pseudo-octahedral faces (by Crystal Maker 4.0).*

Calzirtite is described in the literature with two different structural formula $Ca_2Zr_5Ti_2O_{16}$ and $CaZr_3TiO_9$ (see chapter 2.4). Thin-film analyses (table 4.7.1 and appendix C.6) reveal that the chemical composition of this hydrothermally grown calzirtite is closer to the composition $Ca_2Zr_5Ti_2O_{16}$. This is most obvious in the TiO_2 content, where 16.15–18.65 wt% are measured compared to 18.0 wt% and 15.6 wt% for stoichiometrically ideal $Ca_2Zr_5Ti_2O_{16}$ and $CaZr_3TiO_9$, respectively. These thin-film analyses demonstrate further that the calzirtite formed in these experiments incorporates significant amounts of Na, REEs, and possibly contains up to 5% vacancies on the 8-fold coordinated Ca site. The following average compositions were found for the two types of starting material:

$Ca_{1.33}Na_{0.29}Nd_{0.14}Zr_{5.15}Ti_{1.94}O_{16}$
(Nd-system)

$Ca_{1.30}Na_{0.36}Gd_{0.07}Ce_{0.02}Zr_{4.48}Hf_{0.60}Ti_{2.07}O_{16}$
(Gd–Ce–Hf-system).

4.7.3 Discussion

Crystal chemistry

In contrast to the results obtained for perovskite, the determined chemistry is close to the stoichiometrical composition. No unexpected site occupations are estimated but also no crystal was analyzed by TEM, which allowed detailed analyses for the elemental distribution on the lattice sites (compare appendix D). Therefore the simple substitution on the Ca site is expected:

$$REE^{3+} + Na^{+} <=> 2\,Ca^{2+} \quad (1).$$

But, as for perovskite, the elemental correlation did not confirm this substitution ($R^2 = 0.25$; figure 4.7.2). Additional elemental correlations revealed that the REEs are negatively correlated to Zr ($R^2 = 0.84$; figure 4.7.2), which leads to the assumption of the following multi-site substitution:

$$Ca^{2+} + REE^{3+} <=> Zr^{4+} + Na^{+} \quad (2),$$

which could be confirmed by a negative correlation ($R^2 = 0.70$; figure 4.7.2). In addition, our experimental crystals also reveal the ability for a small exchange of Ti and Zr ($R^2 = 0.80$; figure 4.7.2) as reported for natural calzirtite (Rossell, 1982). Unfortunately, only three crystals could be determined for the Gd–Ce–Hf-doped system. Therefore no prediction could be made for the oxidation state of Ce in calzirtite.

However, calzirtite revealed a smaller capacity to incorporate REEs compared to perovskite, even though it replaces zirconolite and might act as secondary waste form. The conspicuous high Hf content is due to the close elemental relation of Hf to Zr. Even at laboratory scale, Zr may never be separated completely from Hf, which is indicated by the Hf concentration after experiments with the «Hf-free» starting material.

General

By ESEM calzirtite was observed to form twins or multiple twins. In comparison to perovskite, no peculiar growth phenomena like sector zoning were recorded during investigations by TEM. This may be due to its smaller size, its minor occurrence or just because of its different behavior.

4.8 Relations between Perovskite, Calzirtite and Primary Zirconolite

4.8.1 Introduction

Zirconolite, perovskite and calzirtite have several chemical and physical characteristics in common. First they are all oxides, mainly consisting of Ca and Ti (perovskite) and Ca, Ti and Zr (zirconolite and calzirtite). In nature, zirconolite and calzirtite are often associated or even intergrown. In contrast to perovskite, calzirtite and zirconolite are rare accessory minerals. The three mineral phases were described in detail in chapter 2 and further discussions of their phase stability will be made in chapter 5.2.

The secondary phases perovskite and calzirtite (chapter 4.6 and 4.7) replace the primary zirconolite above 500 °C at 50 MPa in a 0.1 M NaOH solution. Both phases attract interest because they incorporate significant amounts of the elements used as analogues for waste elements and/or as neutron poisons released from zirconolite. In our experimental run products, they are always easy to distinguish because of their difference in size and morphology. From time dependent studies in 0.1 M NaOH it is obvious that the crystallization of perovskite starts slightly earlier than that of calzirtite (chapter 4.5.3).

4.8.2 Crystal Chemistry

Elemental distribution

X-ray elemental distribution maps from cross sections show that the Nd content (used to simulate the behavior of rare earth elements and trivalent actinides) of perovskite is higher than that of the primary zirconolite (figure 4.2.4). Similarly, perovskite is enriched in Ti, Ca and Na. The X-ray maps reveal further a different elemental distribution in calzirtite. These results document different capabilities of different phases for the incorporation of the analogue elements and neutron absorbers. Because the zirconolite replacing phases incorporate these elements and thus, act as a secondary waste form, it is useful to estimate the partition coefficients of these elements between these secondary phases.

Three assumptions were made for the calculation of the average partition coefficients of the individual REEs and Hf (figure 4.8.1). Firstly, we have assumed that Ce occurs trivalent and tetravalent in both perovskite and calzirtite,

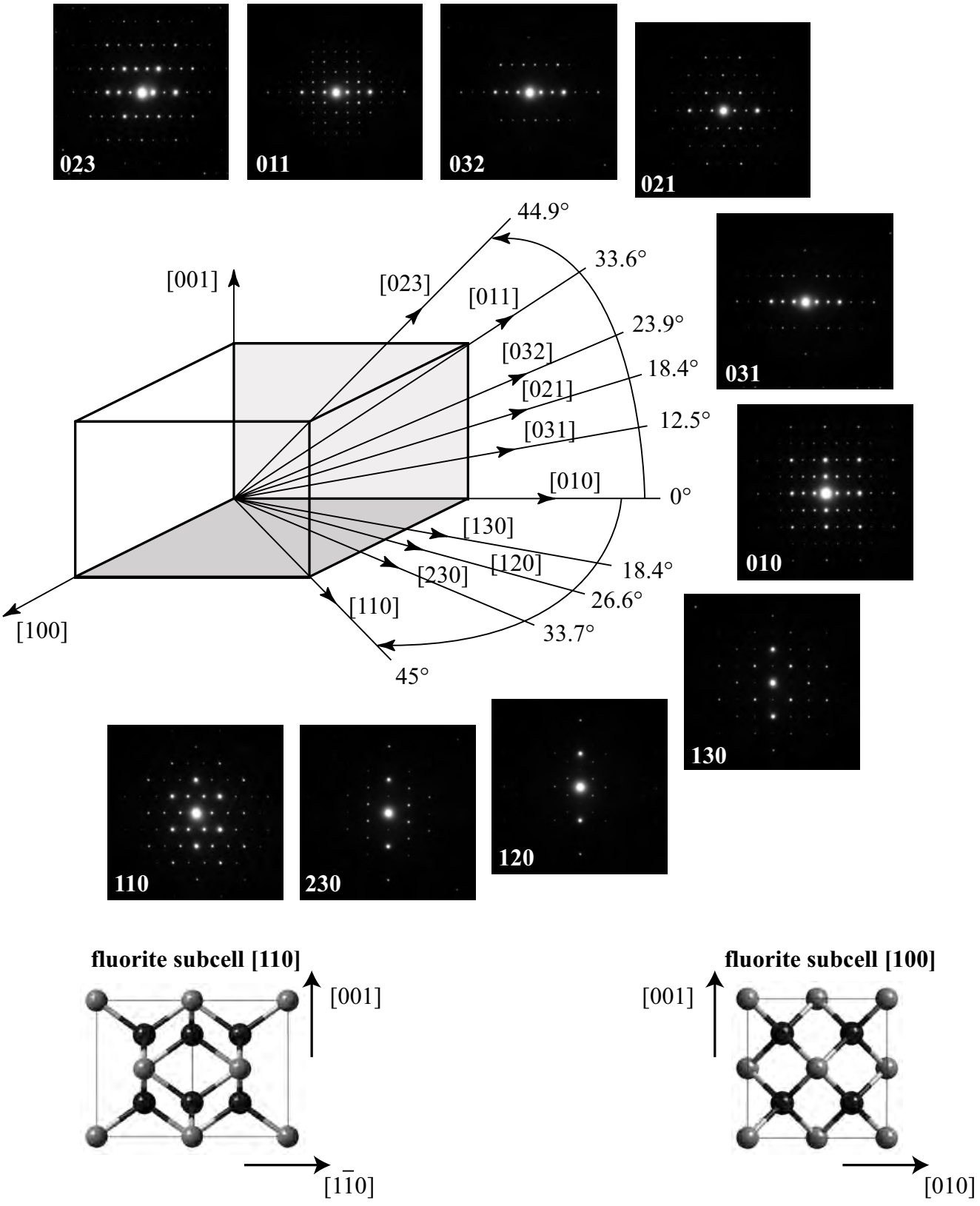

Figure 4.7.1: *Selected area diffraction patterns and a sketch of the crystallographic unit cell of calzirtite. The diffraction pattern [010] shows the cubic fluorite subcell ([100]-type pattern, compare plot by Crystal Maker at bottom) tripled along a and doubled along c. A tilting experiment around the c-axis for 45 degrees shows all zone axes up to order three with their respective tilt angles. [110] shows again the fluorite subcell ([110]-type pattern, compare plot by Crystal Maker at bottom). The equivalent tilting experiment around a shows that this calzirtite is tetragonal. The fluorite subcell is now visible on [023] as a [110]-type pattern.*

Table 4.7.1: *Analytical electron microscopy (AEM) analysis of secondary calzirtite resulting from the two different starting materials (standard deviation (s.)).*

wt%	calzirtite-(Nd) (n=13)				calzirtite-(Gd) (n=3)			
	mean	*s.*	*min*	*max*	*mean*	*s.*	*min*	*max*
Na_2O	1.05	0.30	0.53	1.46	1.17	0.21	1.00	1.40
Al_2O_3	0.14	0.40	0.00	1.41	0.08	0.13	0.00	0.23
CaO	8.11	0.44	7.70	9.44	7.67	0.79	6.76	8.24
TiO_2	17.21	0.75	16.15	18.65	17.38	0.15	17.27	17.55
FeO	0.53	0.27	0.18	0.94	0.66	0.41	0.36	1.13
ZrO_2	68.60	1.28	66.74	70.84	58.09	0.39	57.65	58.35
Ce_2O_3					0.42	0.09	0.37	0.53
Nd_2O_3	3.03	1.07	1.28	4.42				
Gd_2O_3					1.35	0.19	1.17	1.55
HfO_2	1.33	0.26	0.79	1.89	13.19	0.62	12.50	13.70
sum	100.00				100.01			
Formula based on 16 oxygens								
Na	0.31	0.09	0.16	0.43	0.36	0.06	0.31	0.43
Al	0.02	0.07	0.00	0.25	0.01	0.02	0.00	0.04
Ca	1.32	0.06	1.26	1.51	1.30	0.13	1.15	1.40
Ti	1.96	0.08	1.85	2.12	2.07	0.01	2.06	2.08
Fe	0.07	0.03	0.02	0.12	0.09	0.05	0.05	0.15
Zr	5.07	0.10	4.93	5.25	4.48	0.03	4.45	4.50
Ce					0.02	0.01	0.02	0.03
Nd	0.16	0.06	0.07	0.24				
Gd					0.07	0.01	0.06	0.08
Hf	0.06	0.01	0.03	0.08	0.60	0.03	0.56	0.62
sum	8.97				8.99			
∑ REE [1)]	0.16	0.06	0.07	0.24	0.10	0.01	0.08	0.10
∑ Zr, Hf [1)]	5.13	0.10	4.98	5.30	5.07	0.04	5.04	5.12

[1)] This sum is relative to one measurement and not the sum of the min/max of different measurements.

with a similar Ce^{3+} to Ce^{4+} ratio due to unique growth conditions. Secondly, we have assumed that all the trivalent REEs occupy the Ca site of perovskite and calzirtite whereas Hf^{4+} and Ce^{4+} occupy both sites in perovskite (as described for Zr) and only the Zr sites in calzirtite. Finally, we considered the Ca site of perovskite as eight coordinated by ignoring four of the 12 oxygens which lie at distances of up to 0.32 nm away from the central cation (0.25 nm mean distance for eightfold coordination) (Fielding & White, 1987). This facilitates a direct comparison between the Ca sites of calzirtite and perovskite. Using ionic radii for Ce^{3+}, Nd^{3+}, Gd^{3+} in eightfold coordination and for Hf^{4+} and Ce^{4+} in sevenfold coordination (Shannon, 1976), the data from figure 4.8.1 show that elemental partitioning between the secondary phases is mainly controlled by ionic size. The polyhedral volumes of the two eight coordinated Ca sites are significantly different: in calzirtite, this volume is approximately 30% smaller than in perovskite (table 2.5.1). Thus, the large cations (trivalent REEs) have a preference for the large Ca site in perovskite ($D^{C/P} << 1$). On the other hand, the smaller cations (Hf^{4+}) prefer the smaller sites in calzirtite ($D^{C/P} > 1$); here, the Zr site has a polyhedral volume that is approximately 50% smaller than that of the Ca site in perovskite. Therefore it is assumed that Ce^{4+}, which is significantly larger than Zr^{4+} preferentially occupies the larger sites in perovskite than in calzirtite. However, another hypothesis would propose that Ce is tetravalent only in perovskite and trivalent in calzirtite. This is supported by the very low total Ce content in calzirtite.

Lumpkin et al. (1995) described a similar distribution of these elements between perovskite and zirconolite in Synroc. Therefore calzirtite and zirconolite exhibit similar behavior with respect to elemental fractionation in Na-rich systems.

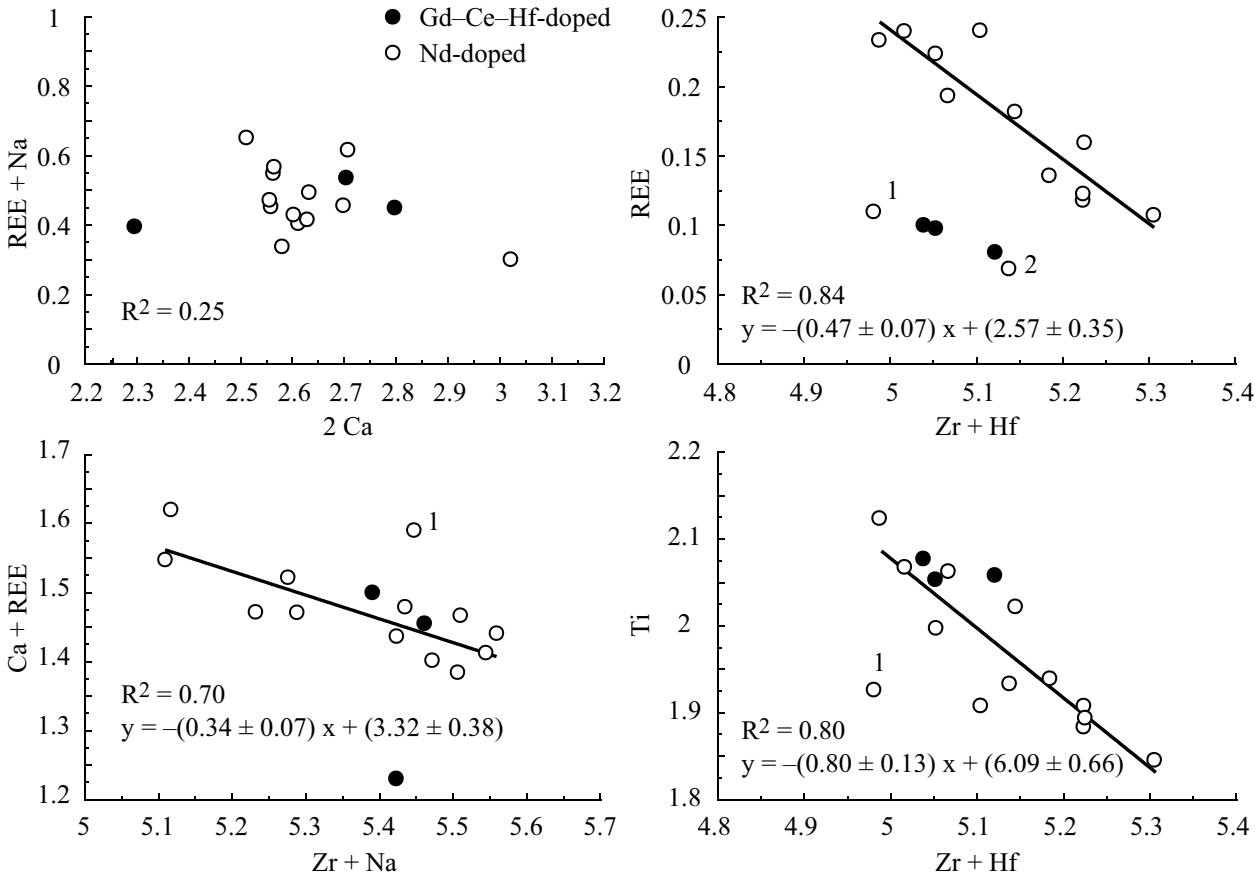

Figure 4.7.2: *Elemental correlation in secondary calzirtite crystals of the Nd-doped system (bright spots) and the Gd–Ce–Hf-doped system (dark spots). Data measured by AEM (appendix C6). Data points Nr.1 and 2 are outliers (> 4 s) and the three points from the Gd–Ce–Hf-doped system are not taken for linear regression calculation. All plotted data have count statistics with 2s < 0.5% revealing that the data points are larger than the error bars would be.*

However, almost no Al^{3+} is accommodated by secondary perovskite and calzirtite (table 4.6.1, 4.7.1, appendix C.6), which is released from the corroded zirconolite. In zirconolite, Al is used as charge balancing element and is accommodated by the Ti site. Zirconolite has a fivefold coordinated Ti site, which is significantly smaller than the sixfold coordinated Ti sites in perovskite and calzirtite and therefore more easily accommodates the small Al^{3+} ion. Until now, no Al-rich secondary phase was observed. Fluid data reveal a very high Al concentration in the fluid compared to all other elements released during the dissolution of zirconolite (see chapter 4.5.3). The high Al content in the leachate may be due to the high solubility of Al in solutions with a high pH, possibly as $Al(OH)_3^0$ or any other hydroxide.

Differences

A comparison of the overall variability of the chemical composition of the two secondary phases perovskite and calzirtite shows that the standard deviation for the main elements Ca, Ti and Zr in calzirtite (table 4.7.1) is much smaller than in perovskite (table 4.6.1). The total amount of the other minor elements (e.g., Na, REEs) is much smaller in calzirtite than in perovskite (figure 4.8.1). This reflects the capability of these phases to substitute other elements and is consistent with observations on natural specimens. As already described in chapter 2.3, natural perovskite is able to substitute up to 50% of Ca on the A and of Ti on the B site with various elements without changing its structure (Anthony & John, 1997), whereas calzirtite shows only a low variation of its stoichiometrical composition.

The results of the experiments revealed for perovskite an even lower Ca content (30–40% of total on that site), but almost no substitution on the B site. They showed also the limited ability for the incorporation of other elements into the crystal lattice of calzirtite. Bellatreccia et al. (1999) described that calzirtite is much less able to accommodate substitutions of Ca, Zr and Ti by REE and actinides than zirconolite, but the two minerals are often intergrown. This need for a narrow defined chemical composition may be explained by the crystal structure of calzirtite, because major chemical changes result in the change of the structure, which results in the formation of other related minerals. Experiments from Zdorik et al. (1961) showed that the structure of calzirtite is very close to the cubic undistorted structure of pyrochlore. The replacement of a certain amount

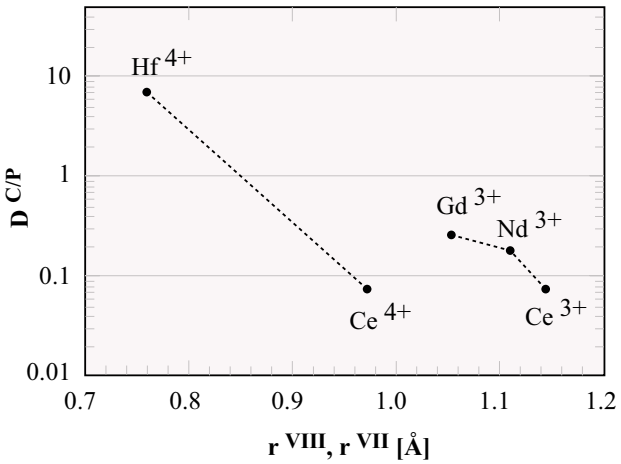

Figure 4.8.1: *Average partition coefficient ($D^{C/P}$: average concentration in calzirtite divided by the average concentration in perovskite in wt%) of Ce^{3+}, Ce^{4+}, Nd^{3+}, Gd^{3+} and Hf^{4+} between the secondary calzirtite and perovskite plotted versus effective ionic radii (Shannon, 1976; trivalent REE eight coordinated, Hf and Ce^{4+} seven coordinated).*

of Zr by Ti theoretically must lead to a distortion of the structure. For the ratio of Zr : Ti = 3 : 1, a set of XRD reflections still fits the cubic structure, and the additional reflections show the distorted tetragonal structure. The authors also found a close structural relation between calzirtite and baddeleyite (lattice parameters close to $^1/_2$ of calzirtite). They also proposed that the Zr : Ti ratio may not vary very much, which is confirmed by our own data in table 4.7.1.

If we exclude the chemical variability in perovskite due to sector zoning (chapter 4.6.3), all measured perovskite and calzirtite crystals exhibit a homogenous internal composition (figure 4.6.4). Therefore the extensive chemical variance between different grains may be due to a heterogeneous fluid composition, possibly caused by a lack of fluid convection in the capsule. The fluid composition would then directly be related to the composition of the dissolved/replaced zirconolite in its microenvironment. It should again be emphasized that the primary zirconolite also shows variable composition (see table 3.2.2). Alternatively, the observed chemical differences between individual crystals of the same product phases could be explained in terms of the fluid boundary layer effect. Thereby only unit layers of the ideal chemical composition (similar to the nucleus) are attached to the mineral surface out of the fluid boundary layer and build a new crystal layer. After a period of time, one element understeps a critical concentration in the fluid and the oscillating fluid system swings back to the starting composition and a new layer of ideal composition may be attached to the crystal (Paterson & Stephens, 1992).

4.8.3 Crystal Boundary

Analyses of the grain boundary between primary zirconolite and the product phases perovskite and calzirtite should provide any clues about the mechanism of the dissolution/precipitation process. To obtain detailed information, investigations by high-resolution TEM were required. In the analyzed TEM-samples, the boundary between zirconolite and perovskite was found but never the boundary between zirconolite and calzirtite or perovskite and calzirtite. This is mainly due to the difficult sample preparation with a high chance of failure.

To analyze the variation of the chemical composition between primary zirconolite and secondary perovskite, EDX-line-scans were made by TEM at a high resolution with the beam diameter set to 1 nm (figures 4.8.2). The large-scale composition profile revealed that the reaction zone at the zirconolite surface is up to 30 nm thick. Na has penetrated up to 30 nm into the zirconolite reaction zone. The fine-scale composition profile showed a concentration gradient that is steeper on the perovskite side compared to the zirconolite side. But this analytical method revealing a sharp chemical border between the two phases is limited by the possibility of beam broadening (several nm) and count statistics (see appendix C.6). Additonally there could be some interaction of the two phases.

High-resolution TEM images revealed an epitaxial overgrowth of secondary perovskite on primary zirconolite and no evidence of any intergranular segregation at the interface. The Ti polyhedral layers of zirconolite are perpendicular to c* and have a measured d spacing of 5.32 Å (figure 4.8.3). The Ti polyhedral layers of perovskite parallel to the (120) layers have a d-spacing of 2.64 Å (figure 4.8.3) which is about one half of the d-spacing between the layers in zirconolite. The orientation of the boundary between the two phases is parallel to $(80\bar{2})$ in zirconolite and parallel to $(\bar{1}1\bar{6})$ in perovskite.

4.8.4 Mass Balance

Introduction

In this chapter, calculations are presented for the estimation of the mass balance during the experiments. The composition of the starting material (solid and fluid), the composition of the determined secondary phases, and the composition of the fluid after the experiment are the required input data. The calculations were made for the Nd-doped system and experiments at 550 °C and 50 MPa in 0.1 M NaOH, because only for these conditions sufficient data were obtained. Unfortunately, the concentration of Ca after the experiment in the fluid could not be determined due to detection limit problems. At ambient conditions, the concentration of Ca in the fluid could be determined by calculating the total charge balance during the experiment, but due to the diffusive loss of hydrogen above 200 °C, its concentration has to be estimated after the calculations.

Calculation

The following part describes the calculations carried out (for details see appendix E), based on the following equation system:

«zirc» + a·NaOH = x ·«pero» + y·«calz» + z·«leachate»

In vector notation, the equation system can be described as follows, where the numbers represent the average composition in moles:

$$\begin{array}{lc} [1] & Ca \\ [2] & Zr \\ [3] & Ti \\ [4] & Nd \\ [5] & Al \\ [6] & Na \\ [7] & O \end{array} \begin{pmatrix} 0.78 \\ 1 \\ 1.8 \\ 0.21 \\ 0.19 \\ 0 \\ 7 \end{pmatrix} = x \cdot \begin{pmatrix} 0.4 \\ 0.15 \\ 0.97 \\ 0.12 \\ 0 \\ 0.33 \\ 3 \end{pmatrix} + y \cdot \begin{pmatrix} 1.33 \\ 5.13 \\ 1.96 \\ 0.16 \\ 0 \\ 0.31 \\ 16 \end{pmatrix} + z \cdot \begin{pmatrix} ? \\ 0.003 \\ 0.02 \\ 0.002 \\ 8 \\ 5 \\ ? \end{pmatrix} - a \cdot \begin{pmatrix} 0 \\ 0 \\ 0 \\ 0 \\ 0 \\ 100 \\ 0 \end{pmatrix}$$

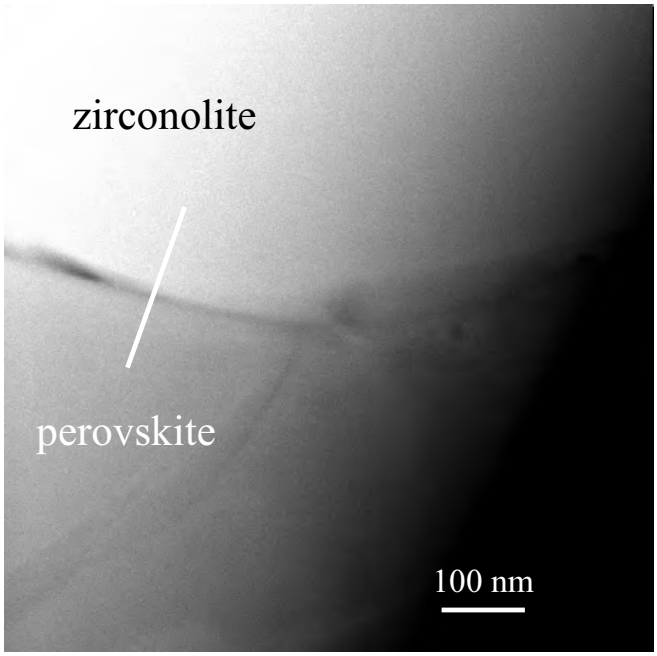

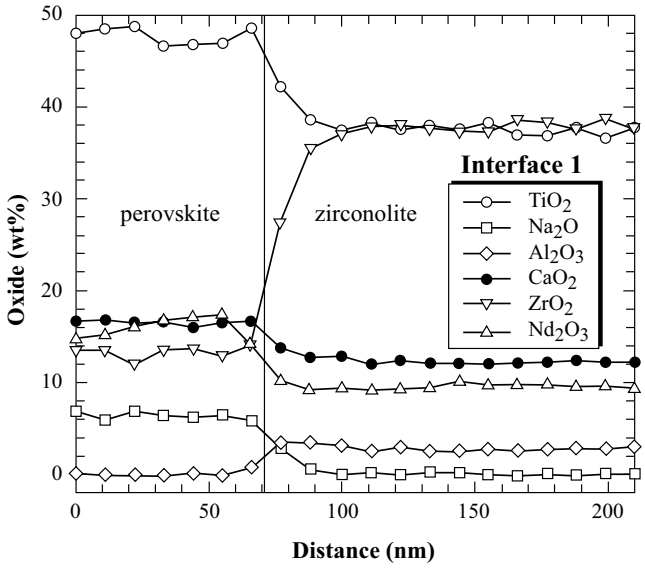

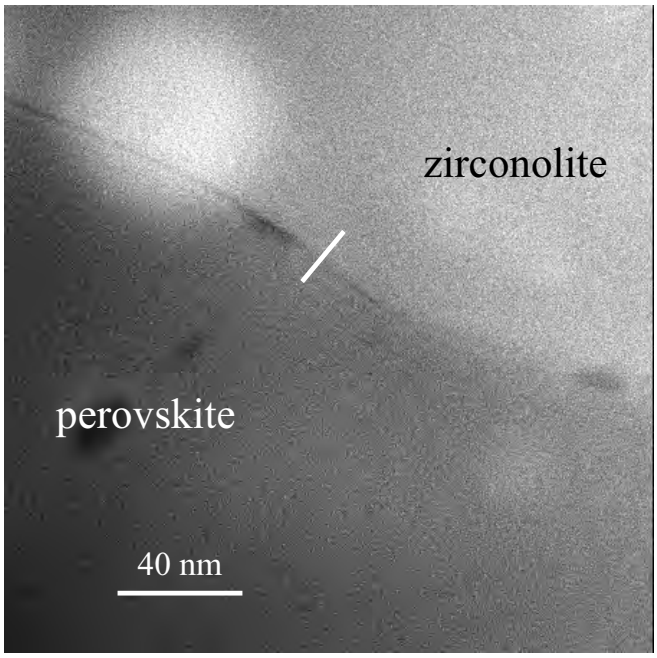

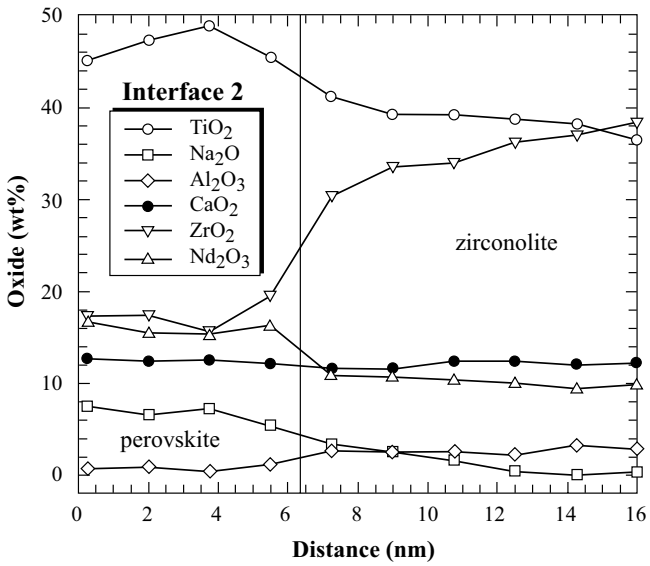

Figure 4.8.2: *TEM bright field images of the boundary between primary zirconolite and secondary perovskite showing the position of the EDX line scans with two different step sizes (10 nm, top; and 2 nm, bottom). The elemental compositions quantified in oxide wt% show the sharp boundary between the two phases. All plotted data are thickness corrected and have count statistics with 2s < 0.5% revealing that the data points are larger than the error bars would be. An indeterminable error is generated by beam broadening and by overlying effects of the two phases due to a not completely vertical grain boundary, which is marked in the plots as a physical grain boundary on the sample surface.*

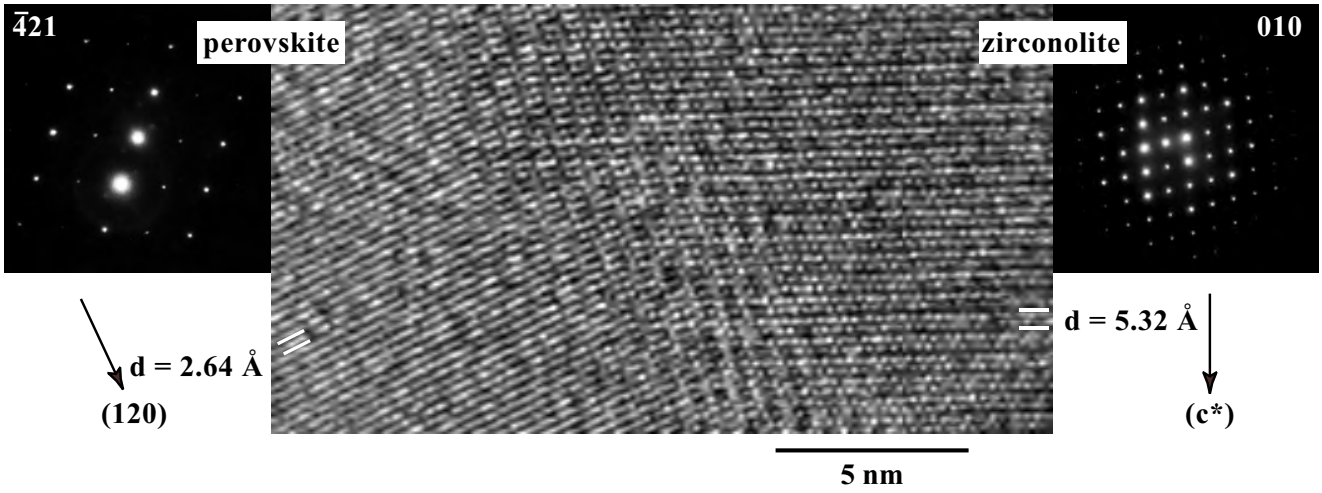

Figure 4.8.3: *High-resolution TEM image of the boundary between perovskite and zirconolite. Also shown are oriented selected area diffraction patterns of perovskite and zirconolite.*

Because the equation system (7 equations) is overdetermined (4 unknowns: a, x, y, z and two questionmarks for the undetermined concentrations of Ca and O in the fluid), several assumptions were made to solve the problem. Firstly, to approximate the stoichiometric coefficients of perovskite (x), calzirtite (y), the leachate (z) and the fluid (a), the 5 equations [2] until [6] were calculated as a matrix by MATLAB™. The results obtained were x = 1.553, y = 0.1495, z = 0.0238, and a = 0.0068. In other words, the molar ratio of perovskite to calzirtite in this doped system is roughly 10.

The fluid analysis determined also the amount of Na preserved in the fluid and not incorporated by the secondary fluid, which was approximately 5% of original mass. This number together with the above calculated coefficients were used to determine the total mass balance (total zirconolite replaced) and to determine the unmeasurable concentration of Ca and O in the leachate according to the relations:

$$a = \frac{Na\ out\ of\ starting\ fluid}{Na\ in\ perovskite\ +\ Na\ in\ calzirtite}$$

$$total\ zirconolite\ replaced = a \cdot M_{zirconolite}$$

$$\boldsymbol{C}_{elements\ in\ fluid} = \boldsymbol{C}_{zirconolite} + \boldsymbol{C}_{NaOH} - \boldsymbol{C}_{perovskite} - \boldsymbol{C}_{calcirtite}$$

Results

First, the calculations showed that roughly 8–10 wt% of the total starting zirconolite is replaced by the secondary phases. Additionally the x and y values revealed that about 10 times more moles perovskite crystallized in comparison to calzirtite. The relation in wt% is about 5 parts of perovskite to 3 calzirtite. These results may be supported from the surface analyses by ESEM and the cross sections analyzed by EPMA. These estimates of corrosion showed that the zirconolite cylinder used in the experiment is corroded to a depth of 20–40 µm, which results in approximately 10 vol% of the total starting material being affected.

Secondly, the result for the concentration of Ca in the fluid gave a slightly negative value. This might be due to the determined fluid composition, which comprises a large source of error as described in chapter 4.4 or any other unknown processes in the system. However, this result means that the system is either undersaturated with respect to Ca or oversaturated with respect to Ti. Therefore two different solutions of the problem were proposed:

1) If all Ca, Zr and Nd is incorporated into the secondary phases, Ti is in excess, which was not determined by ICP-MS. Therefore it is possible that a third secondary phase is present but it was not observed. This phase could be a pure titanate (e.g., brookite) or any alumino-titanate phase.
2) If the system is undersaturated in Ca, some additional Ca could be leached out of the abundantly present primary zirconolite and then be incorporated into the secondary phases.

Unless other results are available to support either one of the two possibilities, both solutions are possible and no results may be proposed.

Interestingly, only 85% of the oxygens released from zirconolite and NaOH were used for the crystallization of perovskite and calzirtite. The excess oxygen is presumably used to hydrate the released Al to $Al(OH)_3^0$ or any other unknown species at present time.

4.9 Corrosion of U-doped Zirconolite

4.9.1 Introduction

Two additional starting materials were used to obtain some information on the behavior of U-doped zirconolite. One of these zirconolites was doped only with U; the other one contained Ce and Hf as well. Unfortunately these zirconolites were not single phase starting materials (figure 4.9.1) as already described in chapter 3.2.5. Results from alteration experiments with two-phase ceramic waste forms do not necessarily reveal data on the behavior of one single phase. For instance the additionally present phase prior the experiment may affect the chemical composition of the solution due to its dissolution and thereby change chemical parameters. Therefore the obtained results may not be compared directly to the results obtained with the experiments carried out with the Nd- and Gd–Ce–Hf-doped zirconolite samples.

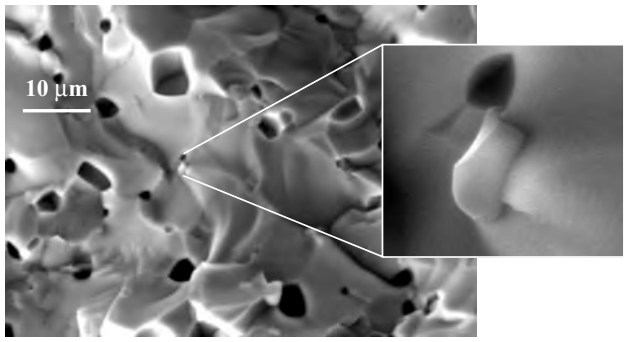

Figure 4.9.1: *Secondary electron images (by ESEM in low vacuum and wet mode) of untreated U-doped zirconolite showing inclusions of $ZrTiO_4$ crystals. This sample, thus, is not single phase and therefore may not be used for more detailed predictions for the stability of pure U-doped zirconolite.*

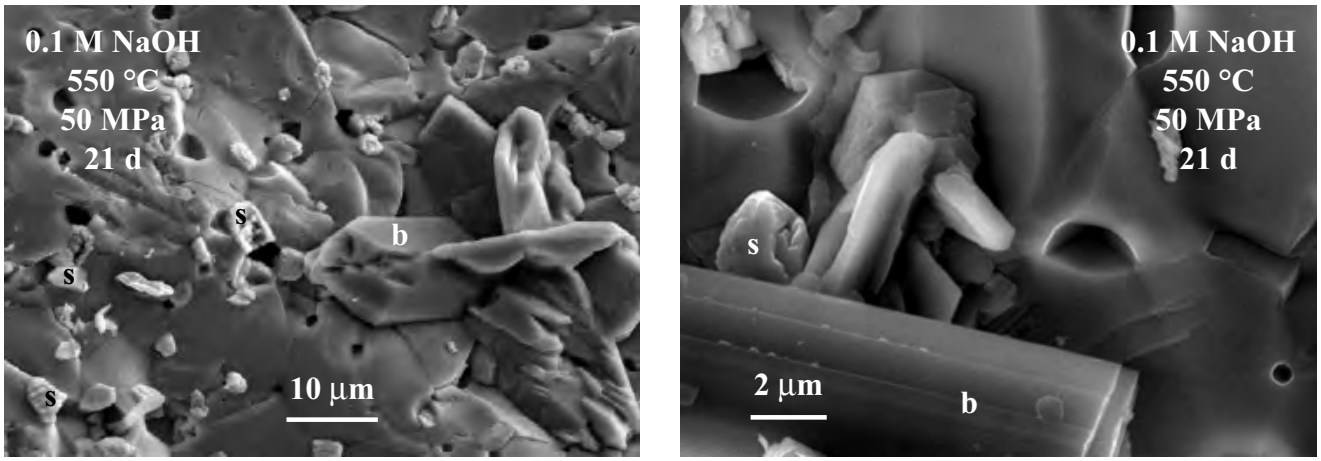

Figure 4.9.2: *Secondary electron images (by ESEM in low vacuum and wet mode) of U-doped zirconolite after the experiment in NaOH forming secondary Ti and U rich crystals (possibly brannerite (b)). The second primary phase $ZrTiO_4$ (s) is better visible after the experiment due to the corrosion of the boundary to zirconolite.*

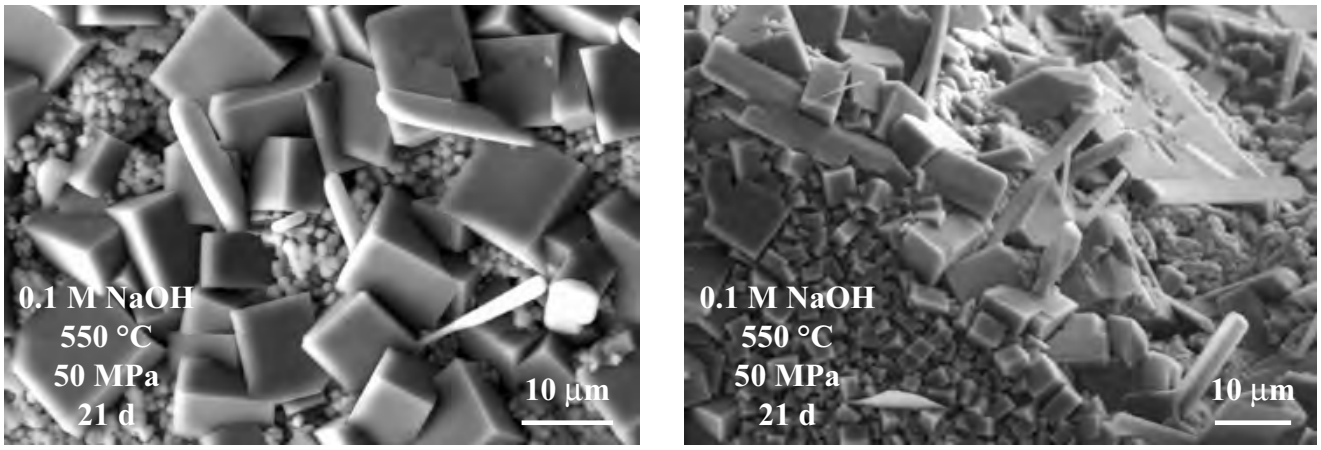

Figure 4.9.3: *Secondary electron images (by ESEM in low vacuum and wet mode) of U–Ce–Hf-doped zirconolite after the experiment in NaOH forming secondary perovskite (cubes), calzirtite (substrate grains), and a third at present unknown phase (blades).*

4.9.2 Pure U-doped Zirconolite

Experiments with a U-doped zirconolite as starting material were carried out at 550 °C and 50 MPa in 0.1 M NaOH for 21 days. The behavior of REE-doped single-phase zirconolite under similar conditions is quite well known (chapter 4.3.3). Figure 4.9.2 (left) shows that the surface of zirconolite and of the second primary phase ($ZrTiO_4$) are both affected by corrosion features. The boundary between them is strongly corroded which helps to distinguish the two primary phases. Additionally secondary phases with short, oblate prismatic stems as morphology were observed (figure 4.9.2). They are frequently orthogonal aggregated and the ESEM/EDX spectra revealed a high Ti and a minor U content.

This result is quite different from the results obtained during similar experiments carried out with Nd- and Gd–Ce–Hf-doped zirconolite samples. The surface seems to be less corroded and much less product phases are present on it after the experiment. As already mentioned, this may be due to the presence of an additional primary phase influencing the fluid composition. On the other hand, the stability field of each phase is dependent on its composition. Therefore, these results indicate that U-doped zirconolite is possibly more resistant than REE-doped zirconolite and that the secondary phases perovskite and calzirtite (present after experiments with REE-doped zirconolite) are only thermodynamically stable with excess REEs under these experimental conditions.

4.9.3 U- and REE-doped Zirconolite

These additional experiments with a U- and REE-doped zirconolite as starting material were planned to provide data as a link between the experiments with pure REE- (chapter 4.3.3) and pure U-doped samples (chapter 4.9.2). The experiments were conducted at the same conditions (550 °C, 50 MPa, 0.1 M NaOH, 21 days). The results revealed extensive corrosion and associated crystallization of three different secondary phases (figure 4.9.3). Two of these phases were determined as perovskite (large cubes) and calzirtite (small grains), both very similar in appearance to those present after experiments with purely REE-doped zirconolite. Compared to the results of experiments with purely U-doped zirconolite, the formation of perovskite and calzirtite seems to be bound to the presence of REEs. Further AEM investigations are needed to obtain information on the U-content of these two secondary phases. However, the presence of U seems to stimulate the formation of a third secondary phase, whose structure and composition are unknown at the present time. It forms long (30 µm) prismatic blades and the ESEM/EDX spectra revealed a high U and Ti content.

Investigations by Raman-spectroscopy on chemically related natural phases (betafite, brannerite, davidite, euxenite, malakon, microlite, monazite, pitchblende, samarskite, thorutite, tazheranite, zirkelite) gave no results because these minerals all were fully metamict due to the radioactive decay of incorporated elements. Morphological comparison with expected phases like brannerite (Gräser & Guggenheim, 1990) or senaite (Oberholzer et al., 1997) did not give any clues either. Therefore further investigations by TEM are required.

5 DISCUSSION

Because zirconolite based waste forms are designed for the disposal in nature, this chapter tries to compare the experimental results described in chapter 4 with similarities described by various authors in natural systems. Specific interest is given on the phase stabilities and different reactions as well as on the mobilization of the elements primarily present in zirconolite.

5.1 Quench-phases or Phase Reactions

5.1.1 Introduction

Quench crystals are typical cooling products of experiments carried out at high temperatures and pressures. They form during rapid cooling from the experimental temperature in a liquid or gaseous environment, because decreasing the temperature leads to a decreasing solubility of many dissolved species and thereby to an oversaturation. Typical quench phases crystallize in shapes similar to snow crystals and form skeletal bodies or, sometimes, rims on preexisting crystals but with different composition. Such crystals have not been observed after any experiment carried out during this entire study.

5.1.2 Experiments in NaOH

The observed crystals after the experiments in NaOH are idiomorphic with well developed crystal faces. Their size was usually larger than 3 µm, and sometimes reached 30 µm. One of the observed secondary perovskites showed sector zoning (see chapter 4.6). This is a crystal growth phenomenon resulting from growth rates that are different for different crystal faces. This would be very unusual to be achieved during a quench process, which lasts only a few seconds. Typical quench phases form at temperatures far below the temperature of dissolution. An experimental series with temperature steps of only 12 °C showed that the secondary phases perovskite and calzirtite formed constantly from 500 up to 700 °C but never formed below 488 °C (chapter 4.6). All these observations are very unusual for quench phases if not impossible (M. Kunz, personal communication).

During some experiments, secondary crystals were also found on the inner wall of the gold capsule (figure 5.1.1). This in general would be typical for quench phases, but these phases on the capsule wall were only found at one specific site, most probably where the zirconolite cylinder was in touch with the gold capsule during the experiment. Quench phases would distribute homogeneously on all inner walls of the capsule as well as on the zirconolite surface. Additionally, different numbers of secondary phases were found on the polished and unpolished surfaces of each zirconolite sample. While the polished surface mostly was completely covered by secondary phases, the unpolished (broken) crystal surface showed much less overgrowth. This indicates that nucleation of secondary phases is easier achieved on mechanically treated surfaces.

Additionally a series of experiments was designed to obtain results on different cooling techniques. They all were conducted at 550 °C in 0.1 M NaOH at 50 MPa. The first series was pressure quenched. The confining pressure was released suddenly at 550 °C making the capsule burst and the fluid disappear within a fraction of a second. Secondly, the experiment was cooled under pressure within several seconds by plunging the pressure vessel into cold water. The third series was cooled by a defined cooling rate of 10 °C per 15 minutes. These were the observations:

- All three methods yielded perovskite with the same shape, size, and morphology.
- Calzirtite shows slightly larger crystals after the defined slow cooling than after fast cooling or the pressure release (figure 5.1.2), but was present after all three experiments.
- No secondary phases were observed around the slit in the capsule, where the fluid disappeared during the sudden pressure release. They were only observed on the zirconolite surface.
- Calzirtite never nucleated on perovskite as would be expected for a quench-phase.
- Most probably calzirtite nucleates as a reaction product and during slow cooling; most elements present in the fluid grow as a second generation on the surface leading to larger calzirtite crystals.

In addition, perovskite and calzirtite did not incorporate any Al, which was released from the dissolved zirconolite. The chemistry of the quench-phases in general is very similar to the chemical composition of the fluid during the experiment, but this was not observed. Both secondary phases could easily incorporate Al into their crystal lattice (see chapter 2).

5.1.3 *Experiments in HCl*

The experiments in HCl produced some very fine-grained phases (< 1 µm), which could not be identified because of their size. Rutile and anatase were the only phases securely determined as slightly larger crystals (1–4 µm). But no detailed information on their structure and composition was obtained (see chapter 4.3.2).

The secondary rutile and anatase are present as idiomorphic crystals with a morphology similar to their natural occurrence. They were never observed as cavernous or skeletal crystals typical for quench phases. Additionally, no secondary phases were observed to crystallize on the inner walls of the capsule as would be expected for quench phases. Compared to the secondary phases formed during the experiments in NaOH, where these phases replace zirconolite, rutile and anatase crystallized only on the zirconolite surface as product of fluid supersaturation (see chapter 4.3). No detailed analysis of the morphology of the small and undetermined phases was made. Therefore, no statement about possible crystallization processes (e.g., quenching) can be made.

5.1.4 *Conclusions*

Following the described analyses and observations, the secondary phases perovskite and calzirtite that appeared during the experiments in NaOH rich fluids are almost certainly not quench-phases, but rather precipitates or reaction products at the attended experimental conditions. During slow cooling some additional overgrowth of the calzirtite (and perovskite?) may occur.

For the experiments in HCl, no clues could be obtained.

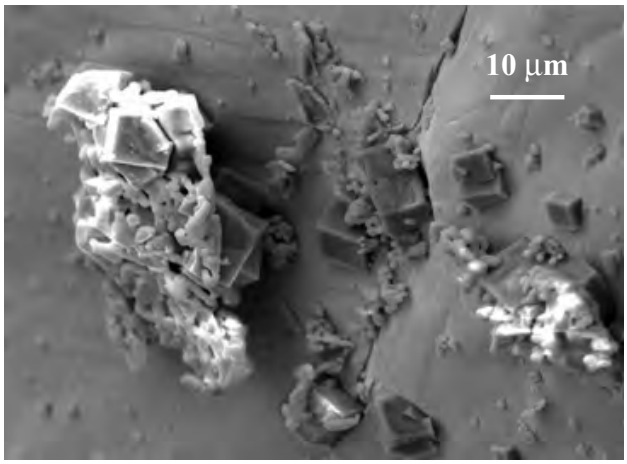

Figure 5.1.1: *Secondary electron images (by ESEM in low vacuum and wet mode) of the internal side of the gold capsule after the experiment showing the secondary phase perovskite near a crack on the wall.*

However, further investigations are required to understand more properly how these product phases crystallize, because this is very important for the applications in radioactive waste disposal (see also chapter 6.3).

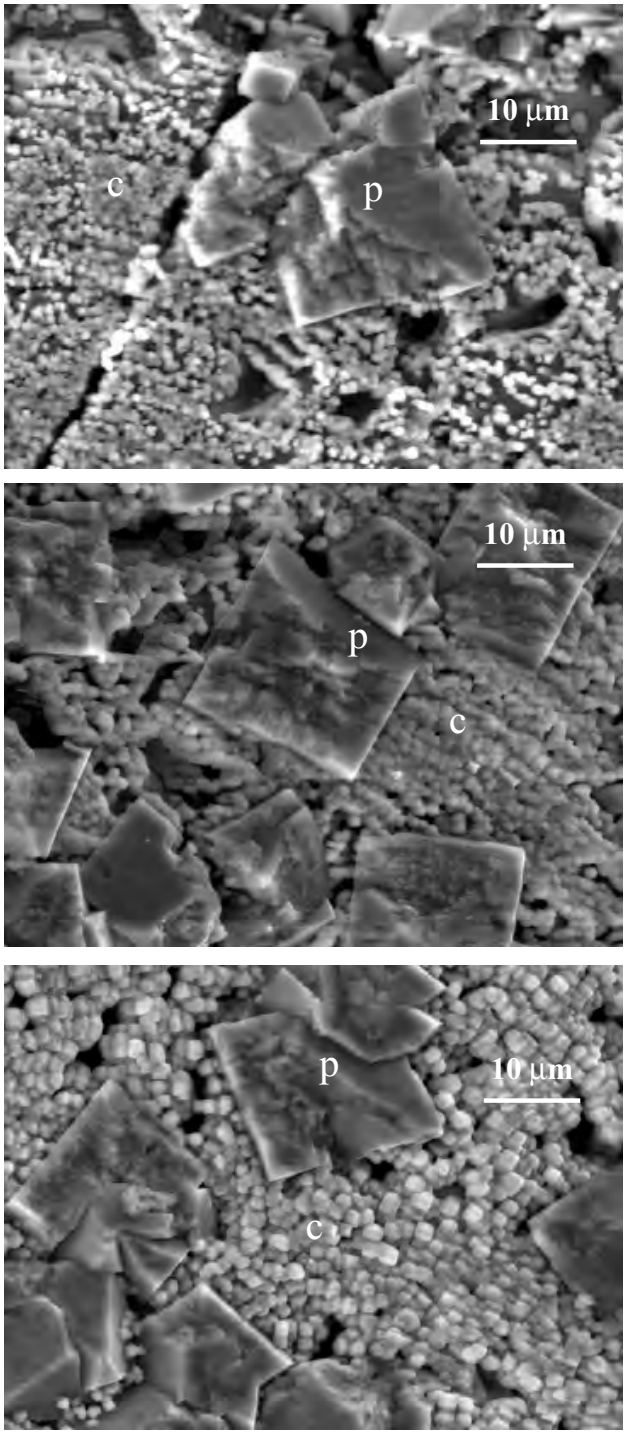

Figure 5.1.2: *Secondary electron images (by ESEM in low vacuum and wet mode) of zirconolite surface showing perovskite (p) and calzirtite (c) after an experiment in 0.1 M NaOH at 550 °C and 50 MPa and quenched by sudden pressure release (top), quenched by fast water cooling (middle) and cooled by controlled slow temperature decrease (bottom).*

5.2 Stability Fields of Experimental Phases

5.2.1 Introduction

The stability and composition of oxides during experimental investigations depends on the external parameters pressure and temperature, the composition of the fluid phase, and on the fugacity of species in the fluid such as, e.g. oxygen fugacity (fO_2; Frost, 1991; Luth, 1989). The fO_2 during the experiments is intrinsically determined by the apparatus and may be controlled by an external buffer. In our case it is controlled by the bombs, which are made of Ni based alloys. Specific experiments conducted at 500 °C and 50 MPa with Fe_2O_3/Fe_3O_4 (HM) and Ni/NiO (NNO) revealed that the intrinsic fO_2 during our experiments is between these two buffers (Huebner, 1971; figure 5.2.1). Therefore our experimental conditions are comparable to experiments carried out with an external NNO-buffer as lower limit and a HM-buffer as upper limit. No additional external buffers were used for our experiments due to the size of the internal capsule, which had already the dimensions of the bore in the pressure vessel (compare Mukhopadhyay & Holdaway, 1994). Smaller inner capsules would have made fluid analysis impossible, which would have resulted in the loss of important data.

The fO_2 present in the capsule during an experiment also determines the valence-state of polyvalent elements. For example the valence-state of Ce (trivalent or tetravalent) is unknown, but may be estimated by its oxidation and reduction potential. The reaction can be written as a reduction half reaction:

$$CeO_2 + 4\ H^+ + e^- = Ce^{3+} + 2\ H_2O$$

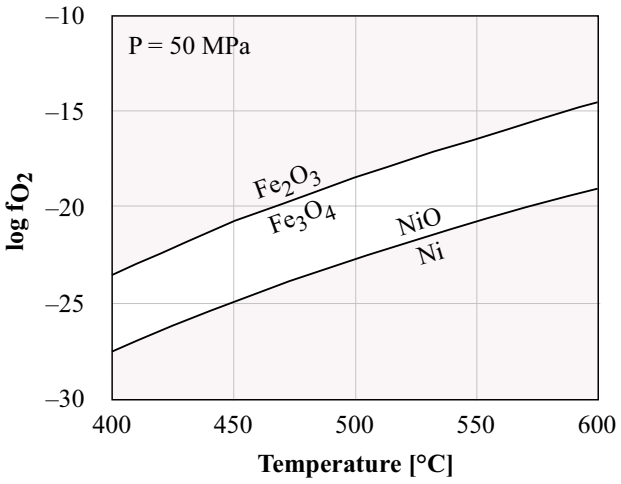

Figure 5.2.1: *Plot of calculated reaction boundary for hematite–magnetite and Ni–NiO buffer reaction at 50 MPa in terms of temperature and oxygen fugacity (fO_2). Experiments showed that the apparatus used for the experiments controls the oxygen fugacity between these two buffer reactions (data from Huebner, 1971).*

The valence state of Ce in zirconolite, in solution and in the secondary phases is important because Ce is used as an analogue element for Pu due to their similar ionic size at the same valence states. The reaction above shows that the Ce activity is largely controlled by pH rather than Eh (de Baar et al., 1988). At a low pH, Ce is present in a trivalent state in solution (Brookins, 1988; figure 5.2.2). The author states that at a neutral to basic pH, any available Ce^{3+} will be oxidized and removed from solution as CeO_2 or any other solid oxide. Ce may also be incorporated into carbonate phases, where it is present as tetravalent or trivalent ion (Brookins, 1989). The authors interpretation, that dissolved Ce^{4+} is negligible, is supported by figure 5.2.2. Other authors propose that at a pH higher than 8, the Ce^{4+} species may become dominant under oxidizing conditions but due to lack of data, this hypothesis may not be confirmed (de Baar et al., 1988). Unfortunately, there are presently insufficient data to evaluate the impact of temperature on the stability of Ce^{4+}. But from studies on divalent and trivalent REE (Wood, 1990b) and from comparison with figure 5.2.1 it is assumed that the importance of Ce^{4+} should decrease with increasing temperature, but increase with increasing pressure. For the results of this study, it is assumed that temperature and pressure nullify each other and therefore are less important compared to pH.

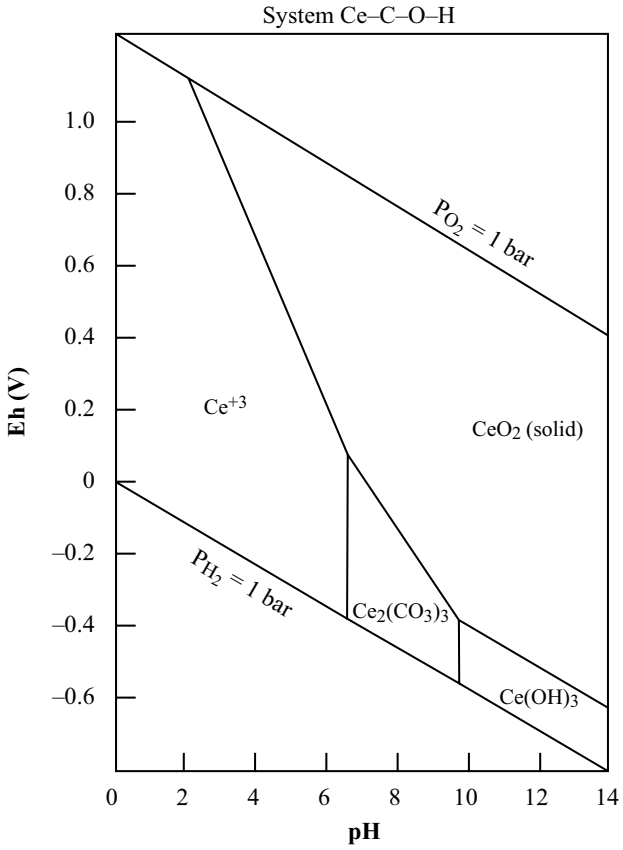

Figure 5.2.2: *Eh–pH diagram for part of the system Ce–C–O–H at 25 °C and 0.1 MPa. Assumed activities for dissolved species are: $Ce = 10^{-8}–10^{-6}$, $C = 10^{-3}$ (after Brookins, 1988).*

Therefore it is expected that Ce is trivalent during our experiments in HCl, but in NaOH it is possible that Ce is tetravalent. These theoretical deliberations are supported by the behavior of Ce in perovskite, where it interacts with Zr^{4+} and thereby causes sector zoning (chapter 4.6).

The following part describes details on the stability of the experimentally observed phases.

5.2.2 Zirconolite

Introduction

The detailed occurrence and petrographic behavior of zirconolite has been described in chapter 2.2. The mineral occurs in a wide range of different host rocks as accessory phase (Gieré et al., 1998; Williams & Gieré, 1996) and is described as product of intense metasomatic alteration of primary pyroxenites (Vlasov, 1966). Its formation is strongly dependent on the chemical composition of the melt, metasomatic fluid or host rock. It generally forms in SiO_2-poor rocks (mostly in the absence of quartz). Exceptionally, in alkaline hydrothermal fluids, zirconolite precipitates in a SiO_2-richer environment together with zircon (Guimarães, 1948). Zirconolite was observed in association with baddeleyite and pyrochlore even though baddeleyite is only stable in SiO_2-undersaturated environments (Vlasov, 1966), but mostly due to progressing reactions (Bulakh et al., 1999). Carbonatite is the most common host rock for this mineral.

Results

Zirconolite, present as starting material, showed a high stability during most hydrothermal experiments (details described in chapter 4.2). Strong corrosion, or instability, was restricted to high temperatures (above ~450 °C) and was only observed at very low and high pH in combination with strong ligands (Cl^-, OH^-) or complexing agent (Na^+) indicating ability to mobilize Ti, Zr and REEs. Rapid replacement was only observed at a high pH in a Na-rich fluid. This observation may be compared to the instability of pyrochlore in alkaline fluids (Jago & Gittins, 1993) where it is replaced by a perovskite type phase. Zirconolite is described as a pyrochlore-derived polytypoid with close structural relationship to pyrochlore (Ondina Figueiredo et al., 1992). The present experiments emphasize now also their similar chemical behavior.

5.2.3 Perovskite

Introduction

Details on perovskite are given in chapter 2.3. Perovskite is known from nature as one of the most important mineral hosts for REEs, which occur in concentrations ranging from trace to major element status (Mitchell, 1996). The chemical composition of the secondary perovskite grown in our experiments is very uncommon. There is a relatively high Na content compared to the REE content (usually trivalent REEs are charge balanced by monovalent Na on the Ca site) and some Zr located on the Ca site (chapter 4.6). Therefore this section is restricted to a discussion of Na-, REE- and/or Zr-rich perovskites as determined in this study.

Discussion

Natural occurrences of high Na contents (6–9 wt%) were described in high-pressure perovskites from Kola Peninsula and named as loparite (Haggerty, 1987). Loparite is a type of dysanalyte (not the IMA approved niobian variety of perovskite) which is particularly rich in REEs (Deer et al., 1966) and is the only perovskite strictly qualified as a distinct rare earth mineral (Mitchell, 1996). Loparite is also reported in carbonatite–ultramafic rock complexes from the Afrikanda complex (Mitchell, 1996), Schryburt Lake (Platt, 1994), and the Lovozero alkaline complex (Mitchell & Chakhmouradian, 1996) in association with a low SiO_2-activity environment.

Only a few perovskite names are IMA approved and many names are obsolete (e.g., dysanalyte, knopite) even if they are still used by various authors. However, the complex compositional variation in natural perovskites calls for prefixes, added to the basic name to reflect the dominant cation present (Mitchell, 1996). Following this procedure, the secondary products of our experiments are named as calcian zirconian loparite and sodian zirconian perovskite. The proper term for these REE minerals would be perovskite-(Nd) or loparite-(Ce) but does not provide any details on its composition. Another classification scheme is based on the valence of the A cations (Nickel & McAdam, 1963).

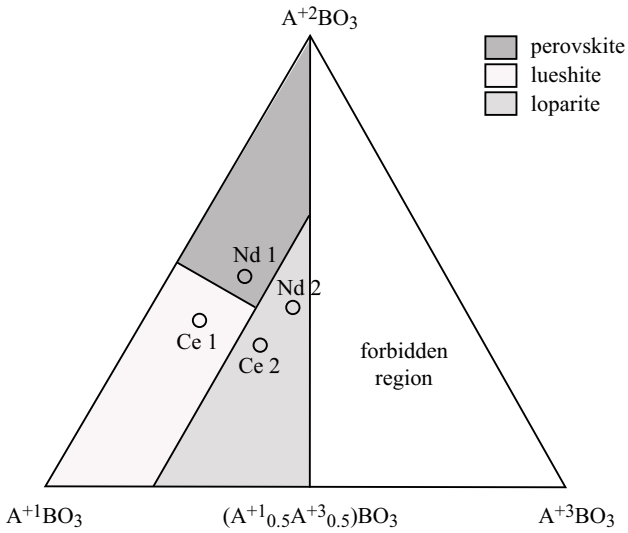

Figure 5.2.3: *Classification of perovskite group phases based on the valence of the A cation as monovalent (Na), divalent (Ca) or trivalent (REE). Ce1 (Gd–Ce–Hf-doped system) and Nd1 (Nd-doped system) consider only Na, Ca and REE, whereas Ce2 and Nd2 include Zr as well.*

According to this classification, phases of the perovskite group are classified as lueshite, perovskite and loparite, respectively, depending on whether the A cation is monovalent (Na), divalent (Ca) or trivalent (REE). For our composition, first only Na, Ca and REE were considered, and in a second stage Zr was included with the REEs (figure 5.2.3). The result ratified the earlier conclusion that the secondary phases have a composition most comparable to loparite. The mineral name loparite has been IMA-approved since 1987.

The only proven occurrence of Zr rich perovskite (2.8–3.3 wt%) has been described from the Polino carbonatite (Lupini et al., 1992). No good analysis is available on uhligit, regarded as a perovskite in which Ti has been replaced by Zr and Al (~22 wt% ZrO_2; Hauser, 1909). But Vlasov (1966) considered that these analyses may be in error.

The hydrothermally grown perovskite revealed that Ce was incorporated as trivalent and tetravalent ion (chapter 4.6.3). In perovskite, the valence of Ce is essentially determined by its chemical composition, and thus Ce may be present in both valence states on the A-site (Begg et al., 1998). This ability to substitute Ce^{4+} on the A-site indicates that Zr^{4+} may be accommodated on the A-site as well (similar ionic size). The authors also described the high ability of perovskite for its «self-charge-compensation».

Results

The experimental stability of our perovskite-type is limited to temperatures above 500 °C and a pressure range of 50–200 MPa. It only grew in solutions with a high pH and Na concentration (0.1 M) revealing its stability in such fluids, similar to the lueshite described by Jago & Gittins (1993). However, perovskite (loparite) showed its high ability for the incorporation of REEs and in combination with its stability at high temperatures may be a proper waste form for HLW in deep boreholes at elevated temperatures.

5.2.4 Calzirtite

Introduction

The generic description of calzirtite is given in chapter 2.4. It has rarely been reported in natural rocks and only limited information on its specific behavior in various environments is available. Up to 30 different mineral phases are found in the rocks, where calzirtite is formed. Of these, magnetite, hematite, ilmenite and goethite are often major components (Van der Veen, 1965). Besides other essential data, Vlasov (1966) indicated that calzirtite occurs mostly with loparite and apatite. In the Guly massif, it is associated with baddeleyite and anatase, and forms intergrowths with loparite (Bulakh et al., 1967). Its natural intergrowths with perovskite are particularly characteristic (Zhabin et al., 1962). Despite the fact that calzirtite is chemically related to and often coexists with zirconolite, it is much less capable of incorporating actinides and REEs into its crystal structure (Bellatreccia et al., 1999; Zdorik et al., 1961). Calzirtite is easily dissolved on heating in concentrated acids and therefore does not likely occur in environments with low pH groundwater (Vlasov, 1966; Zdorik et al., 1961).

Results

The calzirtite phase grown during our experiments, most probably only crystallized at temperatures above 500 °C and at pressures around 50 MPa in a strongly basic and Na rich environment. It was always associated or even intergrown with perovskite, similar to natural occurrences. Its chemical composition supported the perceptions from natural crystals, revealing a lower capability for the incorporation of REEs into its crystal structure than zirconolite and also perovskite. Therefore it may be assumed, that calzirtite would not provide an optimal host phase for HLW compared to the previously mentioned phases, i.e. less good than perovskite and zirconolite.

5.2.5 Baddeleyite

Introduction

This mineral was discovered in the 1890's by Iozeph Baddeley in Ceylon placers. Details on baddeleyite as a rare mineral were initially described from the Kovdor carbonatite complex by Bubovna et al. (1973), where it is often intergrown with zirconolite and pyrochlore. During the initial stage of carbonatite formation, it is a high-temperature mineral crystallizing together with pyrochlore and apatite (Vlasov, 1966). The same author describes baddeleyite as a highly stable mineral, which does not give rise to any new formations. It is also reported that among all Zr minerals, baddeleyite has the least chemical diversity (Bulakh et al., 1999). In alkaline hydrothermal fluids, baddeleyite only precipitates in a SiO_2-undersaturated environment (Guimarães, 1948). Figure 5.3.3 shows the calculated stability dependent on μSiO_2. Additionally, it is often present as secondary phase in kimberlites as microcrystalline to cryptocrystalline coating on zircon. There it is assumed to result from desilification of zircon (Haggerty, 1987). In those rocks, Raber & Haggerty (1979) describe the reaction between ilmenite and zircon yielding Ti-baddeleyite, diopside, calcite and zirconolite. The occurrence of baddeleyite in metamorphic siliceous dolomites is reported from Ferry (1996) and the following prograde reaction was mapped:

zircon + 2 dolomite <=> baddeleyite + forsterite + 2 calcite + 2 CO_2.

Results

The experimental formation of baddeleyite revealed its formation and stability only above a certain temperature (~500 °C) and pressure (~200 MPa) in a Na-rich, high pH fluid. Similar to its natural occurrence, where the conditions of formation are high temperature and adequate

pressure, it grows at higher experimental pressure than calzirtite even though these conditions are not comparable to those of kimberlites.

5.2.6 *Rutile / Anatase*

Introduction

During the experiments in HCl, only rutile and anatase were determined as secondary phases on the surface of zirconolite. Therefore some details on their stability and conditions of formation are necessary.

TiO_2 is known in six different modifications (table 5.2.1). Until now, rutile is very common, anatase and brookite are more or less frequently found in nature, whereas TiO_2 (B) is very rare in nature and always associated with anatase (Banfield et al., 1991); the two high pressure modifications are only known from experiments. The structure of all TiO_2-polymorphs are based on two edge sharing TiO_6 polyhedras, which are linked differently for each type by corner and/or edge sharing to form the three dimensional lattice. Details on all polymorphs are discussed by Vogler-Pazeller (1990). Natural and synthetic samples indicated transformation of anatase to brookite (Suwa et al., 1984) or rutile (Wagner, 1975) and brookite to rutile (Barblan et al., 1944), but no observations on the transformation of brookite to anatase, or rutile to anatase or brookite were made. These studies indicate that rutile seems to be the only stable phase under surface or upper crustal conditions. But because the transformation processes at surface temperatures (25 °C) are extremely slow all three phases may be observed.

TiO_2 polymorphs in the laboratory

Rutile, brookite and anatase may all be synthesized by various techniques and have a wide range of use in industry (e.g., pigment industry). A detailed overview is given by Vogler-Pazeller (1990), complemented with experiments by the author herself. They all may be synthesized from a Ti rich solution (e.g., $TiCl_4$, TiO_2-gel) with various additives. Rutile crystallizes at a wide pH range (0–11) and at temperatures between 360 and 1000 °C, but preferentially in an acidic environment. Brookite is synthesized only at basic conditions and in a temperature range (dependent on the additives) between 200 and 550 °C. Anatase as the low-temperature polymorph can easily be synthesized at room temperature and up to 600 °C at a pH between 3 and 11, but predominantly crystallizes in a neutral milieu. Temperature and pH for optimum crystallization are in general strongly dependent on the cations as additives. The formation of brookite is only possible if Na is present in the system (Vogler-Pazeller, 1990). The author also shows that the crystallization of anatase is enhanced by the presence of Na or K whereas the presence of HCl favors the formation of rutile. Another study revealed all three TiO_2 polymorphs as result from alteration of Synroc at ambient pressure and temperatures of 150 °C (Lumpkin et al., 1995).

Table 5.2.1: *TiO_2 modifications and their crystal structure sorted according to their density, which is directly related to their temperature and pressure stability.*

Formula	*Name*	*Crystal structure*
TiO_2 (B)		cubic, close-packed sphere packing with vacancies
TiO_2	anatase	tetragonal
TiO_2	brookite	orthorhombic
TiO_2	rutile	tetragonal
TiO_2 (II)		α-PbO_2, orthorhombic
TiO_2 (H)		hexagonal, related to fluorite-structure

Solubility experiments on natural rutile revealed that rutile is highly insoluble below 500 °C (Ried, 1994). Above that temperature its solubility is increasing, but strongly dependent on the fluid composition. The author showed also that HF-solutions have the largest impact on rutile.

Natural TiO_2 polymorphs

Rutile is the most common form of TiO_2 in nature, being the high-P–T polymorph due to its smallest unit cell volume compared to anatase and brookite. The natural, hydrothermal occurrence of all three polymorphs is strongly related to the presence of joints and Ti rich host rocks. From their distribution in individual Alpine lithologies, a minimum hydrothermal formation temperature of 230–270 °C and pressure of 170–200 MPa was proposed (Vogler-Pazeller, 1990). In natural systems, the three TiO_2 polymorphs never showed corrosion features and therefore show high resistance to hydrothermal fluids.

In nature, rutile crystallizes only below 400 °C exsolved in SiO_2 as fine needles. Anatase crystallizes below 400 °C at low pressures, and preferably in the presence of additional ions (e.g. K^+, PO_4^{3-}, SO_4^{2-}). It often coexists with calcite. Brookite crystallizes only at specific conditions at temperatures below 650 °C. Its presence is bound to the presence of Na except at high pressures (900 MPa). For comparison see table 5.2.2.

Discussion and results

After our experiments in diluted HCl, rutile and anatase were confirmed as secondary phases on the zirconolite surface (chapter 4.3.2). Their occurrence on the primary zirconolite surface as idiomorphic crystals revealed crystallization from the acidic solution and consumption of dissolved or leached elements.

Table 5.2.2: *TiO_2 modifications and their crystallization conditions (after Vogler-Pazeller, 1990).*

Name	*Temperature*	*Pressure*	*Ph*	*Additives*	*Eh*
TiO_2 (B)	< 500 °C	0.1 MPa			
anatase	< ~400 °C	< ~300 MPa	neutral acidic basic	none SO_4^{2-} K^+	oxidizing
brookite	< ~650 °C	< ~900 MPa	basic	Na^+ (none at 900 MPa)	oxidizing
rutile	< 1855 °C (melting)	> 0.1 MPa	acidic-neutral (T < 400 °C) acidic-basic (T > 400 °C)	none Cl^-, CO_3^{2-}	slightly reducing
TiO_2 (II)	< 600 °C	900–2300 MPa			
TiO_2 (H)		25'000 MPa			

The conditions established to synthesize rutile, brookite and anatase (table 5.2.2) compared to the conditions during the experiments revealed that only anatase and rutile are expected to crystallize. The formation of anatase is supported by observations that its crystallization is assisted by the presence of Al^{3+} (Deer et al., 1966), which was released from the dissolving zirconolite during our experiments. Compared to a natural system, the temperature and pressure of the experiments, combined with a low pH and high Cl content in the fluid are optimal conditions for the crystallization of rutile, but not as typical for anatase (generally a too high temperature and a too low pH). But the high Ca content expected in the fluid (from dissolved zirconolite) seems to stabilize the formation of anatase.

Under these conditions, the crystallization of brookite is impossible because of the low pH and the lack of Na in the system. Therefore only the two TiO_2 polymorphs rutile and anatase are present after the dissolution of zirconolite in HCl at a temperature above 250 and up to 700 °C.

5.3 Comparison of the Experimental Results with Natural Systems

5.3.1 Introduction

In this chapter, the results of the experimentally determined stability and growth conditions of zirconolite and of the secondary phases are compared to their natural occurrence and paragenesis. It will be distinguished between a basic Na-rich fluid and an acidic Cl-rich one. All experiments were conducted in a simple system compared to the complex natural systems. In particular, experiments were mostly conducted in the absence of CO_2 and SiO_2, which is very rare in natural systems.

Additionally, all experiments were conducted in a closed system compared to the mostly open system in nature. But if fluid migration in natural systems is slow, a steady state might be achieved, which is approximated by the experimental system. Dissolution–precipitation processes controlling the formation of secondary phases are strongly dependent on the fluid migration rate, because at a high fluid migration rate many dissolved elements are relocated before precipitation. But in an ideal repository, geologic environments with a low permeability and migration are desired. Therefore, the experimental results on the hydrothermal stability of zirconolite may be looked upon as an approximation to its natural behavior.

5.3.2 NaOH Environment (high pH)

Introduction

The following part is based on the experimental results in the system $CaO–ZrO_2–TiO_2–Al_2O_3–REE_2O_3–NaOH–H_2O$. After experiments at temperatures above 500 °C, pressures above 50 MPa and in a NaOH fluid (0.1 M), the observed phases are primary zirconolite and the secondary phases perovskite, calzirtite and, at higher pressure, baddeleyite. All of these phases, however, were never present simultaneously (see chapter 4.3.3).

As a rough estimation of the pH variation during the experiment, the pH was determined after experiment by pH-paper at 10–10.5. This is less than it was before the experiment (pH 13). This change in pH is a result of a combination of all reaction processes forming perovskite and calzirtite after the breakdown of zirconolite. These processes are charge balanced by H^+ diffusing from outside of the capsule into the fluid resulting in a change of the pH. This means that if Na^+ is incorporated into perovskite from the fluid, it might be replaced by H^+ from outside the capsule.

$$H_2O \Leftrightarrow H^+ + OH^-$$

Reactions

The phase diagram of the ternary system $CaO–TiO_2–ZrO_2$ in figure 3.2.5 (Coughanour et al., 1955) revealed no stability field for calzirtite at 1450 °C. At temperatures below 1350 °C, the appearance of calzirtite makes the

phase equilibrium more complicated within the three phase field baddeleyite – perovskite – zirconolite (figure 5.3.1-a; Rossell, 1992; Swenson et al., 1996). In the pure system, calzirtite lies on the pseudobinary join baddeleyite – perovskite (as shown in figure 5.3.1), revealing that it can not coexist with both phases at the same time (degenerated system). If zirconolite is present, the following three phase assemblages are possible: (1) zirconolite + perovskite + calzirtite, (2) zirconolite + perovskite + baddeleyite, (3) zirconolite + calzirtite + baddeleyite (see also Gieré et al., 1998). However, natural systems are more complex (impurities added to the system) and all four phases are reported to be present in some environments (Bulakh et al., 1967). Table 5.3.1 shows a list of the possible reactions in the system $CaO–TiO_2–ZrO_2–CO_2$ (Gieré et al., 1998). Our experiments were mostly conducted in a CO_2-free environment. Those with CO_2 but no other ligands present in the system, did not affect zirconolite and therefore, the system can be reduced to $CaO–TiO_2–ZrO_2$, where only the two first reactions are possible from pure single-phase zirconolite as starting composition.

In the pure system, these two possible breakdown reactions would additionally produce rutile (table 5.3.1, reactions 1 and 2), which, however, was not observed in the experiments. In the closed system of the experiments, the total elemental composition is given by the starting composition of zirconolite and the added fluid (0.1 M NaOH). The used starting materials are doped with various elements, which may be seen as impurities in the system. This changes the chemographic relationship and enlarges the stability field of each phase according to the total impurity uptake (solid solution). Moreover, as the determined composition of the product phases after the experiments is different from their ideal composition, these phases are located at a different position within the chemography (see figure 5.3.1-b). Perovskite and calzirtite are present as solid solutions and their ratio of Ti to Ca is ~2.4 and ~1.5, respectively (rather than 1.0 for the pure system). This shows that zirconolite lies on a tie-line between perovskite and calzirtite or, at a higher pressure, on a tie-line between perovskite and baddeleyite. Therefore, the formation of rutile is not required in the experimental system. This is supported by mass balance calculations (chapter 4.8.4), and also by the very small concentrations of the elements released by zirconolite in the fluid after the experiment.

As already shown in chapter 4.3.3, the experiments above 500 °C resulted in the formation of perovskite and calzirtite at 50 MPa, and perovskite and baddeleyite at 200 MPa, leading to the formulation of the two reactions:

zirconolite => perovskite + calzirtite + fluid (at 50 MPa)

zirconolite => perovskite + baddeleyite + fluid (at 200 MPa).

These results reveal that in a CO_2-free environment perovskite is stable over a wide range of pressure at a temperature of 500–700 °C. The appearance of calzirtite and baddeleyite seems to be depending on the pressure, and from these observations it appears that the reaction

calzirtite <=> 2 perovskite + 5 baddeleyite

can be formulated, as also seen on the pseudobinary join baddeleyite – perovskite (figure 5.3.1-a). These three reactions are schematically shown in figure 5.3.2 together with the Schreinemaker diagram for the pure system. According to the above discussed chemography, the Schreinemaker diagram is slightly different for the doped system of the conducted experiments. The stability fields of the phases with impurity elements will be enlarged and the system will not be degenerated anymore.

Table 5.3.1: *List of zirconolite consuming reactions (involving the breakdown of zirconolite) in the pure system $CaO–ZrO_2–TiO_2–CO_2$ (data from Gieré et al., 1998).*

Primary phases:	*Secondary phases:*
zirconolite	perovskite + baddeleyite + rutile
5 zirconolite	3 perovskite + calzirtite + 5 rutile
zirconolite + CO_2	calcite + baddeleyite + 2 rutile
5 zirconolite + 3 CO_2	3 calcite + calzirtite + 8 rutile
2 zirconolite + 3 baddeleyite	calzirtite + 2 rutile
5 zirconolite + 5 calcite	8 perovskite + calzirtite + 5 CO_2
zirconolite + calcite	2 perovskite + baddeleyite + CO_2
zirconolite + 4 baddeleyite + calcite	calzirtite + CO_2

Discussion and conclusions

The experiments in NaOH demonstrated that zirconolite is highly durable in aqueas media up to temperatures of ~500 °C. This is supported by the fact that the stability field of zirconolite in the presence of a CO_2-poor and H_2O-rich fluid expands to much lower temperatures (Allen & Ellis, 1996b). The authors showed that in a CO_2-free fluid, zirconolite must be stable down to room temperature and pressure as there is no other combination of phases without carbonate which is chemically equivalent to zirconolite in the system. However, no details may be given on the experimental phase stability, because at low temperatures the reaction rates are orders of magnitudes lower than at high temperatures. At temperatures above 500 °C, in a Na rich fluid (0.1 M NaOH) zirconolite breaks down to perovskite and calzirtite, at higher pressures to perovskite and baddeleyite, respectively (see also figure 5.3.2).

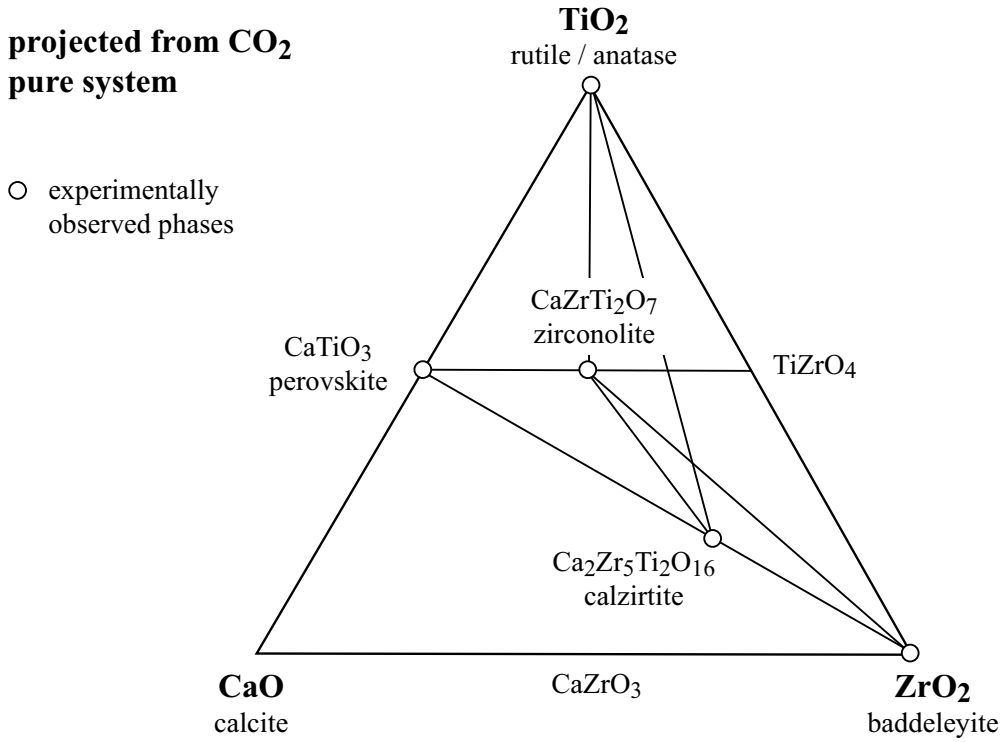

Figure 5.3.1-a: *Chemography (projected from CO_2) of the pure quaternary system CaO–TiO_2–ZrO_2–CO_2, showing the coexistence of the pure phases zirconolite, perovskite, calzirtite, baddeleyite, rutile, and anatase (all observed in the experimental runs). The pure system is degenerated because perovskite, calzirtite and baddeleyite are colinear.*

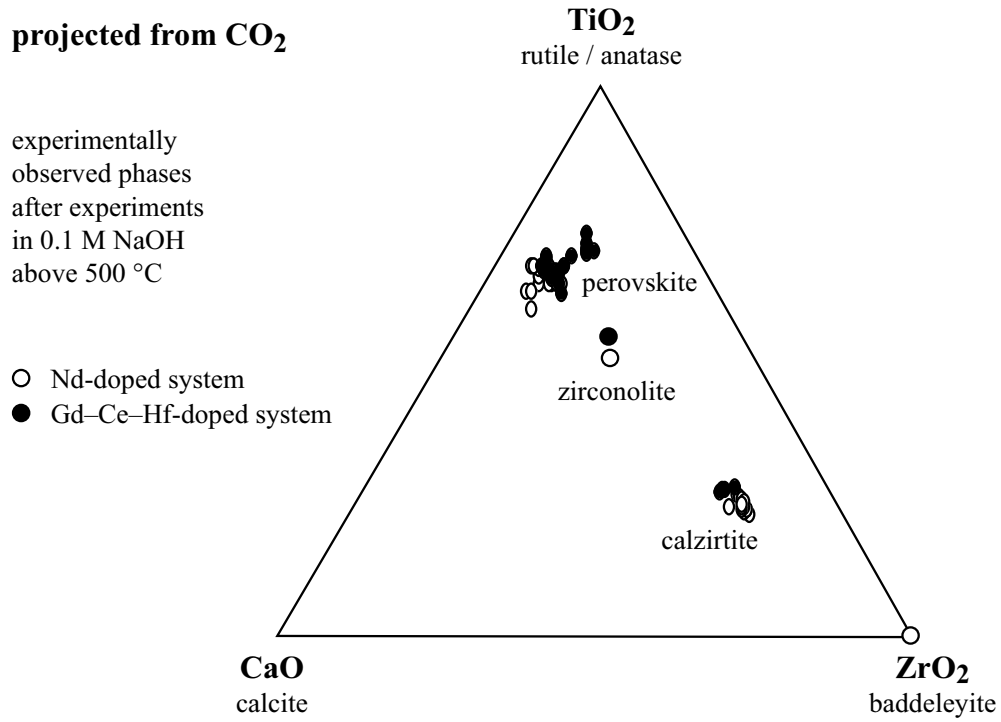

Figure 5.3.1-b: *Experimentally determined phase diagram (projected from CO_2) of the quaternary system CaO–TiO_2–ZrO_2–CO_2, showing the position of the phases zirconolite, perovskite, calzirtite, and baddeleyite as observed after the experiments in 0.1 M NaOH above 500 °C at different pressures. This chemography reveals that the four phases present are almost colinear.*

The natural system in the Kovdor carbonatites, Russiak, indicates that zirconolite crystallized later, and in some cases replaces, baddeleyite, perovskite, calzirtite and other Zr minerals (WILLIAMS, 1996). No explanations were given by the author, but this relationship could be due to decreasing temperatures, which would imply that zirconolite crystallizes at lower temperatures than perovskite, calzirtite and baddeleyite, similar to our experimental results in a pure H_2O system. But such sequences could also be due to changes in the oxygen fugacity or fluid composition (e.g., increase in X_{CO_2}, ligand activities; MITCHELL, 1996). A similar crystallization sequence was also established by BULAKH & NESTEROV (1996): perovskite – baddeleyite – calzirtite/zirkelite/zirconolite – pyrochlore. The authors describe calzirtite, zirkelite and zirconolite as mineralogical equivalents and that their formation depends principally on the chemical environment. A newer study gives the following sequences (BULAKH et al., 1999):

a) perovskite – baddeleyite – zirconolite
b) calzirtite – zirkelite – pyrochlore
c) baddeleyite – zirconolite – pyrochlore.

Our experimental results support the theoretical calculations of ALLEN & ELLIS (1996a) pointing out that perovskite and zirconolite may crystallize not only in high temperature igneous rocks, but also at lower temperatures (~500 °C) in metamorphosed rocks at shallow depths in the crust.

It has to be emphasized that the systems investigated are very alkaline, and that natural geologic systems are much more complex. This is shown by a study on the solubility and stability of natural pyrochlore in alkali carbonate liquids (JAGO & GITTINS, 1993). The authors show that in a water-bearing calcitic liquid (CO_2-rich) the solubility of pyrochlore is relatively high and decreases with increasing alkali content. In the $CaCO_3$ – Na_2CO_3 liquid, pyrochlore is soluble and unstable and reacts with the liquid to form lueshite or other minerals with the perovskite structure. But with approximately 1 wt% F present in the same liquid, pyrochlore precipitates rather than lueshite and any perovskite-type mineral existent would become unstable and react to form pyrochlore [$A_2B_2O_6(OH,F)$], where F is incorporated. JAGO & GITTINS (1993) conclude that in carbonatites, perovskite crystallizes earlier than pyrochlore, which is consistent with the results from BULAKH & NESTEROV (1996) and BULAKH et al. (1999).

In the $CaO–TiO_2–ZrO_2–CO_2$ system, the reaction

zirconolite + calcite <=> 2 perovskite + baddeleyite + CO_2

is predicted and lies close to the reaction of

calcite + quartz <=> wollastonite + CO_2,

which is proposed between 550 and 650 °C at low pressures (50–200 MPa; ALLEN & ELLIS, 1996a with the data of ROBIE et al., 1978). These theoretical calculations may be endorsed by the experiments carried out in the CO_2 free system in this study. In the presence of a CO_2-rich fluid phase at shallow crustal depths, perovskite is not thermodynamically stable below 550–600 °C (MITCHELL & CHAKHMOURADIAN, 1998b) because of the reaction:

CO_2 + perovskite <=> calcite + rutile,

but it is proposed that the stability of perovskite extends to lower temperatures with a lower CO_2 content (ALLEN & ELLIS, 1996a). These results are supported by our own phase stability calculations by VERTEX (CONNOLLY, 1990) in the system $CaO–TiO_2–SiO_2–H_2O–CO_2$ at temperatures between 500 and 600 °C and at pressures of 50 and 200 MPa. They were carried out using thermodynamic data from HOLLAND & POWELL (1998) except for perovskite from ROBIE et al. (1978). The system was saturated in fluid and $CaCO_3$ and the phases perovskite, rutile and titanite depend on the activities of CO_2 and SiO_2 (see figure 5.3.3). This plot indicates the breakdown of perovskite to rutile and calcite directly related to X_{CO_2}. With increasing μSiO_2, perovskite or rutile plus calcite, respectively, are replaced by titanite. The triple point (A1) is shifted to a lower μ_{SiO_2} but a higher X_{CO_2} with increasing temperature (A2), but to a higher μ_{SiO_2} and a lower X_{CO_2} with increasing pressure. In addition, the stability of baddeleyite (no thermodynamic data for calzirtite are available) related to μ_{SiO_2} was calculated and revealed that the transformation of baddeleyite to zircon is always at higher μ_{SiO_2} than the reaction from perovskite to titanite. Therefore, baddeleyite covers the entire stability field of perovskite.

5.3.3 HCl Environment (low pH)

Introduction

This part is based on the experimental results in the system $CaO–ZrO_2–TiO_2–Al_2O_3–REE_2O_3–HCl–H_2O$. As already shown in chapter 5.2.6, temperature and pressure of the experiments combined with a low pH and high Cl content in the fluid are optimal conditions for the crystallization of the observed rutile. Anatase was also observed despite experimental conditions that are not as typical for its crystallization (generally a too high temperature and a too low pH; VOGLER-PAZELLER, 1990), but the high Ca content (from zirconolite) might stabilize anatase similar to the results of VOGLER-PAZELLER (1990). From the author described as a metastable phase, anatase should therefore be replaced by rutile with time, but the transformation kinetics depends on temperature, pressure, and time and is slow below 600 °C. Therefore rutile is considered here as the stable secondary TiO_2 polymorph.

Results

As apparent in figure 5.3.1-a, the formation of only rutile and anatase from dissolved zirconolite may not be explained by the chemography in the pure system $CaO–ZrO_2–TiO_2$. Therefore possible explanations are: (1) Ti is

selectively leached out of the zirconolite structure to a high extent; (2) a TiO_2-layer crystallizes on the zirconolite surface and all other elements released from the dissolved zirconolite stay in solution (compare LUMPKIN et al., 1991); or (3) that the undetermined secondary phases consist of these elements (e.g., Zr). The first idea may be rejected, because leaching is restricted to the surface area, which is not enough for the amount of rutile and anatase observed. In addition, Ca mainly shows a higher ability to be leached out than Ti (RINGWOOD et al., 1988). The fluid data of these experiments do not support the second hypothesis (figure 4.4.1). Finally, (3) is the most probable explanation because undetermined secondary phases were observed. And, although Ca in the fluid could not be determined (see chapter 4.4), it is expected that Ca is present in solution at a high concentration (chapter 5.4.2). Therefore the undetermined secondary phases could contain Zr and possibly Ca, and to a minor extent Al, REE, and Ti as well. For acidic and Cl^- rich environments, stable phases for example could be baddeleyite (ZrO_2), corundum (Al_2O_3) and/or hibonite ($CaO \cdot 6\,Al_2O_3$) and possibly calzirtite. But those could not be confirmed because of their size (< 1 µm) and number. Especially the presence of baddeleyite or calzirtite would be interesting, because this could document their formation at lower pressure for a lower pH compared to the experiments in NaOH.

5.3.4 Conclusions

All experiments revealed, that zirconolite is very resistant to all tested fluids during the hydrothermal treatment up to temperatures ~250 °C. It is then highly resistant to deionized water up to temperatures of 550 °C.

The experiments with a CO_2-rich fluid did not show any enhanced dissolution of zirconolite compared to those in pure deionized water (chapter 4.3.4). The CO_2 content only decreases the activity of water, but as long as no other ions

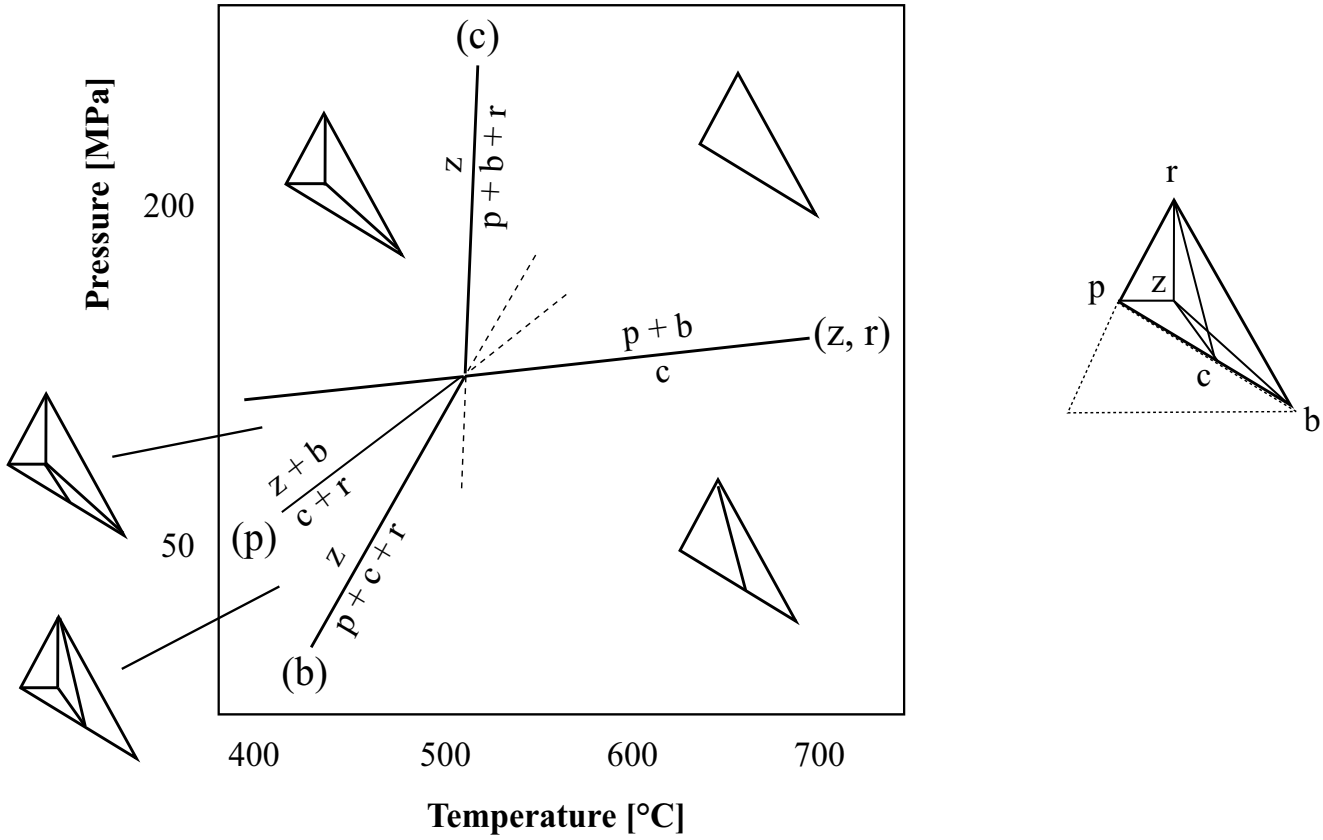

Figure 5.3.2: *Schreinemakers diagram for the five phase assemblage baddeleyite (b) – zirconolite (z) – perovskite (p) – calzirtite (c) – rutile (r) in the P–T-space. Estimated location of the three reactions inferred to take place in the experimental NaOH – H_2O system are drawn in thick lines. The following four reactions are possible:*

baddeleyite absent (b):	*zirconolite = perovskite + calzirtite + rutile*
calzirtite absent (c):	*zirconolite = perovskite + baddeleyite + rutile*
zirconolite and rutile absent (z, r):	*calzirtite = perovskite + baddeleyite*
perovskite absent (p):	*zirconolite + baddeleyite = calzirtite + rutile*

The last of these four reactions was not observed during the experiment because it lies in the zirconolite stability field and no other phases were present at these conditions.

are present in the fluid as possible ligands to mobilize the elements primarily present in zirconolite, the starting material remains uncorroded. Otherwise the following reaction is possible:

zirconolite + CO_2 <=> calcite + baddeleyite + 2 rutile

The experiments in pure H_2O–SiO_2 fluid had no influence either because the fluid remained pH neutral and rather non corrosive. Additional experiments with the combination of NaOH, SiO_2 and CO_2 as fluid would provide insights into the stability of the secondary phases. Thereby the phases calcite, zircon, titanite, wollastonite and quartz could also be present as replacement products of zirconolite (Allen & Ellis, 1996a, b).

In an alkali-rich fluid with a high pH, zirconolite is unstable at temperatures above 500 °C and is replaced by different secondary Ca–Zr–Ti-phases (perovskite, calzirtite, and baddeleyite). At low pH in strong HCl, TiO_2-polymorphs form at the expense of the starting mineral. Interestingly, at high temperatures in hydrothermal fluids (> 500 °C) perovskite converts directly to TiO_2 by the influence of acidic fluids and vice versa (Chakhmouradian & Mitchell, 1999a). A possible and explaining reaction would be:

$$CaTiO_3 + 2\,HCl <=> TiO_2 + CaCl_2 + H_2O.$$

Because $CaCl_2$ is highly soluble at a low pH, the reaction would strongly favor the product side of the reaction (e.g., TiO_2).

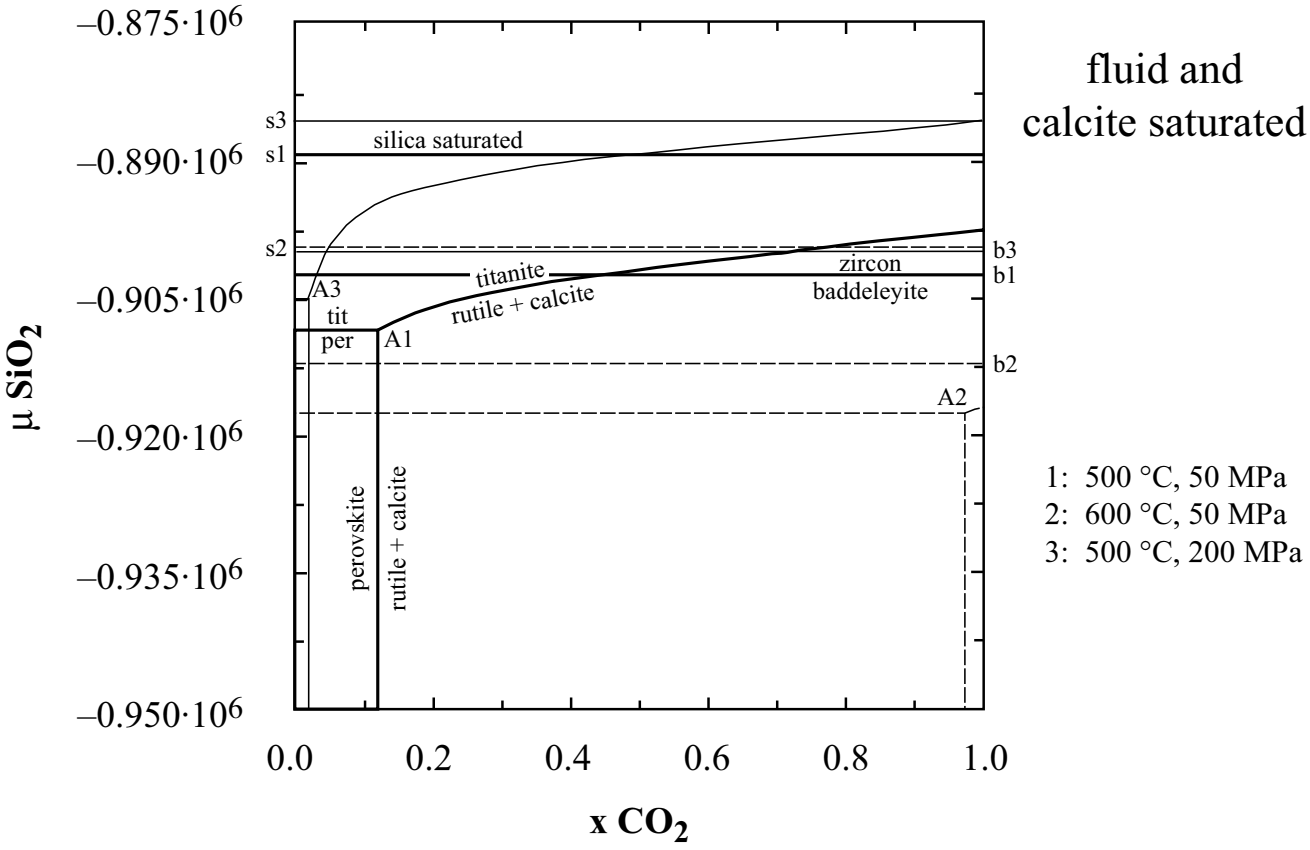

Figure 5.3.3: *Phase stability calculations by VERTEX (Connolly, 1990) in the system CaO–TiO_2–SiO_2–H_2O–CO_2 at fluid and calcite saturation for 500 °C and 50 MPa (1), for 600 °C and 50 MPa (2) and for 500 °C and 200 MPa (3) revealing the three stability fields of perovskite, rutile and titanite dependent on X_{CO_2} and μ_{SiO_2}. A1, A2 and A3 are the three different triple points for the three different physical conditions, respectively. The horizontal lines s1, s2, and s3 indicate silica saturation and the horizontal lines b1, b2, and b3 show the stability of baddeleyite (its replacement by zircon is directly related to μ_{SiO_2}). The used thermodynamic data are from Holland & Powell (1998), except for perovskite from Robie et al. (1978). The following list shows all reactions:*

perovskite + CO_2 = rutile + calcite
perovskite + SiO_2 = titanite
rutile + calcite + SiO_2 = titanite + CO_2
baddeleyite + SiO_2 = zircon

5.4 Mobilization and Solubility of Elements during the Experiments and their Implications on Natural Fluid Systems

5.4.1 Introduction

In this part, the hydrothermal mobility and solubility of compounds initially present in zirconolite is discussed. Generally, the ionic potential divides the chemical elements into three groups, based on the solubility of many of their compounds in water: (1) Elements whose most frequently observed ions have an ionic potential of < 3 (e.g., Ca^{2+}, Na^{+}) have highly soluble oxides and hydroxides. (2) those with an ionic potential between 3 and 12 (e.g., Ti^{4+}, Zr^{4+}) hydrolyze easily in solution but their hydroxides and oxides are sparingly soluble. (3) Elements whose most frequently present ions have an ionic potential of > 12 (e.g., P^{5+}) form soluble oxyacids in solution (BARTH, 1952). The second group, involving the high field strength elements (HFSE, e.g. Ti, Zr, Hf, REE), have long been considered to be immobile during metamorphism or alteration. But there is increasing evidence for transport by metamorphic fluids under specific geological conditions due to the formation of chemical complexes (e.g., GIERÉ, 1990a; RIED, 1994). Similar to a metasomatic environment, the elemental composition of the secondary phases (alteration products) reflects the mobility of these elements during the experiment in the fluid. Mobility involves the dissolution of solids, fluid transport and finally precipitation. In the metasomatic fluids close to the Bergell contact aureole it is assumed, that F^{-} and PO_4^{3-} are the likely ligands for complexing REE and HFSE (GIERÉ, 1986; GIERÉ, 1990b). These two ligands were also important in addition to K^{+} and Cl^{-} for the metasomatic fluid transport of the high-valence cations at the Adamello contact (GIERÉ, 1990a; GIERÉ, 1990b; GIERÉ & WILLIAMS, 1992; GIERÉ, 1996). With regard to our experiments, where zirconolite is replaced by perovskite and calzirtite in a NaOH rich fluid above 500 °C, it is interesting that large amounts of Ti, Zr and REE were found in Na rich and strongly basic (pH 12) groundwater from the Lovozero alkaline massif (KRAYNOV et al., 1969). This demonstrates that basic, alkalic fluids are capable to transport REE and HFSE.

The experiments in CO_2 or SiO_2 rich water showed no corrosion features and a highly resistant zirconolite. But it cannot be assumed that CO_2 and SiO_2 have no importance on the stability of zirconolite. It is only suggested that they have no influence on the corrosion strength of a fluid (no element mobilization due to the missing complexing agent) if no other ligands are present. Presumably CO_2 and SiO_2 would have a large effect on the development of the secondary phases. CO_2 can change the phase relations (e.g., reaction 3 in table 5.3.1), whereas SiO_2 adds the large field of silicate minerals to the system (e.g., figure 5.3.3). Experiments on natural zirconolite leached in silica saturated solutions at 150 °C (HELEAN et al., 1999) mainly resulted in the formation of cheralite (monazite group) and thorianite.

5.4.2 Ca

Ca^{2+} as an alkaline-earth cation is known as a highly mobile element in various natural fluids and is highly soluble over a wide range of pH. All alkaline-earth ions seem to hydrolyze more extensively than any other metal cations, but because of uncertainties in their interactions, their equilibrium constants can be determined only with limited accuracy (BAES & MESMER, 1976). As already mentioned (chapter 4.8.4), it was impossible to determine the concentration of Ca in the leachate after the experiments. For the experiments with HCl, it is assumed, that all Ca released from zirconolite goes into solution possibly as Ca^{2+}. The experiments in NaOH formed two Ca-rich phases, perovskite and calzirtite. Presumably most Ca released from the primary zirconolite is incorporated into the secondary phases (chapter 4.8.4). This shows a high mobilization of Ca in the NaOH rich system above 500 °C.

5.4.3 Ti

The solubility and mobility of Ti is very low at metamorphic conditions in aqueous fluids. At ambient conditions (25 °C, 0.1 MPa), Ti is very insoluble at a pH above 3 and forms $Ti(OH)_4$ complexes (NABIVANETS & LUKACHINA, 1964). At a pH below 3 together with Cl^{-} the formation of a hydroxyl complex, either TiO^{2+} or $Ti(OH)_2^{2+}$ has been reported (NABIVANETS & KUDRITSKAYA, 1967). At high pH, its increasing solubility (forming complex with OH^{-}) was experimentally demonstrated (NABIVANETS & OMELCHENKO, 1986). Solubility experiments by RIED (1994) revealed that rutile is more soluble in an acidic environment than in basic fluids, and barely soluble under neutral conditions. The solubility of Ti-oxides in geologic fluids is strongly temperature dependent (RIED, 1994; VAN BAALEN, 1993). For example, above 900 °C, the solubility of TiO_2 increases strongly with increasing temperature and with decreasing pressure (AYERS & WATSON, 1993). These authors also show that at high temperatures the solubility, as single ion or as hydroxide, depends on the activity of water but otherwise is insensitive to fluid composition. Rutile (and possibly other polymorphs) precipitates from a Ti-rich aqueous fluid if the activity of H_2O decreases. This may result from decarbonation reactions or by addition of salts and diluents. An example is discussed by GIERÉ (1990b), where a TiO_2 rich fluid, which was derived from the Bergell intrusion, reacted with a dolomite country rock. The reaction between dolomite and water produces an increase in CO_2 in the fluid, which leads to the formation of many Ti-rich minerals such as rutile, titanite, titanian clinohumite, geikielite and zirconolite. Such release of CO_2 from the fluid leading to a aqueous fluid with a higher ability to dissolve components was described by TROMMSDORFF & SKIPPEN (1986).

The presence of Ti rich minerals (e.g., rutile, anatase, perovskite) in the experiments implies Ti mobility. After the experiments with HCl, many TiO_2 polymorphs crystallized at the expense of zirconolite, but no Ti was measured

in the leachate (figure 4.4.1). This shows that either the solubility of Ti was low but the mobilization was high during the experiments, or that some rutile and anatase crystallized as quench product during cooling. The solubility of TiO_2 in an aqueous fluid with 50 mol% CO_2 is reported to be immeasurable (Ayers & Watson, 1993). Our own experiment with a high CO_2 content in the fluid did not show any zirconolite corrosion with the resulting secondary phases. This could reveal that zirconolite as a Ti rich phase is very stable in a CO_2 rich environment comparable with rutile, if no Cl^- is present.

5.4.4 Zr and Hf

The two HFSE Zr^{4+} and Hf^{4+} both occur at the same oxidation state. Their ions are nearly identical in size (about 0.79 Å) and they reveal similar chemical properties and therefore will be considered together. Generally they behave similarly to Ti, which is of the same element group. At ambient conditions, the minimum solubility is at a pH between 5 and 6, where they form $M(OH)_4$ complexes. At more basic pH, the complex changes to $M(OH)_5^-$ and the solubility increases strongly. The highest solubility was determined below pH 2, where $M(OH)_2^{2+}$ complexes are dominant (Baes & Mesmer, 1976). F^- is reported as most complexing element in acidic fluids, OH^- in basic ones (Aja et al., 1995). Interestingly the same author revealed that in very alkaline solutions $NaZr(OH)_4^+$ complexes might become very important. Rubin et al. (1993) gave an overview on Zr mobility in hydrothermal systems developed in a broad range of igneous geochemical environments. The authors indicated that Zr mobility is mostly associated with a F-rich, alkalic igneous fluid. They also showed that not only the fluid determines the Zr mobility but also the host phase with different leaching behavior.

Our experiments showed no significant difference in Zr contents in the leachate after experiments in HCl and in NaOH (figure 4.4.1), indicating a similar solubility behavior at strong basic and strong acidic conditions (Baes & Mesmer, 1976). Therefore Cl^-, Na^+, and OH^- show a high ability to mobilize Zr and Hf at elevated temperatures.

5.4.5 REE

The rare earth elements Nd, Ce and Gd used in this study are expected to be relatively immobile like the other high valence cations Ti and Zr. While Nd and Gd are trivalent cations, Ce may be present as a trivalent and tetravalent cation. Under certain conditions in a hydrothermal system REEs are assumed to migrate as complexes (Balashov & Krigman, 1975; Kosterin, 1959; Mineyev, 1963; Wood, 1990a and b). In solution at ambient conditions, the trivalent ions exhibit strong complexing with hard ligands such as F^-, SO_4^{2-}, PO_3^{2-},CO_3^{2-} and OH^- and moderate complexing with Cl^- and NO_3^- (Wood, 1990a). At higher temperatures (> 300 °C), the REE-Cl^- complexes are expected to have greater significance (Wood, 1990b). Haas et al. (1995) revealed that at acidic and neutral pH conditions, the LREEs (La–Sm) are complexed more strongly by Cl^- compared to the HREEs, which are more strongly complexed by F^-. At basic pH conditions LREEs and HREEs strongly associate with OH^- to an equivalent degree. Baes & Mesmer (1976) show that the solubility product of all REE-hydroxides is inversely proportional to their ionic size. Another study revealed that the solubility of the REE increased with a decreasing pH (Wood & Williams-Jones, 1994). The same authors predicted a constant solubility for increasing temperature, but Haas et al. (1995) revealed the increasing importance of REE complexation at higher temperatures. In regard to the application of nuclear waste management, it is important to mention the formation of complexes with organic ligands (Wood, 1993).

In addition to the trivalent state of Nd and Gd, a tetravalent state is possible for Ce. Compared to the trivalent REE, Ce^{4+} is reported to hydrolyze extensively (Baes & Mesmer, 1976). Unfortunately insufficient data are available to evaluate the change in stability, but the importance of the tetravalent state should decrease with increasing temperature, but increase with increasing pressure (Wood, 1990b).

Although the most likely ligand in most natural fluid systems is F^- (Gieré, 1986), the possibility of transporting REE as Cl^--and Na^+-complexes during our experiments may be assumed similar to the complex formation of Ti and Zr. The results of these experiments revealed that more REEs were in solution at low pH (0.1 M HCl) than at higher pH (0.1 M NaOH) by two to three orders of magnitude (figure 4.4.1), similar to the results of Wood & Williams-Jones (1994). This may show their preferred formation of Cl^--complexes compared to OH^- or Na^+-complexes or that they are preferentially incorporated into perovskite with respect to the fluid.

5.4.6 Al

As one of the major rock forming elements, Al has a generally low solubility in aqueous fluids even at elevated pressure and temperature (Baumgartner & Eugster, 1988; Ragnarsdottir & Walther, 1985), which is inconsistent with geologic evidence for Al-mobility (e.g., vein assemblages). But experimental results in F- and Cl-rich fluids reveal increasing solubility of Al (Zaraisky, 1995). The author showed that the solubility is only increasing dramatically at temperatures above 450 °C and at HCl concentrations above 0.1 M. This may be supported by our own results, where at similar conditions, zirconolite is heavily corroded and thereby Al is mobilized. At these low pH, Al is not hydrolyzed in solution (Baes & Mesmer, 1976).

At high pH (> 8) the solubility is strongly increasing and Al forms mononuclear species $Al(OH)_4^-$. At temperatures above 500 °C complex formation with Na^+ and K^+ beside Cl^- and F^- is assumed (Zaraisky, 1995). This Na complexing could be the supporting mechanism for the high Al-solubility determined for the experiments in 0.1 M NaOH (figure 4.4.1).

5.4.7 Conclusions

The results of all experiments indicate that all elements may be mobile under certain physical and chemical conditions of the experiment. But a high mobilization of the HFSE Ti, Zr and REEs initially present in zirconolite was only observed during experiments at temperatures above 500 °C in strong HCl or NaOH solutions. The whole process may be split into three different steps. First, the mobilization of these elements is caused by dissolution and/or leaching of primary zirconolite.

Secondly, the dissolved anionic species play an important role in the transport of the elements with a high-valence ionic state. During our experiments Cl^- and OH^- were the most effective complexing ligands similar to natural system (Balashov & Krigman, 1975; Kosterin, 1959). Additionally they might have formed mixed-metal polynuclear complexes with Na^+. This is suggested from natural Ti- and Zr-rich skarns where these metals migrated along with K^+ and Na^+ (Konev, 1978; Zhuravleva et al., 1976). Metasomatic veins in the Malenco serpentinites (close to eastern Bergell) reveal no need for potassium or fluorine rich fluids (main ligands in the Bergell and Adamello contact aureoles) for the transport and the subsequent precipitation of Ti-rich phases (e.g., perovskite; Trommsdorff & Evans, 1980). At the same site, Ti-andradite in an assemblage of other phases (e.g., perovskite) is hydrothermally crystallized and demonstrates Ti-mobility under moderate metamorphic conditions (450 °C, 500 MPa), with OH^- as most probable ligand complexing Ti (Müntener & Hermann, 1994).

As third step, the deposition of these elements as secondary phases is linked to the supersaturation of the fluid with respect to the less soluble compounds. Precipitation of high-field strength element rich phases may be due to fluid mixing. Zr is mobilized in a Ca-free metal leaching environment (e.g., F-rich) and then deposited in a Ca-rich environment (Salvi & Williams-Jones, 1996). During our experiments at NaOH conditions, supersaturation (followed by precipitation of secondary phases) is due to the progressive dissolution of the primary zirconolite and the decrease of the Na content in the fluid due to its incorporation into the secondary phases. It could otherwise be dependent on changing physical properties (e.g., decreasing temperature). The textural relationship between one of the secondary phases (perovskite) and primary zirconolite shows epitactic growth of idiomorphic phases, which would not occur as a quench phenomenon due to fast changing physical properties. During these experiments, the pH and the Na concentration are high enough to keep Al hydrolyzed or as complex in solution.

The physical conditions of the experiments revealed that high element mobilization is above 500 °C and above 50 MPa. These conditions are similar to those of natural hydrothermal systems revealing mobility of high field strength elements (table 5.4.1). Interestingly, the oxygen fugacity from most metasomatic fluids transporting HFSE was reported to be low (Müntener & Hermann, 1994; Onuki et al., 1982; table 5.4.1).

Table 5.4.1: *Conditions under which high field strength elements revealed high mobility.*

Location	*Temperature [°C]*	*Pressure [MPa]*	*log fO_2*	*x CO_2*	*Elements*	*Ligands*
Adamello [1]	~ 600	200	–20	~ 0.2	Ti, Zr, REE, Act	F^-, Cl^-, PO_4^{3-}, K^+
Malenco [2]	520	300			Ti, Ca	OH^-
Malenco [3]	400 – 450	400 – 700	low	< 0.05	Ti	OH^-
Mary Kathleen [4]	550 – 670				REE, U	
Shibukawa [5]	300 – 400	400 – 700	low	low	Ti, Al	
Bellinzona [6]	690 – 730	650 – 850			Ti, Fe	
Francon Quarry [7]	360 – 400	45		< 0.03	Zr, Nb, Ti, Al	Cl^-, S^{2-}, alkalis
Strange Lake [8]	~ 350		low	low	Zr, REE	F^-, Na^+
New Idria [9]	~ 300		low		Ti	no F^-

1) Gieré, 1990;
2) Trommsdorff & Evans, 1980;
3) Müntener & Hermann, 1994;
4) Kwak & Abeysinghe, 1987;
5) Onuki et al., 1982;
6) Schmidt, 1989;
7) Vard & Williams-Jones, 1993;
8) Salvi & Williams-Jones, 1990 and Salvi & Williams-Jones, 1996;
9) Van Baalen, 1993.

6 CONCLUSIONS

6.1 Summary

All experimental data obtained during this thesis provide essential information about the interaction between different fluids and zirconolite under closed system conditions at elevated temperature and pressure. The primary results of the experiments indicate that zirconolite is highly durable under various fluid conditions (HCl, NaOH, and deionized water) up to temperatures of 250 °C at a pressure of 50 MPa. Above 250 °C, zirconolite corrosion increases with increasing temperature and is directly related to the ionic strength of the diluted acidic or basic fluids. At 500°C and 50 MPa in a NaOH-rich fluid (0.1 M), zirconolite rapidly breaks down and its replacement proceeds according to the general reaction:

zirconolite + NaOH <=> perovskite + calzirtite + $Al_{(aq)}$.

At similar conditions but at a higher pressure of 200 MPa, zirconolite breaks down according to the following general reaction:

zirconolite + NaOH <=> perovskite + baddeleyite + $Al_{(aq)}$.

However, the break down reaction of zirconolite stops with decreasing Na concentration in the fluid and the formation of perovskite is directly related to the presence of REEs (e.g., Nd, Ce, Gd) in the system.

In an HCl-rich fluid at temperature above 400 °C, zirconolite is increasingly corroded and secondary rutile and anatase crystallize on the zirconolite surface out of the fluid possibly as quench products. But in contrast to the experiments in NaOH, no temperature-sensitive break down was observed.

As shown in the present study, the REEs and Hf initially present in zirconolite as actinide analogues and neutron absorbers are present in the leachate at a much higher concentration at a low pH (e.g., HCl as fluid) than at a high pH. Under high pH conditions, these elements are preferentially incorporated into the solid secondary phases possibly crystallizing during the break down of zirconolite. With respect to the fluid, these elements distribute between the break down product phases according to their ionic radii. For the mobilization of the HFSE, the presence of Na or possibly other alkalis in the fluid is important. Perovskite and calzirtite are expected to crystallize in natural alkali-rich fluids.

Detailed investigations on the crystal structure of the product phases revealed an orthorhombic perovskite with a very unusual chemical composition. It has several wt% of Zr apparently accommodated on the A site, but this requires further study. The total chemistry is closest to loparite. The other break down product is tetragonal calzirtite, which at higher pressures is replaced by baddeleyite. No details on the structure and chemistry of rutile and anatase alteration products were observed due to their small size and number.

From all observed product phases, perovskite revealed the highest ability to accommodate significant concentrations of these doping elements. Perovskite, like zirconolite may serve as host phase for HLW (chapter 1.2.4). This is demonstrated by the fact that zirconolite as a primary waste form breaks down leaving a surface layer of perovskite and calzirtite which act as a secondary waste form and retain the major part of the critical elements studied. But the stability of perovskite as part of a ceramic waste form has been seriously questioned (Kastrissios et al., 1987; Nesbitt et al., 1981). Our findings and those of other authors (Mitchell & Chakhmouradian, 1999a; Vance & Thorogood, 1991) indicate that the introduction of Na or possibly other cations into the structure of perovskite increase greatly its stability. However, other studies indicate that perovskite is unstable in a CO_2-rich fluid environment, where it decomposes to kassite and further to anatase, calcite, ilmenite and/or titanite (Mitchell & Chakhmouradian, 1998b). Importantly, anatase and ilmenite as major replacement products are not capable of accommodating the waste elements. Therefore it is expected that they are retained in the leachant fluid and migrate from the site of disposal. On the other hand, the perovskite (loparite) break down results from leaching of Na from the A-site. An increase in alkalinity results in a decreasing leaching rate of Na from perovskite leading to a higher stability (Chakhmouradian et al., 1999b). Therefore it is necessary to choose a CO_2-free (or low) but alkaline rich geologic environment to enable the formation of the secondary wasteform, if the primary zirconolite breaks down due to the high temperatures and corroding fluid in the repository.

6.2 Relevance to Nuclear Waste Management

The results obtained during the hydrothermal experiments document the durability of zirconolite in specific fluids at specific temperatures and pressures in a closed system for short time periods. These results may help to predict the

behavior of zirconolite at a disposal site for radioactive waste for up to millions of years. However, these results are only a small part in the large field of nuclear waste management.

As already explained in chapter 1, most present schemes for nuclear waste disposal are based on a multi barrier system, where the wasteform itself is the most internal barrier. Its durability becomes very important if the geological and geotechnical barriers as well as the canisters, which contain the wasteform itself, fail. As a matter of course, these results are only relevant for zirconolite based wasteforms (e.g., Synroc).

If all other barriers were to fail and ground water reaches the ceramic waste form, the experimental results of this study indicate that zirconolite is corrosion resistant up to ~250 °C in various fluids over a wide range of pH. This result is very important because it reveals a much higher corrosion resistance than previously known. Moreover, zirconolite is more durable than glass waste forms (see chapter 1.2). During experiments above that temperature and up to ~500 °C, zirconolite shows only limited corrosion. At higher temperature, zirconolite is heavily corroded by acidic and basic fluids (Malmström et al., 1999). The experiments in HCl showed that the REEs and Hf used to simulate actinides and/or neutron absorbers may go into solution, whereas in NaOH-rich fluids, these elements are almost quantitatively incorporated into the secondary phases perovskite and calzirtite (Malmström et al., 2000).

As explained in chapter 3, the ionic strength of the fluids used in the experiments is similar to those of natural granitic groundwater. Natural groundwaters, however, are always more complex than the fluids used during the experiments where only single components were diluted in water. However, these experiments indicate which elements have a major (e.g., Na) or only minor (e.g., Si) impact on the stability of zirconolite due to their ability to mobilize the actinides and REE. The composition of the fluid also determines if the mobilized elements stay in solution or, if they lead to the formation of product phases as observed after the experiments with NaOH. The formation of such product phases with the ability to incorporate actinides and neutron absorbers is an important mechanism in the prevention of radioactive element migration to the biosphere, should such high temperatures be attained. Our results indicate that fluids reaching the waste form should have a high pH and be enriched in alkalis. Such a fluid is expected, because before the fluid reaches the wasteform, it has to percolate the bentonite backfill, where it will be saturated in Na and reach a basic pH (Murinen & Lehikoinen, 1998). In addition, the pH of a fluid increases when it is in contact with the concrete from the technical barrier.

As we know that zirconolite is not corroded by fluids up to 250 °C, it should be desired that the waste form never reaches higher temperatures, because:

a) even if product phases replace zirconolite, some elements still may be released from the repository system;
b) perovskite as secondary waste form is stable at 500 °C, but less stable than zirconolite after cooling back down to moderate temperatures;
c) if the fluid percolation in the repository is too high to reach steady state, the formation of the product phases is impossible;
d) the desired phase transformation for self-curing is dependant on many factors which are not fully understood from laboratory experiments carried out during this thesis.

Therefore the idea to dispose Pu- and U-rich waste separately from the short-life and heat-generating fission products (mainly ^{90}Sr, ^{137}Cs) is supported, because it limits the heat generation through radioactive decay to several tens of degrees compared to the several hundreds of degrees generated from waste containing all elements.

It has to be mentioned that the hydrothermal experiments were carried out in a closed system and therefore the results are only comparable to a natural system with a very slow fluid flow through, where elemental saturation of the fluid may be reached (steady state). This should be assumed, because high flow through over a long period of time is an undesirable scenario for any type of repository. But the high durability of zirconolite up to 250 °C indicates that even in a system with high fluid percolation rates zirconolite most probably could retain the actinides and neutron absorbers.

The results from the experiments with the U-doped zirconolite (chapter 4.9) showed that it is important to not only carry out experiments with analogue elements, because they behave only in a similar, but not identical way.

Finally it is safe to postulate that:

1) Zirconolite is stable up to 250 °C in various fluids over a wide range of pH.
2) These experiments are relevant for zirconolite waste forms and for the case that all other barriers fail and fluid reaches the waste form.
3) Disposal of U or Pu waste (separated from the fission products) would strongly reduce the radiogenic heat generation – thereby temperatures above 250 °C could be prevented.
4) If the temperature in the disposal cavern reaches several hundred degrees (due to the decay of fission products for a time of several hundred years), and the outer barriers would fail, then zirconolite may be corroded. But if the fluid is basic and Na-rich, the waste form will self-cure by dissolution/precipitation processes and will retain the major part of the waste elements.
5) The results of this study support the further development of ceramic waste forms in contrast to glass waste forms, because they are more temperature resistant.

6) It is important to use a backfill, which promotes the formation of a basic, Na-rich fluid.
7) Future investigations are needed to be made with U- or Pu-doped samples to better understand their behavior in a possible repository.

6.3 Suggestions for further work

The results of these experiments offer potential for improvement. Some possible interesting topics for future studies are:

- The characterization of all smaller secondary phases (especially for U-doped zirconolite and in the HCl system) requires further study using TEM.
- In-situ fluid analysis using «Goldbag»-technique (Bridgman seal-type autoclaves with a flexible gold reaction-cell system).
- In-situ measurement of reactive volumes using pressure analysis (Mok & Girsperger, 2000) to determine the crystallization process of the product phases (see chapter 5.1).
- Investigation of the influence of CO_2 or SiO_2 on the stability of the secondary phases obtained during the experiments in NaOH or HCl.
- Forcing the reaction of zirconolite to perovskite and calzirtite or baddeleyite by additives (e.g., Na) to enhance the formation of the secondary waste form.
- Using TEM EELS for a proper determination of the valence state of Ce in the solid product phases.
- Direct measurements of Ca in the fluid with ICP-MS coupled with a dynamic reaction cell.

Experimental studies in combination with field work may give help for a better understanding of reaction processes and element mobility in the earth crust.

REFERENCES

AJA, S. U., WOOD, S. A. & WILLIAMS-JONES, A. E. (1995): The aqueous geochemistry of Zr and the solubility of some Zr-bearing minerals. Applied Geochemistry, 10, 603–620.

ALLEN, C. M. & ELLIS, D. J. (1996a): A theoretical analysis of the stability and phase relations involving zirconolite in the $CaO–ZrO_2–TiO_2–SiO_2–CO_2$ system under crustal and upper mantle conditions. In: Unpublished Report for ANSTO, pp. 22, Department of Geology, Faculty of Science, The Australian National University, Canberra, ACT.

ALLEN, C. M. & ELLIS, D. J. (1996b): Stability of zirconolite and its occurrence in the crustal environment. In: Unpublished Report for ANSTO, pp. 66, Department of Geology, Faculty of Science, The Australian National University, Canberra, ACT.

ANTHONY, I. & JOHN, W. (1997): Handbook of Mineralogy. Mineral Data Publishing, Tucson, Arizona 85740.

AYERS, J. C. & WATSON, E. B. (1993): Rutile solubility and mobility in supercritical aqueous fluids. Contrib. Mineral. Petrol., 114, 321–330.

BAES, C. F. & MESMER, R. E. (1976): The Hydrolysis of Cations. Wiley-Interscience Publication.

BAIR, W. J. & THOMPSON, R. C. (1974): Plutonium: Biomedical Research. Science, 183, 715–722.

BALASHOV, Y. U. A. & KRIGMAN, L. D. (1975): The effects of alkalinity and volatiles on rare earth separation in magmatic systems. Geochem. Int., 12 (6), 165–170.

BALL, C. J., THOROGOOD, G. J. & VANCE, E. R. (1992): Thermal expansion coefficient of zirconolite ($CaZrTi_2O_7$) and perovskite ($CaTiO_3$) from X-ray powder diffraction analysis. Journal of Nuclear Materials, 190, 298–301.

BANFIELD, J. F., VEBLEN, D. R. & SMITH, D. J. (1991): The identification of naturally occurring TiO_2 (B) by structure determination using high-resolution electron microscopy, image simulation, and distance-least-squares refinement. American Mineralogist, 76, 343–353.

BARBLAN, F., BRANDENBERGER, E. & NIGGLI, P. (1944): Geregelte und ungeregelte Strukturen von Titanaten und Ferriten und geregelte Umwandlung der TiO_2-Modifikationen. Helv. Chim. Acta, 27, 88–96.

BARTH, T. F. W. (1952): Theoretical Petrology. Wiley, New York.

BAUMGARTNER, L. P. & EUGSTER, H. P. (1988): Experimental determineation of corundum solubility and Al speciation in supercritical H_2O–HCl solutions. Geological Society of America Abstracts with Programs, 22, A191.

BAYLISS, P., MAZZI, F., MUNNO, R. & WHITE, T. J. (1989): Mineral nomenclature: zirconolite. Mineral. Mag., 53, 565–569.

BEGG, B. D. & VANCE, E. R. (1997): The incorporation of cerium in zirconolite. In: Scientific Basis for Nuclear Waste Management XX (eds. GRAY, W. J. & TRIAY, I. R.) Materials Research Society, Boston, USA, 333–340.

BEGG, B. D., VANCE, E. R. & HUNTER, B. A. (1998a): Zirconolite transformation under reducing conditions. Journal of Materials Research, 13 (11), 3181–3190.

BEGG, B. D., VANCE, E. R. & LUMPKIN, G. R. (1998b): Charge compensation and the incorporation of cerium in zirconolite and perovskite. In: Scientific Basis for Nuclear Waste Management XXI (eds. MCKINLEY, I. G. & MCCOMBIE, C.) Materials Research Society, Davos, Switzerland, 79–86.

BELLATRECCIA, F., DELLA VENTURA, G., CAPRILLI, E., WILLIANS, C. T. & PARODI, G. C. (1999): Crystal-chemistry of zirconolite and calzirtite from Jacupiranga, Sao Paulo (Brazil). Mineral. Mag., 63 (5), 649–660.

BIRD, G. W. & FYFE, W. S. (1982): The nuclear waste disposal problem – an overview from a geological and geochemical perspective. Chemical Geology, 36, 1–13.

BLACKFORD, M. G., SMITH, K. L. & HART, K. P. (1992): Microstructure, Partitioning and Dissolution Behavior of Synroc Containing Actinides. In: Scientific Basis for Nuclear Waste Management XVI Materials Research Society, Boston, USA, 243–249.

BOATNER, L. A. & SALES, B. C. (1988): Monazite. In: Radioactive Waste Form for the Future (eds. LUTZE, W. & EWING, R. C.), pp. 495–564, North Holland, Amsterdam.

BRENAN, J. M., SHAW, H. F., PHINNEY, D. L. & RYERSON, F. J. (1994): Rutile–aqueous fluid partitioning of Nb, Ta, Hf, Zr, U and Th: implications for high field strength element depletions in island-arc basalts. Earth and Planetary Science Letters, 128, 327–339.

BROOKINS, D. G. (1988): Eh–pH Diagrams for Geochemistry. Springer, Berlin.

BROOKINS, D. G. (1989): Aqueous Geochemistry of Rare Earth Elements. Reviews in Mineralogy, 21, 201–225.

BRUNO, J., CERA, E., DEPABLO, J., DURO, L., JORDANA, S. & SAVAGE, P. (1997): SKB Technical Report.

BUBOVNA, M. I., KOCHUROVA, T. L., RIMSKAYA-KORSAKOV, O. M. & FILATOV, S. K. (1973): Structural typomorphic properties of baddeleyite of the Kovdor Massif. Leningrad Univ., Vestn., Geol. Geogr., 18, 56–61.

BULAKH, A. G., ANASTASENKO, G. F. & DAKHIYA, L. M. (1967): Calzirtite from Carbonatites of Northern Siberia. American Mineralogist, 52, 1880–1885.

BULAKH, A. G. & NESTEROV, A. R. (1996): Zirkelite, Zirconolite, Calzirtite: Re-examination of unique materials

from museum collections. Acta Mineralogica-Petrographica, Szeged, XXXVII (Supplementum), 25.

Bulakh, A. G., Nesterov, A. R., Anastasenko, G. F. & Anisimov, I. S. (1999): Crystal morphology and intergrowths of calzirtite $Ca_2Zr_5Ti_2O_{16}$, zirkelite (Ti, Ca, Zr) O_{2-x}, zirconolite $CaZrTi_2O_7$ in phoscorites and carbonatites of the Kola Penninsula (Russia). Neues Jahrb. Mineral. Mh., 1/99, 11–20.

Callegari, A., Mazzi, F. & Ungaretti, L. (1997): The crystal structure of orthorhombic calzirtite of Val Malenco (Italy). Neues Jahrb. Mineral. Mon., 10, 467–480.

Chakhmouradian, A. R. & Mitchell, R. H. (1999a): Primary, agpaitic and deuteric stages in the evolution of accessory Sr, REE, Ba and Nb-mineralization in nepheline-syenite pegmatites at Pegmatite Peak, Bearpaw Mts, Montanta. Mineralogy and Petrology, 67, 85–110.

Chakhmouradian, A. R., Mitchell, R. H., Pankov, A. V. & Chukanov, N. V. (1999b): Loparite and metaloparite from the Burpaoa alkaline complex, Baikal Alkaline Province (Russia). Mineral. Mag., 63 (4), 519–534.

Chan, H. M., Harmer, M. P. & Smyth, D. M. (1986): Compensating defects in highly donor-doped $BaTiO_3$. J. Am. Ceram. Soc., 69 (6), 507–510.

Cheary, R. W. (1992): Zirconolite $CaZr_{0.92}Ti_{2.08}O_7$ from 294 to 1173 K. Journal of Solid State Chemistry, 98, 1–7.

Clarke, D. R. (1983): Ann. Rev. Mater. Sci., 13, 191.

Coelho, A. A., Cheary, R. W. & Smith, K. L. (1997): Analysis and Structural Determination of Nd-substituted zirconolite-4M. J. Solid State Chem., 129, 346–359.

Connolly, J. A. D. (1990): Multivariable Phase Diagrams: An Algorithm Based on Generalized Thermodynamics. American Journal of Science, 290, 666–718.

Coughanour, L. W., Roth, R. S., Marzullo, S. & Sennett, F. E. (1955): Solid-state reactions and dielectric properties in the systems magnesia–zirconia–titania and lime–zirconia–titania. Journal of Research of the National Bureau of Standards, 54 (4), 191–199.

Cressey, G., Wall, F. & Cressey, B. A. (1999): Differential REE uptake by sector growth of monazite. Mineralogical Magazine, 63 (6), 813–828.

de Baar, H. J. W., German, C. R., Elderfield, H. & vanGaans, P. (1988): Rare earth element distribution in anoxic waters of the Cariaco Trench. Geochim. Cosmochim. Acta, 52, 1203–1219.

de Marsily, G. (1979): High level nuclear waste isolation: borosilicate glass versus crystals. Nature, 278, 210–212.

Deer, W. A., Howie, R. A. & Zussman, J. (1966): An Introduction to the Rock Forming Minerals. Longmans, London.

Deutsch, W. J., Jenne, E. A. & Krupka, K. M. (1982): Solubility in basalt aquifers: the Columbia Plateau, eastern Washington, USA. Chemical Geology, 36, 15–34.

Dowty, N. (1976): Crystal Structure and Crystal Growth: II. Sector Zoning in Minerals. American Mineralogist, 61, 460–469.

Ebbinghaus, B. (1998): Fabrication process using nitrates and alkoxides. Lawrence Livermore National Laboratory.

Ewing, R. C., Haaker, R. F., Headley, T. J. & Hlava, P. F. (1982): Zirconolites from Sri Lanka, South Africa and Brazil. In: Scientific Basis for Nuclear Waste Management XVIII Materials Research Society, Boston, USA.

Ewing, R. C. & Headley, T. J. (1983): Alpha-recoil damage in natural zirconolite. J. Nucl. Mater., 119, 102–109.

Ewing, R. C., Weber, W. J. & Clinard, F. W. (1995): Radiation Effects in Nuclear Waste Forms for High-Level Radioactive Waste. In: Progress in Nuclear Energy, pp. 63–127, Pergamon.

Ferry, J. M. (1996): Three novel isograds in metamorphosed siliceous dolomites from the Ballachulish aureole, Scotland. American Mineralogist, 81, 485–494.

Fielding, P. E. & White, T. J. (1987): Crystal chemical incorporatin of high level waste species in aluminotitanate-based ceramics: Valence, location, radiation damage, and hydrothermal durability. J. Mater. Res., 2 (3), 387–414.

Fritz & Lodemann (1990): Die salinaren Tiefenwässer der KTB-Vorbohrung. Die Geowissenschaften, 9, 273–274.

Fritz, P. & Frape, S. K. (1982): Saline groundwaters in the Canadian Shield – a first overview. Chemical Geology, 36, 179–190.

Frost, B. R. (1991): Introduction to Oxygen Fugacity and Its Petrologic Importance. In: Oxide Minerals: Petrologic and Magnetic Significance (ed. Lindsley, D. H.) Reviews in Mineralogy, Mineralogical Society of America.

Gatehouse, B. M., Grey, I. E., Hill, R. J. & Rossell, H. J. (1981): Zirconolite, $CaZr_xTi_{3-x}O_7$; structure refinements for near-end-member combositions with x = 0.85 and 1.30. Acta Cryst., B37, 306–312.

Gieré, R. (1986): Zirconolite, allanite and hoegbomite in a marble skarn from the Bergell contact aureole: implications for mobility of Ti, Zr and REE. Contrib. Mineral. Petrol., 93, 459–470.

Gieré, R. (1990a): Hydrothermal mobility of Ti, Zr and REE: examples from the Bergell and Adamello contact aureoles (Italy). Terra Nova, 2, 60–67.

Gieré, R. (1990b): Quantification of element mobility at a tonalite/dolomite contact (Adamello Massif, Provincia di Trento, Italy). Unpubl. Ph.D. Thesis, ETH Zürich, Zürich, Switzerland.

Gieré, R. (1996): Formation of rare earth minerals in hydrothermal systems. In: Rare Earth Minerals: Chemistry, origin and ore deposits (eds. Jones, A. P., Wall, F. & Williams, C. T.), pp. 105–150, Chapman & Hall, London.

Gieré, R. (1999): Nuclear Waste Forms. In: Toxic Waste Disposal: A Geologic Approach (ed. Ricci, C. A.), pp. 67–78, ISSN, Siena.

Gieré, R., Guggenheim, R., Düggelin, M., Mathys, D., Williams, C. T., Lumpkin, G. R., Blackford, M. G., Hart, K. P. & McGlinn, P. (1994): Retention of actinides during alteration of aperiodic zirconolite. In: 13th International Congress on Electron Microscopy, Applications in Materials Sciences 2B, Paris, 1269–1270.

Gieré, R. & Williams, C. T. (1992): REE-bearing minerals in a Ti-rich vein from the Adamello contact aureole (Italy). Contrib. Mineral. Petrol., 112, 83–100.

GIERÉ, R., WILLIAMS, C. T. & LUMPKIN, G. R. (1998): Chemical characteristics of natural zirconolite. Schweiz. Mineral. Petrogr. Mitt., 78, 433–459.

GRAESER, S. & GUGGENHEIM, R. (1990): Brannerite from Lengenbach, Binntal (Switzerland). Schweiz. Mineral. Petrogr. Mitt., 70, 325–331.

GUIMARÃES, D. (1948): The Zr ore deposits of the Pocos de Caldas plateau, Brazil, and Zr geochemistry. Bol. Inst. Techn. Ind. Minas Gerais, 6, 1–40.

GÜNTHER, D., AUDÉTAT, A., FRISCHKNECHT, R. & HEINRICH, C. A. (1998): Quantitative analysis of major, minor and trace elements in fluid inclusions using LA-ICP-MS. Journal of Analytical Atomic Spectrometry, 13, 263–270.

GÜNTHER, D., FRISCHKNECHT, R., AUDÉTAT, A., ULRICH, T. & HEINRICH, C. A. (in prep): Enhanced sensitivity in LA-ICP-MS using helium as aerosol carrier.

GÜNTHER, D., FRISCHKNECHT, R., HEINRICH, C. A. & KAHLERT, H. J. (1997a): Capabilities of an Argon Fluoride 193 nm Excimer Laser for Laser Ablation Inductively Coupled Plasma Mass Spectrometry Microanalysis of Geological Materials. Journal of Analytical Atomic Spectrometry, 12, 939–944.

GÜNTHER, D., FRISCHKNECHT, R., MÜSCHENBORN, H. J. & HEINRICH, C. A. (1997b): Direct liquid ablation: a new calibration strategy for laser ablation-ICP-MS microanalysis of solids and liquids. Fresnius J. Anal. Chem., 359, 390–393.

HAAS, J. R., SHOCK, E. L. & SASSANI, D. C. (1995): Rare earth elements in hydrothermal systems: Estimates of standard partial molal thermodynamic properties of aqueous complexes of the rare earth elements at high pressures and temperatures. Geochim. Cosmochim. Acta, 59 (21), 4329–4350.

HAGGERTY, S. E. (1987): Metasomatic mineral titanites in upper mantle xenoliths. In: Mantle Xenoliths (ed. NIXON, P. H.), pp. 690, John Wiley & Sons Ltd.

HARKER, A. B. (1988): Tailored ceramics. In: Radioactive Waste Forms for the Future (eds. LUTZE, W. & EWING, R. C.), pp. 335–392, Elsevier, New York.

HARKER, A. B. & FLINTOFF, J. F. (1984): Hot Isostatically Pressed Ceramic and Glass Forms for Immobilizing Hanford High-Level Waste. Advances in Ceramics, 8, 222–233.

HART, K. P., LUMPKIN, G. R., ELLIS, D. J., ALLEN, C. M., GIERÉ, R., WILLIAMS, C. T. & VANCE, E. R. (1997): Further analysis of the applicability of naturally occurring zirconolites as analogues for HLW waste matrices. In: 7th EC Natural Analogue Working Group Meeting, Report EU 17851 (eds. VON MARAVIC, H. & SMELLIE, J.) European Commission, Stein am Rhein, Switzerland, 3–8.

HART, K. P., LUMPKIN, G. R., GIERÉ, R., WILLIAMS, C. T., MCGLINN, P. J. & PAYNE, T. E. (1996): Naturally-Occurring Zirconolites – Analogues for the Long-Term Encapsulation of Actinides in Synroc. Radiochimica Acta, 74, 309–312.

HART, K. P., ROBINSON, B. J., PAYNE, T. E., VAN ISEGHEM, P. & LEMMENS, K. (1995): Interactions between Np-doped Synroc and boom clay. In: Scientific Basis for Nuclear Waste Management XVIII (eds. MURAKAMI, F. & EWING, R. C.), Materials Research Society, Boston, USA, 841–845.

HART, K. P., VANCE, E. R., STEWART, M. W. A., WEIR, J., CARTER, M. L., HAMBLEY, M., BROWNSCOMBIE, A., DAY, R. A., LEUNG, S., BALL, C. J., EBBINGHAUS, B., GRAY, L. & KAN, T. (1998): Leaching Behavior of Zirconolite Rich Synroc Used to Immobilise «High-Fired» Plutonium Oxide. In: Scientific Basis for Nuclear Waste Management XXI (eds. MCKINLEY, I. G. & MCCOMBIE, C.), Mat. Res. Soc., pp. 161–168.

HAUSER, O. (1909): He Uhligite Cornu. Zeit. Anorg. Chem., 63, 240.

HAYWARD, P. J. (1988): Glass Ceramics. In: Radioactive Waste Forms for the Future (eds. LUTZE, W. & EWING, R. C.), pp. 427–494, North-Holland, Amsterdam.

HELEAN, K. B., LUTZE, W. & EWING, R. C. (1999): Surface features and alteration products of natural zirconolite leached in silica-saturated solutions. In: Scientific Basis for Nuclear Waste Management XXII (eds. WRONKIEWICZ, D. J. & LEE, J. H.) Materials Research Society, Boston, USA, 157–164.

HIEMSTRA, S. A. (1955): Baddeleyite from Phalaborwa, Eastern Transvaal. American Mineralogist, 40, 275–282.

HOLLAND, T. J. B. & POWELL, R. (1998): An internally consistent thermodynamic data set for phases of petrological interest. J. Metamorphic Geology, 16, 309–343.

HOLMQUIST, P. J. (1897): Synthetische Studien über die Perovskit- und Pyrochlormineralien. Unpubl. Ph.D. Thesis, University of Uppsala, Uppsala, Sweden.

HRMA, P. & CASLER, D. G. (1999): Non-isothermal kinetics of spinel crystallization. In: Scientific Basis for Nuclear Waste Management XXII (eds. WRONKIEWICZ, D. J. & LEE, J. H.) Materials Research Society, Boston, USA, 125–132.

HU, M., WENK, H. R. & SINITSYNA, D. (1992): Microstructures in natural perovskites. American Mineralogist, 77, 359–373.

HUEBNER, J. S. (1971): Buffering techniques for hydrostatic systems at elevated pressures. In: Research techniques for high pressure and high temperature (ed. ULMER, G.), pp. 123–177, Springer Verlag.

IAEA (1993): Radioactive Waste Management Glossary, International Atomic Energy Agency, Vienna.

IAEA (1994): Prospects and Strategies for Nuclear Power, International Atomic Energy Agency, London.

IAEA (1995): Minimization of Radioactive Waste from Nuclear Power Plants and the Back End of the Nuclear Fuel Cycle, pp. 84, International Atomic Energy Agency, Vienna.

JAGO, B. C. & GITTINS, J. (1993): Pyrochlore crystallization in carbonatites: the role of fluorine. South African Journal of Geology, 96 (3), 149–159.

JANECZEK, J. & EWING, R. C. (1995): Mechanisms of lead release from uraninite in the natural fission reactors in Gabon. Geochim. Cosmochim. Acta, 59 (10), 1917–1931.

JIANG, C. (1996): Activity Coefficients of Hydrochloric Acid in Concentrated Electrolyte Solutions. J. Chem. Eng. Data, 41, 113–116.

JOSTSONS, A., VANCE, E. R., LUMPKIN, G. R., HART, K. P. & EBBINGHAUS, B. B. (2000): Titanite Ceramic Phases for Surplus Plutonium Immobilization. In: Tucson'00, Tucson, Arizona.

JOSTSONS, A., VANCE, E. R., MERCER, D. J. & OVERSBY, V. M. (1995): Synroc for immobilising excess weapons plutonium. In: Scientific Basis for Nuclear Waste Management XVIII (eds. MURAKAMI, F. & EWING, R. C.), Materials Research Society, Boston, USA, 775–781.

KASTRISSIOS, T., STEPHENSON, M., TURNER, P. S. & WHITE, T. J. (1987): Hydrothermal Dissolution of Perovskite: Implications for Synroc Formulation. J. Am. Ceram. Soc., 70 (7), C-144–146.

KAY, H. F. & BAILEY, P. C. (1957): Structure and properties of $CaTiO_3$. Acta Cryst., 10, 219–226.

KESSON, S. E. & RINGWOOD, A. E. (1981): Immobilization of sodium in Synroc. Nuclear and Chemical Waste Management, 2, 53–55.

KESSON, S. E., SINCLAIR, W. J. & RINGWOOD, A. E. (1983): Solid solution limits in Synroc zirconolite. Nuclear and Chemical Waste Management, 4, 259–265.

KONEV, A. A. (1978): Les mineraux de titane et de zirconium dans les skarns du massif alcalin de Tagerane (Baikal, Siberie). Bull. Mineral., 101, 387–389.

KOOPMANS, H. J. A., VAN DE VELDE, G. M. H. & GELLINGS, P. J. (1983): Powder neutron diffracition study of the perovskites $CaTiO_3$ and $CaZrO_3$. Acta Cryst., C39, 1323–1325.

KOSTERIN, A. V. (1959): The possible modes of transport for the rare earths by hydrothermal solutions. Geochem. Int., 4, 381–387.

KOUCHI, A., SUGAWARA, Y., KASHIMI, K. & SUNAGAWA, I. (1983): Laboratory growth of sector zoned clinopyroxenes in the system $CaMgSi_2O_6 – CaTiAl_2O_6$. Contrib. Mineral. Petrol., 83, 177–184.

KRAYNOV, S. R., MERKOV, A. N., PETROVA, N. G., BATURINSKAYA, I. V. & ZHARIKOVA, V. M. (1969): Highly alkaline (pH 12) fluosilicate waters in the deeper zones of the Lovozero massif. Geochim. Int., 6 (4), 635–640.

KRZEMNICKI, M. S. (1996): Mineralogical investigations on hydrothermal As- and REE-bearing minerals withing the gneisses of the Monte Leone nappe (Binntal region, Switzerland). Unpubl. Ph.D. Thesis, Universität Basel, Basel.

KWAK, T. A. P. & ABEYSINGHE, P. B. (1987): Rare earth and uranium minerals present as daughter crystals in fluid inclusions, Mary Kathleen U-REE skarn, Queensland, Australia. Mineral. Mag., 51, 665–670.

LARSON, E. M., ELLER, P. G., PURSON, J. D., PACE, C. F., EASTMAN, M. P., GREEGOR, R. B. & LYTLE, F. W. (1988): Synthesis and structural characterization of $CaTiO_3$ doped with 0.05–7.5 Mole% Gadolinium(III). J. Solid State Chem., 73, 480–487.

LAVEROV, N. P., OMEL'YANENKO, B. I., YUDINTSEV, S. V. & NIKONOV, B. S. (1996): Zirconolite as a Matrix for Immobilization of High-Level Radioactive Wastes. Geology of Ore Deposits, 38(5), 345–352.

LETURCQ, G. (1998): Altération et comportement a long terme de différentes classes de matériaux innovants pour le confinement des radionucléides a vie longue. Unpubl. Ph.D. Thesis, Uni Paul Sabatier, Toulouse, France.

LEVINS, D. M., REEVE, K. D., BUYKX, W. J., RYAN, R. K., SEATONBERRY, B. W. & WOOLFREY, J. L. (1986): Fabrication and Performance of Synroc. In: Topical Meeting on Waste Management, pp. 1137, American Nuclear Society, Pittsburgh, PA, Niagara Falls, USA.

LEVINS, D. M., REEVE, K. D., RYAN, R. K., WOOLFREY, J. L., BUYKX, W. J. & SEATONBERRY, B. W. (1985): Performance of Synroc under conditions relevant to repository disposal. Australian Atomic Energy Commission Report to the IAEA under Research Agreement.

LEVINS, D. M. & SMART, R. S. C. (1984): Nature, 309, 776.

LUMPKIN, G. R. (1992): Determination of Site Occupancies in Silicate Garnets Using Axial ALCHEMI and Multivariate Statistical Analysis. Journal of Computer-Assisted Microscopy, 4 (2), 155–159.

LUMPKIN, G. R. & EWING, R. C. (1995): Geochemical alteration of pyrochlore group minerals: Pyrochlore subgroup. American Mineralogist, 80, 732–743.

LUMPKIN, G. R. & EWING, R. C. (1996): Geochemical alteration of pyrochlore group minerals: Betafite subgroup. American Mineralogist, 81, 1237–1248.

LUMPKIN, G. R., EWING, R. C., CHAKOUMAKOS, B. C., GREEGOR, R. B., LYTLE, F. W., FOLTYN, E. M., CLINARD, F. W., BOATNER, L. A. & ABRAHAM, M. M. (1986): Alpha-recoil damage in zirconolite. J. Mater. Res., 1, 564–576.

LUMPKIN, G. R., HART, K. P., MCGLINN, P. J., PAYNE, T. E., GIERÉ, R. & WILLIAMS, C. T. (1994a): Retention of actinides in natural pyrochlores and zirconolites. Radiochimica Acta, 66/67, 469–474.

LUMPKIN, G. R., SMITH, K. L. & BLACKFORD (1995a): Development of secondary phases on Synroc leached at 150 °C. In: Scientific Basis for Nuclear Waste Management XVIII (eds. MURAKAMI, F. & EWING, R. C.), Materials Research Society, Boston, USA, 855–862.

LUMPKIN, G. R., SMITH, K. L. & BLACKFORD, M. G. (1991): Electron microscope study of Synroc before and after exposure to aqueous solutions. J. Mater. Res., 6 (10), 2218–2233.

LUMPKIN, G. R., SMITH, K. L. & BLACKFORD, M. G. (1995b): Partitioning of uranium and rare earth elements in Synroc: effect of impurities, metal additive, and waste loading. J. Nucl. Mater., 224, 31–42.

LUMPKIN, G. R., SMITH, K. L., BLACKFORD, M. G., GIERÉ, R. & WILLIAMS, C. T. (1994c): Determination of 25 elements in the complex oxide mineral zirconolite by analytical electron microscopy. Micron, 25 (6), 581–587.

LUMPKIN, G. R., SMITH, K. L., BLACKFORD, M. G., GIERÉ, R. & WILLIAMS, C. T. (1998): The crystalline-amorphous transformation in natural zirconolite: evidence for long-term annealing. In: Scientific Basis for Nuclear Waste Mangement XXI (eds. MCKINLEY, I. G. & MCCOMBIE, C.), Materials Research Society, Davos, Switzerland, 215–222.

LUMPKIN, G. R., SMITH, K. L., BLACKFORD, M. G., HART, K. P., MCGLINN, P. J., GIERÉ, R. & WILLIAMS, C. T. (1994b): Prediction of the long-term performance of crystalline nuclear waste form phases from studies of mineral analogues. In: 9th Pacific Basin Nuclear conference, 94/6 (ed. MCDONALD, N. R.), The Institution of Engineers, Sydney, Australia, 879–885.

LUMPKIN, G. R., SMITH, K. L. & BLAKE, R. G. (1996): TEM study of radation damage and annealing of neutron irradiated zirconolite. In: Scientific Basis for Nuclear Waste Management XIX (eds. MURPHY, W. M. & KNECHT, D. A.), Materials Research Society, Boston, USA, 329–336.

LUMPKIN, G. R., SMITH, K. L. & GIERÉ, R. (1997): Application of analytical electron microscopy to the study of radiation damage in natural zirconolite. Micron, 28, 57–68.

LUPINI, L., WILLIAMS, C. T. & WOOLLEY, A. R. (1992): Zr-rich garnet and Zr- and Th-rich perovskite from the Polina carbonatite, Italy. Mineral. Mag., 56, 581–586.

LUTH, R. W. (1989): Natural versus experimental control of oxidation state: Effects on the composition and speciation of C–O–H fluids. American Mineralogist, 74, 50–57.

LUTZE, W. (1988): Silicate Glasses. In: Radioactive Waste Forms for the Future (eds. LUTZE, W. & EWING, R. C.), pp. 1–159, North-Holland, Amsterdam.

LUTZE, W. & EWING, R. C. (1988): Radioactive Waste Forms for the Future. North Holland, Amsterdam.

MAESTRATI, R. (1989): Contribution a l'Edification du Catalogue Raman des Gemmes. Unpubl. Diplome Thesis, Université de Nantes, Nantes.

MALMSTRÖM, J. C., REUSSER, E., GIERÉ, R., LUMPKIN, G. R., BLACKFORD, M. G., DÜGGELIN, M., MATHYS, D., GUGGENHEIM, R. & GÜNTHER, D. (2000): Formation of perovskite and calzirtite during zirconolite alteration. In: Scientific Basis for Nuclear Waste Management XXIII Materials Research Society, Boston, USA, in press.

MALMSTRÖM, J. C., REUSSER, E., GIERÉ, R., LUMPKIN, G. R., DÜGGELIN, M., MATHYS, D. & GUGGENHEIM, R. (1999): Zirconolite Corrosion in Dilute Acidic and Basic Fluids at 180–700 °C and 50 MPa. In: Scientific Basis for Nuclear Waste Management XXII (eds. WRONKIEWICZ, D. J. & LEE, J. H.), Materials Research Society, Boston, USA, 165–172.

MALMSTRÖM, J. C., REUSSER, E., GÜNTHER, D., GIERÉ, R. & LUMPKIN, G. R. (1998): Zirconolite Leachates: UV-LA-ICP-MS Trace Element Data. In: American Geophysical Union, pp. 955, San Francisco, Cal.

MAZZI, F. & MUNNO, R. (1983): Calciobetafite (new mineral of the pyrochlore group) and related minerals from Campi Flegrei, Italy; crystal structures of polymignyte and zirkelite: comparison with pyrochlore and zirconolite. American Mineralogist, 68, 262–276.

MCGLINN, P. J., HART, K. P., LOI, E. H. & VANCE, E. R. (1995): pH dependence of the aqueous dissolution rates of perovskite and zirconolite at 90 °C. In: Scientific Basis for Nuclear Waste Management XVIII (eds. MURAKAMI, F. & EWING, R. C.), Materials Research Society, Boston, USA, pp. 847–854.

MCHALE, J. M. & COPPA, N. V. (1996): Instantaneous formation of Synroc-B phases at ambient pressure. In: Scientific Basis for Nuclear Waste Management XIX (eds. MURPHY, W. M. & KNECHT, D. A.), Materials Research Society, Boston, USA, 297–303.

MERCOLLI, I., SKIPPEN, G. & TROMMSDORFF, V. (1987): The tremolite veins of Campolungo and their genesis. Schweiz. Mineral. Petrogr. Mitt., 67, 75–84.

MINEYEV, D. A. (1963): Geochemical differentiation of the rare-earths. Geochem. Int., 12, 1129–1149.

MITCHELL, R. H. (1996): Perovskites: a revised classification scheme for an important rare earth element host in alkaline rocks. In: Rare Earth Minerals (eds. JONES, A. P., WALL, F. & WILLIAMS, C. T.), pp. 41–76, Chapman & Hall.

MITCHELL, R. H. (1997): Preliminary studies of the solubility and stability of perovskite group compounds in the synthetic carbonatite system calcite–portlandite. Journal of African Earth Sciences, 25 (1), 147–158.

MITCHELL, R. H. & CHAKHMOURADIAN, A. R. (1996): Compositional Variation of Loparite from the Lovozero Alkaline Complex, Russia. Canadian Mineralogist, 34, 977–990.

MITCHELL, R. H. & CHAKHMOURADIAN, A. R. (1998a): A Structural Study of the Perovskite Series $Na_{1/2+x}La_{1/2-3x}Th_{2x}TiO_3$. J. Solid State Chem., 138, 307–312.

MITCHELL, R. H. & CHAKHMOURADIAN, A. R. (1998b): Instability of perovskite in a CO_2-rich environment: examples from carbonatite and kimberlite. Canadian Mineralogist, 36 (4), 939–952.

MITCHELL, R. H. & CHAKHMOURADIAN, A. R. (1999a): Solid solubility in the system $NaLREETi_2O_6$ – $ThTi_2O_6$: experimental and analytical data. Phys. Chem. Minerals, 26, 396–405.

MOK, U. (1993): Volumetric determinations in the systems NaCl–H_2O and KCl–H_2O to 450 MPa and 900 °C. Unpubl. Ph.D. Thesis, ETH Zürich, Zürich, Switzerland.

MOK, U. & GIRSPERGER, S. (2000): In-situ Measurement of Reactive Volumes using Pressure Analysis. Schweiz. Mineral. Petrogr. Mitt., 80, 1–16.

MORGAN, P. E. D. & RYERSON, F. J. (1982): A new «cubic» crystal compound. Journal of Materials Science Letters, 1, 351–352.

MOUNTAIN, B. W. & WILLIAMS-JONES, A. E. (1994): Experimental simulation of fluid-rock interaction: the effect of surface area on the rate of alteration. Mineral. Mag., 58A, 631–632.

MUKHOPADHYAY, B. & HOLDAWAY, M. J. (1994): Cordierite–garnet–sillimanite–quartz equilibrium: I. New experimental calibration in the system FeO–Al_2O_3–SiO_2–H_2O and certain P–T–X_{H2O} relations. Contrib. Mineral. Petrol., 116, 462–472.

MULJA, T., WILLIAMS-JONES, A. E., MARTIN, R. F. & WOOD, S. A. (1996): Compositional variation and structural state of columbite–tantalite in rare-element granitic pegmatites of the Preissac-Lacorne batholith, Quebec, Canada. American Mineralogist, 81, 146–157.

MÜNTENER, O. & HERMANN, J. (1994): Ti-andradite in a metapyroxenite layer from the Malenco ultramafics

(Italy): implications for Ti-mobility and low oxygen fugacity. Contrib. Mineral. Petrol., 116, 156–168.

MURDOCH, J. (1951): Perovskite. American Mineralogist, 36, 573–580.

MURINEN, A. & LEHIKOINEN, J. (1998): Evolution of the porewater chemistry in compacted bentonite. In: Scientific Basis for Nuclear Waste Management XXI (eds. MCKINLEY, I. G. & MCCOMBIE, C.), Materials Research Society, Davos, Switzerland, 415–422.

MYHRA, S., DELOGU, P., GIORGI, R. & RIVIERE, J. C. (1988): Scanning and high-resolution Auger analysis of zirconolite/perovskite surfaces following hydrothermal treatment. Journal of Materials Science, 23, 1514–1520.

MYHRA, S., SMART, R. S. C. & TURNER, P. S. (1987): Scientific and Technical Evaluation of the Synroc Fabrication Program, Griffith University, F.B. Neale.

NABIVANETS, B. I. & KUDRITSKAYA, L. N. (1967): Russ. J. Inorg. Chem., 12, 789.

NABIVANETS, B. I. & LUKACHINA, V. V. (1964): Hydroxyl complexes of titanium. Ukr. Khim. Zh., 30, 1123–1128.

NABIVANETS, B. I. & OMELCHENKO, Y. A. (1986): Carbonate-complexes of titanium in solution. Zhurnal Neorganicheskoi Khimii, 31, 356–359.

NAGRA (1990): Reference groundwater of crystalline, Nagra, CH-Wettingen.

NESBITT, H. W., BANCROFT, G. M., FYFE, W. S., KARKHANIS, S. N., NISHIJIMA, A. & SHIN, S. (1981): Thermodynamic stability and kinetics of perovskite dissolution. Nature, 289, 358–362.

NICKEL, E. H. & MCADAM, R. C. (1963): Niobian perovskite from Oka, Quebec: A new classification for minerals of the perovskite group. Canadian Mineralogist, 7, 683–697.

OBERHOLZER, W. F., GRAESER, S. & REUSSER, E. (1997): Senait, ein weiteres Vorkommen in einer alpinen Zerrkluft. Schweiz. Mineral. Petrogr. Mitt., 77, 233–236.

ONDINA FIGUEIREDO, M., CORREIA SANTOS, A., PARADA CORTINA, C. & JOAO BASTO, M. (1992): The pyrochlore line in the system CaO–ZrO_2–TiO_2: implications on Synroc phase assemblages. In: Scientific Basis for Nuclear Waste Management XV (ed. SOMBRET, C. G.), Materials Research Society, Boston, USA, 251–256.

ONUKI, H., AKASAKA, M., YOSHIDA, T. & NEDACHI, M. (1982): Ti-rich Hydroandradites from the Sanbagawa Metamorphic Rocks of the Shibukawa Area, Central Japan. Contrib. Mineral. Petrol., 80, 183–188.

ORLHAC, X., FILLET, C. & PHALIPPOU, J. (1999): Study of the Crystallization Mechanisms in the French Nuclear Waste Glass. In: Scientific Basis for Nuclear Waste Management XXII (eds. WRONKIEWICZ, D. J. & LEE, J. H.), Materials Research Society, Boston, USA, 133–140.

OVERSBY, V. M. & RINGWOOD, A. E. (1982): Radioactive Waste Management. Nuclear Fuel Cycle, 2, 223.

OVERSBY, V. M., VAN KONYNENBURG, R. A., GLASSLEY, W. E. & CURTIS, P. G. (1994): Immobilization in ceramic waste forms of the residues from treatment of mixed wastes. In: Scientific Basis for Nuclear Waste Management XVII (eds. BARKATT, A. & VAN KONYNENBURG, R. A.). Materials Research Society, Boston, USA, 285–292.

OVERSBY, V. M. & VANCE, E. R. (1995): Comparison of ceramic waste produced by hot uniaxial pressing and by cold pressing and sintering. In: Scientific Basis for Nuclear Waste Management XVIII (eds. MURAKAMI, F. & EWING, R. C.), Materials Research Society, Boston, USA, 825–832.

PARK, S. E., CHUNG, S. J., KIM, I. T. & HONG, K. S. (1994): Nonstoichiometry and the long-range cation ordering in crystals of $(Na_{1/2}Bi_{1/2})TiO_3$. J. Am. Ceram. Soc., 77 (10), 2641–2647.

PATERSON, B. A. & STEPHENS, W. E. (1992): Kinetically induced compositional zoning in titanite: implications for accessory phase/melt partitioning of trace elements. Contrib. Mineral. Petrol., 109, 373–385.

PHILIPP, R. W. (1988): Phasenbeziehungen im System MgO–H_2O–CO_2–NaCl. Unpubl. Ph.D. Thesis, ETH Zürich, Zürich, Switzerland.

PLATT, R. G. (1994): Perovskite, loparite and Ba–Fe hollandite from the Schryburt Lake carbonatite complex, northwestern Ontario, Canada. Mineral. Mag., 58, 49–57.

PREDA, M., REHNER, H. H. & NICOLESCU, C. (1997): The stabilization of zirconium dioxide in the ternary system CaO–TiO_2–ZrO_2. Journal of the European Cermaic Society, 17, 891–896.

PUDOVKINA, Z. V., DUBAKINA, L. S., LEVEDEVA, S. I. & PYATENKO, Y. A. (1974): Zap. Vses. Mineral. Obstch., 103, 368.

PYATENKO, Y. A. (1971): Izv. Akad. Nauk SSSR Neorg. Mater., 7, 630–633.

PYATENKO, Y. A. & PUDOVKINA, Z. V. (1964): The lattice meter of $CaZrTi_2O_7$ crystals. Kristallografiya, 9, 98–100.

RABER, E. & HAGGERTY, S. E. (1979): Zircon oxide reactions in diamond bearing kimberlites. In: Kimberlites, diatremes and diamonds: their geology, petrology and chemistry (eds. BOYD, F. R. & MEYER, H. O. A.), pp. 229–240, AGU, Washington.

RAGNARSDOTTIR, V. & WALTHER, J. V. (1985): Experimental determination of corundum solubilities in pure water between 400–700 °C and 1–3 kbar. Geochim. Cosmochim. Acta, 49, 2109–2115.

RAZ, U. (1983): Thermal and volumetric measurements on quartz and other substances at pressures up to 6 kbars and temperatures up to 700 °C. Unpubl. Ph.D. Thesis, ETH Zürich, Zürich, Switzerland.

REEVE, K. D., LEVINS, D. M., RAMM, E. J. & WOOLFREY, J. L. (1982): The development and evaluation of Synroc for high-level radioactive waste immobilization. IAEA-SM, 261/1, 375–390.

REEVE, K. D., LEVINS, D. M., RAMM, E. J., WOOLFREY, J. L., BUYKX, W. J., RYAN, R. K. & CHAPMAN, J. F. (1981): The development and testing of Synroc for high level radioactive waste fixation. Proc. Waste Management, 81 (1), 249–266.

REEVE, K. D., LEVINS, D. M., SEATONBERRY, B. W., RYAN, R. K., HART, K. P. & STEVENS, G. T. (1987): Final report on Fabrication and Study of Synroc Containing Radioactive Waste Elements, Australian Atomic Energy Commision.

REEVE, K. D., LEVINS, D. M., WOOLFREY, J. L. & RAMM, E. J. (1983): Immobilization of HLW in Synroc. In: Advances in Ceramics, American Ceramic Society, Columbus, OH, 200–208.

RELLER, A. (1993): Chemical and physical implications of cationic and anionic modifications in perovskite related metal oxides. Philosophical Magazine A, 68 (4), 641–652.

RIED, F. (1994): Titanmobilität: Metasosmatische, titanreiche Adern am Kontakt von Dolomitmarmoren zur Bergeller Intrusion. Unpubl. Ph.D. Thesis, ETH Zürich, Zürich, Switzerland.

RINGWOOD, A. E. (1978): Safe Disposal of High-Level Nuclear Reactor Wastes: A New Strategy. Australian National University Press, Canberra.

RINGWOOD, A. E. & KELLY, P. M. (1986): Philos. Trans. R. Soc. London Ser. A, 319, 63.

RINGWOOD, A. E., KESSON, S. E., REEVE, K. D., LEVINS, D. M. & RAMM, E. J. (1988): Synroc. In: Radioactive Waste Forms for the Future (eds. EWING, R.C. & LUTZE, W. L.), Elsevier, New York, 233–334.

RINGWOOD, A. E., KESSON, S. E., WARE, N., HIBBERSON, W. & MAJOR, A. (1979): Immobilisation of high-level nuclear reactor waste in Synroc. Nature, 278, 219–223.

RINGWOOD, A. E., MAJOR, A., RAMM, E. J. & PADGETT, J. (1983): Uniaxial Hot-Pressing in Bellows containers. Nucl. Chem. Waste Management, 4, 135–140.

RINGWOOD, A. E., OVERSBY, V. M., KESSON, S. E., SINCLAIR, W., WARE, N., HIBBERSON, W. & MAJOR, A. (1981): Immobilization of high-level nuclear reactor wastes in Synroc: a current appraisal. Nucl. Chem. Waste Management, 2, 287–305.

ROBERTS, W. L., CAMPBELL, T. J. & RAPP, G. R. (1990): Encyclopedia of minerals. New York Reinhold, 979.

ROBIE, R. A., HEMINGWAY, B. S. & FISHER, J. R. (1978): Thermodynamic Properties of Minerals and Related Substances at 298.15 K and 1 bar (10^5 Pascal) Pressure and at Higher Temperatures. USGS Bulletin, 1452.

ROSSELL, H. J. (1980): Zirconolite – a fluorite-related superstructure. Nature, 283, 282–283.

ROSSELL, H. J. (1982a): Calzirtite – a fluorite-related superstructure. Acta Cryst., B38, 593–595.

ROSSELL, H. J. (1982b): Short Structural Paper. Acta Cryst., B38, 593–595.

ROSSELL, H. J. (1992): Solid Solution of Metal Oxides in the Zirconolite Phase $CaZrTi_2O_7$. II: The Ternary Phase $CaZr_xTi_{3-x}O_7$. Journal of Solid State Chemistry, 99, 52–57.

ROSSOUW, C. J., TURNER, P. S. & WHITE, T. J. (1988a): Axial electron-channelling analysis of perovskite: I. Theory and experiments for $CaTiO_3$. Philosophical Magazine B, 57 (2), 209–225.

ROSSOUW, C. J., TURNER, P. S. & WHITE, T. J. (1988b): Axial electron-channelling analysis of perovskite: II. Site identification of Sr, Zr and U impurities. Philosophical Magazine B, 57 (2), 227–241.

ROSSOUW, C. J., TURNER, P. S., WHITE, T. J. & O'CONNOR, A. J. (1989): Statistical analysis of electron channelling microanalytical data for the determination of site occupancies of impurities. Philosophical Magazine Letters, 60 (5), 225–232.

ROTH, R. S. (1957): Classification of perovskite and other ABO_3-type compounds. Journal of Research of the National Bureau of Standards, 58 (2), 75–88.

RUBIN, J. N., HENRY, C. D. & PRICE, J. G. (1993): The mobility of zirconium and other «immobile» elements during hydrothermal alteration. Chemical Geology, 110, 29–47.

RYBACH, L. (1975): Thermische Fragen der Lagerung von radioaktiven Abfällen in Anhydrit. Bull. Ver. schweiz. Petroleum-Geol. u. -Ing., 41, 1–13.

RYERSON, F. J. (1984): Phase equilibria of nuclear waste ceramics: the effect of oxygen fugacity. J. Am. Ceram. Soc., 67 (2), 75–82.

SALVI, S. & WILLIAMS-JONES, A. E. (1990): The role of hydrothermal processes in the granite-hosted Zr, Y, REE deposit at Strange Lake, Quebec / Labrador: Evidence from fluid inclusions. Geochim. Cosmochim. Acta, 54, 2403–2418.

SALVI, S. & WILLIAMS-JONES, A. E. (1996): The role of hydrothermal processes in concentrating high-field strength elements in the Strange Lake peralkaline complex, northeastern Canada. Geochim. Cosmochim. Acta, 60, 1917–1932.

SCHMIDT, M. W. (1989): Petrography and structural evolution of ophiolitic remnants in the Bellinzona Zone, Southern Steep Belt, Central Alps (CH, I). Schweiz. Mineral. Petrogr. Mitt., 69, 393–405.

SCHUBNEL, H.-J. (1992): La Microsonde Raman en Gemmologie. Revue de Gemmologie, Juin 1992, 60.

SHANNON, R. D. (1976): Revised effective ionic radii and systematic studies of interatomic distances in halides and chalcogenides. Acta Cryst., A32, 751–767.

SHVAROV, Y. (1976): Dokl. Akad. Nauk SSSR, 229 (5), 1224.

SINCLAIR, W. & EGGLETON, R. A. (1982): Structure refinement of zirkelite from Kaiserstuhl, West Germany. American Mineralogist, 67, 615–620.

SINCLAIR, W., EGGLETON, R. A. & MCLAUGHLIN, G. A. (1986): Structure refinement of calzirtite from Jacupiranga, Brazil. American Mineralogist, 71, 815–818.

SINCLAIR, W. J. & RINGWOOD, A. E. (1981): Alpha-recoil damage in natural zirconolite and perovskite. Geochemical Journal, 15, 229–243.

SIZGEK, E., BARTLETT, J. R. & BRUNGS, M. P. (1998): Production of titanate microspheres by sol-gel and spray-drying. Journal of Sol-Gel Science and Technology, 13, 1011–1016.

SIZGEK, E., BARTLETT, J. R., WOOLFREY, J. L. & VANCE, E. R. (1994): Production of Synroc ceramics from titanate gel microspheres. In: Scientific Basis for Nuclear Waste Management XVII (eds. BARKATT, A. & VAN KONYNENBURG, R. A.), Materials Research Society, Boston, USA, 305–312.

SMITH, D. K. & NEWKIRK, H. W. (1965): The Crystal Structure of Baddeleyite and its Realtion to the Polymorphism of ZrO_2. Acta Crystallographica, 18, 983–991.

SMITH, K. L., BLACKFORD, M. G., LUMPKIN, G. R., HART, K. P. & ROBINSON, B. J. (1996): Neptunium doped Synroc: partitioning, leach data and secondary phase development. In: Scientific Basis for Nuclear Waste Management XIX (eds. MURPHY, W. M. & KNECHT, D. A.), Materials Research Society, Boston, USA, 313–319.

SMITH, K. L., COLELLA, M., THOROGOOD, G. J., BLACKFORD, M. G., LUMPKIN, G. R., HART, K. P., PRINCE, K., LOI, E. & JOSTSONS, A. (1997a): Dissolution of Synroc in deionised water at 150 °C. In: Scientific Basis for Nuclear Waste Management XX (eds. GRAY, W. J. & TRIAY, I. R.), Materials Research Society, Boston, USA, 349–354.

SMITH, K. L. & LUMPKIN, G. R. (1993): Structural features of zirconolite, hollandite and perovskite, the major waste-bearing phases in Synroc. In: Defects and Processes in the Solid State: Geoscience Applicartions (eds. BOLAND, J. N. & FITZ GERALD, J. D.), Elsevier: The McLaren Volume, 401–422.

SMITH, K. L., LUMPKIN, G. R. & BLACKFORD, M. G. (1993): Uranium and Rare Earth Partitioning in Synroc. In: Scientific Basis for Nuclear Waste Management XVI, Materials Research Society, Boston, USA, 129–136.

SMITH, K. L., LUMPKIN, G. R., BLACKFORD, M. G., DAY, R. A. & HART, K. P. (1992): The durability of Synroc. Journal of Nuclear Materials, 190, 287–294.

SMITH, K. L., LUMPKIN, G. R., BLACKFORD, M. G., HAMBLEY, M., DAY, R. A., HART, K. P. & JOSTSONS, A. (1997b): Characterization and Leaching behavior of Plutonium-bearing Synroc C. In: Scientific Basis for Nuclear Waste Management XX (eds. GRAY, W. J. & TRIAY, I. R.), Materials Research Society, Boston, USA, 1267–1272.

SMITH, K. L., ZALUZEC, N. J. & LUMPKIN, G. R. (1997c): In situ studies of ion irradiated zirconolite, pyrochlore and perovskite. Journal of Nuclear Materials, 40230, 1–17.

SOBOLEV, I. A., STEFANOVSKY, S. V. & LIFANOV, F. A. (1995): Synthetic melted rock-type wasteforms. In: Scientific Basis for Nuclear Waste Management XVIII (eds. MURAKAMI, F. & EWING, R. C.), Materials Research Society, Boston, USA, 833–840.

SOLOMAH, A. G. (1983): Nuclear Technology, 62, 311.

SOLOMAH, A. G. & ZUMWALT, L. R. (1982): Nucl. Chem. Waste Management, 3, 111.

SPEAR, F. S. (1993): Metamorphic Phase Equilibria and Pressure–Temperature–Time Paths. Mineralogical Society of America, Monograph.

STALDER, R., FOLEY, S. F., BREY, G. P., FORSYTHE, L. M. & HORN, I. (1997): First Results from a new Experimental Technique to Determine Fluid/Solid Trace Element Partition Coefficients Using Diamond Aggregate Extraction Traps. Neues Jahrb. Mineral. Abh., 172, 117–132.

STROBEL, G. (1971): Mineralogie und Kristallographie. Verlag Studiengemeinschaft Kamprath, Darmstadt.

SUWA, Y., INAGAKI, M. & NAKA, S. (1984): Polymorphic transformation of titanium dioxide by mechanical grinding. J. Mater. Sci., 19, 1397–1405.

SWENSON, D., NIEH, T. G. & FOURNELLE, J. H. (1996): The $CaO–TiO_2–ZrO_2$ system at 1200 °C and the solubilities of Hf and Gd in zirconolite. In: Scientific Basis for Nuclear Waste Management XIX (eds. MURPHY, W. M. & KNECHT, D. A.), Materials Research Society, Boston, USA, 337–344.

TROMMSDORFF, V. & EVANS, B. W. (1980): Titanian hydroxyl-clinohumite: Formation and breakdown in antigorite rocks (Malenco, Italy). Contrib. Mineral. Petrol., 72, 229–242.

TROMMSDORFF, V. & SKIPPEN, G. (1986): Vapour loss («Boiling») as a mechanism for fluid evolution in metamorphic rocks. Contrib. Mineral Petrol., 94, 317–322.

TROMMSDORFF, V. & SKIPPEN, G. (1987): Metasomatism involving fluids in $CO_2–H_2O–NaCl$. In: Chemical Transport in Metasomatic Processes (ed HELGESON, H. C.), 133–152.

TSYPLENKOV, V. S. (1993): The IAEA coordinated research programme on the performance of high-level waste forms and packages under repository conditions. In: Scientific Basis for Nuclear Waste Management XVI (eds. INTERRANTE, C. G. & PABALAN, R. T.), 719–723.

USDOE (1994): Compendium of Corrosion Characteristic, United States Department of Energy.

VAN BAALEN, M. R. (1993): Titanium mobility in metamorphic systems: a review. Chemical Geology, 110, 233–249.

VAN DER VEEN, A. H. (1965): Calzirtite and Associated Minerals from Tapira, Brazil. Mineral. Mag., 35, 544–547.

VAN ISEGHEM, P., JIANG, W., BLANCHAERT, M., HART, K. & LODDING, A. (1996): The interaction between Synroc-C and pure water or boom clay. In: Scientific Basis for Nuclear Waste Management XIX (eds. MURPHY, W. M. & KNECHT, D. A.), Materials Research Society, Boston, USA, 305–312.

VAN KONYNENBURG, R. A., HOPPER, R. W., RARD, J. A., RYERSON, F. J., PHINNEY, D. L., HUTCHEON, I. D. & CURTIS, P. G. (1996): Ceramic waste form for residues from molten salt oxidation of mixed wastes. In: Scientific Basis for Nuclear Waste Management XIX (eds. MURPHY, W. M. & KNECHT, D. A.), Materials Research Society, Boston, USA.

VANCE, E. R. (1994): Synroc: A Suitable Waste Form for Actinides. MRS Bulletin, XIX (12), 28–32.

VANCE, E. R., ANGEL, P. J., BEGG, B. D. & DAY, R. A. (1994a): Zirconolite-rich titanate ceramics for high-level actinide waste. In: Scientific Basis for Nuclear Waste Management XVII (eds. BARKATT, A. & VAN KONYNENBURG, R. A.) Materials Research Society, Boston, USA, pp. 293–298.

VANCE, E. R., BALL, C. J., BLACKFORD, M. G., CASSIDY, D. J. & SMITH, K. L. (1990a): Crystallisation of zirconolite from an alkoxide precursor. Journal of Nuclear Materials, 175, 58–66.

VANCE, E. R., BALL, C. J., DAY, R. A., SMITH, K. L., BLACKFORD, M. G., BEGG, B. D. & ANGEL, P. J. (1993): Actinide and rare-earth incorporation in zirconolite, $CaZrTi_2O_7$. Actinides, 93, 1–5.

VANCE, E. R., BALL, C. J., DAY, R. A., SMITH, K. L., BLACKFORD, M. G., BEGG, B. D. & ANGEL, P. J. (1994b):

Actinide and rare earth incorporation into zirconolite. Journal of Alloys and Compounds, 213/214, 406–409.

VANCE, E. R., BEGG, B. D., DAY, R. A. & BALL, C. J. (1995): Zirconolite-rich ceramics for actinide wastes. In: Scientific Basis for Nuclear Waste Management XVIII (eds. MURAKAMI, F. & EWING, R. C.), Materials Research Society, Boston, USA, 767–774.

VANCE, E. R., CASSIDIY, D. J., BALL, C. J. & THOROGOOD, G. J. (1992a): High-temperature study of $CaZrTi_2O_7$. Journal of Nuclear Materials, 190, 295–297.

VANCE, E. R., CASSIDY, D. J., SMITH, K. L. & WOOLFREY, J. L. (1990b): Calcination, redox control and waste loading of Synroc. Ceramic Transactions, 9, 71–81.

VANCE, E. R., DAY, R. A., CARTER, M. L. & JOSTSONS, A. (1996a): A melting route to Synroc for Hanford HLW immobilization. In: Scientific Basis for Nuclear Waste Management XIX (eds. MURPHY, W. M. & KNECHT, D. A.), Materials Research Society, Boston, USA, 289–295.

VANCE, E. R., DAY, R. A., ZHANG, Z., BEGG, B. D., BALL, C. J. & BLACKFORD, M. G. (1996b): Charge Compensation in Gd-Doped $CaTiO_3$. Journal of Solid State Chemistry, 124, 77–82.

VANCE, E. R., DAY, R. A., ZHANG, Z., BEGG, B. D., BALL, C. J. & BLACKFORD, M. G. (1998): Reply to «Does Lanthanide Substitution Reduce Titanium from Ti^{4+} to Ti^{3+} in the Perovskite $CaTiO_3$ Fired at 1550 °C in Air?». J. Solid State Chem., 137, 357–358.

VANCE, E. R., HART, K. P., DAY, R. A., BEGG, B. D., ANGEL, P. J., LOI, E., WEIR, J. & OVERSBY, V. M. (1996c): Excess Pu disposition in zirconolite-rich Synroc containing nepheline. In: Scientific Basis for Nuclear Waste Management XIX (eds. MURPHY, W. M. & KNECHT, D. A.), Materials Research Society, Boston, USA, 49–55.

VANCE, E. R., JOSTSONS, A., DAY, R. A., BALL, C. J., BEGG, B. D. & ANGEL, P. J. (1996d): Excess Pu disposition in zirconolite-rich Synroc. In: Scientific Basis for Nuclear Waste Management XIX (eds. MURPHY, W. M. & KNECHT, D. A.), Materials Research Society, Boston, USA, 41–47.

VANCE, E. R., SMITH, K. L., THOROGOOD, G. J., BEGG, B. D., MORICCA, S. S., ANGEL, P. J., STEWART, M. W. A., BLACKFORD, M. G. & BALL, C. J. (1992b): Alternative Synroc formulations. In: Scientific Basis for Nuclear Waste Management XV (ed. SOMBRET, C. G.), Materials Research Society, Boston, USA, 235–241.

VANCE, E. R., STEWART, M. W. A., DAY, R. A., HART, K. P., HAMBLEY, M. J. & BROWNSCOMBE, A. (1997): Pyrochlore-rich Titanate Ceramics for Incorporation of Plutonium, Uranium and Process Chemicals, ANSTO, Materials Division.

VANCE, E. R. & THOROGOOD, G. J. (1991): Immobilisation of sodium in perovskite. J. Am. Ceram. Soc., 74 (4), 854–855.

VARD, E. & WILLIAMS-JONES, A. E. (1993): A fluid inclusion study of vug minerals in dawsonite-altered phonolite sills, Montreal, Quebec: implications for HFSE mobility. Contrib. Mineral. Petrol., 113, 410–423.

VAVRECKA-SIDLER, D. M. (1998): Aluminium tschermak substitution in chlorite in the system $MgO–Al_2O_3–SiO_2–H_2O$ – A theoretical and experimental approach. Unpubl. Ph.D. Thesis, ETH Zürich, Zürich, Switzerland.

VLASOV, K. A. (1966): Mineralogy of Rare Elements. Academy of Science of the USSR, Jerusalem.

VOGLER-PAZELLER, G. I. (1990): Untersuchungen über hydrothermale TiO_2-Vorkommen der Schweizer Alpen. Unpubl. Ph.D. Thesis, ETH Zürich, Zürich, Switzerland.

WAGNER, A. (1975): Beobachtungen an Titanmineralien aus alpinen Zerrklüften. Urner Mineralienfreund, 13, 31–36.

WATSON, E. B. & LIANG, Y. (1995): A simple model for sector zoning in slowly grown crystals: Implications for growth rate and lattice diffusion, with emphasis on accessory minerals in crustal rocks. American Mineralogist, 80, 1179–1187.

WEBER, W. J., WALD, J. W. & MATZKE, H. (1985): Self-radiation damage in $Gd_2Ti_2O_7$. Mater. Lett., 3, 173–180.

WHITE, T. J. (1984): The microstructure and microchemistry of synthetic zirconolite, zirkelite and related phases. American Mineralogist, 69, 1156–1172.

WHITE, T. J., EWING, R. C., WANG, L. M., FORRESTER, J. S. & MONTROSS, C. (1994a): Temperature dependence of amorphization for zirconolite and perovskite irradiated with 1 MeV Krypton ions. In: Scientific Basis for Nuclear Waste Management XVIII (eds. MURAKAMI, T. & EWING, R. C.), Materials Research Society, Boston, USA, 1413–1420.

WHITE, T. J., MITAMURA, H., HOJOU, K. & FURUNO, S. (1994b): Radiation stability of ceramic waste forms determined by in situ electron microscopy and He ion irradiation. In: Scientific Basis for Nuclear Waste Management XVII (eds. BARKATT, A. & VAN KONYNENBURG, R. A.), Materials Research Society, Boston, USA.

WHITE, T. J., SEGALL, R. L., BARRY, J. C. & HUTCHISON, J. L. (1984a): Twin Boundaries in Perovskite. Acta Cryst., B41, 93–98.

WHITE, T. J., SEGALL, R. L., HUTCHISON, J. L. & BARRY, J. C. (1984b): Polytypic behaviour of zirconolite. Proc. R. Soc. Lond., A 392, 343–358.

WILLIAMS, C. T. (1996): The occurrence of niobian zirconolite, pyrochlore and baddeleyite in the Kovdor carbonatite complex, Kola Penninsula, Russia. Mineral. Mag., 60, 639–646.

WILLIAMS, C. T. & GIERÉ, R. (1988): Metasomatic zonation of REE in zirconolite from a marble skarn at the Bergell contact aureole (Switzerland/Italy). Schweiz. Mineral. Petrogr. Mitt., 68, 133–140.

WILLIAMS, C. T. & GIERÉ, R. (1996): Zirconolite: a review of localities worldwide, and a compilation of its chemical compositions. Bulletin of the Natural History Museum, London (Geology), 52 (1), 1–24.

WOOD, S. A. (1990a): The aqueous geochemistry of the rare-earth elements and yttrium: 1. Review of available low-temperature data for inorganic complexes and the inorganic REE speciation of natural waters. Chemical Geology, 82, 159–186.

WOOD, S. A. (1990b): The aqueous geochemistry of the rare-earth elements and yttrium: 2. Theoretical predic-

tions of speciation in hydrothermal solutions to 350 °C at saturation water vapor pressure. Chemical Geology, 88, 99–125.

WOOD, S. A. (1993): The aqueous geochemistry of the rare-earth elements: Critical stability constants for complexes with simple carboxylic acids at 25 °C and 1 bar and their application to nuclear waste management. Engineering Geology, 34, 229–259.

WOOD, S. A. & WILLIAMS-JONES, A. E. (1994): The aqueous geochemistry of the rare-earth elements and yttrium: 4. Monazite solubility and REE mobility in exhalative massive sulfide-depositing environments. Chemical Geology, 115, 47–60.

WOOLFREY, J. L., CASSIDY, D., BUYKX, W. J., DICKSON, F. & WHITE, T. J. (1988): The calcination of Synroc powders. In: Proceedings of Bicentennial Conference, pp. 105–111, Institute of Metals and Materials Australasia.

WORLDSCAN, N. E. (1999): World Report 1998.

WYSS, W. (1995): Synthese und thermochemische Eigenschaften von oxidischen Perowskiten mit Sr, La, Fe und Zr. Unpubl. Ph.D. Thesis, Universität Zürich, Zürich.

YAMANAKA, H., NISHII, J., AKAI, T., YAMASHITA, M. & WAKABAYASHI, H. (1995): Preparation of hydrated glass as a model of long-term leached nuclear waste glass. In: Scientific Basis for Nuclear Waste Management XVIII (eds. MURAKAMI, F. & EWING, R. C.), Materials Research Society, Boston, USA.

ZARAISKY, G. P. (1995): The influence of acidic fluoride and chloride solutions on the geochemical behaviour of Al, Si and W. In: Fluids in the Crust (ed. SHMULOVICH, K. I.), pp. 139–162, Chapman and Hall.

ZDORIK, T. B., SIDORENKO, G. A. & BYKOVA, A. V. (1961): A new titanozirconate of calcium-calzirtite. Translation of Doklady Akademii Nauk SSSR, 137 (3), 443–446 (original 681–684).

ZHABIN, A. G., PUDOVKINA, Z. V. & BYKOVA, A. V. (1962): Calzirtite from the carbonatites of the Gula ultrabasic intrusion in polar siberia. Translation from Doklady Akademii Nauk SSSR, 146 (6), 140–141 (original 1399–1400).

ZHURAVLEVA, L. N., BEREZINA, L. A. & GULIN, Y. E. N. (1976): Geochemistry of rare and radioactive elements in apatite–magnetite ores in alkali-ultrabasic complexes. Geochem. Int., 13 (5), 147–166.